FABRICATION AND STUDY OF ZnO NANOWIRES, rGO AND rGO-ZnO NANOCOMPOSITE BASED GAS SENSORS

A THESIS

Submitted in partial fulfilment of the requirements for the award of the degree of

DOCTOR OF PHILOSOPHY

in

NANOTECHNOLOGY

by

NAGESH KUMAR

CENTRE OF NANOTECHNOLOGY
INDIAN INSTITUTE OF TECHNOLOGY ROORKEE
ROORKEE-247 667 (INDIA)
MARCH, 2014

INDIAN INSTITUTE OF TECHNOLOGY ROORKEE
ROORKEE

CANDIDATE'S DECLARATION

I hereby certify that the work which is being presented in the thesis entitled "**FABRICATION AND STUDY OF ZnO NANOWIRES, rGO AND rGO-ZnO NANOCOMPOSITE BASED GAS SENSORS**" in partial fulfilment of the requirements for the award of the Degree of Doctor of Philosophy and submitted in Centre of Nanotechnology, Indian Institute of Technology Roorkee is an authentic record of my own work carried out during a period from January, 2008 to March, 2014 under the supervision of **Dr. G. D. Varma**, Associate Professor, Department of Physics and Centre of Nanotechnoloy, Indian Institute of Technology Roorkee, Roorkee, India.

The matter presented in the thesis has not been submitted by me for the award of any other degree of this or any other Institute.

(NAGESH KUMAR)

This is to certify that the above statement made by the candidate is correct to the best of my knowledge.

Date: .....

(G.D.Varma)
Supervisor

The Ph. D. Viva-Voce Examination of **Mr. Nagesh kumar**, Research Scholar, has been held on ……..... at .....……..

Signature of Supervisor Chairman, SRC Signature of External Examiner

Head of the Department/Chairman, ODC

ABSTRACT

When a bulk material is transformed to nanoscale material (at least one dimension between 1 to 100 nm), its electronic structure changes which in turns modifies its various chemical and physical properties. Thus nanoscale material behaves differently from its bulk counterpart and can be considered as a new material. Among all the nanoscale materials, metal oxide nanostructures have been studied extensively because of their numerous technological applications. It has been observed that only a few metal oxides, which possess either d^0 (TiO_2, WO_3, Sc_2O_3, V_2O_5, CrO_3 and perovskites such as $ScTiO_3$, $LiNbO_3$) or d^{10} (ZnO, SnO_2, Cu_2O, In_2O_3) electronic configuration of cations, exhibit feasible gas sensing properties. Although there exist a few metal oxides with d^n ($0<n<10$) configuration of cations (NiO, VO_2, Cr_2O_3, RuO_2 etc.) which are sensitive to the environment in their vicinity, but these are structurally unstable under oxidation or reduction processes. Among the metal oxide nanostructures, ZnO is one of the most studied semiconducting materials. It possesses thermodynamically highly stable wurtzite (hexagonal close packed) crystal structure in which lattice constant ratio c/a ~ 1.60 deviates slightly from the ideal value of hexagonal cell (c/a = 1.633) due to difference in electronegativity values of Zn^{2+} and O^{2-} ions. ZnO exhibits almost all the unique properties required to make it a feasible gas sensor such as moderate direct band gap (3.37 eV), high mobility of conduction electrons, better chemical and thermal stability under ambient conditions and good activity in redox reactions.

It has been reported that when the size of a nanostructure material reduces to less than or equal to the Debye length of the material, the mobile charge carrier density within the whole nanostructure will depend on the surface redox process. This implies that nanostructures with smaller grain size or better aspect ratio will exhibit higher sensitivity. Thus 0D, 1D, 2D and 3D nanostructure of ZnO have been extensively studied worldwide to utilize their excellent gas sensing properties for fabrication of improved gas sensing devices at low cost. Moreover, the longer dimension of 1D ZnO nanostructures (nanotubes, nanowires and nanorods) makes them suitable to connect with the macroscopic world for electrical and many other physical measurements. Therefore, 1D nanostructures are more appropriate for the fabrication of nanoelectronic devices like gas sensors, electron-field emitters and logic devices etc. However, in order to have a control over the material properties and developing functional devices, it is necessary to synthesize nanostructures with high degree of regularity and alignment at low cost. A number of techniques have

been developed in this regard so far but most of them are very sensitive to precursor composition and decomposition conditions. In addition, some of these techniques are expensive too, thus a reliable and low cost synthesis technique which may be used to synthesize ordered 1D nanostructures is still being sought. Many research groups have reported that gas sensors based on an individual nanostructure exhibit excellent gas sensing properties but the processing of an individual nanostructure is not so easy hence not suitable for the mass production of the sensor. This problem can be minimized by using bunches or bundles of well-aligned nanostructures as the sensing material for gas sensors. Furthermore, ZnO, due to its direct band gap of 3.37 eV at room temperature and much higher exciton binding energy (60 meV) as compared to other semiconductor materials, has potential applications in short wavelength optoelectronic devices such as blue-, violet-, and UV- light emitting diodes (LEDS) and laser diodes (LDs).

In the present thesis we report the facile synthesis of highly ordered luminescent ZnO nanowire arrays using low temperature anodic aluminum oxide (AAO) template route which can be economically produced in large scale quantity. The as synthesized ordered ZnO nanowire arrays based gas sensor has been fabricated using simple micromechanical technique.

Another important nanosacle material, which we have investigated in the present research work, is a 2D allotrope of carbon known as graphene. Graphene is an atomic thin layer of carbon atoms arranged in a honeycomb hexagonal lattice with sp^2 hybrization. The other graphitic nanomaterials like 0D fullerenes and 1D carbon nanotubes can be considered as the different geometrical forms of it. Graphene has become a big hub for numerous applications in diverse research domains that exploit its excellent mechanical, electrical, chemical, biological, thermal and optical properties after its experimental discovery in 2004. Along with other fascinating properties graphene, with high surface area to volume ratio offers a large exposed area for gas molecules. Graphene with high conductivity and metallic transport properties (Fermi velocity (v_F)=10^6 m/s) exhibits very little Johnson's noise which makes it a potential material for gas sensing applications.

In the present thesis we have chemically synthesized thin films of graphene oxide (GO) and reduced graphene oxide (rGO) and investigated their electrical, optical, sensing and antibacterial properties. Furthermore, we have also investigated the gas sensing properties of rGO-ZnO nanocomposite at different temperatures.

The present thesis is divided into six chapters. The **first chapter** contains an introductory aspect of the concern research field, summary of previous work carried out by different research groups and motivation of the present work.

In the **second chapter** we have given detailed description of the synthesis techniques like anodization, vacuum injection, spin coating and hydrolysis used to prepare samples. This chapter also contains a brief description of the experimental techniques used for the characterization of the synthesized samples. Structural and surface morphological studies were performed using X-ray diffraction (XRD), transmission electron microscopy (TEM), field emission scanning electron microscopy (FE-SEM) in secondary electron (SE) imaging mode, and atomic force microscopy (AFM). Energy dispersive X-ray (EDX) spectroscopy has been used for elemental analysis and mapping. Thermogravimetric analysis (TGA), photoluminescence spectroscopy (PL) and other spectroscopic techniques like X-ray photo electron spectroscopy (XPS), Fourier Transform Infrared Spectroscopy (FTIR) and Raman spectroscopy have been used to investigate the stability, quality and the extent of graphitization of the samples.

In the **third chapter**, we have described the fabrication and successful detaching of AAO template from the Al substrate. In this chapter, empty pores of the template were filled with saturated aqueous solution of $Zn(NO_3)_2$ through indigenously developed vacuum injection technique. After sintering in air at 435°C the template was dissolved in NaOH solution and the collected ZnO nanowires were used for further characterization. From the microscopic studies (FE-SEM and TEM), we found that the ZnO nanowires were polycrystalline, dense and uniform throughout the length. In this chapter we have designed a two-Cu electrode set-up to investigate the NH_3 gas sensing properties of as synthesized ZnO nanowires arrays at room temperature. Our measurements show that this sensor possesses good % response and fast response- and recovery- times against different concentrations of NH_3 gas. Here we also discussed the possible mechanism which explains the observed sensing properties of the sensor.

The **fourth chapter** describes the synthesis of GO powder and fabrication of GO and rGO thin films. The successful synthesis of GO and rGO was verified using XRD, TEM, PL, Raman and XPS. TEM micrograph of rGO reveals the presence of a few wrinkles, which is expected on the graphene surfaces. AFM and FESEM images revealed that the synthesized rGO film is almost continuous and homogeneous. The optical, electrical and gas sensing properties of the rGO thin film have been extensively monitored. It is observed that rGO thin film possesses good electrical conductivity ~104 S m^{-1} at room

temperature and exhibits good gas sensing properties for various concentrations of Cl_2 and NO_2 gases. Furthermore, the as-synthesized GO and rGO thin films show excellent bacterial toxicity for both Gram +ve (B. cereus) and Gram -ve (E. coli) models of bacteria which implies that GO and rGO can be used as effective antibacterial coatings.

The **fifth chapter** describes the synthesis of rGO-ZnO nanocomposite (ZrGO) and rGO powders. The prepared samples were characterized through microscopic techniques (FE-SEM and TEM) to explore the surface morphology and uniformity of the samples. XRD, TEM, EDAX and other spectroscopic techniques (Raman, XPS and FTIR) were employed to verify the quality of the samples and to confirm the presence of ZnO and rGO in the composite. TGA data reveals that ZrGO sample possesses better stability than pristine rGO. The order of stability for the samples is GO < rGO < ZrGO. We have used coil sensors with two Pt terminals and a heating arm to monitor the effect of temperature on electrical and gas sensing properties of the rGO and rGO-ZnO nanocomposite samples. We find that rGO-ZnO nanocomposite possesses better electrical and NO_2 gas sensing properties compared to pristine rGO. It is also observed that rGO-ZnO nanocomposite sensor exhibits highest response (~32%) for 50 ppm NO_2 at relatively low temperature (50°C). We have also checked the repeatability of the sensor for five successive cycles for fixed ppm NO_2 concentration. It is observed that % response initially decreases slighltly but later it become almost constant.

The **sixth chapter** contains a brief summary of the work presented in the thesis, concluding remarks and the scope for future work.

LIST OF PUBLICATIONS

A. Publications Related to the Thesis

1. **Nagesh Kumar,** G.D. Varma, R. Nath and A.K. Srivastava, "Synthesis of ordered ZnO nanowire arrays from aqueous solution using AAO template", Appl Phys A, **104**, 1169 (2011).
2. **Nagesh Kumar,** A.K Srivastava, R. Nath, Bipin Kumar Gupta and G.D.Varma, "Probing a highly efficient room temperature ammonia gas sensing properties of luminescent ZnO nanowires array via AAO assisted template route" Dalton Trans., **43,** 5713 (2014).
3. **Nagesh Kumar,** Bipin Kumar Gupta, A.K Srivastava, H.S.Patel, Indradeep Banerjee Tharangattu N. Narayanan and G.D.Varma, "Multifunctional antibacterial reduced graphene oxide two dimensional thin film for high-performance gas sensing applications", Sci. Adv. Mater. (Under Review).
4. **Nagesh Kumar,** A.K Srivastava, H.S. Patel, Bipin Kumar Gupta and G.D.Varma "Synthesis of ZnO-rGO nanocomposite and its gas sensing behavior towards NO_2", Sensors and Actuators B: Chemical. (Submitted after Minor revision).

B. Other Publications

1. **Nagesh Kumar,** Anurag Gaur and G.D. Varma, "Enhanced magnetization and magnetoelectric coupling in hydrogen treated hexagonal $YMnO_3$", J. Alloys Compd., **509,** 1060 (2011).
2. Sudesh, **Nagesh Kumar**, S. Das, C. Bernhard and G. D. Varma, "Effect of graphene oxide doping on superconducting properties of bulk MgB_2" Supercond. Sci. Technol., **26**, 095008 (2013).

C. Conferences

1. **Nagesh Kumar**, Anurag Gaur and G.D. Varma, "Magnetoelectric effects in $YMnO_3$-LSMO composites", Proceedings of the 54th DAE Solid State Physics Symposium 14 – 18, December (2009).
2. **Nagesh Kumar**, U. K. Gaur, A.K Srivastava and G.D. Varma, "Fabrication of anodized alumina template and synthesis of metal oxide nanowires using it",

National Conference on Advances in Physics (NCAP - 2012), held at IIT Roorkee, Roorkee, Uttarakhand during March 26 –27, 2012.

3. Amit Sanger, **Nagesh Kumar**, GD Varma "Synthesis of NiO nanoparticles and studying their structural, optical, and magnetic properties", 6th India Singapore Joint Physics Symposium (ISJPS-2013) on Physics of Advance Materials February 25-27, 2013.

4. Sudha, **Nagesh Kumar** and GD Varma, "Synthesis of Pure and Mn doped tin oxide (SnO_2) Nanoparticles and studying their strutural properties", 6th India Sing--apore Joint Physics Symposium (ISJPS-2013) on Physics of Advance Materials February 25-27, 2013.

My research work involved the contributions and cooperation from many people to whom I would always remain thankful.

First of all, I would like to express my sincere sense of gratitude to my respected supervisor, Dr. G. D. Varma for his guidance, inspiration and encouragement throughout this work. I was fortunate enough to have an opportunity to work under his supervision and gain from his knowledge and experience.

I also have deep sense of gratitude to Prof. Vijaya Agarwala, H. O. D, Centre of Nanotechnology and Prof. A. K. Jain, H. O. D, Department of Physics for providing me all the necessary facilities required for the accomplishment of this work. I am also grateful to my SRC members, Prof. Anil Kumar (Chairman, Centre of Nanotechnology and Department of Chemistry), Prof. R. Nath (External Member, Department of Physics), and Prof. T. Nautiyal (Internal Member, Centre of Nanotechnology and Department of Physics) for constructive criticism and valuable suggestions at every stage of the work.

I am also grateful to all other faculty members associated with Centre of Nanotechnology for their keen interest in this work. I am highly obliged and express my sincere thanks to the official and technical staff of Centre of Nanotechnology Mr. Rawan Pal, Mr. Abdul Hacq, Mr. Vinod, Moh. Riyaj, and Mr. Naresh Kumar.

I would like to thanks the technical staff of the Institute Instrumentation Center (I.I.C), I.I.T. Roorkee, Mr. S. D. Sharma, Mr. Shiv Kumar Saini, Mr. Shiv Kumar and Mr. Virendra Singh for their help at the various stages for the characterization of the samples.

I am deeply indebted to Dr. A. K. Srivastava (RRCAT, Indore) and Dr. Bipin Gupta (NPL, New Delhi) for their valuable suggestions and discussion.

I express my special thanks to my seniors Dr. Anurag Gaur, Dr. Yogesh Sharma, Dr. Vijay Kumar Sharma and Dr. Nigamananda Ojha for their encouragement and support when needed.

I greatly enjoyed working with all my lab mates Dr. Kamlesh Yadav, Miss. Sudesh, Mr. Umesh Kumar Gaur, Miss. Stuti rani and Mr. Rohit.

The inspiration, support, cooperation and patience which I have received from my friends are beyond the scope of any acknowledgement, yet I would like to express my heartfelt thank to my friends, Dr. Ramesh Dhiman, Ritesh Sharma, Arvind Panwar, Indredeep Banerjee, Rajwant Singh, Ajit Katiyar, Dr. Ashok Nandam, Dr. Shubhchintak, A. V. Reddy, Hempal, Sant Kumar, Venu, Rahul Barman, Babita, Reena, Raman Bhullar,

Lata, Jyoti, Nidhi, Amit Sangar, Ashwani Chhokar, Vipul Bhardwaj, Sushil Vashisth, Vinay, Rajan Rathi, Dr. Parmod, Ovindar, Sandeep Mogha and all other research scholars of Centre of Nanotechnology and Physics Department for their company and for the quality time that I spent with them.

I express my heartfelt gratitude to my highly respectable and adorable parents, Sri. Puran Chand and mother, Smt. Raj Bala Devi for their unconditional love, encouragement and blessing.

I also express gratitude to my elder sisters Neeraj and brother-in-law Sqn Ldr Amit Sharma for their love, moral support and encouragement and a lot of love to my lovely nephew Madhur.

I thank with love my wife Rekha Sharma for her patience and unconditional trust. She has been my best friend and a great companion who loved, supported, encouraged and helped me to get through this period in the most positive way.

I also want to express my sincere thanks to all those who directly and indirectly helped me at various stage of the work but I would not mention their name due to shortage of the space.

The financial support provided by Board of Research in Nuclear Sciences (BRNS) through JRF scheme and Council of Scientific & Industrial Research (CSIR) through SRF scheme is gratefully acknowledged. Lastly but most importantly, I would like to thank God for his blessings.

I.I.T. Roorkee **(Nagesh Kumar)**

March, 2014

CONTENTS

LIST OF FIGURES

LIST OF TABLES

0D	Zero dimensional
1D	One dimensional
2D	Two dimensional
3D	Three dimensional
AC	Alternating current
AAO	Anodized Aluminum oxide
ZnO	Zinc Oxide
GO	Graphite Oxide
rGO	Reduced graphene oxide
ZrGO	rGO-ZnO nanocomposite
CVD	Chemical vapor deposition
DLE	Deep level emission
LED	Light emitting diode
PL	Photoluminescence
UV	Ultraviolet
LD	Laser diodes
CNT	Carbon Nanotube
E	Electric field
S	% response
C	Concentration
hrs	Hours
ppm	Part per million
nm	nanometer
Relative humidity	RH%
In plane crystalline size	*La*
CIE	International Commission on Illumination
FTIR	Fourier Transform InfraRed
SEM	Scanning Electron Microscopy
FE-SEM	Field Emission Scanning Electron Microscopy
EDX	Energy Dispersive X-ray Spectroscopy
XRD	X-ray Diffraction
AFM	Atomic Force Microscope

TEM	Transmission Electron Microscopy
HRTEM	High-resolution Transmission Electron Microscope
SAED	Selected area electron diffraction
XPS	X-ray Photoelectron Spectroscopy
TGA	Thermogravimetric Analysis
HOPG	Highly Oriented Pyrolytic Graphite
VRH	Variable range hoping
PTFE	Polytetrafluoroethylene
DLE	Deep level emission
DMF	Dimethylformamide
SiC	Silicon carbide
NP	Nanoparticles
NS	Nanostructures
DI	De-Ionized

Chapter-1

INTRODUCTION

Legendary physicist Richard P. Feynman was the first person who talked about imaginative nanoworld and nanomachining in his two famous seminar lectures: 'There's plenty of room at the bottom' in 1959 and "Tiny Machines." in 1984. This is why some people gave him credit for kick-starting nanotechnology. However, the term nanotechnology was first used by Japanese scientist Norio Taniguchi in 1974. Undoubtedly Feynman's vision initially motivated the researchers towards nanotechnology which now has been transformed to global nanotechnology race. Today nanotechnology has impact on every aspect of life as well as on every research field such as electronic, material science, medical science, chemical science, engineering, computing and communications. Several nanotechnology based products (including medicines and excellent devices) have been fabricated so far and according to Global Information Inc (GII) the global market for nanotechnology based products is projected to reach $3.3 trillion by 2018 [1]. It will enhance the opportunities for nanotechnology industries in the upcoming years.

1.1 NANOTECHNOLOGY PAST, PRESENT AND FUTURE

According to Feynman vision, nanotechnology is the development of nanomachines which can build another nanomachines (e.g. tiny robots) or other systems by manipulating matter at the atomic scale and it seemed unrealistic until the development of first scanning tunneling microscope by Gerd Binnig and Heinrich Rohrer in 1981 which makes possible to see individual atoms. Thus the development of modern nanotechnology began just 30 years ago after the development of scanning tunneling microscope (STM) and the atomic force microscope (AFM).

Today nanoscale science (length scale of approximately 1 to 100 nanometers) has occupied more or less a portion in almost every research laboratory of the world. Although, nanotechnology is a modern concept but in the ancient time too people were using nanoscale science unknowingly in various parts of the world and a few examples are

given here. (1) A portion of **Lycurgus cup** (a 4th-century Roman glass cage cup) contains gold-silver alloyed nanoparticles which look brilliant red when light passes through it. (2) **Maya blue** (a corrosion resistance pigment) is a composite material derived from palygorskite, a natural clay which possesses nanopores in it and indigo dye which fills the nanopores forms an environmentally-stable pigment. (3) Blades of **Damascus steel sword** contain carbon nanotubes and cementite nanowires which provide them extreme hardness, flexibility and exceptionally sharp cutting edge. These blades were forged directly from small cakes of steel (named 'wootz') produced in ancient India [2]. (4) A mixture of nanoparticles of copper or silver with clay was often used as a thin coating (known as **luster**) on ceramics across the Renaissance Mediterranean world to produce brilliant metallic reflections of different color and iridescence.

Thus, people in the ancient time were really hard worker and intelligent. They developed these wonderful materials by trial and error method, although they knew nothing about the mechanism involved and the reason for such excellent properties of these materials. In the present time researchers have developed and still developing different methods to deliberately synthesize nanostructures of different materials in order to make use of their enhanced properties such as higher strength, lighter weight, greater chemical reactivity, better thermal, electrical, magnetic and anti bacterial properties. These enhanced properties of the nanomaterials, which are analyzed through nanoscience, are being used in the further development and applications of nanotechnology.

Nanoscience and nanotechnology are spreading rapidly and soon it will be the part of each and every science stream known to us. The development of nanotechnology will exceptionally reduce the size of electronic circuits which will significantly improve the speed and durability of computers and other electronic devices at low cost. Scientific community is very enthusiastic about nanotechnology and expecting that it will provide the solution of most of the human problems related to health and wealth. Feynman's exact concept of nanotechnology i.e, nanomachining or nanorobotics, is still an imaginary concept because the scientists are still unable to create non-biological nanorobots in the laboratory. These nanorobots (nanobots, nanoids or nanites) in the future would be able to complete human duties as well as duties which humans could never perform.

1.2 NANOSCALE MATERIALS

When a bulk material is transformed to nanoscale material (at least one dimension less than 100 nm) it behaves differently from its bulk counterpart and can be considered as

a new material. The nanoscale materials possess much higher surface area to volume ratio in comparison to the similar quantity of larger-scale materials, which enhance their chemical reactivity and modify their strength. On reducing size of a material below 100 nm the quantum effects become pronounced, which in turn modify the electrical, optical, mechanical, chemical and magnetic properties of the materials. Thus, in nanoscale materials properties like electrical conductivity, fluorescence, chemical reactivity, melting point and magnetic permeability etc. become a function of the particle diameter. Nanoscale materials of different dimensions (D) have been synthesized so far using various methods. Materials with at least 1D in nanoscale are thin films, thin layers and surface coatings. Materials with 2D in nanoscale are nanowires, nanotubes and nanoribbons while materials with 3D in nanoscale are quantum dots, nanoparticles array and core-shell nanoparticles etc. Nanoscale materials due to their unique properties have potential applications in advanced computing, electronics, cancer treatment (nanoparticles for targeting breast cancer cells), energy storage (cathodes fabricated from nanomaterials), engineered textiles (nanofibers), environment, metallurgy, packaging (nanocomposite plastics) and pharmaceuticals.

1.3 METAL OXIDES AND THEIR APPLICATIONS

Among all the nanoscale materials, the metal oxide nanostructures (TiO_2, ZnO, NiO, SnO_2, CuO, Al_2O_3, Fe_2O_3, SiO_2, In_2O_3, WO_3, TeO_2, CdO, and MoO_3 etc.), which are made up of metallic positive (+ve) and oxygen negative (- ve) ions, are extensively studied because of their potential applications in various technological areas, such as electronics, lasers, electron-field emitters, optoelectronics, biological and chemical sensors, logic devices, nanoscale memory, coating systems, superconductivity and catalysis [3-13]. Recently, many research groups have extensively investigated the various properties of metal oxide nanonstructures of different dimensions (D) and they observed that only some of these, which possess either d^0 (TiO_2, WO_3, Sc_2O_3, V_2O_5, CrO_3 and perovskites such as $ScTiO_3$, $LiNbO_3$) or d^{10} (ZnO, SnO_2, Cu_2O, In_2O_3) electronic configuration of cations, exhibit feasible gas sensing properties [14]. Although there exist a few metal oxides with d^n ($0<n<10$) configuration of cations (NiO, VO_2, Cr_2O_3, RuO_2 etc.) which are sensitive to the environment in their vicinity, but these are structurally unstable under oxidation or reduction processes.

1.4 ZnO AND ITS PROPERTIES

Amid the metal oxide nanostructures, ZnO is one of the most studied semiconducting materials. It exhibits unique semiconducting, piezoelectric as well as pyroelectric properties. Here, we will present an overview of the basic properties of ZnO, which are related to the present research work such as crystal structure, optical and electronic characteristics.

1.4.1 Crystal structure

Theoretically, ZnO crystallize in four different forms: (a) cubic zinc blende (B3), (b) rocksalt (NaCl) (B1), (c) cubic caesium chloride (B2) and (d) hexagonal wurtzite (B4 type) structure. Among all structures, wurtzite (hexagonal close packed) crystal structure is thermodynamically the most stable and most common ZnO phase under ambient conditions. The zinc blende state of ZnO structure is found stable only when grown on the substrates with cubic lattice [15]. The rocksalt or Rochelle salt (NaCl) structure is a metastable phase forming at relatively high pressures (~10 GPa). Cubic cesium chloride phase of ZnO exists theoretically at very high temperature [16]. In the present work we will discuss only about wurtzite crystal structure since our synthesized ZnO nanowires/na-

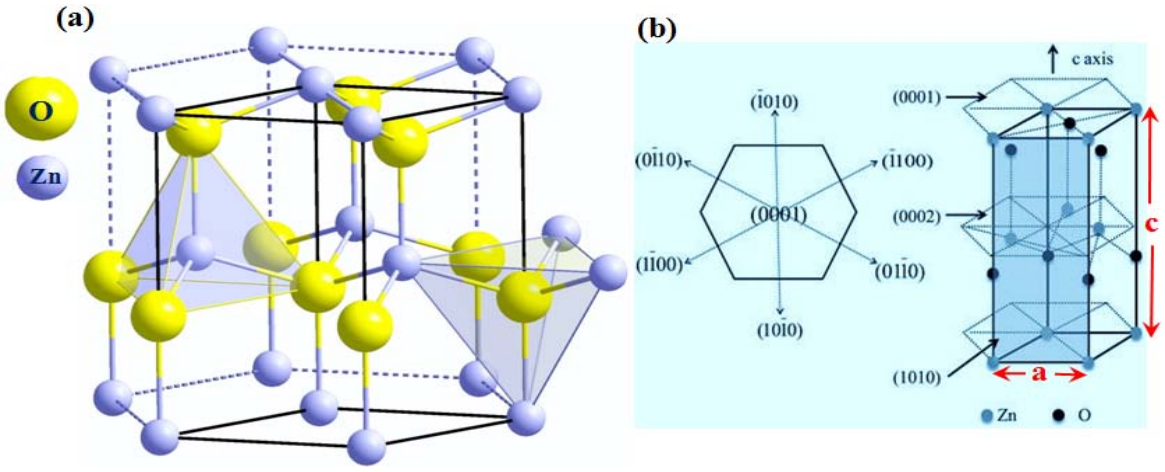

Figure 1.1: Schematic of **(a)** Wurtzite crystal structure of ZnO [adapted from http:// www. edm.com/design/led/4391796/White-LEDs-Printed-on-Paper-A-Doctoral-Thesis-Part-I]. **(b)** Bravais lattice and one unit cell is outlined for clarity [adapted from S. Das et al., "Fabrication of different morphologies of ZnO superstructures in presence of synthesized ethylammonium nitrate (EAN) ionic liquid: synthesis, characterization and analysis", Dalton Trans., **42**, 1645 (2013)].

-noparticles exhibit hexagonal crystal structure. The wurtzite structure is an ABAB hexagonal close packing (hcp) bravais lattice belonging to the space group $P6_3mc$ [17]. The ZnO wurtzite structure possesses two interconnecting sublattices of Zn^{2+} and O^{2-} ions which are shown along the c-axis by the Zn-O bond length in Fig. 1.1(a). In these sublattices O^{2-} ion is surrounded by tetrahedra of Zn^{2+} ions, and vice versa. This tetrahedral coordination in ZnO results in a noncentral symmetric structure with polar symmetry along the c - axis which is not only responsible for piezoelectricity, pyroelectricity and spontaneous polarization, but is also a deciding factor in crystal growth and defect generation in ZnO. In wurtzite ZnO unit crystal there are four most common face terminations. Among these, both the c-axis oriented Zn terminated (0001) and O terminated $(000\bar{1})$ polar faces are Zn^{2+} enriched planes as shown in Fig. 1.1(a), (b) [18]. The non-polar faces $(11\bar{2}0)$ (a-axis) and $(10\bar{1}0)$ contain an equal number of Zn and O atoms. The polar faces are known to have different chemical and physical properties. The (0001) plane is a basal plane, which is most common polar surface. Moreover, O-terminated face has slightly different electronic structure relative to the other three faces [19]. For ZnO the lattice parameters (a = 3.250 Å and c = 5.206 Å) give rise to lattice constant ratio c/a ~ 1.60, which deviates slightly from the ideal value of hexagonal cell (c/a = 1.633) due to difference in the electronegativity values of Zn^{2+} and O^{2-} ions [17]. Additionally, the variation in lattice parameters also depends on the presence of defects and impurities in the ZnO crystal.

1.4.2 Electronic model of ZnO

In wurtzite crystal structure of ZnO all the atoms are sp^3 hybridized and each one type of atom (Zn/O) is surrounded by a tetrahedra of other type of atoms. The electronic band structure of ZnO with high symmetry lines in the hexagonal Brillouin zone is shown in Fig. 1.2 (a) [20]. Here, the maxima of valence band and minima of conduction band occur at the same point in Brillouin zone known as Γ point k = 0, which implies that ZnO is a direct band gap semiconductor. The band gap of ZnO as determined by standard Local Density Approximation (LDA) is ~3.0 eV. However, LDA does not accurately model the Zn 3d electrons. After incorporating atomic self-interaction corrected pseudopotentials (SIC-PP), the Zn *3d* electrons can be accurately accounted and the value of band gap comes out to be 3.77 eV, which is almost equal to the experimental value of 3.4 eV [20]. Fig. 1.2(a) illustrates the LDA band structure of bulk wurtzite ZnO calculated using dominant atomic self-interaction-corrected pseudopotentials (SIC-PP). In Fig. 1.2(a) the 10 bands, around -9 eV, are associated with Zn *3d* levels while 6 bands from -5 eV to 0 eV

correspond to O *2p* bonding states. Here, first two conduction band states are strongly Zn localized and stand for empty Zn *3s* levels. The higher conduction band states are free-electron-like. The O *2s* bands (not shown here), which occur around -20 eV, are related to

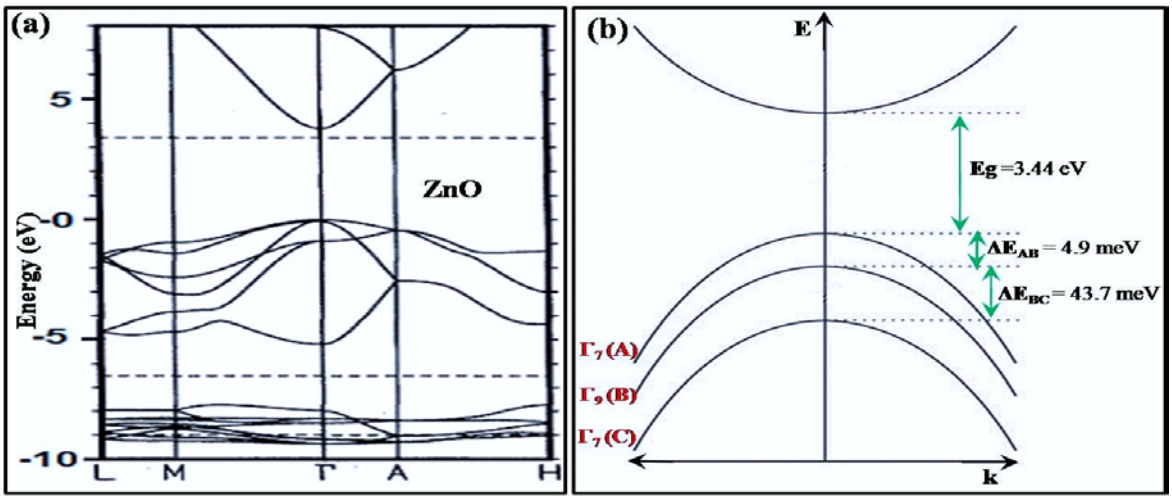

Figure 1.2: (a) The LDA band structure of bulk wurtzite ZnO calculated using dominant atomic self-interaction-corrected pseudopotentials (SIC-PP) [adapted from D. Vogel, et al., "Ab initio electronic-structure calculations for II-VI semiconductors using self-interaction-corrected pseudopotentials", Phys. Rev. B, **52**, 14316 (1995)]. **(b)** Schematic diagram illustrating the splitting of the valence band of ZnO into 3 subbands (A,B,C) by the crystal field and spin-orbit splitting at 4.2 K [adapted from B. K. Meyer, et al., "Bound exciton and donor-acceptor pair recombinations in ZnO", Physica Status Solidi (b), **241**, 231 (2004)].

core-like energy states. Further, it has been reported experimentally that ZnO valence band can split via crystal field and spin orbit interaction into three suband states, A, B and C under the wurtzite symmetry [21]. Fig. 1.2 (b) illustrates this splitting schematically. The A, B and C sub valence bands are reported to have Γ7, Γ9 and Γ7 symmetry, respectively [21]. The zinc oxide band gap exhibits temperature dependence in the temperature range 0- 300 K through the relationship:

$$E_g(T) = E_g(T=0)\,\frac{5.05 \times 10^{-4}\,T^2}{900 - T} \qquad (1.1)$$

1.4.3 Optical Properties of ZnO

The optical properties of ZnO are greatly influenced by its electronic band structure and lattice dynamic. However, the intrinsic and extrinsic effects also play an important role in deciding the optical properties of the semiconducting materials like ZnO [22, 23]. The intrinsic optical transition is termed as transition between the electrons in conduction band and holes in valence band. The extrinsic optical transitions are associated with the electronic states formed in the bandgap by dopants/impurities. These electronic states generally influence both the optical absorption and emission processes. The high purity ZnO crystal is found optically transparent in the visible range of the spectrum and possesses a typical refractive index (n_ω) of the order of 2.008 [24, 25]. Usually, ZnO crystals are red, green or yellow in color and both the intrinsic and extrinsic defects are assumed as the potential coloration centers (levels) within the bandgap of ZnO [23, 26, 27] (Fig. 1.3 (a)). These defects, known as deep level defects, consist of oxygen vacancies (Vo) [28-30], Zn vacancies (V_{Zn}) [31-33], interstitial Zn (Z_{ni}) [34], interstitial oxygen (O_i)

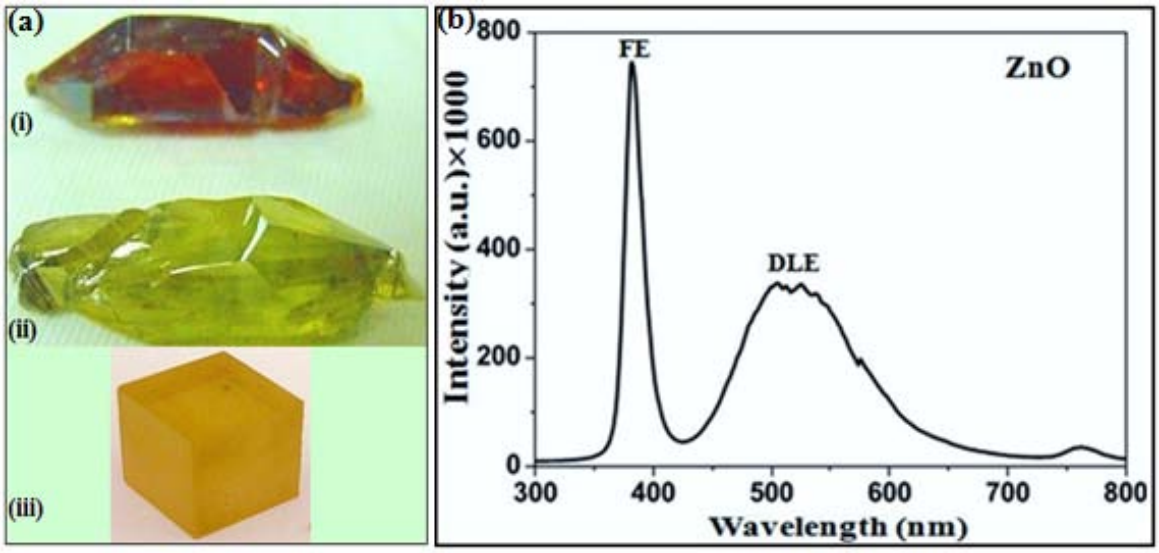

Figure 1.3: (a) ZnO crystals: red (i), green (ii) [adopted from wikipedia.org/ wiki/ Zinc_ oxide] and yellow (iii) [adopted from http://www.cradley-crystals.com/CCinit.php?id= pro ductso_3], **(b)** PL spectrum of ZnO nanowires [adopted from H. Kim, et. al., "Direct grow--th of oxide nanowires on CuOx thin film", Nanotechnology, **23** 045604 (2012)].

[35] and extrinsic impurities such as substitutional Cu, Li, Ga, H,..etc [36]. ZnO with wurtzite (hexagonal close packed) crystal structure possesses moderate direct band gap

(3.37 eV). The wide bandgap semiconducting materials are reported to have higher density of free carrier trapping centers. These increase the possibility of more efficient radiative recombination processes in the material. It has been reported that for the existence of stable electron-hole pair at room temperature, the binding energy of the exciton must be larger than the thermal energy at room temperature (k_BT = 25meV). This is why ZnO, which possesses higher exciton binding (60 meV) as compared to other semiconductor materials such as ZnSe (22 meV), ZnS (40 meV) and GaN (25 meV), exhibits excellent luminescent properties [37]. The room temperature photoluminescence (PL) spectrum of ZnO is shown in Fig. 1.3 (b). It consists of a UV emission band attributed to an intense near-band–edge (NBE) excitonic transition known as recombination of the free excitons. The broad peak, extending from ~ 400 nm to ~ 700 nm in the PL spectra of ZnO, is termed as deep level emission band (DLE) and linked to the deep level defects. Through several investigations the deep level defects are assumed responsible for red luminescence (~1.9 eV) which has been assigned as Z_{ni} [22, 27]. The violet-blue and blue luminescences were attributed to Z_{ni} and V_{Zn}, respectively [22]. The observed green emission (~2.36 eV) has been ascribed to V_O [27]. Finally, the yellow luminescence of ZnO has been attributed to surface defects [38].

1.4.4 Electrical properties of ZnO

ZnO due to its non-stoichiometry (Zn rich) growth under normal conditions behaves as an n-type semiconducting material and the main reason for this n-type behavior is associated with native (intrinsic) defects either oxygen vacancies (V_O) or Zn interstitial (Zni). It is assumed that either V_O or Zni acts as shallow donor in pure ZnO. However, the

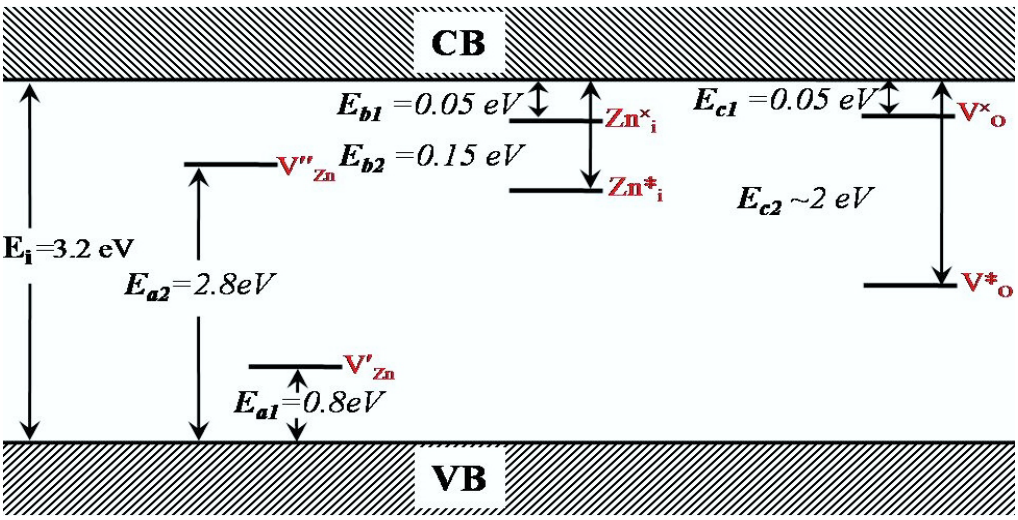

Figure 1.4: Schematic of electronic energy levels of native defects in ZnO [39].

role of these two defects in the origin of n-type behavior of ZnO is still a matter of debate. After extensive study of electrical and optical properties of ZnO and of diffusion process, the energy levels of these native defects in the mid-gap of ZnO were estimated by Kroger [39]. These estimated energy levels are shown in Fig. 1.4. Kroger considered that in Zn rich condition V_O and in O rich condition V_{Zn} will dominate and behave as effective donor and acceptor, respectively. In Fig. 1.4 the V'_{Zn} and V''_{Zn} represent the Zn vacancies with effective charges of -q and -2q and their activation energies are given by E_{a1}= 0.8 eV and E_{a2}= 2.8 eV, respectively. The Zn interstitials are denoted by $Zn^{\times}_i$ and Zn^{*}_i with effective charges of 0 and +q, respectively, similarly the oxygen vacancies are represented by $V^{\times}_O$ and V^{*}_O with effective charges of 0 and +q, respectively. The binding energies of $Zn^{\times}_i$, Zn^{*}_i, $V^{\times}_O$ and V^{*}_O energy levels as estimated by Kroger are shown in Fig. 1.4. Here we can conclude that both V_O and Zn_i can act as shallow donors but which one is the dominant defect and responsible for n-type behavior is still a matter of debate [40].

1.5 POTENTIAL APPLICATIONS OF ZnO

ZnO is a versatile material and it has been proved to be a boon for material science. ZnO possesses several unique properties, such as optical, electrical, thermal, antibacterial and UV-protection. It has potential applications in chemical and physical areas. ZnO has significant commercial importance also as it is widely used in rubber manufacturing [41], ceramic industry **[**42**]**, corrosion prevention in nuclear reactors [43], coatings [44], medicine [45, 46] and in food industry [47, 48]. In particular, ZnO based nanostructures are potentially attractive for flat screen displays [49, 50], LEDs [51, 52], field emission sources [53], gas, chemical and biological sensors [54,55,56], thermal stability [57], solar cell [58], UV light emitters [59], optical switches [60] and piezoelectric nanogenerators [61]. Here, we have studied the gas sensing application of ZnO nanowires synthesized via AAO template method.

1.5.1 ZnO as a potential gas sensing material

ZnO exhibits almost all the unique properties required to make it a feasible gas sensor such as moderate direct band gap (3.37 eV), high mobility of conduction electrons, better chemical and thermal stability under ambient conditions and good activity in redox reactions. It has been reported that when the size of a nanostructure material reduces to less than or equal to the Debye length of the material, the mobile charge carrier density within

the whole nanostructure will depend on the surface redox process. This implies that nanostructures with smaller grain size or better aspect ratio will exhibit higher sensitivity as the larger amount of nanomaterial can come into contact with surrounding. Moreover, in the family of metal oxide nanostructures, ZnO is supposed to have the largest family of 0D (quantum dots [62], nanoparticles array [63], nanocages [64], nanospheres [65], core-shell nanoparticles [66]), 1D (nanowires [67], nanotubes [68], nanorods [69], nanoribbons [70]), 2D (nanoprisms [71], nanoplates [72], nanosheets [73], nanowalls [74], nanodisks [75]) and 3D (dendritic structures [76], nanospring [77], nanocones [78], nanopillers [79] and nanoflowers [80]) nanostructures which have been extensively studied worldwide to utilize their excellent gas sensing properties for fabrication of improved gas sensing devices at low cost. However, the longer dimension of 1D ZnO nanostructures (nanotubes, nanowires and nanorods) makes them suitable to connect with the macroscopic world for electrical and many other physical measurements. Therefore, 1D nanostructures are more appropriate for the fabrication of nanoelectronic devices like gas sensors, electron-field emitters and logic devices etc.

Various methods like pulse laser deposition (PLD), vapor-liquid-solid (VLS), molecular beam epitaxy (MBE), metal organic vapor phase epitaxy (MOVPE), chemical vapor deposition (CVD), thermal evaporation and template assisted methods like electro-deposition and sol-gel etc. have been developed to synthesize 1D ZnO nanostructures [81-88]. Unfortunately all these techniques except sol-gel method are very sensitive to precursor composition and decomposition conditions. Furthermore, some are very expensive too. Sol-gel method is one of the simplest and cheapest methods for template assisted nanowires fabrication. AAO templates possess a uniform and parallel porous structure which can be filled easily. AAO template route is the most impressive way because of its low growth temperatures and good potential for uniform large scale synthesis of 0D and 1D nanostructures [89]. It the present work we will synthesize ordered ZnO nanowires of uniform size and study their gas sensing properties at room temperature.

1.6 GRAPHENE

Another important nanoscale material, which we have investigated in the present research work, is a 2D allotrope of carbon known as graphene. Graphene is an atomic thin layer of carbon atoms arranged in a honeycomb hexagonal lattice with sp^2 hybrization. Graphene is considered as the basic building block for other carbon nanomaterials, such as 0D fullerenes, 1D carbon nanotubes, 2D nanographite sheets and 3D graphite (structure of

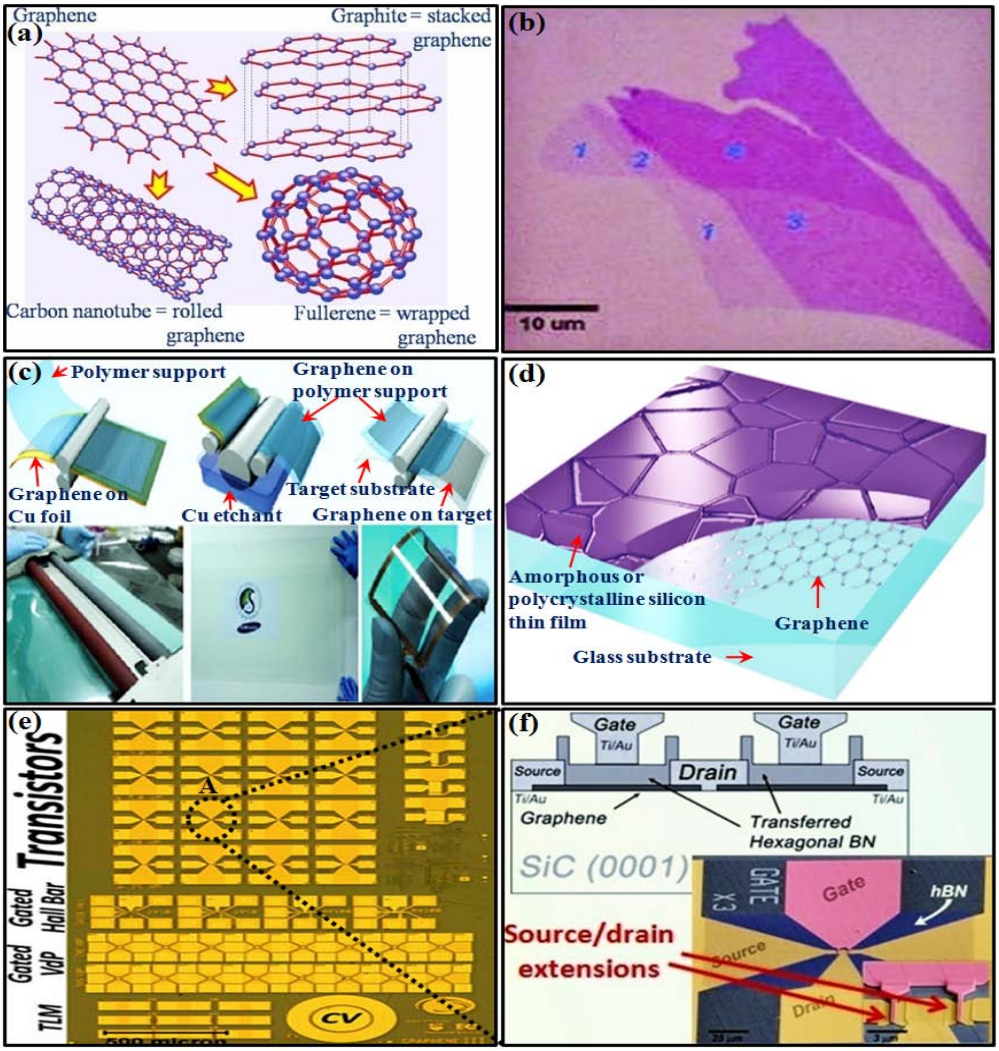

Figure 1.5: (a) Schematic diagram of a graphene sheet which act as a precursor for all other allotropic forms of carbon such as 0D fullerenes, 1D carbon nanotubes and 3D graphite [adapted from A. H. Castro Neto et al., "Drawing conclusions from graphene", Physics World, **19**, 33 (2006)]. **(b)** Optical image of one, two, three, and four layers of graphene [adapted from Z. H. Ni, et al "Graphene thickness determination using reflection and contrast spectroscopy", Nano Lett.,**7**, 2758 (2007)]. **(c)** Schematic of the process used for the large-scale fabrication of high-quality graphene films for practical applications [adapted from S. Bae, et al "Roll-to-roll production of 30-inch graphene films for transparent electrodes", Nat. Nanotechnol., **5**, 574 (2010)]. **(d)** Schematic of a typical graphene thin-film solar cell in which, a single graphene sheet is sandwiched between the glass substrate and a thin layer of silicon [adapted from http://phys.org/news/2013-10-major-graphene-solar-cells-retains.html "Major leap towards graphene for solar cells: Graphene retains its properties even when coated with silicon"]. **(e)** Optical image of various devices on wafer scale graphene wafers and magnified "A" region is shown in **(f)** which represents schematic diagram and SEM image of the graphene transistor [adapted fromhttp://www.mri.psu.edu/facilities/nanofab/research/graphene/devices/"Epitaxial grap--hene devices and basic research" and http://www.ndcl.ee.psu.edu/research.asp "Graphene based RF devices and circuits].

stacked graphene layers held together through weak van der Waals forces) (see Fig. 1.5 (a), (b)) [90]. Graphene has become a big hub for numerous applications in diverse research domains that exploit its exceptional electrical, chemical, optical, mechanical, biological and thermal properties after its experimental discovery in 2004 by A. Geim and K. Novoselov at Manchester University [91-93]. Due to its extraordinary crystal and electronic structure, graphene exhibits a few new physical phenomena and potential applications in flexible electronics, transparent electrodes, solar cells, high speed transistors and other devices on wafer scale graphene wafers (Fig. 1.5 (c) - (f)) [99-106]. This is why, within a very short time period this wonder material become a rising star on the horizon of materials science and condensed-matter physics. Now different research groups all around the world are working on graphene extensively as a result large number of graphene-based articles are appearing every year and more predicted to come in the future [94].

1.6.1 METHODS OF GRAPHENE SYNTHESIS

First graphitic layers of limited thickness (mono- and multi-layered) were produced by B. Lang et al. in 1975 via thermal decomposition of ethylene onto platinum crystal faces [107]. In 2001 H. Shioyama, reported a method to cleave graphite with a unit of graphene and in the same year Dutch physicist Walt de Heer observed that a graphene sheet possesses many of the same properties as carbon nanotubes [108, 109]. However, K.S. Novoselov et al. first time reported a reproducible method to synthesize mono layer graphene in 2004 [91]. Although this method is very simple and fruitful but have no commercial importance. Taking this into account various methods have been developed to synthesize graphene and in every method either graphite, graphite oxide or some another source of carbon is used as the starting material. Some of the major reported methods used to successfully synthesize graphene are given below:

1.6.1.1 TOP DOWN APPROACH

1.6.1.1.1 Micromechanical exfoliation of graphite (Scotch tape or peel-off method)

This method was first used by A. K. Geim and K. S. Novoselov to synthesize single crystal mono layer graphene sheet in 2004 [110]. Although this method is very simple and produces best quality graphene samples, but has very low throughput and thus makes it unsuitable for bulk production. In this method a chunk of highly ordered pyrolytic graphite (HOPG) (Fig. 1.6 (a) and (b)) is peeled off repeatedly using scotch tape, until a single layer

graphene is obtained (Fig. 1.6 (c)). In order to transfer a layer of graphene from the scotch tape onto the surface of the desired substrate, the scotch tape is pressed against the substrate and due to the strong adhesion between bottom layer of graphene and substrate, a mono layer of high quality graphene is transferred (Fig. 1.6(c)). Generally, optical microscopy is used to identify the thickness of the transferred graphene layer on the substrates (usually, SiO_2/Si). Here graphene flakes of different thickness produces different interference colors with respect to the empty substrate (see Fig. 1.5(b) [90] and Fig. 1.6 (d) [111]). This optical contrast makes even a single layer graphene visible through naked eyes.

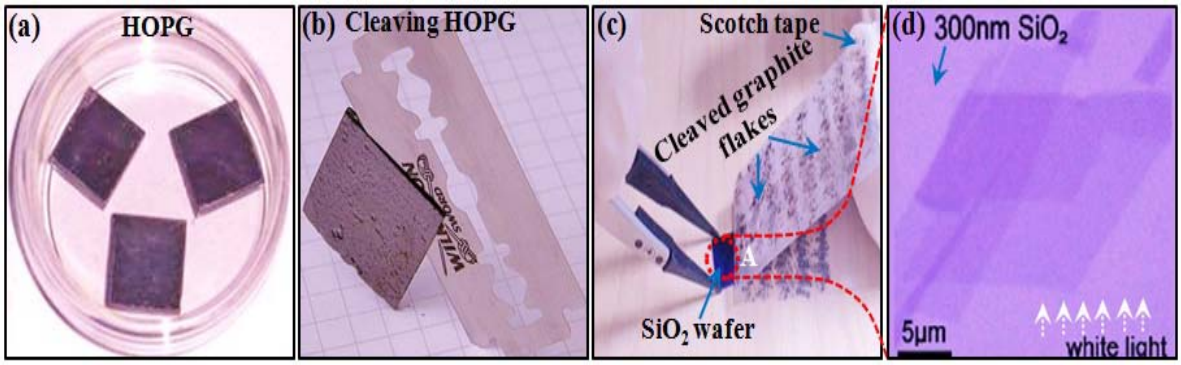

Figure 1.6: (a) Highly ordered pyrolytic graphite (HOPG) [adapted from http://www.nano scopy.net /en/hopg.shtm], **(b)** HOPG cleaved using a thin razor blade [ad apted from http://commons.wikimedia.org/wiki/File:Cleaving_HOPG.jpg], **(c)** Cleaving of HOPG sa- ple using scotch tape and transferring the graphene layers on to the SiO_2 substrate [adapted from http://fear-of-lightning.wonderhowto.com/inspiration/graphene-an other-amazing-carbon product-0148101/], **(d)** Magnified optical image of "A" region, whi- ch shows different thickness of the graphene layers with respect to the variation in contrast of the layers [adapted from P. Blake and E. W. Hill "Making graphene visible", Appl. Phys. Lett., **91**, 063124 (2007)].

1.6.1.1.2 Wet chemistry or solution method

This method is suitable for the bulk production of graphene sheets at low cost. Here graphite is chemically oxidized to graphite oxide (GO) using strong oxidizing agents such H_2O_2, $KMnO_4$. GO is hydrophilic in nature and can be exfoliated in various solvents easily via ultrasonication (Fig. 1.7(a)-(c) [112-114]). This makes it suitable for the synthesis of large area thin films and composites. Unlike graphene, GO is electrically

insulating and in

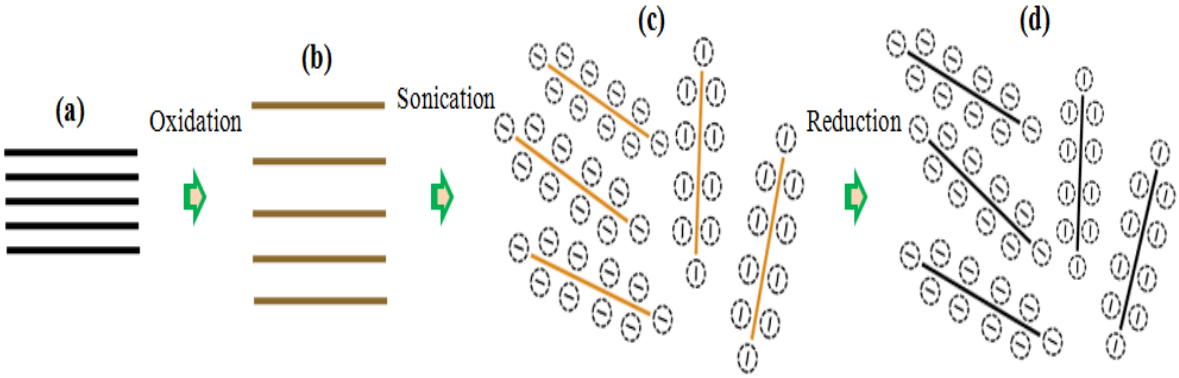

Figure 1.7: (a) Graphite powder, **(b)** Graphite oxide, with greater inter planer spacing than graphite powder, **(c)** GO dispersion in water stabilized by electrostatic repulsion, **(d)** Chemically reduced graphene oxide (rGO) dispersion.

order to make it electrically active it must be deoxidized either thermally or chemically (Fig. 1.7 (d) [115]). GO was first synthesized by B. C. Brodie in 1859 but the most accepted method, which is still in use with some modification, was given by W. S. Hummers et.al in 1959 [116-119]. A brief description of an improved Hummers method, as reported by N. I. Kovtyukhova et al. [119], is given here. In this method 20 gm graphite powder is added into the mixture of 30 mL H_2SO_4 (98 %), 10 g $K_2S_2O_8$ and 10 g P_2O_5 at 80 °C. The resultant mixture is allowed to cool down to room temperature and left for 6 h. After that it is diluted, filtered, and washed repeatedly with distilled water until the pH become neutral. The final product so obtained is dried over night at ambient conditions and subjected to further oxidation by Hummers' method [116]. 20 g of this oxidized powder is mixed with 460 mL chilled H_2SO_4 and 60 gm $KMnO_4$ is added into it gradually with stirring. During this process temperature of the mixture is maintained below 20 °C. Further, 920 mL distilled water is added into it and stirred through magnetic stirrer at 35 °C for 2 hrs. Afterwards, the addition of 2.8 L distilled water and 50 mL 30% H_2O_2 solution is added, which terminate the reaction. Here color of the mixture turns bright yellow. The obtained mixture is filtered and washed thoroughly with 5 L, 1:10 HCl solution to remove any kind of remaining metal ions. Final GO product could be obtained either centrifuging the mixture at 4000 rpm for 4 h or through filtration.

GO can also be synthesized using a "bottom-up" approach. Here, hydro-thermal method is utilized to synthesis GO nanosheet and glucose is used as the source of carbon. The main draw backs of "Top-up" approach, i.e. Hummers' method or improved Hummers' methods, are the use of strong oxidizing agents and small lateral size of GO

nanosheets. This new method is environmental friendly and can be used to synthesize GO nanosheets of larger lateral size at a low cost [120].

1.6.1.1.3 Ionic liquid-assisted electrochemical exfoliation method

Recently, researchers have tried to find out cheaper, fast and environmental friendly methods to synthesize good quality graphene [121-124]. In this regard Liu et al. [121] have developed a one-step electrochemical approach to produce graphene nanosheets via chemical exfoliation of graphite anode in the presence of ionic liquid (IL) and water. In this method 1:1 ratio of alkylimidazolium hexafluorophosphate (RIMPF6) and water is used as an electrolyte. An operational voltage as high as 15 V is applied between the two graphite electrodes (rods) at room temperature. After 6 hrs of electrochemical exfoliation a black precipitate of graphene nanosheets is formed at the bottom of the anode. Schematic diagram of the experimental setup used is shown in Fig. 1.8. The obtained black precipitate

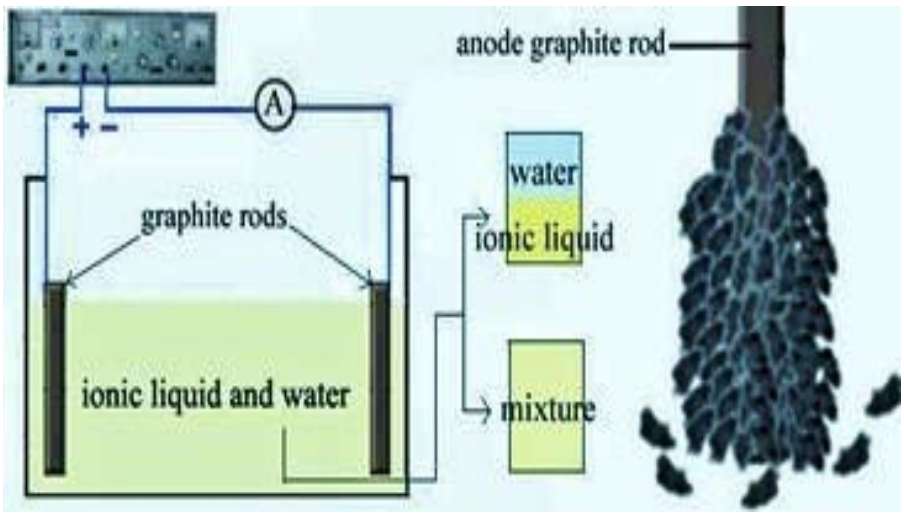

Figure 1.8: Electrochemical exfoliation of graphite, Experimental set-up (left) and exfoliated graphiteanode (right). [adapted from N. Liu, F. Luo, H. Wu, Y. Liu, C. Zhang, J. Chen "One-step ionic-liquid-assisted electrochemical synthesis of ionic-liquid functionalized graphene sheets directly from graphite", Adv. Funct. Mater., **18**, 1518 (2008)].

of graphene nanosheets is insoluble in water but can be dispersed easily after a brief ultrasonic treatment in polar aprotic solvents such as dimethylformamide (DMF), dimethyl sulfoxide (DMSO), and N-methylpyrrolidone (NMP) solution. Lu et al. [122] have reported that electrochemical exfoliation of graphite not only generates graphene sheet but

it also, after controlling the ratio of water to ILs in the electrolyte, produce carbon nanoparticles and nanoribbons.

1.6.1.2 BOTTOM UP APPROACH

1.6.1.2.1 Chemical vapor deposition (CVD) method

This is one of the most common methods to produce graphene thin film on metallic substrates such as Cu, Ni, Co, Pd, Ir, Ru, etc. in a controlled way [125-129]. It has been reported that good quality large area continuous monolayer and few layer graphene thin films can be synthesized on polycrystalline Ni and Cu substrates by CVD method. Recently, R. S. Ruoff et al. have reported that growth of CVD graphene on Ni surface occurs either due to the segregation or precipitation of carbon atoms [130]. Q. Yu et al. have demonstrated that the amount of carbon segregated at metal surface can be controlled easily by controlling the cooling rate (Fig. 1.9) [131]. However, the CVD-grown graphene

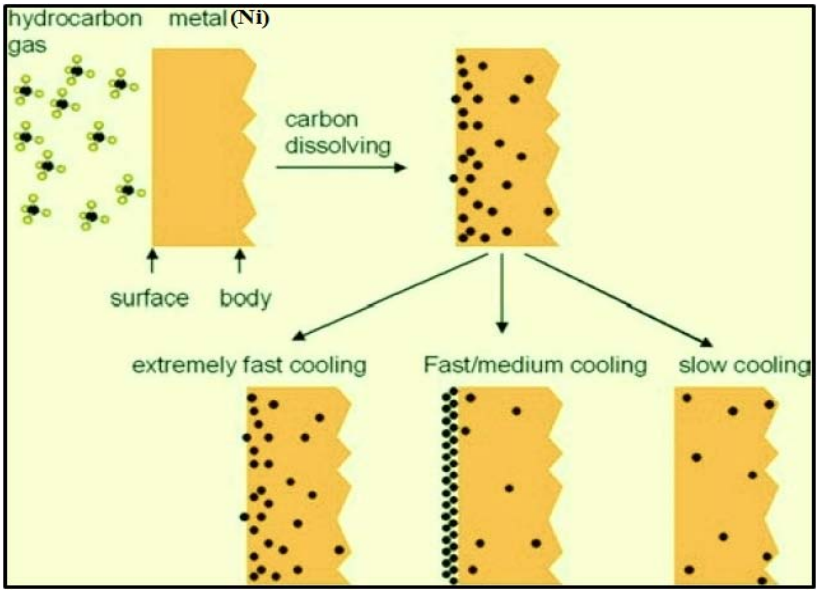

Figure 1.9: Carbon segregation at metal (Ni) surface [adapted from Q. Yu, J. Lian, et al., "Graphene segregated on Ni surfaces and transferred to insulators", Appl. Phys. Lett., **93**, 113103 (2008)].

films on Ni foil/film are not uniform monolayer throughout the film area but have a wide variation in thickness. In contrast to Ni, high quality large-area uniform mono layer and few layer graphene thin films can be grown over polycrystalline Cu films and Cu foils due to the low solubility of C in Cu [130]. Moreover, R. S. Ruoff et al. have reported a surface adsorption growth mechanism for this case [130]. Some research groups have suggested

that a continuous uniform layer of polycrystalline graphene with numerous domain boundaries originates on Cu foil/film due to nucleation of graphene at defects on the surface imperfections and/or grain boundary edges [131-133]. Furthermore, Cu foils are easily available and in order to transfer deposited graphene film onto desired substrates it can be etched by commonly used solvents in the laboratories. This make Cu metal a potential metallic substrate for large scale production of CVD-grown graphene. A brief description of one of the CVD method, reported by P. M. Ajayan et al. is given below [134]. In this method 25μm thick Cu foil is loaded in a horizontal quartz tube, which is placed inside a split furnace and a rough vacuum of 10^{-2} Torr is created within it. Cu foil is then heated to 950°C using split furnace in Ar/H_2 ambient (with flow rate of~400 sccm) at a pressure of ~ 8-9 Torr. Flow of Ar/H_2 is stopped as the desired temperature is achieved inside the tube and hexane vapor is allowed to enter with flow rate of ~ 4mL/h to maintain the pressure of 500 mTorr inside the tube for 4 min. A schematic of the experimental set-up is shown in Fig. 1.10. A thin layer of PMMA (polymethyl metha-acrylate) is coated over the CVD grown graphene and Cu foil is removed by dissolving it either in $FeCl_3$ or

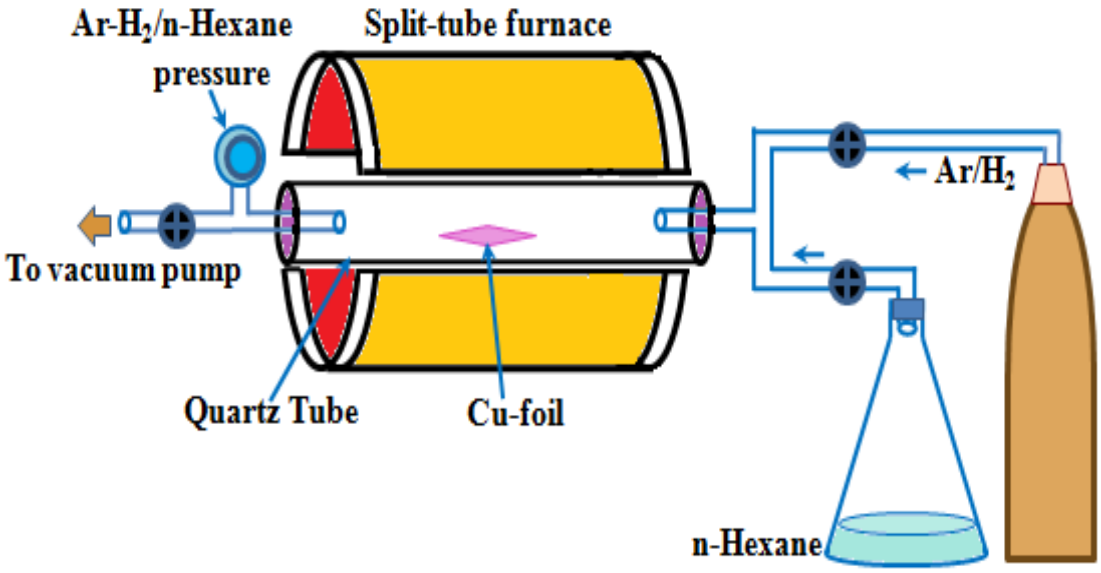

Figure 1.10: Schematic diagram of the set-up used for CVD grown graphene film [134].

dilute nitric acid. After Cu dissolution, graphene with PMMA film is transferred onto desired substrate (SiO_2/Si, ITO etc.) and PMMA film is removed by dissolving it in acetone. The whole systematic process is shown in Fig. 1.11.

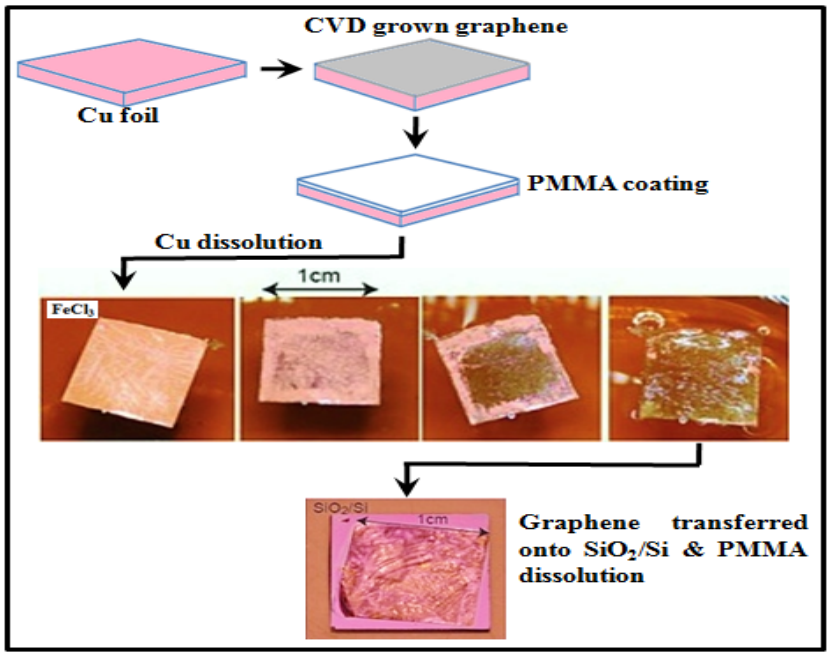

Figure 1.11: A schematic illustration of the transfer processes of CVD grown graphene from metallic surface on to the desired substrate [adopted from http://emps.exeter.ac.uk/engineering/research/functionalmaterials/researchinterests/graphne].

1.6.1.2.2 Epitaxially grown graphene on Silicon Carbide (SiC)

This method is used to synthesize large-scale high-quality graphene on insulating silicon carbide (SiC) substrate, which possesses almost all the salient features of ideal graphene. Epitaxially grown graphene (EG) on SIC has been found more suitable for electronic applications and has several other advantages over CVD grown graphene on metallic substrates, for example, it does not need to be transferred from metal substrate to another insulating substrate for electric measurements. Another advantage is that interface between EG and SIC has been studied extensively and no trapped impurities have been found under the EG [135]. Moreover, this interface can be modified by passivation and intercalation. One of the most important advantages of EG sheets is that it can be grown at the desired place just by proper tailoring the SIC substrate. Additionally, the graphene ribbons, which have been synthesized by this method, exhibit no bandgaps or mobility gaps. One of the best methods to synthesize EG is given by Walt de Heer et al. (Fig. 1.12 (a)). In this method a SIC wafer is heated around 1500 °C in high vacuum conditions. Here evaporation of silicon starts which leave behind a single or few layers of graphene (Fig. 1.12 (b)).

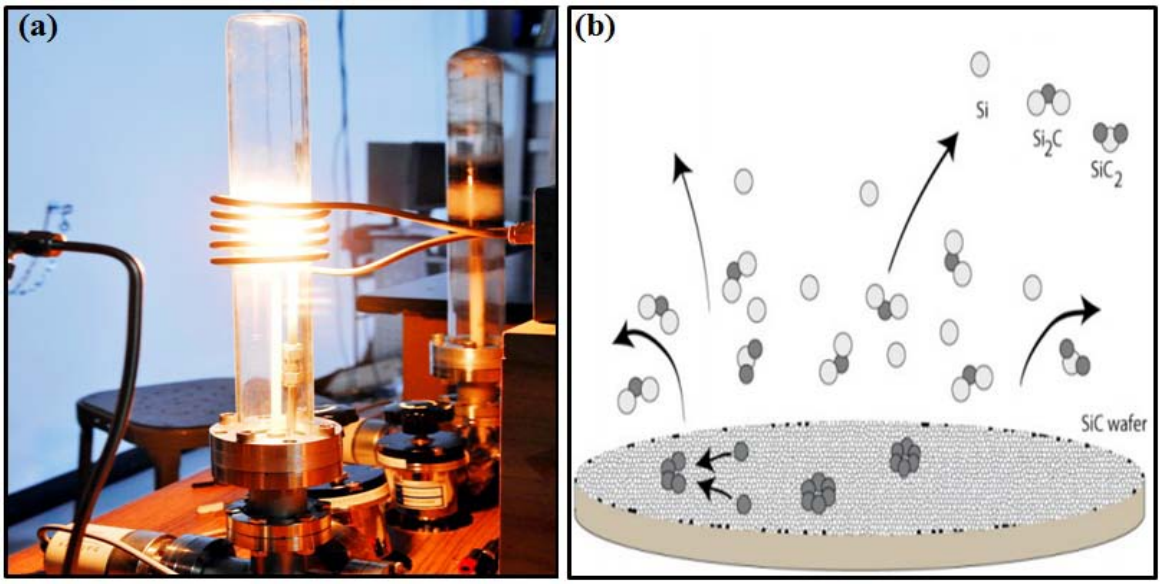

Figure 1.12: (a) A high temperature furnace is used to grow epitaxial graphene on a SIC wafer [adopted from http://www.gtresearchnews.gatech.edu/confinement-controlled-sublimation/], (b) Sublimation of vapor species from SIC substrate to left behind a graphene layer [adopted from http://ec.europa.eu/information society/apps/projects/logos/9/257829/080/deliverables/001_ConceptGrapheneD12Report.pdf] [136].

1.6.2 STRUCTURE AND PROPERTIES OF GRAPHENE

Graphene with charge-carrier mobility greater than 200,000 $cm^2\ V^{-1}\ s^{-1}$ is one of the good electrical conductors discovered till date [93, 95]. Graphene is about 200 times stronger than steel with tensile strength of 130 GPa [96]. Thermal conductivity of suspended single-layer graphene has been reported to lie between $(4.84\pm 0.44) \times 10^3$ and $(5.30\pm0.48) \times 10^3$ W $m^{-1}\ K^{-1}$ which is better than any other known material [97]. It possesses high optical transparency (97.7% [98]). All the excellent properties of graphene are associated with its unique crystal structure.

Fig. 1.13 (a) represents the 2D hexagonal lattice of crystalline structure of graphene with two interpenetrating triangular sublattices and the locations of one sublattice (green) are at the centers of the triangles formed by the other sublattices (orange). In the lattice of graphene each primitive cell contains two carbon atoms, namely A and B, and each A atom is covalently bonded with three B atoms and vice versa [137, 138]. In Fig. 1.13 (a) three bonds are directed along the vectors $\boldsymbol{\delta_1}$, $\boldsymbol{\delta_2}$ and $\boldsymbol{\delta_3}$ and angle between two successive bonds

is 120°. Here, $\overrightarrow{a_1}$ and $\overrightarrow{a_2}$ represent the primitive translation vectors of the graphene lattice. Fig. 1.13 (b) is the first Brillion Zone of graphene reciprocal lattice [139]. In the structure of graphene, carbon atoms are sp^2 hybridized in which s, p_x and p_y atomic orbitals form a trigonal planar hexagonal shape (Fig. 1.14). The sp^2 states give rise to covalent σ- bonds, which hold the honey comb structure together and provide the exceptional chemical and

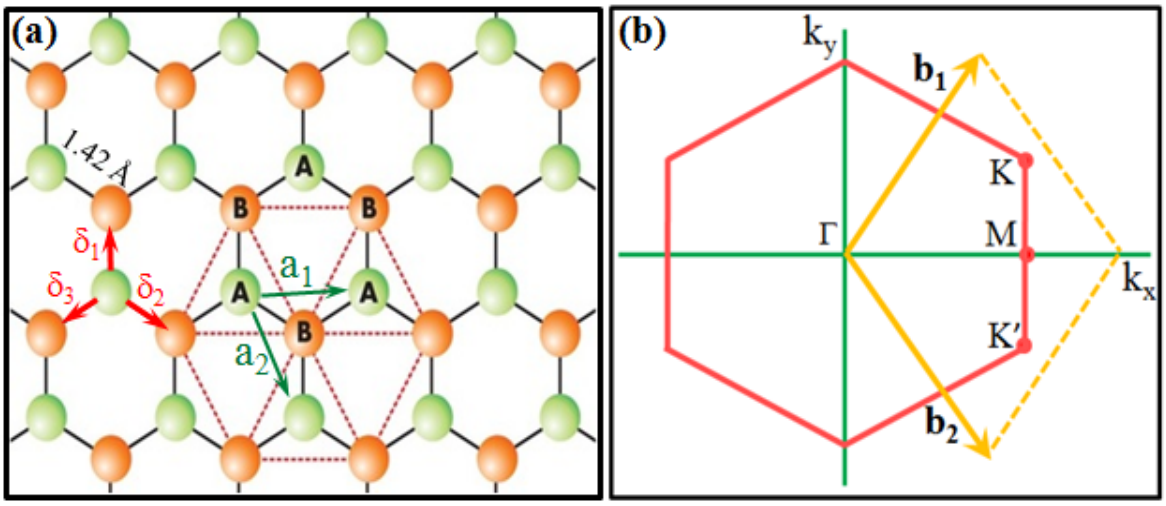

Figure 1.13: (a) Geometry of the graphene lattice, each carbon atom in sublattice "A" is covalently bonded with three carbon atoms in sublattice "B" and vice versa [adopted from A. K. Geim, A. H. MacDonald, "Graphene: Exploring carbon flatland", Physics Today, **60**(8), 35 (2007)]. **(b)** First Brillion Zone of graphene reciprocal lattice [139].

mechanical stability. The remaining unhybridized orbital of each carbon atom (perpendic ular to the planar surface) form a π-bond between two carbon atoms by the parallel overla-

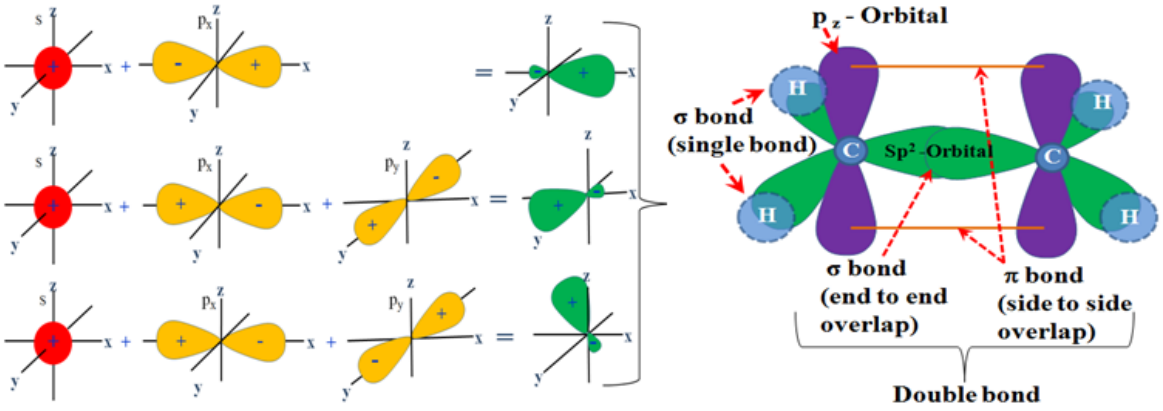

Figure 1.14: sp^2 hybridization of atomic orbitals in carbon atoms.

pping of π-electrons, which reside in the π-bond and are responsible for the unique electrical, optical and thermal properties of graphene. Additionally, the unit cell of monolayer graphene possesses two carbon atoms, which give rise two 'conical' points per Brillouin zone where band crossing takes place and upper and lower portions of the π-band touch each other. These points are termed as Dirac points (valleys) and referred to as K and K' (Fig. 1.15) [140]. In monolayer graphene, the available two electrons from two carbon atoms per unit cell occupy the lower energy band which indicates the presence of Fermi energy level at the Dirac points. This is why, pristine graphene is termed as zero band gap semiconductor with linear dispersion around the Fermi-energy and exhibits quite low electrical conductivity. As a consequence of the linear energy–momentum dispersion in the vicinity of Dirac points, the charge carrier dynamics are effectively described by relativistic Dirac equation, $E = |\hbar k| v_F$, where v_F is the Fermi velocity of electrons or holes which replaces the speed of light and $\hbar k$ is the momentum. This implies that in monolayer graphene charge carrier behave as massless, relativistic fermions [140]. This is the most important behavior of graphene which attracts much attention of the researchers.

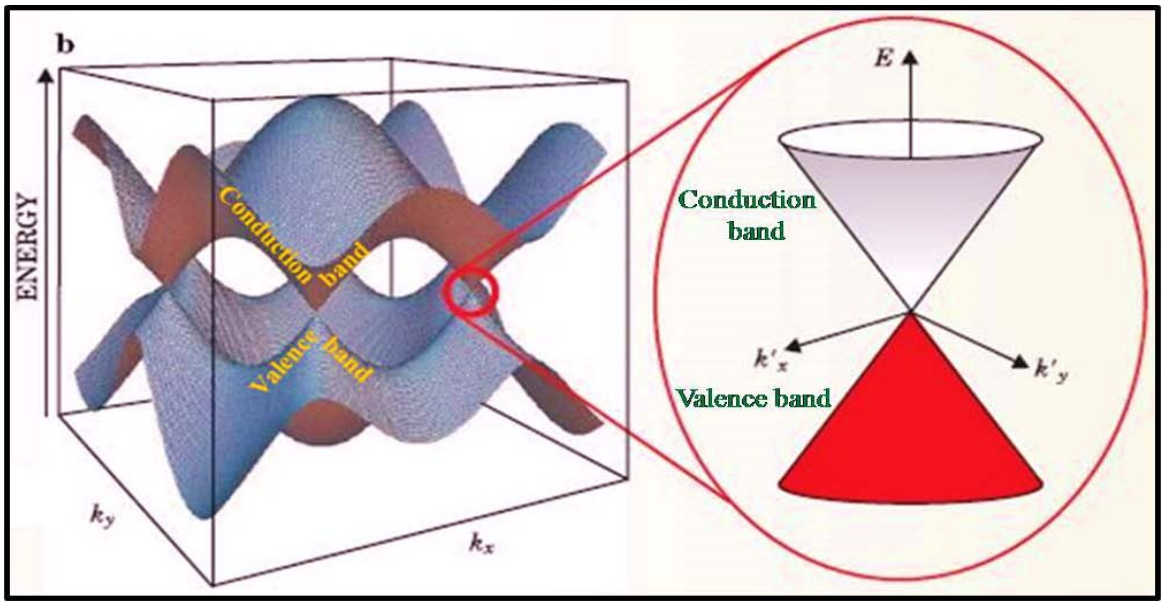

Figure 1.15: Left: the energy band structure of graphene. Right: zoomed conical energy bands in the vicinity of K and K points (Dirac points) [adapted from M. Wilson, "Electrons in atomically thin carbon sheets behave like massless particles", Physics Today **59**(1), 21 (2006)]

All the properties of graphene which we have discussed here are associated with single layer graphene and the production of single sheet graphene via micromechanical

exfoliation of graphite is limited to the fundamental study. Although CVD method and epitaxial method of graphene growth on silicon carbide (SiC) can be used to synthesize large area single or few layer graphene films. But uniform growth of single and few layers graphene in the terms of mass production in an economical way is still a challenge. Wet chemical or solution method, which we have discussed above, is well suited for high volume production of single or few layers chemically reduced graphene oxide (rGO) and most appropriate to chemical functionalization. In the solution method graphite is oxidized to graphene oxide (GO) via strong oxidizing agents. GO is hydrophilic in nature and can be dispersed in aqueous medium easily just by sonication [141]. GO is electrically insulating due to attached oxygen functional groups at the basal plane and disruption of pristine graphitic sp^2 network. A portion of oxygen functional groups can be removed from GO after reduction via any of the chemical [142-145], thermal [146, 147] and ultraviolet-assisted methods [148]. After chemical reduction sp^2 network is partially restored in rGO, but still interrupted by voids and sp^3-bonded areas. This is why electrical conductivity of rGO is much better than GO. The electrical conductivity of rGO is a little bit smaller than pristine graphene but it is high enough to be used in the fabrication of energy-storage devices [149, 150], liquid crystal devices [151], solar cells [152-154], polymer composites [155-157], sensors [158, 159] and paper-like materials [160, 161] and mechanical resonators [162]. CNT exhibits excellent potential in biosensors [163-165], biofuel cells [166] and polymer electrolyte membrane (PEM) fuel cells [167, 168] but rGO based devices exhibit better electrocatalytic activity [169, 170] and macroscopic scale conductivity [170] than CNT which implies that in these fields rGO can also be effectively used [171]. Further, very high surface-to-volume ratios, excellent mechanical, electrical, optical properties, and availability from natural resource graphite, make rGO very attractive for the synthesis of lighter nanocomposites at lower costs. Moreover, in dry state single or few layers rGO sheets stack to multiple layers, which possess very small surface area and behave similar to bulk graphite platelets. So, for practical electronic applications we have to reduce the stacking degree of rGO nanosheets in the dry state by some means. For this to occur rGO nanosheets are decorated by metal and semiconducting nanoparticles. Such rGO nanocomposites have potential applications in solar energy conversion [172, 173], gas sensors [174], in the detection of organic pollutants [175] and bio medicals [176].

1.6.3 GRAPHENE AS A GAS SENSOR

The charge carriers in graphene are massless Dirac fermions that show ballistic transport properties as potential barriers, within the rest mass of electron limit, are transparent to the charge carriers due to the Klein Paradox [177, 178]. This ensures charge carrier velocities close to the speed of light (v_F~10^6 m/s). Graphene is a semimetal with its valence and conduction bands touching each other at the Dirac point [179,180]. The band gap of graphene can be tuned from 0-2.5 eV by breaking the inversion symmetry on application of a perpendicular electric field to a bilayer dual gate graphene based field effect transistor [181, 182].

Graphene exhibits unique electronic properties like high charge-carrier mobility (200,000 cm^2 V^{-1} s^{-1}) and tunable band gap (from 0-2.5 eV), ballistic transport and quantum hall effect at room temperature [183,184]. Graphene has a very high theoretical specific surface area (2630 m^2g^{-1}) and thus possess highest surface area to volume ratio among known layered materials [185]. Thus, it offers the largest exposed area for gas molecules. Its high conductivity and metallic transport properties (v_F=10^6 m/s) lead to very little Johnson's noise [178]. These properties make graphene a potential gas sensing material.

The gas sensing properties of graphene are associated with adsorption/desorption of test gas molecules on the graphene surface, which influences the conductance of graphene and the change in conductance is related to the concentration of the test gas in the vicinity of the graphene sensor [186]. For graphene, gaseous molecules act either electron donor or acceptor depending on the nature of the target gases. The high sensitivity and fast response of graphene is a consequence of exceptional charge carriers mobility in graphene, which allow extremely low noise sensing at room temperature. In case of chemically reduced graphene oxide (rGO) some of the oxygen containing functional groups such as carboxylic and epoxide remain attached to the basal plane even after the reduction of graphene oxide (GO) by the chemical reductants. Due to these residual groups rGO film exhibits a p-type semiconducting behavior [187]. Hydrazine reduced GO based sensors have performed extremely well in the detection of NO_2, NH_3, acetone and explosive agents [188, 189]. One of the drawbacks of rGO based sensors is poor recovery time in comparison to other metal oxide based gas sensors. To eliminate this problem and to improve the performance of the graphene based sensors several research groups are working on lattice modified rGO thin films, rGO hybrid films and rGO composite based gas sensors [189, 190, 192-196].

1.7 BASIC PROPERTIES OF A GAS SENSOR

Gas sensor is a transducer, i.e. converts one form of input signal into another more desirable output form. It can detect different gas molecules present in its vicinity and produce corresponding electrical signal with a magnitude proportional to the concentration of the test gas. Gas sensor is composed of sensing material depending on the test gas, and heating element. Gas sensors have great importance because these are used to detect flammable and toxic gases and oxygen depletion. Most of the gas sensors are battery operated and as a sensor's detection exceeds a preset alarm level, the alarm or signal will be activated. To investigate the performance of a gas sensor some of the following parameters are used:

1.7.1 Specificity or selectivity

If a sensor responds to a particular gas more effectively in the presence of other gases then it is said to be selective for that. However, every gas sensor has some cross-sensitivity because it is usually very difficult in practice to fabricate absolutely selective gas sensor. Cross-sensitivity is the term for detecting a gas which we are not interested in detecting. This can skew the sensors results misleading the sensor and user as to the presence of the gas in which we are interested. For instance, a typical carbon monoxide (CO) sensor may respond significantly to hydrogen, ethylene, and isobutylene. By registering the presence of these gases, the sensor is telling the user CO is present, which may not be true. Sensor makers compensate for this phenomenon by using filters (like charcoal) or through software and the micro processing of the readings.

1.7.2 % response

The % response (S) of a sensor is defined as:

$$\%\ \text{response (S)} = \left|\frac{R_g - R_a}{R_a}\right| \times 100 = \left|\frac{\Delta R}{R_a}\right|$$

where, R_a and R_g are resistances of the sensing material in air and in gas, respectively.

1.7.3 Sensitivity

Sensitivity is the derivative of gas response as a function of gas concentration.

1.7.4 Response time and recovery time

Response and recovery times of the sensors are defined as the time required to reach 90% of the saturation value and 90% of initial value, respectively

1.7.5 Detection limit

It is the lowest concentration of the target gas or analyte, which a sensor can detect under given physical conditions.

1.7.6 Working temperature

It is the temperature at which gas sensor exhibit maximum % response or sensitivity for a fixed amount or concentration of the analyte.

1.8 MOTIVATION AND SCOPE OF THESIS

From the above discussions we conclude that Zinc oxide is one of the most promising metal oxides, which exhibits excellent physical, chemical and biological properties together. Although various properties of ZnO have been studied extensively yet researchers are investigating the potential of different nanostructural forms of this material worldwide and a simple cost effective way to synthesize ordered, uniform nanostructures of different metal oxides still has importance.

In the present work we synthesize ordered ZnO nanowires of uniform size using AAO template route which is the most impressive way because of its low growth temperatures and good potential for uniform large scale synthesis of 0D and 1D nanostructures. AAO templates possess a uniform and parallel porous structure which can be filled easily with the desired material either by electrodeposition or vacuum injection technique. We have found that vacuum-injection method is one of the simplest and cheapest methods for template assisted nanowires fabrication (see chaper 2 for details). Since processing of an individual nanostructure is slightly difficult and not suitable for mass production, therefore gas (NH_3) sensing properties of bunches or bundles of well-aligned ZnO nanowires have been investigated. Our study will also helpful in the mass production of other metal oxide nanowires and studying their gas sensing properties.

Although metal oxide gas sensors exhibit good gas sensing properties but most of them are operated at high temperatures (up to 300 °C) to activate the adsorption and desorption processes of gas molecules which limits their use in low temperature applications. In this regard graphene is an important material which exhibit excellent

electrical properties with highest surface area to volume ratio. These two properties are essential for a material to be a gas sensor. Here we have fabricated GO, rGO thin films and study their gas sensing behavior along with optical, electrical and antibacterial properties. However, as sensing is a surface phenomena, decoration of graphene surface by metal nanoparticles (NP) or metal oxide nanostructures (NS) will affect the sensing performance of the graphene based sensing devices. In light of this, we have also synthesized graphene-ZnO nanocomposite (ZrGO) and studied its temperature dependent electrical and gas sensing properties successfully. Our experimental results suggest that doping of ZnO nanoparticles in rGO enhances its electrical and sensing properties.

References

1. Bio-Medicine, “Global Market for Nanotechnology to Reach $3.3 Trillion by 2018” Global Industry Analysts, Inc, (2012).
2. M. Reibold, P. Paufler, A. A. Levin, W. Kochmann, N. Pätzke, D. C. Meyer, “Materials: Carbon nanotubes in an ancient Damascus sabre”, Nature, **444**, 286 (2006).
3. R. Kumar, N. Khare, “Temperature dependence of conduction mechanism of ZnO and Co-doped ZnO thin films”, Thin Solid Films, **516**, 1302 (2008).
4. H. Yan, J. Johnson, M. Law, R. He, K. Knutsen, J. R. Mc Kinney, J. Pham, R. Saykally, P. Yang, “ZnO nanoribbon microcavity lasers” Adv. Mater. **15**, 907 (2003).
5. J. Singh, S. S. Patil, M. A. More, D. S. Joag, R. S. Tiwari, O. N. Srivastava, “Formation of aligned ZnO nanorods on self-grown ZnO template and its enhanced field emission characteristics” Appl. Surf. Sci., **256**, 6157 (2010).
6. T. Yu, F.-C. Cheong, C.-H. Sow, “Manipulation and Assembly of CuO nanorods with line optical tweezers”, Nanotechnology, **15**, 1732 (2004).
7. Y. Li, P.-C. Hsu, S.-M. Chen, “Multi-functionalized biosensor at WO_3–TiO_2 modified electrode for photoelectrocatalysis of norepinephrine and riboflavin”, Sens. Actuators B: Chem. **174**, 427 (2012).
8. G. Shin, M.Y. Bae, H. J. Lee, S. K. Hong, C. H. Yoon, G. Zi, J. A. Rogers, J. S. Ha, Gunchul Shin,“SnO2 nanowire logic devices on deformable nonplanar substrates”, ACS Nano, **5** (12), 10009 (2011).
9. L. Guo, E. Leobandung, S.Y. Chou, “Nanoscale silicon field effect transistors fabricated using imprint lithography,” Appl. Phys. Lett., **70**, 850 (1997).
10. R. Cooper, H. P. Upadhyaya, T. K. Minton, M. R. Berman, X. Du, S. M. George, “Protection of polymer from atomic-oxygen erosion using Al_2O_3 atomic layer deposition coatings”, Thin Solid Films, **516**, 4036 (2008).
11. S. Raghu, S. B. Chung , S. Lederer, “Theory of 'hidden' quasi-1D superconductivity in Sr_2RuO_4”, Journal of Physics: Conference Series, **449**, 012031 (2013).
12. W. Oelerich, T. Klassen, R. Bormann, “Metal oxides as catalysts for improved hydrogen sorption in nanocrystalline Mg-based materials”, J. Alloys Compd., **315**, 237 (2001).

13. V. Balouria, S. Samanta, A. Singh, A. K. Debnatha, A. Mahajan, R. K. Bedi, D. K. Aswal, S. K. Gupt, "Temperature dependent H_2S and Cl_2 sensing selectivity of Cr_2O_3 thin films" Sens. Actuators B: Chem., **176**, 38 (2013).
14. (a) C. Wang, L. Yin , L. Zhang, D. Xiang, R. Gao, "Metal oxide gas sensors: sensitivity and influencing factors", Sensors, **45**, 2088 (2010).
(b) G. Korotcenkov, "Metal oxides for solid-state gas sensors: What determines our choice?", Mater. Sci. Eng. B, **139**, 1 (2007).
15. A. B. M. A. Ashrafi, A. Ueta, A. Avramescu, H. Kumano, I. Suemune, Y.-W. Ok, T.-Y. Seong, "Growth and characterization of hypothetical zinc-blende ZnO films on GaAs (001) substrates with ZnS buffer layers", Appl. Phys. Lett. **76**(5), 550 (2000).
16. J. E. Jaffe, J. A. Snyder, Z. Lin, A. C. Hess, "LDA and GGA calculations for high-pressure phase transitions in ZnO and MgO", Physical Review B, **62**(3), 1660 (2000).
17. Ü. Özgür, Ya. I. Alivov, C. Liu, A. Teke, M. A. Reshchikov, S. Doğan, V. Avrutin, S.-J. Cho, H. Morkoç, J. Appl. Phys., **98**, 041301 (2005).
18. S. Das, S. Ghosh, "Fabrication of different morphologies of ZnO superstructures in presence of synthesized ethylammonium nitrate (EAN) ionic liquid: synthesis, characterization and analysis", Dalton Trans., **42**, 1645 (2013).
19. O. Dulub, L. A. Boatner, U. Diebold, "STM study of the geometric and electronic structure of ZnO(0001)-Zn, (View the MathML source)-O, (View the MathML source), and (View the MathML source) surfaces", Surf. Sci., **519** (3), 201 (2002).
20. D. Vogel, P. Krüger, J. Pollmann, "Ab initio electronic-structure calculations for II-VI semiconductors using self-interaction-corrected pseudopotentials", Phys. Rev. B, **52**, 14316 (1995).
21. B. K. Meyer, H. Alves, D. M. Hofmann, W. Kriegseis, D. Forster, F. Bertram, J. Christen, A. Hoffmann, M. Straßburg, M. Dworzak, U. Haboeck, A. V. Rodina, "Bound exciton and donor–acceptor pair recombinations in ZnO", phys. status solidi (b), **241**, 231 (2004).
22. Ü. Özgür, Y. I. Alivov, C. Liu, A. Teke, M. A. Reshchikov, S. Doğan, V. Avrutin, S. J. Cho H. Morkoç, "A comprehensive review of ZnO materials and devices", J. Appl. Phys., **98**, 041301 (2005).
23. C. Jagadish, S. Pearton (Editors), "Zinc oxide bulk, thin films and nanostructures", Elsevier Limited, 175 (2006).

24. V. A. Coleman, C. Jagadish, "Chapter 1 - Basic Properties and Applications of ZnO, in: J. Chennupati, P. Stephen (Eds.) Zinc Oxide Bulk", Thin Films and Nanostructures, Elsevier Science Ltd, Oxford, 1-20 (2006).
25. S. J. Pearton, D. P. Norton, K. Ip, Y. W. Heo, T. Steiner, "Recent progress in processing and properties of ZnO", Superlattice Microst, **34**, 3 (2003).
26. D. Schulz, S. Ganschow, D. Klimm, K. Struve, "Inductively heated Bridgman method for the growth of zinc oxide single crystals", J. Cryst. Growth., **310**, 1832 (2008).
27. A. B. Djurišić, Y. H. Leung, "Optical properties of ZnO nanostructures", Small, **2**, 944 (2006).
28. P. H. Kasai, "Electron spin resonance studies of donors and acceptors in ZnO", Phys. Rev., **130**, 989 (1963).
29. K. Vanheusden, W. L. Warren, C. H. Seager, D. R. Tallant, J. A. Voigt, B. E. Gnade, "Mechanisms behind green photoluminescence in ZnO phosphor powders", J. Appl. Phys., **79**, 7983 (1996).
30. S. Yamauchi, Y. Goto, and T. Hariu, "Photoluminescence studies of undoped and nitrogen-doped ZnO layers grown by plasma-assisted epitaxy", J. Cryst. Growth, **260**, 1 (2004).
31. M. Liu, A. H. Kitai, P. Mascher, "Point defects and luminescence centres in zinc oxide and zinc oxide doped with manganese", J. Lumin., **54**, 35 (1992).
32. E. G. Bylander, "Surface effects on the low-energy cathodoluminescence of zinc oxide", J. Appl. Phys., **49**, 1188 (1978).
33. X. Yang, G. Du, X. Wang, J. Wang, B. Liu, Y. Zhang, D. Liu, D. Liu, H. C. Ong, S. Yang, J. Cryst. Growth, **252**, 275 (2003).
34. K. Johnston, M. O. Henry, D. M. Cabe, T. Agne, T. Wichert, Proceedings of the Second Workshop on SOXESS European Network on ZnO, 27-30 October (2004), Caernarfon, Wales, UK.
35. J. Zhong, A. H. Kitai, P. Mascher, W. Puff, "The influence of processing conditions on point defects and luminescence centers in ZnO", J. Electrochem. Soc., **140**, 3644 (1993).
36. R. Dingle, "Luminescent transitions associated with divalent copper impurities and the green emission from semiconducting zinc oxide", Phys. Rev. Lett., **23**, 579 (1969).

37. M. H. Huang, S. Mao, H. Feick, H. Q. Yan, Y.Y. Wu, H. Kind, E. Weber, R. Russo, P. Yang, “Room-temperature ultraviolet nanowire nanolasers”, Science, **292**, 1897 (2001).
38. A. B. Djurisic, Y. H. Leung, K. H. Tam, L. Ding, W. K. Ge, H. Y. Chen, S. Gwo, “Green, yellow, and orange defect emission from ZnO nanostructures: Influence of excitation wavelength”, Appl Phys Lett. **88**, 103107 (2006).
39. F. A. Kroger, The chemistry of imperfect crystals, North-Holland Publishing Company, Amsterdam, 691 (1964).
40. V. Bhosle, A. Tiwari, J. Narayan, “Metallic conductivity and metal-semiconductor transition in Ga-doped ZnO”, Appl. Phys. Lett., **88**, 032106 (2006).
41. G. Heideman, J. W. M. Noordermeer, R. N. Datta, B. van Baarle, “Zinc loaded clay as activator in sulfur vulcanization: A new route for zinc oxide reduction in rubber compounds”, Rubber Chem. Technol., **77**, 336 (2004).
42. A. Moezzi, A. M. McDonagh, M. B. Cortie, “Zinc oxide particles: Synthesis, properties and applications”, Chem. Eng. J., **185**, 1 (2012).
43. R. L. Cowan, "BWR water chemistry?a delicate balance" Nucl Energ”, **40**(4), 245 (2001).
44. C. Klingshirn, “ZnO: Material, Physics and applications”, Chem Phys Chem., **8**, 782 (2007).
45. K. H. Brown, K. R. Wessells, S. Y. Hess, “Zinc bioavailability from zinc-fortified foods”, Int. J. Vitam. Nutr. Res., **77**, 174 **(**2007).
46. K. H. Brown, S. Y. Hess, “Preventive zinc supplementation among infants, preschoolers, and older prepubertal children”, Food Nutrit. Bull., **30**, (2009).
47. N. Padmavathy, R. Vijayaraghavan, “Enhanced bioactivity of ZnO nanoparticles—an antimicrobial study”, Sci. Technol. Adv. Mater., **9**, 035004 (2008).
48. C. J. Frederickson, J.-Y. Koh, A. I. Bush, “The neurobiology of zinc in health and disease”, Nat. Rev. Neurosci., **6**, 449 (2005).
49. T.-H. Hwang, I.-S. Yang, O.-K. Kwon, M.-K. Ryu, C.-W. Byun, C.-S. Hwang, S.-H. K. Park, “Inverters using only N-type indium gallium zinc oxide thin film transistors for flat panel display applications”, Jpn. J. Appl. Phys., **50**, 03CB06 (2011).
50. G. M. Nama, M. S. Kwonb, “Transparent conducting Ga-doped ZnO thin film for flat-panel displays with a sol-gel spin coating”, J. Inform. Display, **9**, 8 (2008).

51. A. Tsukazaki, T. Onuma, M. Ohtani, T. Makino, M. Sumiya, K. Ohtani, S. F. Chichibu, S. Fuke, Y. Segawa, H. Ohno, H. Koinuma, M. Kawasaki, "Blue light-emitting diode based on ZnO", Nature. Mater., **4**, 42 (2005).
52. A. Ohtomo, A. Tsukazaki, "Pulsed laser deposition of thin films and superlattices based on ZnO", Semicond. Sci. Technol., **20**, S1 (2005).
53. S. D. Shindea, S. M. Jejurikarb, S. S. Patila, D. S. Joaga, S. K. Datea, M. A. Morea, S. Kaimalc, T. Shripathi, K. P. Adhi, "Pulsed laser deposited Ga doped ZnO/SiO_x/Si(100) thin films and their field emission behavior", Solid State Sci., **13**, 1724 (2011).
54. S. K. Gupta, A. Joshi, M. Kaur, "Development of gas sensors using ZnO nanostructures", J. Chem. Sci., **122**, 57 (2010).
55. O. Singh, N. Kohli, R. C. Singh, "Precursor controlled morphology of zinc oxide and its sensing behaviour", Sensors and Actuators B Chem., **178**, 149 (2013).
56. S. Palanisamy, S. Cheemalapati, S.-M. Chen, "Enzymatic glucose biosensor based on multiwalled carbon nanotubes-zinc oxide composite", Int. J. Electrochem. Sci., **7**, 8394 (2012).
57. S. Razdan, P. Patra, Y. Kim, S. Warner, "Spherulitic morphology and thermal stability of PP/ZnO nanocomposites", Mat. Res. Soc. Symp. Proc., **788**, 297 (2004).
58. W.-H. Lin, T.-F. M. Chang, Y.-H. Lu, T. Sato, M. Sone, K.-H. Wei, Y.-J. Hsu, "Supercritical CO_2-assisted electrochemical deposition of ZnO mesocrystals for practical photoelectrochemical applications", J. Phys. Chem. C, **117**, 25596 (2013).
59. B. Cao, Y. Li, G. Duan, W. Cai, "Growth of ZnO nanoneedle arrays with strong ultraviolet emissions by an electrochemical deposition method", Cryst. Growth Des., **6**, 1091 (2006).
60. Y. Zhu, H. I. Elim, Y.-L. Foo, T. Yu, Y. Liu, W. Ji, J.-Y. Lee, Z. Shen, A.T.-S. Wee, J. T.-L. Thong, C.-H. Sow, Adv. Mater., **18**, 121 (2006).
61. Z. L. Wang, J. Song,"Piezoelectric nanogenerators based on Zinc Oxide nanowire arrays", Science, **312**, 242 (2006).
62. A. Forleo, L. Francioso, S. Capone, P. Siciliano, P. Lommens, Z. Hens, "Synthesis and gas sensing properties of ZnO quantum dots", Sens. Actuators B Chem., **146**, 111 (2010).
63. S.-P. Chang, K.-Yu Chen, "UV Illumination room-temperature ZnO nanoparticle ethanol gas sensors", ISRN Nanotechnology **2012**, (2012).

64. X.-L. Yu, H.-M. Ji, H.-L. Wang, J. Sun, X.-W. Du, "Synthesis and sensing properties of ZnO/ZnS nanocages", Nanoscale Res Lett., **5**(3), 644 (2010).
65. L. Wang, Z. Lou, T. Fei, T. Zhang, "Templating synthesis of ZnO hollow nano spheres loaded with Au nanoparticles and their enhanced gas sensing properties", J. Mater. Chem. **22**, 4767 (2012).
66. Y. I-Chuan, L. Pang, T. T.-Yuen, "Hydrogen gas sensors using ZnO–SnO_2 core–shell nanostructure", Adv. Sci. Lett., **3**, 548 (2010).
67. N. S. Ramgir, M. Kaur, P. K. Sharma, N. Datta, S. Kailasaganapathi, S. Bhattacharya, A.K. Debnath, D.K. Aswal, S.K. Gupta, "Ethanol sensing properties of pure and Au modified ZnO nanowires", Sens. Actuators B Chem., **187,** 313 (2013).
68. T.-J. Hsueh, S.-J. Chang, C.-L. Hsu, Y.-R. Lin, C. Chen, "ZnO Nanotube ethanol gas sensors", J. Electrochem. Soc., **155**, K152 (2008).
69. L. Wang,Y. Kang, X. Liu, S. Zhang, W. Huang, S. Wang, "ZnO nanorod gas sensor for ethanol detection", Sens. Actuators B Chem., **162**, 237 (2012).
70. L. Peng, D. Wang, M. Yang, T. Xie, Q. Zhao, "The characteristic of photoelectric gas sensing to oxygen and water based on ZnO nanoribbons at room temperature", Appl. Surf. Sci., **254,** 2856 (2008).
71. L. Shi, A. J. T. Naik, Josephine, B. M. Goodall, C. Tighe, R. Gruar, R. Binions, I. Parkin, J. Darr, "Highly sensitive ZnO nanorod- and nanoprism-based NO_2 gas sensors: Size and shape control using a continuous hydrothermal pilot plant", Langmuir, **29**, 10603 (2013).
72. Z. Jingand, J. Zhan, "Fabrication and gas-sensing properties of porous ZnO nanoplates", Adv. Mater., **20**, 4547 (2008).
73. S.-L. Zhang, J.-O. Lim, J.-S. Huh, J.-S. Noh, W. Lee, "Two-step fabrication of ZnO nanosheets for high-performance VOCs gas sensor", Curr. Appl. Phys., **13**, S156 (2013).
74. T. P. Chen, S. P. Chang, F. Y. Hung, S. J. Chang, Z. S. Hu, K. J. Chen, "Simple fabrication process for 2D ZnO nanowalls and their potential application as a methane sensor", Sensors (Basel) **13**, 3941 (2013).
75. Z. Li, W. Pan, D. Zhang, J. Zhan, "Morphology-dependent gas-sensing properties of ZnO nanostructures for chlorophenol", Chem. Asian J., **5**, 1854 (2010).

76. N. Zhang, K. Yu, Q. Li, Z. Q. Zhu, Q. Wan, "Room-temperature high-sensitivity H_2S gas sensor based on dendritic ZnO nanostructures with macroscale in appearance", J. Appl. Phys., **103**, 104305 (2008).
77. V. Dobrokhotov, L. Oakes, D. Sowell, A. Larin, J. Hall, "ZnO coated nanospring-based chemiresistors", J. Appl. Phys., **111**, 044311 (2012).
78. Y. Sun, K. E Addison, M. N. R. Ashfold, "Growth of arrays of Al-doped ZnO nanocones by pulsed laser deposition", Nanotechnology, **18,** 495601 (2007).
79. L.-J. Bie, X.-N. Yan, J. Yin,Y.-Q. Duan, Z.-H. Yuan, "Nanopillar ZnO gas sensor for hydrogen and ethanol", Sens. Actuators B Chem., **126**, 604 (2007).
80. W. Guoa, T. Liu, H. Zhang, R. Sun, Y. Chen, W. Zeng, Z. Wang, "Gas-sensing performance enhancement in ZnO nanostructures by hierarchical morphology", Sens. Actuators B Chem., **166**, 492 (2012).
81. C. H. Bae, S. M. Park, S. C. Park, J. S. Ha, "Growth of arrays of Al-doped ZnO nanocones by pulsed laser deposition", Nanotechnology, **17**, 381 (2006).
82. M. H. Huang, Y. Y. Wu, H. Feick, N. Tran, E. Weber, P. D. Yang, "Increased efficiency and controlled light output from a microstructured light-emitting diode", Adv. Mater., **13**, 113 (2001).
83. J. Grabowska, K. K. Nanda, E. McGlynn, J. P. Mosnier, M. O. Henry, "Studying the growth conditions, the alignment and structure of ZnO nanorods", Surf. Coat. Technol., **200**, 1093 (2005).
84. Y. W. Hoe, V. Varadarajan, M. Kaufman, K. Kim, D. P. Nort, "Microstructural evaluation of multicomponent ZnO ceramics", Appl. Phys. Lett., **81**, 3046 (2002).
85. W. I. Park, Y. H. Jun, S. W. Jung, G. C. Yi, "ZnO nanocoral structures for photoelectrochemical cells", Appl. Phys. Lett., **82**, 964 (2003).
86. J. J. Wu, S. C. Liu, "Hot electron relaxation dynamics of gold nanoparticles embedded in $MgSO_4$ powder compared to solution: The effect of the surrounding medium", J. Phys. Chem. B, **106**, 945 (2002).
87. J. B. Yi, H. Pan, J. Y. Lin, J. Ding, Y. P. Feng, S. Thongmee, T. Liu, H. Gong, L. Wang, "Ferromagnetism in ZnO nanowires derived from electro-deposition on AAO template and subsequent oxidation", Adv. Mater., **20**, 1170 (2008).
88. S. Öztürk, N. Tasaltin, N. Kilinc, Z.Z. Öztürk, "Fabrication of ZnO nanotubes using AAO template and sol-gel method", J. Optoelectronic Biomed. Mater., **1**, 15 (2009).

89. Y. Liu, J. Goebl, Y. Yin, "Templated synthesis of nanostructured materials", Chem. Soc. Rev., **42,** 2610 (2013).
90. A. H. C. Neto, F. Guinea, N. M. R. Peres, "Drawing conclusions from graphene", Physics World, **19**, 33 (2006).
91. K. S. Novoselov, A. K. Geim, S. V. Morozov, D. Jiang, Y. Zhang, S. V. Dubonos, I. V.Grigorieva, A. A. Firsov, "Electric field effect in atomically thin carbon films", Science, **306**, 666 (2004).
92. A. K. Geim, "Graphene: Status and prospects", Science, **324**, 1530 (2009).
93. A. K. Geim, K. S. Novselov, "Material witness: Technology takes tiny steps", Nat. Mater., **6**, 183 (2007).
94. V. Dhand, K. Y. Rhee, H. J. Kim, D. H. Jung, "A comprehensive review of graphene nanocomposites: Research status and trends", J. Nano Mat., **2013**, (2013).
95. S. V. Morozov, K. S. Novoselov, M. I. Katsnelson, F. Schedin, D. C. Elias, J. A. Jaszczak, A. K. Geim, "Giant intrinsic carrier mobilities in graphene and its bilayer", Phys. Rev. Lett., **100**, 016602 (2008)
96. C. Lee, X. D. Wei, J. W. Kysar, J. Hone, "Measurement of the elastic properties and intrinsic strength of monolayer graphene", Science, **321**, 385 (2008).
97. A. A. Balandin, S. Ghosh, W. Bao, I. Calizo, D. Teweldebrhan, F. Miao, C. N. Lau, "Superior thermal conductivity of single-layer graphene", Nano Lett., **8**(3), 902 (2008).
98. D. E. Sheehy, J. Schmalian, "Optical transparency of graphene as determined by the fine-structure constant", Phy. Rev. B, **80**, 193411 (2009).
99. S. Park, K.-S. Lee, G. Bozoklu, W. Cai, S. T. Nguyen, R. S. Ruoff, "Graphene oxide papers modified by divalent ions enhancing mechanical properties via chemical cross-Linking", ACS Nano, **2**, 572 (2008).
100. Q. M. Yan, B. Huang, J. Yu, F. Zheng, Zang, J. Wu, B.-L. Gu, F. Liu, W. Duan, "Intrinsic current–voltage characteristics of graphene nanoribbon transistors and effect of edge doping", Nano Lett., **7**, 1469 (2007).
101. B. Obradovic, R. Kotlyar, F. Heinz, P. Matagne, T. Rakshit, M. D. Giles, M. A. Stettler and D. E. Nikonov, "Analysis of graphene nanoribbons as a channel material for field-effect transistors", Appl. Phys. Lett., **88**, 142102 (2006).

102. V. Barone, O. Hod, G. E. Scuseria, "Electronic structure and stability of semiconducting graphene nanoribbons", Nano Lett., **6**, 2748 **(**2006).

103. S. Bae, H. Kim, Y. Lee, X. Xu, J.-S. Park, Y. Zheng, J. Balakrishnan, T. Lei, H. R. Kim, Y. I. Song, Y.-J. Kim, K. S. Kim, B. Özyilmaz, J.-H. Ahn, B. H. Hong, S. Iijima, "Roll-to-roll production of 30-inch graphene films for transparent electrode", Nat.Nanotechnol., **5,** 574 (2010).

104. J. A. Robinson, M. Hollander, M. Labella, III, K. A. Trumbull, R. Cavalero, D. W. Snyder "Epitaxial Graphene Transistors: Enhancing Performance via Hydrogen Intercalation", Nano Lett., **11**, 3875 (2011).

105. M. J. Hollander, M. Labella, Z. R. Hughes, M. Zhu, K. A. Trumbull, R. Cavalero, D. W. Snyder, X. Wang, E. Hwang , S. Datta, J. A. Robinson, "Enhanced transport and transistor performance with oxide seeded high-κ gate dielectrics on wafer-scale epitaxial graphene", Nano Lett., **11** (9), 3601 **(**2011).

106. M. A. Gluba, D. Amkreutz, G. V. Troppenz, J. Rappich, and N. H. Nickel, "Embedded graphene for large-area silicon-based devices", Appl. Phys. Lett., **103**, 073102 (2013).

107. B. Lang,"A leed study of the deposition of carbon on platinum crystal surfaces", Surf. Sci., **53**, 317 (1975).

108. H. Shioyama, "Cleavage of graphite to graphene", J. Mater. Sci. Lett., **20**, 499 (2001).

109. Walt A. de Heer, "Early development of graphene" http://hdl. Handle .net /1853 /31 270.

110. "This Month in Physics History: October 22, 2004: Discovery of Graphene", APS News. Series II, **18** (9), 2 (2009).

111. P. Blake, E. W. Hill, A. H. Castro Neto, K. S. Novoselov, D. Jiang, R. Yang, T. J. Booth, A. K. Geim, "Making graphene visible", Appl. Phys. Lett., **91**, 063124 (2007)

112. S. Stankovicha, D. A. Dikina, R. D. Pinera, K. A. Kohlhaas, A. Kleinhammes, Y. Jia, Y. Wu, S. T. Nguyen, R. S. Ruoff, "Synthesis of graphene-based nanosheets via chemical reduction of exfoliated graphite oxide", Carbon, **45**, 1558 (2007).

113. J. I. Paredes, S. V.-Rodil , A. M.-Alonso, J. M. D. Tascon, "Graphene oxide dispersions in organic solvents", Langmuir, **24**, 10560 (2008).

114. G. G. W allace, R. B. Kaner, M. Muller, S. Gilje, D. Li, "Processable aqueous dispersions of graphene nanosheets", Nat. Nanotechnol., **3**(2), 101 (2008).

115. S. Pei, H.-M. Cheng, "The reduction of graphene oxide", Carbon, **50**, 3210 (2012).

116. B. C. Brodie, "On the atomic weight of graphite", Philos. T. Roy. Soc. London, **149**, 249 (1859).

117. W. S. Hummers, R. E. Offeman, "Preparation of graphitic oxide", J. Am. Chem. Soc., **80**, 1339 (1958).

118. D. C. Marcano, D.V. Kosynkin, J. M. Berlin, A. Sinitskii, Z. Z. Sun, A. Slesarev, L. B. Alemany, W. Lu, J.M. Tour, "Improved synthesis of graphene oxide", ACS Nano, **4**, 4806 (2010).

119. N. I. Kovtyukhova, P. J. Ollivier, B. R. Martin, T. E. Mallouk, S. A. Chizhik, E. V. Buzaneva, A. D. Gorchinskiy, "Layer-by-layer assembly of ultrathin composite films from micron-sized graphite oxide sheets and polycations, Chem. Mater., **11**, 771 (1999).

120. S.-Y. Kwon, C. V. Ciobanu, V. Petrova, V. B. Shenoy, J. Bareno,V. Gambin, I. Petrov, S. Kodambaka, Growth of Semiconducting Graphene on Palladium, Nano Lett., **9**, 3985 (2009).

121. N. Liu, F. Luo, H. Wu, Y. Liu, C. Zhang, J. Chen, "One-step ionic-liquid-assisted electrochemical synthesis of ionic-liquid-functionalized graphene sheets directly from graphite, Adv. Funct. Mater, **18**, 1518 (2008).

122. J. Lu, J.-x. Yang, J. Wang, A. Lim, S. Wang, K. P. Loh, "One-pot synthesis of fluorescent carbon nanoribbons, nanoparticles, and graphene by the exfoliation of graphite in ionic liquids", ACS Nano, **3**, 2367 (2009).

123. M. Mao, M. Wang, J. Hu, G. Lei, S. Chen, H. Liu, "Simultaneous electrochemical synthesis of few-layer graphene flakes on both electrodes in protic ionic liquids", Chem. Commun., **49**, 5301 (2013).

124. C.-Y. Su, A.-Y. Lu, Y. Xu, F.-R. Chen, A. N. Khlobystov, L.-J. Li, "High-quality thin graphene films from fast electrochemical exfoliation", ACS Nano, **5**, 2332 (2011).

125. L. Tang, X. Li, R. Ji, K. S. Teng, G. Tai, J. Ye, C. Wei, S. P. Lau, "Bottom-up synthesis of large-scale graphene oxide nanosheets", J. Mater. Chem., **22**, 5676 (2012).

126. Q. Yu, J. Lian, S. Siriponglert, H. Li, Y. P. Chen, S.-S. Pei, "Graphene segregated on Ni surfaces and transferred to insulators", Appl. Phys. Lett., **93**, 113103 (2008).

127. A. Reina, X. Jia, J. Ho, D. Nezich, H. Son, V. Bulovic, M. S. Dresselhaus, J. Kong, "Large area, few-layer graphene films on arbitrary substrates by chemical vapor deposition, Nano Lett., **9**, 30 (2009).

128. K. S. Kim, Y. Zhao, H. Jang, S. Y. Lee, J. M. Kim, K. S. Kim, J. H. Ahn, P. Kim, J. Y. Choi, B. H. Hong, "Large-scale pattern growth of graphene films for stretchable transparent electrodes", Nature, **457**, 706 (2009).

129. X. Li, W. Cai, J. An, S. Kim, J. Nah, D. Yang, R. Piner, A. Velamakanni, I. Jung, E. Tutuc, S. K. Banerjee, L. Colombo, R. S. Ruoff, "Large-area synthesis of high-quality and uniform graphene films on copper foils", Science, **324**, 1312 (2009).

130. X. Li, W. Cai, L. Colomb, R. S. Ruoff, "Evolution of graphene growth on Ni and Cu by carbon isotope labeling, Nano Lett., **9**, 4268 (2009).

131. X. Li, C. W. Magnuson, A. Venugopal, J. An, J. W. Suk, B. Han, M. Borysiak, W. Cai, A. Velamakanni, Y. Zhu, L. Fu, E. M. Vogel, E. Voelkl, L. Colombo, R. S. Ruoff, "Graphene films with large domain size by a two-step chemical vapor deposition process", Nano Lett., 10, 4328 (**2010**).

132. J. M. Wofford, S. Nie, K. F. Mc Carty, N. C. Bartelt, O. D. Dubon, "Graphene islands on Cu foils: The interplay between shape, orientation, and defects", Nano Lett., **10**, 4890 (2010).

133. P. Y. Huang, C. S. Ruiz-Vargas, A. M. van der Zande, W. S. Whitney, M. P. Levendorf, J. W. Kevek, S. Garg, J. S. Alden, C. J. Hustedt, Y. Zhu, J. Park, P. L. McEuen, D. A. Muller, "Grains and grain boundaries in single-layer graphene atomic patchwork quilts" Nature, **469**, 389 (2011).

134. A. Srivastava, C. Galande, L. Ci, L. Song, C. Rai, D. Jariwala, K. F. Kelly, P. M. Ajayan, "Novel liquid precursor-based facile synthesis of large-area continuous, single, and few-layer graphene films", Chem. Mater., **22**, (2010).

135. J. Hass, J. E. Millán-Otoya, P. N. First, E. H. Conrad, "Interface structure of epitaxial graphene grown on 4H-SiC(0001)", Phys. Rev. B, **78**, 205424 (2008).

136. W. A. de Heer, C. Berger, M. Ruan, M. Sprinkle, X. Li, Y. Hu, B. Zhang, J. Hankinson, E. Conrad, "Large area and structured epitaxial graphene produced by confinement controlled sublimation of silicon carbide", Proc. Natl. Acad. Sci. USA, **108**, 16900 (2011).

137. P. R. Wallace, "The band theory of graphite", Phys. Rev., **71**, 622 (1947).

138. A. K. Geim, A. H. MacDonald, "Graphene: Exploring carbon flatland", Physics Today, **60**(8), 35 (2007).

139. A. H. Castro Neto, F. Guinea, N. M. R. Peres, K. S. Novoselov, A. K. Geim, "The electronic properties of graphene", Rev. Mod. Phys., **81**, 109 (2009).

140. M. Wilson, “Electrons in atomically thin carbon sheets behave like massless particles”, Physics Today, **59**(1), 21 (2006).

141. S. Stankovich, R. D. Piner, X. Chen, N. Wu, S. T. Nguyen, R. S. Ruoff, “Stable aqueous dispersions of graphitic nanoplatelets via the reduction of exfoliated graphite oxide in the presence of poly(sodium 4-styrenesulfonate)”, J. Mater. Chem., **16**, 155 (2006).

142. J. R. Lomeda, C. D. Doyle, D. V. Kosynkin, W.-F. Hwang, J. M. Tour, “Diazonium functionalization of surfactant-wrapped chemically converted graphene sheets”, J. Am. Chem. Soc., **130**, 16201 (2008).

143. V. C. Tung, M. J. Allen, Y. Yang, R. B. Kaner, “High-throughput solution processing of large-scale graphene”, Nature Nanotech., **4**, 25 (2008).

144. G. Wang, J. Yang, J. Park , X. Gou , B. Wang, H. Liu, J. Yao, “Facile synthesis and characterization of graphene nanosheets”, J. Phys. Chem. C, **112**, 8192 (2008).

145. R. Muszynski, B. Seger, P. V. Kamat, “Decorating graphene sheets with gold nanoparticles”, J. Phys. Chem. C, **112**, 5263 (2008).

146. H. C. Schniepp, J. L. Li, M. J. McAllister, H. Sai, M. H. Alonso, D. H. Adamson, R. K. Prudhomme, R. Car, D. A. Saville, I. A. Aksay, “Functionalized single graphene sheets derived from splitting graphite oxide”, J. Phys. Chem. B, **110**, 8535 (2006).

147. M. J. McAllister, J. L. Li, D. H. Adamson, H. C. Schniepp, A. A. Abdala, J. Liu, M. H.-Alonso, D. L. Milius, R. Car, R. K. Prudhomme, I. A. Aksay, “Single sheet functionalized graphene by oxidation and thermal expansion of graphite”, Chem. Mater., **19**, 4396 (2007).

148. G. Williams, B. Serger, P. V. Kamat, “TiO2-graphene nanocomposites. UV-assisted photocatalytic reduction of graphene oxide”, ACS Nano, **2**, 1487 (2008).

149. M. D. Stoller, S. Park,Y. Zhu, J. An, R. S. Ruoff, “Graphene-based ultracapacitors”, Nano Lett., **8**, 3498 (2008).

150. Chaohe Xu, Binghui Xu, Yi Gu, Zhigang Xiong, Jing Sunb, X. S. Zhao, “Graphene-based electrodes for electrochemical energy storage”, Energy Environ. Sci., **6**, 1388 (2013).

151. P. Blake, P. D. Brimicombe, R. R. Nair, T. J. Booth, D. Jiang, F. Schedin, L. A. Ponomarenko, S. V. Morozov, H. F. Gleeson, E. W. Hill, A. K. Geim, K. S. Novoselov, “Graphene-based liquid crystal device”, Nano Lett., **8** (6), 1704 (2008).

152. Y.-J. Jeona, J.-M. Yunb, D.-Y. Kimb, S.-I. Naa, S.-S. Kimc, "High-performance polymer solar cells with moderately reduced graphene oxide as an efficient hole transporting layer", Sol. Energy Mat. Sol. C., **105**, 96 (2012).

153. J.-M. Yun, J.-S. Yeo, J. Kim, H.-G. Jeong, D.-Y. Kim, Y.-J. Noh, S.-S. Kim, B.-C. Ku, S.-I. Na, "Organic solar cells: Solution-processable reduced graphene oxide as a novel alternative to PEDOT:PSS hole transport layers for highly efficient and stable polymer solar cells", Adv. Mater., **23**, 4923 (2011).

154. Z. Li, F. Gong, G. Zhou, Z.-S. Wang, "NiS2/Reduced graphene oxide nanocomposites for efficient dye-sensitized solar cells", J. Phys. Chem. C, **117** (13), 6561 (2013).

155. S. Stankovich, D. A. Dikin, G. H. B. Dommett, K. M. Kohlhaas, E. J. Zimney, E. A. Stach, R. D. Piner, S. B. T. Nguyen, Rodney S. Ruoff, "Graphene-based composite materials", Nature, **442**, 282 (2006).

156. T. Ramanathan, A. A. Abdala, S. Stankovich, D. A. Dikin, M. Herrera-Alonso, R. D. Piner, D. H. Adamson, H. C. Schniepp, X. Chen, R. S. Ruoff, S. T. Nguyen, I. A. Aksay, R. K. Prud'Homme, L. C. Brinson, "Functionalized graphene sheets for polymer nanocomposites", Nature Nanotechnology, **3**, 327 (2008).

157. P. M. Sudeep, T. N. Narayanan, A. Ganesan, M. M. Shaijumon, H. Yang, S. Ozden, P. K. Patra , M. Pasquali, R. Vajtai, S. Ganguli, A. K. Roy, M. R. Anantharaman, P. M. Ajayan, "Covalently interconnected three-dimensional graphene oxide solids", ACS Nano, **7** (8), 7034 (2013).

158. N. Hu, Z. Yang, Y. Wang, L. Zhang, Y. Wang, X. Huang, H. Wei, L. Wei, Y. Zhang, "Ultrafast and sensitive room temperature NH_3 gas sensors based on chemically reduced graphene oxide", Nanotechnology, **25**, 025502 (2014)

159. A. Lipatov, A. Varezhnikov, P. Wilson, V. Sysoev, A. Kolmakov, A. Sinitskii, "Highly selective gas sensor arrays based on thermally", Nanoscale, **5**, 5426 (2013).

160. D. A. Dikin, S. Stankovich, E. J. Zimney, R. D. Piner, G. H. B. Dommett, G. Evmenenko, S. T. Nguyen, R. S. Ruoff, "Preparation and characterization of graphene oxide paper", Nature, **448**, 457 (2007).

161. S. Park, K. Seok Lee, G. Bozoklu, W. Cai , S. T. Nguyen, R. S. Ruoff, "Graphene oxide papers modified by divalent ions—enhancing mechanical properties via chemical cross-linking", ACS Nano, **2**, 572 (2008).

162. J. Robinson, M. Zalalutdniov, J. Baldwin, J. Burgess, Z. Wei, P. Sheehan, E. Snow, B. Houston, "Graphene and chemically Modified Graphene Nanomechanical Resonators", http://meetings.ap s.org/link/BAPS. 2010. MAR.V21.5.

163. V. Desai, S. Sanisetty, B. Steber, E. Sapi, B. Aliane, S. Sinha, P. Patra, "Intermediate frequency AC signal analysis for bionanosensor", Journal of Nanotechnology, **2011**, (2011).

164. S. Palanisamy, S. Cheemalapatil, S.-M. Chen, "Enzymatic glucose biosensor based on multiwalled carbon nanotubes-zinc oxide composite", Int. J. Electrochem. Sci., **7**, 8394 (2012).

165. J. Wang, Y. H. Lin, "Functionalized carbon nanotubes and nanofibers for biosensing applications", Trac – Trends Anal. Chem., **27**, 619 (2008).

166. I. Willner, Y. M. Yan, B. Willner, R. Tel-Vered, "Integrated enzyme-based biofuel cells–a review", Fuel Cells, **9**,7 (2009).

167. K. P. Gong, F. Du, Z. H. Xia, M. Durstock, L. M. Dai, "Nitrogen-doped carbon nanotube arrays with high electrocatalytic activity for oxygen reduction", Science, **323**, 760 (2009).

168. Y. Shao, J. Liu, Y. Wang, Y. Lin, "Novel catalyst support materials for PEM fuel cells: current status and future prospects", J. Mater. Chem., **19**, 46 (2009).

169. Y. Wang, Y. Li, L. Tang, J. Lu, J. Li, "Application of graphene-modified electrode for selective detection of dopamine", Electrochem. Commun, **11**, 889 (2009).

170. S. Alwarappan, A. Erdem, C. Liu, C. Z. Li, "Probing the electrochemical properties of graphene nanosheets for biosensing applications", J. Phys. Chem. C, **113**, 8853 (2009).

171. A. Barth, W. Marx, "Graphene-A rising star in view of scientometrics", arXiv:0808.3320v3, (2008).

172. I. V. Lightcap, T. H. Kosel, P. V. Kamat, "Anchoring semiconductor and metal nanoparticles on a 2-dimensional catalyst mat. storing and shuttling electrons with reduced graphene oxide", Nano Lett., **10**, 577 (2010).

173. H. Hayashi, I. V. Lightcap, M. Tsujimoto, M. Takano, T. Umeyama, P. V. Kamat, H. Imahori, "Electron transfer cascade by organic/inorganic ternary composites of porphyrin, zinc oxide nanoparticles and reduced graphene oxide on a tin oxide electrode that exhibits efficient photocurrent generation", J. Am. Chem. Soc., **133**, 7684 (2011).

174. H. Zhang, J. Feng, T. Fei, S. Liu, T. Zhang, "SnO_2 nanoparticles-reduced graphene oxide nanocomposites for NO_2 sensing at low operating temperature", Sensors and Actuators B, **190**, 472 (2014).

175. Y. Zhao, X. Song, Q. Song, Z. Yina, "A facile route to the synthesis copper oxide/reduced graphene oxide nanocomposites and electrochemical detection of catechol organic pollutant", Cryst Eng Comm., **14**, 6710 (2012).

176. C. M. Santos, J. Mangadlao, F. Ahmed, A. Leon, R. C. Advincula, D. F. Rodrigues "Graphene nanocomposite for biomedical applications: fabrication, antimicrobial and cytotoxic investigations", Nanotechnology, **23**, 395101 (2012).

177. K. S. Novoselov, A. K. Geim, S. V. Morozov, D. Jiang, M. I. Katsnelson, I. V. Grigorieva, S. V. Dubonos, A. A. Firsov, "Two-dimensional gas of massless Dirac fermions in graphene", Nature, **438**, 197 (2005).

178. M. I. Katsnelson, K. S. Novoselov, A. K. Geim, "Chiral tunnelling and the Klein paradox in graphene" Nat. Phys., **2**, 620 (2006).

179. A. H. C. Neto, F. Guinea, N. M. R. Peres, K. S. Novoselov, A. K. Geim, "The electronic properties of graphene", Rev. Mod. Phys., **81**, 109 (2009).

180. W. J. Beenakker, "Colloquium: Andreev reflection and Klein tunneling in graphene", Rev. Mod. Phys., **80**, 1337 (2008).

181. Y. Zhang, T. Tung, "Direct observation of a widely tunable bandgap in bilayer graphene", Nature, **459**, 820 (2009**)**.

182. E .V. Castro, K. S. Novoselov, "Biased bilayer graphene: Semiconductor with a gap tunable by the electric field effect", Phys. Rev. Lett., **99**, 216802 (2007).

183. X. Du, I. Skachko, A. Barker, E. Y. Andre, "Approaching ballistic transport in suspended graphene", Nat. Nanotechnol., **3**, 491 (2008).

184. K. S. Novoselov, Z. Jiang, Y. Zhang, S. V. Morozov, H. L. Stormer, U. Zeitler, J. C. Maan, G. S. Boebinger, P. Kim , A. K. Geim, "Room-temperature quantum Hall effect in graphene, Science, **315**, 1379 (2007).

185. M. D. Stoller, S. Park, Y. Zhu, J. An, R. S. Ruoff, "Graphene-based ultracapacitors", Nano Lett., **8**, 3498 (2008).

186. F. Schedin, A. K. Geim, S.V. Morozov, E. W. Hill, P. Blake, M.I. Katsnelson, K.S. Novoselov, "Detection of individual gas molecules adsorbed on graphene", Nat. Mater., **6**, 652 (2007).

187. S. Gilje, S. Han, M. Wang, K. L. Wang, R. B. Kaner, "A chemical route to graphene for device applications", Nano Lett., **7**, 3394 (2007).

188. J. T. Robinson, F. K. Perkins, E. S. Snow, Z. Wei, P. E. Sheehan, "Reduced graphene oxide molecular sensors" Nano Lett., **8,** 3137 (2008).

189. J. D. Fowler, M. J. Allen, V. C. Tung, Y. Yang, R. B. Kaner, B. H. Weiller, "Practical chemical sensors from chemically derived graphene", ACS Nano, **3**, 301 (2009).

190. R. Ghosh, A. Midya, S. Santra, S. K Ray, P. K. Guha, "Chemically reduced graphene oxide for ammonia detection at room temperature", ACS Appl. Mater. Interfaces, **5**, 7599 (2013).

191. J. D. Fowler, M. J. Allen, V. C. Tung, Y. Yang, R. B. Kaner, B. H. Weiller, "Practical chemical sensors from chemically derived graphene", ACS Nano, 3, 301 (2009).

191. W. Yuan, A. Liu, L. Huang, C. Li, G. Shi, "High-performance NO_2 sensors based on chemically modified graphene", Adv. Mater., **25**, 766 (2013).

192. S. Palanisamy, S.-M. Chen, R. Saraswathi, "A novel nonenzymatic hydrogen peroxide sensor based on reduced graphene oxide/ZnO composite modified electrode", Sensors and Actuators B Chem., **166**, 372 (2012).

193. L. Zhang, C. Li, A. Liu, G. Shi, "Electrosynthesis of graphene oxide/polypyrene composite films and their applications for sensing organic vapors", J. Mater. Chem., **22**, 8438 (2012).

194. R. Zou, G. He, K. Xu, Q. Liu, Z. Zhang, J. Hu, "ZnO nanorods on reduced graphene sheets with excellent field emission, gas sensor and photocatalytic properties", J. Mater. Chem., **A 1**, 8445 (2013).

195. V. Mani, B. Devadas and S.-M. Chen, "Direct electrochemistry of glucose oxidase at electrochemically reduced graphene oxide-multiwalled carbon nanotubes hybrid material modified electrode for glucose biosensor", Biosensors and Bioelectronics, **41**, 309 (2013).

196. Q. Lin, Y. Li, M. Yang, "Tin oxide/graphene composite fabricated via a hydrothermal method for gas sensors working at room temperature", Sens. and Actuators B Chem., **173**, 139 (2012).

SYNTHESIS AND PROCESSING OF NANOSTRUCTURES

2.1 INTRODUCTION

The main objectives of the present investigations are to synthesize ordered ZnO nanowires, reduced graphene oxide (rGO) thin film, rGO powder and rGO-ZnO nanocomposite (ZrGO) and study their structural, optical, electrical and gas sensing properties. In this chapter, we described and discussed the various standard experimental techniques employed for the (a) synthesis of samples, (b) characterization of structural-microstructural features and (c) measurement of electrical, optical and gas sensing properties. In the present work, the polycrystalline ZnO nanowires were synthesized using anodized aluminium oxide (AAO) template. Further, GO, rGO thin films were fabricated using spin coater and rGO, ZrGO powder samples were synthesized through hydrolysis method. Structural and surface morphological studies of the synthesized samples were performed using X-ray diffraction (XRD), transmission electron microscopy (TEM), field emission scanning electron microscopy (FE-SEM) in secondary electron (SE) imaging mode and atomic force microscopy (AFM). Energy dispersive X-ray (EDX) spectroscopy was used for elemental analysis and mapping. Thermogravimetric analysis (TGA), photoluminescence spectroscopy (PL) and other spectroscopic techniques like X-ray photo electron spectroscopy (XPS), Fourier transform infrared spectroscopy (FTIR) and Raman spectroscopy were used to investigate the stability, quality and the extent of graphitization of the samples.

2.2 SAMPLE PREPARATION

The porous AAO template was fabricated through anodization of highly pure Al foil. To obtain ordered ZnO nanowires empty pores of the template are filled with saturated zinc nitrate solution using indigenously developed vacuum-injection technique. Spin coater and hydrolysis techniques were used to synthesize GO, rGO thin films and rGO, ZrGO powder samples. Brief descriptions of synthesis routes are given in the next subsections.

2.2.1 Fabrication of ZnO nanowire array based gas sensor

2.2.1.1 Fabrication of AAO template

The porous AAO template was fabricated through the anodization of highly pure Al foil. Anodization is an electrochemical process in which polishing and shaping of a suitable semiconducting or metallic surface occur. Over the past decades, the anodization has been used for the production of durable dielectric and corrosion-resistive oxide films on the metallic surfaces [1-3]. Recently, anodization has employed extensively to form self-organized nanoporous structures by the anodic oxidation of a few semiconducting and metallic materials, such as Si [4-7], InP [8, 9], Al [10-12], Ti [13, 14], Zr [15, 16], Hf [17], Sn [18], Nb [19, 20]. Among all these materials, Al is well suited for anodization process because a highly ordered, porous structure of aluminum oxide (alumina) grows over the entire Al substrate after anodizing it.

In the present work AAO templates were fabricated by a two-step anodization process [21]. A schematic diagram and a digital image of the Teflon electrochemical cell, used in the experiment, are shown in Fig. 2.1 (a) and (b), respectively. Here a Pt mesh is used as cathode and a Cu block as anode. For anodization to take place a suitable voltage is

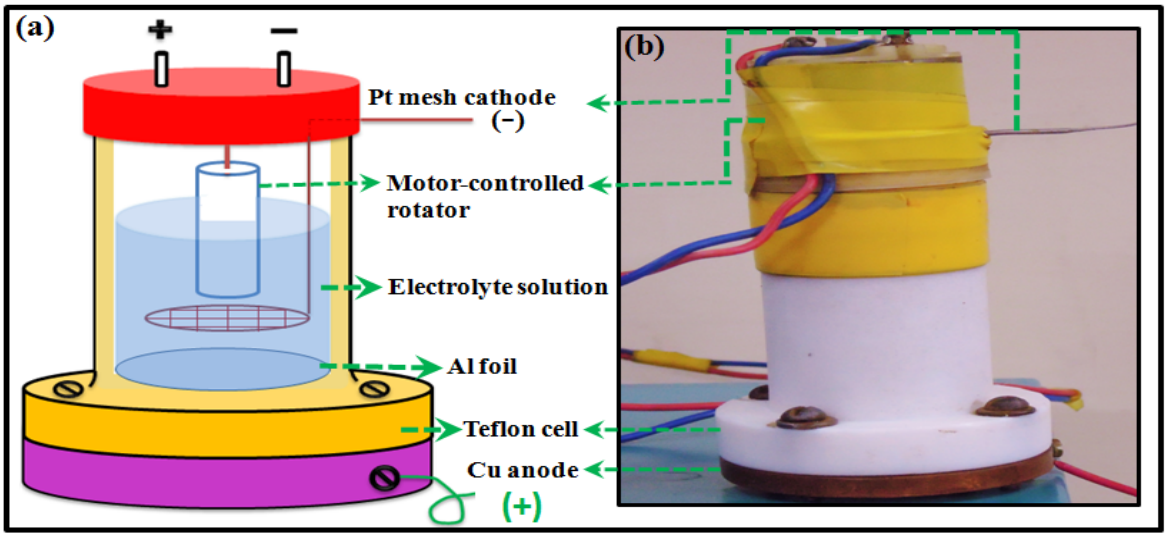

Figure 2.1: (a) Schematic diagram of electrochemical cell. **(b)** Digital image of cell used in the experiment.

applied between these two electrodes. During anodization process the electrolyte was vigorously stirred with the help of a motor-controlled rotator. As the temperature of the electrolyte is an important factor, which greatly influences the growth of ordered porous

structure on the surface of Al sheet therefore, it is controlled with the help of a chiller. Whole experimental set-up is shown in Fig. 2.2.

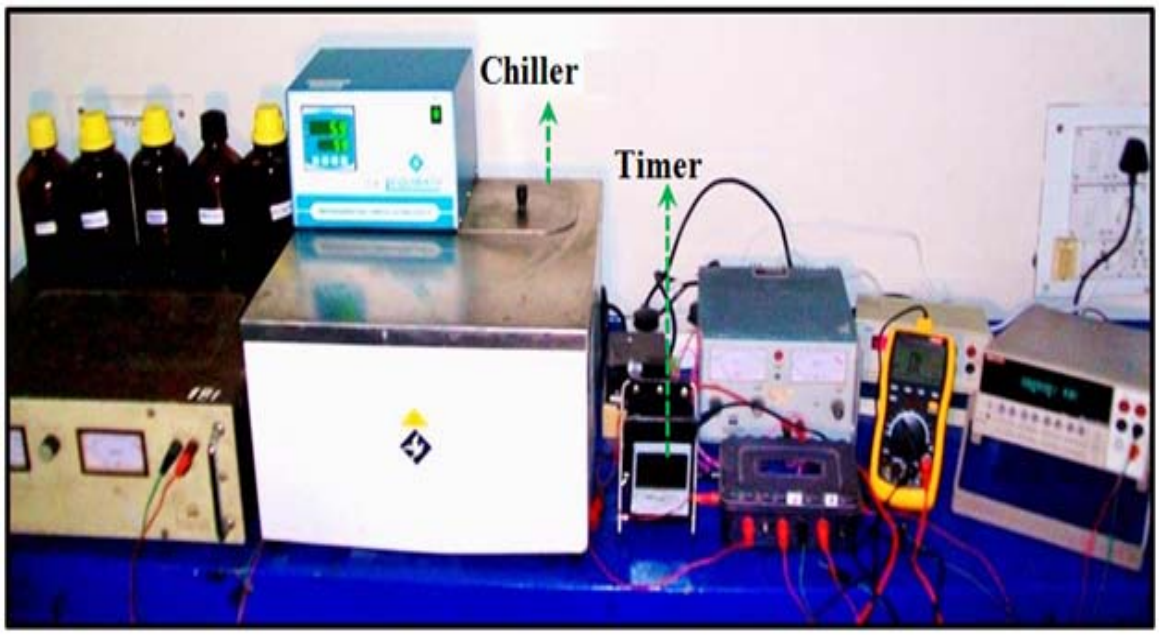

Figure 2.2: Digital image of experimental set-up used.

Prior to anodization, Al foil with purity >99.9%, thickness 0.3 mm and width 30 mm (Merck, 1.01057.0250) was cleaned in acetone by ultrasonic vibrations. The surface impurities were removed by immersing the cleaned Al foil for 20 s in a solution containing 1% HF, 10% HNO_3, 20% HCl and 69% H_2O by volume [22]. So cleaned Al foil was washed with distilled water and then electropolished in an electrochemical cell containing 85% ethanol (C_2H_5OH, 99.9%), 10% perchloric acid ($HClO_4$,70%) and 5% ethylene glycol ($C_2H_6O_2$, 99%) at 18 V for about 15 min. The electropolished Al foil was subjected to first anodization in 0.3 M oxalic acid solution under a constant dc voltage of 40 V for 2 h. During whole process the electrolyte was vigorously stirred and the bath temperature was kept constant at 3°C. The alumina (Al_2O_3) layer so formed over the Al foil was removed by immersing anodized Al foil in a mixture of 6.0 wt% phosphoric acid and 1.8 wt% chromic acid at 60°C for 30 min. This removal of alumina film left behind a well-ordered concave pattern on the surface of anodized Al foil. For the second anodization process, which was carried out under the same conditions as described in the first anodization process for 8 h, the ordered concave pattern acted as the sites for deep pore growth and helped in growing the uniform porous oxide film [23]. The so formed porous AAO template, having ordered nanopores of diameters 45-50 nm and thickness ~12 µm, was detached

from the Al substrate using electrochemical method. In this method we took 70% perchloric acid aqueous solution in an electrochemical cell and applied 45 volts between Pt cathode and Cu anode just for 15 s at 1°C.

2.2.1.2 Synthesis of ordered ZnO nanowires

To synthesize ordered ZnO nanowires of uniform size we make use of indigenously developed vacuum injection technique. Here, AAO templates, detached from Al substrate, were first subjected to pore widening treatment in 6 wt% phosphoric acid solution for 25 min at room temperature and then mounted on the porous base of a hollow cylindrical box which was inserted into the glass tube after applying a small amount of vacuum grease. Fig

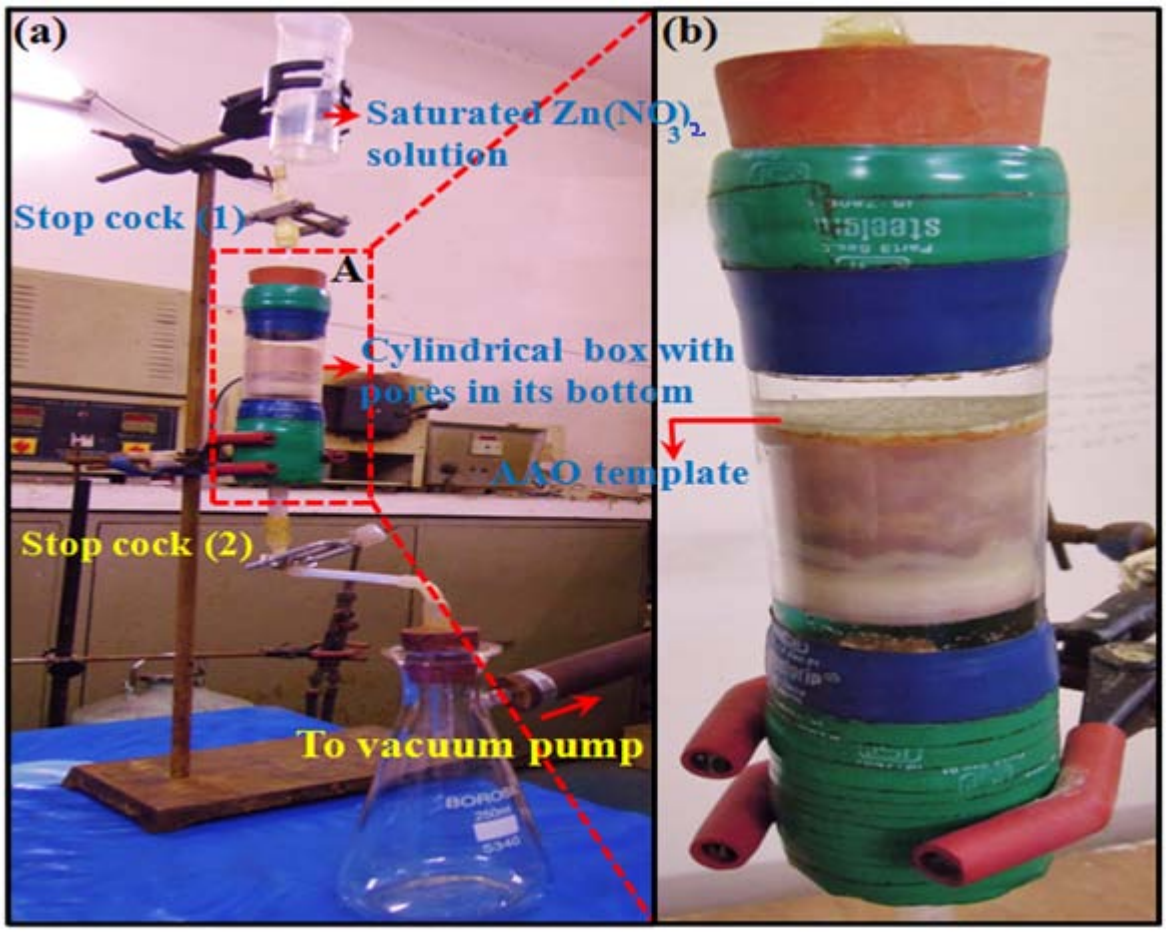

Figure 2.3: (a) Digital image of vacuum injection set-up used and a magnified image of portion "A" is shown in **(b)**.

. 2.3 (a) is the digital image of used vacuum injection set-up and a magnified region "A" is shown in (b). The bottom end of the glass tube was connected to a vacuum flask through a thin rubber pipe and stop cock (2). After attaining the desired vacuum (3–4 $\times 10^{-2}$ torr) in

the glass tube, stopcock (1) in Fig. 2.3(a) was opened slowly to allow saturated zinc nitrate solution pass over AAO template. Stopcock (1) was closed again as soon as the solution in the container was about to finish. Due to vacuum, some solution from glass tube entered into the vacuum flask and after that stopcock (2) was closed. It should be noted that during whole injection process template inside the glass tube remain dipped in the solution. Sometimes bubbles appear in the solution just above the template surface which prevent the solution from entering into the pores of the template. This problem was overcome by pushing more solution into the glass tube through stopcock (1) and the system was left in this condition for approximately 8 h. Later, AAO template was removed from the cylindrical box and kept in an electric oven at ~ 70°C for 6 h. Finally, it was annealed at 435°C for 40 h to obtain wurtzite ZnO nanowires.

2.2.1.3 Designing of ZnO nanowire array based gas sensor

In order to study the gas sensing and electrical properties of as synthesized ZnO nanowires, we fabricated a simple two electrode system as described below: here we took two thin Cu wires and the curvature of one end of each wire was reduced either by pressing or hitting it gently. These wires were fixed on glass plate which is covered with an insulating tape, and the gap between two flat ends of the wires was adjusted to be less than 10 µm with the help of optical microscope. Using this technique we make 2-3 such pairs of

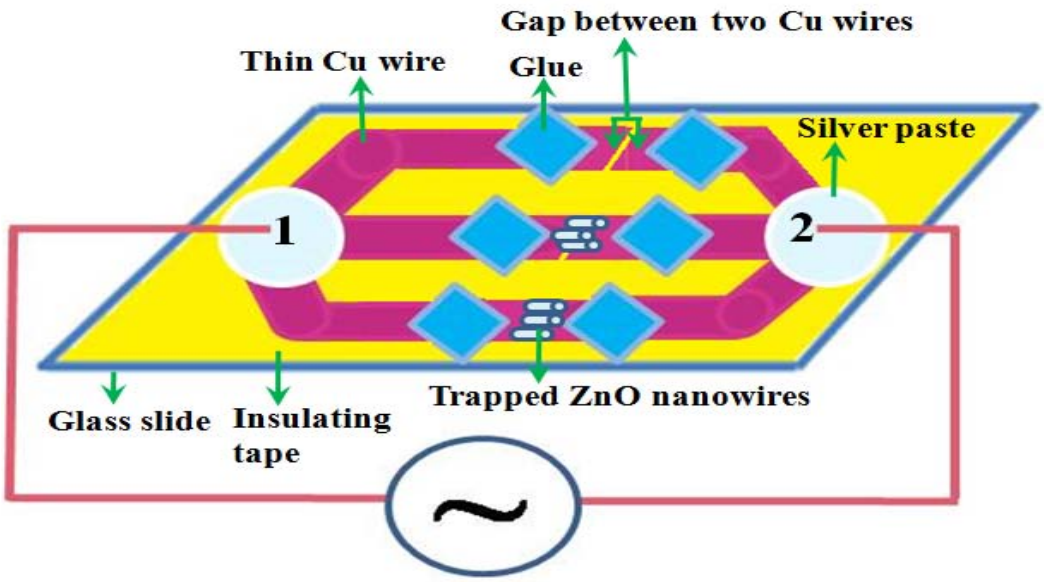

Figure 2.4: Schematic diagram of the sensor fabricated through dielectrophoresis process.

Cu wires on the same glass plate. A drop of the suspension of as synthesized ZnO nano-wires in ethanol was dropped between the gap of each pair of Cu wires and to trap ZnO nanowires between the two Cu electrodes an ac electric field of magnitude 15 Vpp (peak to peak) at 0.5 MHz was applied between points "1" and "2" (Fig. 2.4). In order to measure gas sensing properties, this sensor was kept in an air tight sensing box and desired ppm of the test gas was inserted into the box using calibrated micro-syringe.

2.2.2 Fabrication of rGO thin film based gas sensor

2.2.2.1 Synthesis of GO

GO was synthesized using customized method [24]. Here 6 g of graphite powder (SP-I Carbon) was dispersed in a 9:1 mixture of H_2SO_4: H_3PO_4 and stirred at 50°C for 2 h. 18 g of $KMnO_4$ (Aldrich) was then added to the mixture in parts. During $KMnO_4$ addition, a highly exothermic reaction was observed along with an increase in temperature up to 90 °C. Upon addition of $KMnO_4$, the color of this solution changed from black to dark brown.

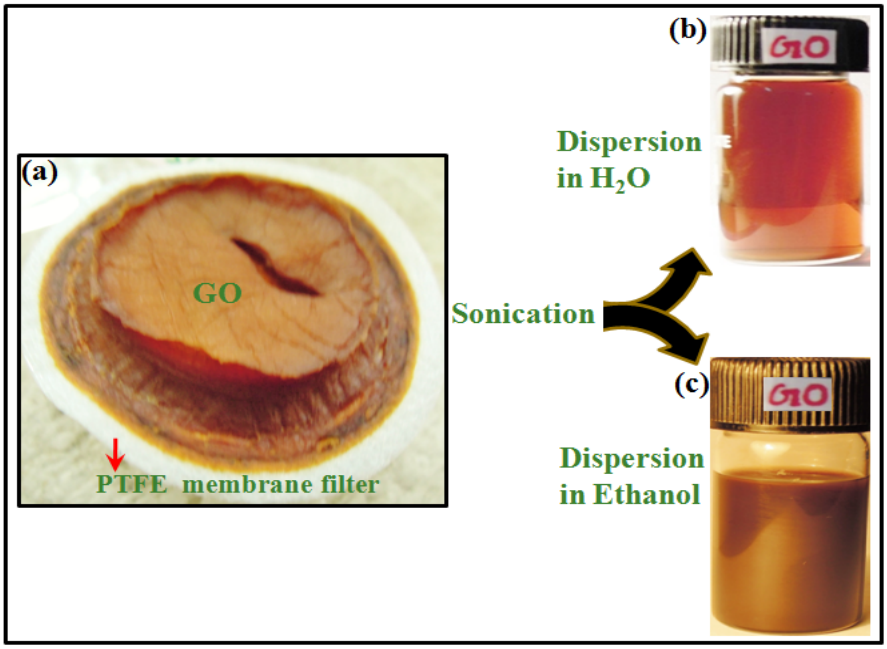

Figure 2.5: (a) GO as residue on PTFE membrane filter after filtration. Dispersion of GO in H_2O **(b)** and in ethanol **(c)**.

After that solution was left to stir overnight at 90°C and then poured over a mixture of ice and 10 mL H_2O_2, which resulted in effervescence and evolution of yellowish-brown color. This mixture was centrifuged at 4000 rpm for 4 h at room temperature and the collected

material was washed with 200 ml of 30 wt% HCl, water and 200 mL ethanol repeatedly for 3 times. After the final decantation the obtained residue was coagulated with 200 ml of diethyl ether and the suspension was passed through a Polytetrafluoroethylene (PTFE) membrane of 0.2 microns pore size. The solid sample, now having a distinct brownish tinge color, indicate the formation of GO (Fig. 2.5 (a)). Finally, the sample was dried in a vacuum oven for three days to remove remnant traces of moisture.

2.2.2.2 Preparation of GO and rGO thin films

GO can be dispersed easily in various solvents via ultrasonication [25]. The dispersions of GO in distilled water (1 mg/mL) and in ethanol (6 mg/mL) have been shown in Fig. 2.5 (b) and (c), respectively. Thin films of GO sheet were prepared by spin coating a drop (20 µL) of the GO suspension in ethanol (6 mg/mL) on the precleaned quartz substrates. Spin coating was performed using a programmable spin coater (Spin NXG P-1, Fig. 2.6) with program 1st 2000 rpm - Acc 5s – Ctime - 15s and program 2nd 4000 rpm - Acc 5s – Ctime - 15s. The as deposited GO film is electrically insulating and in order to make it ele-

Figure 2.6: Spin coater model, Spin NXG P-1

ctrically active it must be deoxidized either thermally or chemically. In a chemical route several strong chemical reductants like hydrazine hydrate, sodium borohydride, hydroquinone, p-phenylene diamine, have been used for the reduction of GO [26-29]. In the present thesis work for hydrazine vapor reduction, GO thin film was placed on the glass slide in 500 ml glass beaker and 0.5 mL hydrazine hydrate (Merck, 80%) solution was spread on the bottom of the beaker. This beaker was covered with Al foil and heated at 90°C in an oil bath for 3 h.

2.2.2.3 Designing of rGO thin films based gas sensing set-up

In order to investigate the electrical and gas sensing properties of rGO thin films we designed a complete sensing set-up as shown in Fig. 2.7(a). For heating the sample a nichrome heater was fabricated using nichrome wire of 28 gauge and 56 cm in length. This wire was wrapped over mica sheet and then covered by ceramic paste (Fig. 2.7 (b)). A power supply of 15 volts and 2 A is sufficient in order to raise the temperature of this heater up to 400 °C. An alumina sheet was placed on this heater to avoid the direct contact between sample and heater. This alumina sheet also worked as the base for test samples. A K-Type (Chromel/Alumel) thermocouple (Model STC-040 scientific equipment Roorkee, India) was used to measure temperature of the sample. A four probe technique was used to make electrical contacts on sensing materials (rGO thin films) as shown in Fig. 2.7 (c). This sensing assembly, containing nichrome heater, thermocouple and test sample, was kept inside a stainless steel chamber of volume 500 cm^3. 1000 ppm canisters of test gases (NO_2 and Cl_2), purchased from Chemtron Science Laboratories Pvt. Ltd. Mumbai, India, were used in the experiment. After utilizing the relation (capacity of syringe used × ppm level mentioned on canister = capacity of sensing container × required ppm level) desired

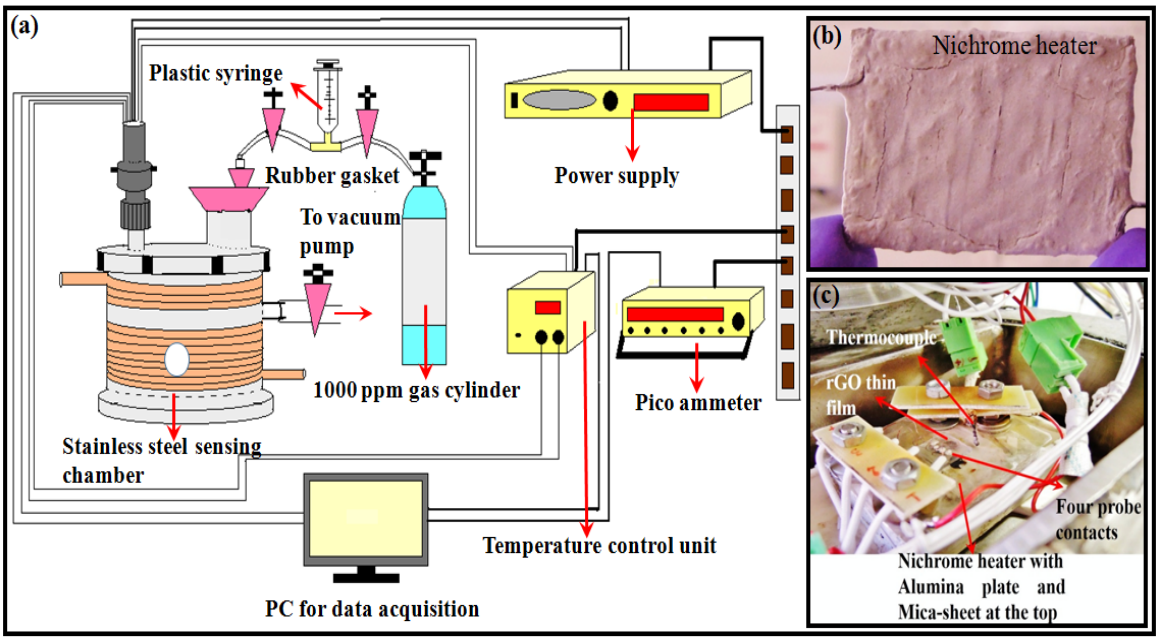

Figure 2.7: (a) Schematic diagram of the sensing set-up used. **(b)** Digital images of nichrome heater. **(c)** Digital images of sensing assembly with nichrome heater, thermocou--ple and test sample.

ppm concentrations were injected into the sensing chamber using plastic syringe. As the sensor reached at the state of saturation gas was removed from the chamber by opening the rubber gasket and simultaneously operating the vacuum pump (Fig.2.7(a)). Throughout this expriment N_2 was used as the carrier gas and all expriments were performed at relative humadity (RH) ~ 57%.

2.2.3 Antibacterial activity of GO and rGO thin films

Antimicrobial activity of GO and rGO thin films on quartz substrates was examined against both Gram +ve (B. cereus) and Gram-ve (E. coli) models of bacteria. In order to establish the antimicrobial activity of GO and rGO films, seed cultures of E. coli DH5α and B. cereus were prepared by inoculation in Luria Bertani (LB) broth and incubation for 12-14 h at 37°C and 150 rpm. Further, 5mL fresh LB broth was inoculated with 2% seed culture of each bacteria. To investigate the antimicrobial activity against B. cereus, 100 µL culture of 0.5 optical density (O.D.) was spread on LB agar plate and GO, rGO thin films along with a pristine quartz sheet were placed on these LB agar plates and incubated at 37°C for 24 h. Pristine quartz substrates were taken as control of GO and rGO thin films for comparative measurements. In order to understand the antimicrobial activity against E. coli DH5α, 1mL culture of 0.5 O.D. was centrifuged at 6000 rpm for 10 min. After centrifugation, supernatant was discarded and cell pellet was applied on GO, rGO films and kept in laminar air flow for 5 to 10 min for air drying. Afterwards, these bacteria treated films and substrate were placed on fresh LB agar plates and incubated for 24 h at 37°C.

2.2.4 Fabrication of rGO and ZrGO powder based gas sensors

2.2.4.1 Synthesis of rGO and ZrGO powder samples

In order to synthesize rGO-ZnO nanocomposite (ZrGO), 40 mg of GO was first dispersed in 80 mL of millipore water (18 MΩ-cm) through 4 h of intense ultrasonication using bath sonicator (Wensar, 150W, 40±3 kHz). Henceforth, the pH was adjusted to 10 by addition of 28% ammonia solution. To this solution 20 mL of (10 mM) $ZnCl_2$ solution was added along with vigorous stirring by a magnetic stirrer. After addition of 25µL of 85% hydrazine hydrate this solution was refluxed in a 250 mL round bottom flask in silicon oil bath at 90°C for 5h (Fig. 2.8). After reflux, mixture was filtered through nylon membrane filter (47 mm, 0.2 micron pore size) mounted on a vacuum filter assembly and to remove

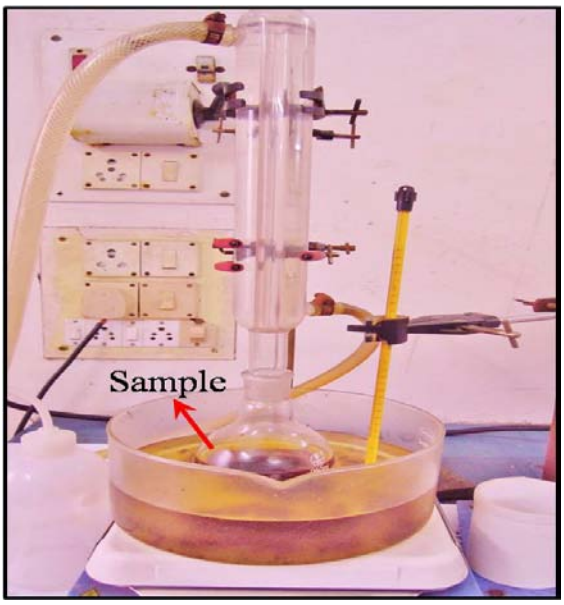

Figure 2.8: Reflux system used for the synthesis of rGO and ZrGO powder samples.

unreacted chloride ions the residue was washed with deionized water and ethanol 3 times each, respectively. The obtained product was vacuum dried at 45°C for 12 h and finally annealed in nitrogen atmosphere at 500°C for 5 h. For comparison, samples of reduced graphene oxide (rGO) and ZnO were also synthesized following the same method as mentioned above.

2.2.4.2 Designing of rGO and ZrGO based gas sensors

To fabricate sensing device using ZrGO and rGO powder samples two Pt wires of diameter 0.3 mm were tightly wrapped about 1mm apart on a small quartz tube and these two wires, when connected to outside electronics for monitoring the resistance change, act as two terminals of the device. A ceramic coil heater, which was fabricated using nichrome wire of 28 gauge and 35 cm in length, was inserted into this small quartz tube. The working temperature of ceramic coil heater was controlled by tuning the heating voltage and the temperature was read using K-Type thermocouple. The powder sensing material was gently ground with a little amount of ethanol in an agate mortar and then coated between the gap of two Pt electrodes with the help of drawing brush. After that this system was dried at 60°C for 5 h in a vacuum oven. A ZrGO sensor fabricated in this way is shown in Fig. 2.9. The sensing assembly, containing sensing material coated Pt electrod-

es, heating coil and temperature sensor, was put in a stainless steel housing of volume 500 cm^3. To find out the gas sensing performance of rGO and ZrGO sensing material based gas

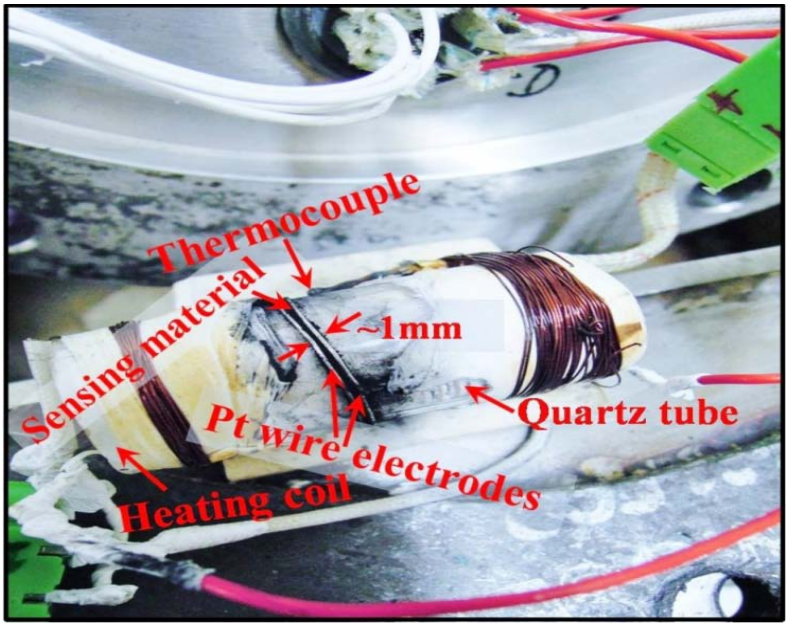

Figure 2.9: rGO/ZrGO coil sensor with heating coil and thermocouple.

sensors different concentrations of NO_2 were inserted into the sensing chamber through inserting window using calibrated plastic syringe. As the sensor achieved the state of saturation, test gas was removed from the sensing chamber with the help of rubber gasket and vacuum pump.

2.3 CHARACTERIZATION TECHNIQUES

In the present work we have used various characterization techniques to understand in-depth the materials structure, surface morphology, elemental composition, optical properties and sample stability. Here, we are giving a brief description of the working principles of all the techniques used like XRD, FESEM, TEM (HRTEM), XPS, Raman spectroscopy and photoluminescence (PL) spectroscopy.

2.3.1 X-rays Diffraction (XRD)

X-rays are electromagnetic radiation with very short wavelength of the order of 0.5 - 2.5 Å. X-rays are produced when a highly energetic e-beam is allowed to fall on a heavy metallic target such as Cu, Fe, Co, Mo and Cr. The diffraction of monochromatic X-rays by the crystals was first reported by German physicist Max von Laue in 1912. However,

the principle of X-rays diffraction by the crystals was first given by W. H. Bragg in 1913 and today this principle is known as Bragg's law. Bragg's law or Bragg's equation is the fundamental law of X-rays crystallography and it is used extensively to get the information about crystal structure of the test material. The Bragg's law relates the possibility of a plane wave to be diffracted constructively by a family of lattice planes to the inter-planer spacing of the planes in the crystal as follows [30]

$$2d\ sin\theta = n\lambda \tag{2.1}$$

where d is the inter-planer spacing between planes, θ is the angle of incidence (Bragg's angle) that the X-ray beam makes with the plane of atoms (hkl), λ is the wavelength of the incident beam of monochromatic X-rays and n is an integer that indicates the order of the reflection.

X-ray powder diffraction is a most powerful non-destructive technique widely used for the characterization of crystalline materials. This method has been traditionally used for determining the crystal structure, orientation, unit cell dimensions, lattice constants, stress/ strain, structure imperfections and for phase identification [31]. In the present investigations, XRD technique has been mainly used for phase identification of the synthesized samples. In the present work we utilized **ADVANCED BRUKER D8** powder diffractometer with CuK_α radiation (λ=1.5406 Å) and nickel filter, operating at 40 kV and 30 mA. In such a modern X-rays powder diffractometer a detector is used to receive diffracted X-rays instead of photographic film and we get structural information in the form of series of peaks instead of diffraction rings. The schematic diagram of utilized X- ray diffractometer is shown in Fig. 2.10. In this measurement powder sample is filled in the hole of a sample holder and collimated X-rays beam, from the tube, is allowed to fall on it. In practice, sample is positioned such that if incident beam of X-rays makes an angle θ with the lattice plane, the detector will set at the corresponding angle 2θ. This arrangement of diffractometer is referred to as θ-2θ scan (Fig. 2.10). Here, detector works similar to proportional or scintillation counter and helps to generate diffraction pattern which is characteristic to the material. The positions and intensities of the peaks in the diffraction pattern give information about cell parameters, *d*-spacing and crystallinity of the materials. Each diffraction peak in the pattern corresponds to *d*-spacing of a family of lattice planes and possesses its own set of indices (hkl). The process used to find out the *d*-values and corresponding indices (hkl) is termed as indexing the pattern. The accurately determined values of indices (hkl) and *d*-spacing can be used to find out the lattice parameters of the

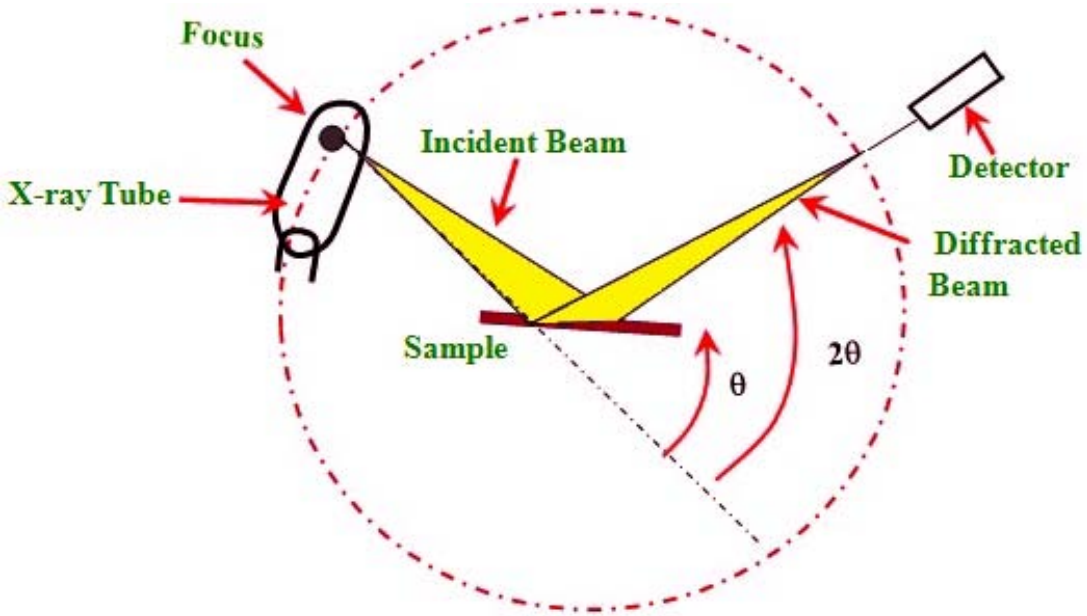

Figure 2.10: Schematic diagram of X-ray diffractometer.

crystalline material e.g. in case of ZnO (hexagonal system) following equation can be used to find out lattice parameters [30].

$$\frac{1}{d^2} = \frac{4}{3}\left[\frac{h^2 + hk + k^2}{a^2}\right] + \frac{l^2}{c^2} \qquad (2.2)$$

Today various computer programs such as TREOR, VISOR, ITO, CELL, UNITCELL, POWDER INDEXING etc. are also in used to find lattice parameters.

2.3.2 Field Emission Scanning Electron Microscopy (FE-SEM)

The field emission scanning electron microscope (FE-SEM) is a powerful high vacuum instrument which is capable of producing high-resolution topographical images of tiny structures as small as 2 nm in size. It is also used to calculate the size of particles present on the surface of the material [32-36]. In the present study we utilized **FEI QUANTA 200F** system equipped with EDX facility to find out the surface morphology and chemical composition of the materials. In FE-SEM an electron beam from field emission gun is accelerated by a voltage in the range of 10 to 30 kV and directed towards the sample using electromagnetic lenses present in the vertical column of the microscope.

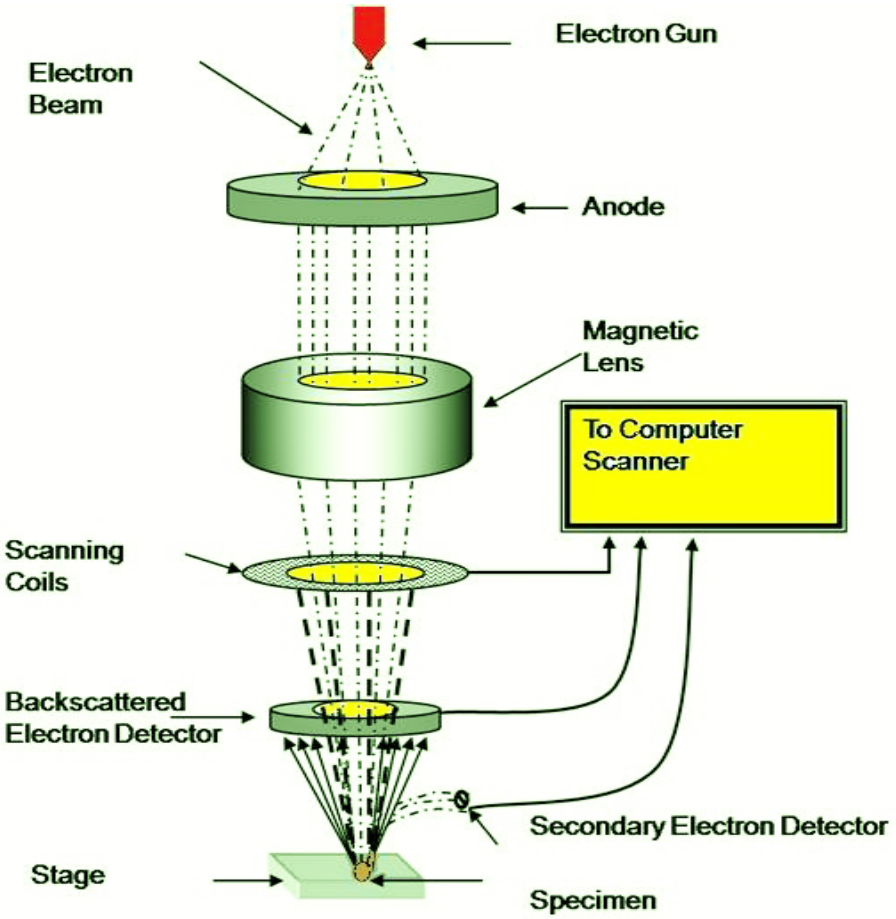

Figure 2.11: Schematic diagram of FE-SEM

2.3.2.1 Principles of scanning electron microscopy

When accelerated electron beam falls on the specimen different types of radiation, such as secondary electrons, back scattered electrons, characteristics X-rays, auger electrons, emit out from its surface. Different detectors are used to detect these emitted electrons and X-rays in the FESEM system and final image of the sample is displayed on a monitor. The schematic diagram of FE-SEM is shown in Fig. 2.11. The schematic diagrams of interaction of electron beam with a thin specimen are shown in Fig. 2.12 (a) and (b) which represent the emission of different signals and their interaction volume, respectively. As the electron beam falls on the sample surface primary electrons (incident electrons) penetrate into the sample and the important radiations which come out from the material with different energies are given below:

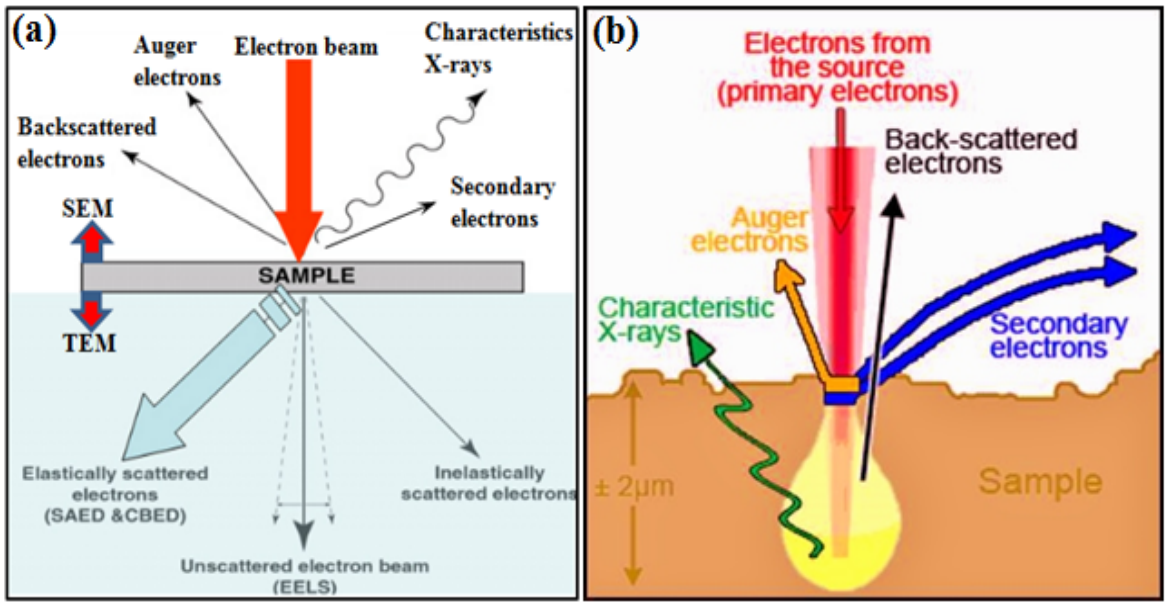

Figure 2.12: A schematic representations of **(a)** interaction of electron beam with a thin specimen and **(b)** interaction volume of different signals inside the sample [adopted from http://www.vcbio.science.ru.nl/en/fesem/eds].

(i) Secondary electrons: These are the local electrons which come out from the shells of the surface atoms as the energy of some incident electrons transfered to them. In comparison to primary electrons these are less energetic electrons (~5 eV) and come out from the depth of just 5-10 nm inside the specimen surface. The secondary electrons (SE) produce the high resolution topographical image of the samples as they come out from the upper surface of the specimen.

(ii) Back scattered electrons: These are the incident electrons, which get reflected back by the atoms at the depth 10-100 nm from the surface of the sample. The back scattered electrons (BE) possess energy greater than that of SE. Since the number of BE depends on the atomic number therefore, the brighter portion in the BE image corresponds to the elements of higher atomic numbers. BE images have poor resolution in comparison to SE images.

(iii) Characteristic X-rays: As the primary electrons knock off the electrons from inner most orbits, holes are created and when an electron from a higher shell jumps to fill this vacancy an X-ray photon with energy equal to the difference between two energy states is emitted. These X-rays are characteristic to the material and produced at the depth of 1-3

μm from the surface of the sample. In SEM, characteristic X-rays give information about chemical composition of the material.

(iv) Auger electrons: When an electron jumps from higher state to fill vacancy in K shell, energy is released. This energy can eject an electron from external M shell which is termed as Auger electron. The kinetic energy of Auger electron is characteristic to the emitting atom present in the material. The number of Auger electrons identified with certain energy corresponds to concentration of the concerned element. Auger electrons are used in a highly sensitive surface analysis technique as they come from the depth of 5-75 Å of the specimen.

For FESEM analysis the surface of testing sample should be electrically conductive, otherwise electron beam would charge up the surface [37]. In case of ZnO and other insulating materials a thin conducting film of gold (Au) is sputtered on their top surfaces by glow discharge sputtering which helps to bypass the excess charges present on the surface of the samples.

In the present work elemental composition of the samples was determined using energy dispersive X- ray spectroscopy (**EDXS**) attached with the FESEM system. In this technique energies of characteristic X-rays are utilized to identify the elements while intensities of the emitted X-rays give information about the quantity of the elements present in the sample. EDX spectrum exhibits different peaks corresponding to different energy levels of the elements and intensity of these peaks represents the concentration of the particular element in the sample.

2.3.3 Transmission Electron Microscopy (TEM)

The transmission electron microscopy (TEM) is the most powerful high vacuum instrument which is extensively used to obtain morphological, compositional and crystallo-graphic information of the test sample. The point-to-point and lattice resolutions of TEM are about 0.19 nm and 0.10 nm respectively. The working principle of TEM is almost similar to FESEM. But unlike FESEM in TEM, transmitted electrons are utilized to get information about the ultra thin specimen (Fig. 2.12 (a)). In TEM, images formed by transmitted electrons are focused by the objective lens onto imaging devices such as phosphor screen or charge coupled device (CCD) camera. When magnified and focused image strikes the phosphor screen light is produced which allow the user to see the image. A block diagram of TEM is shown in Fig.2.13 (a) while Fig. 2.13 (b) represents a ray

diagram for the diffraction. As the incident electron beam pass through the sample, some of these are scattered by the atoms in the specimen. The electromagnetic objective lens pr-

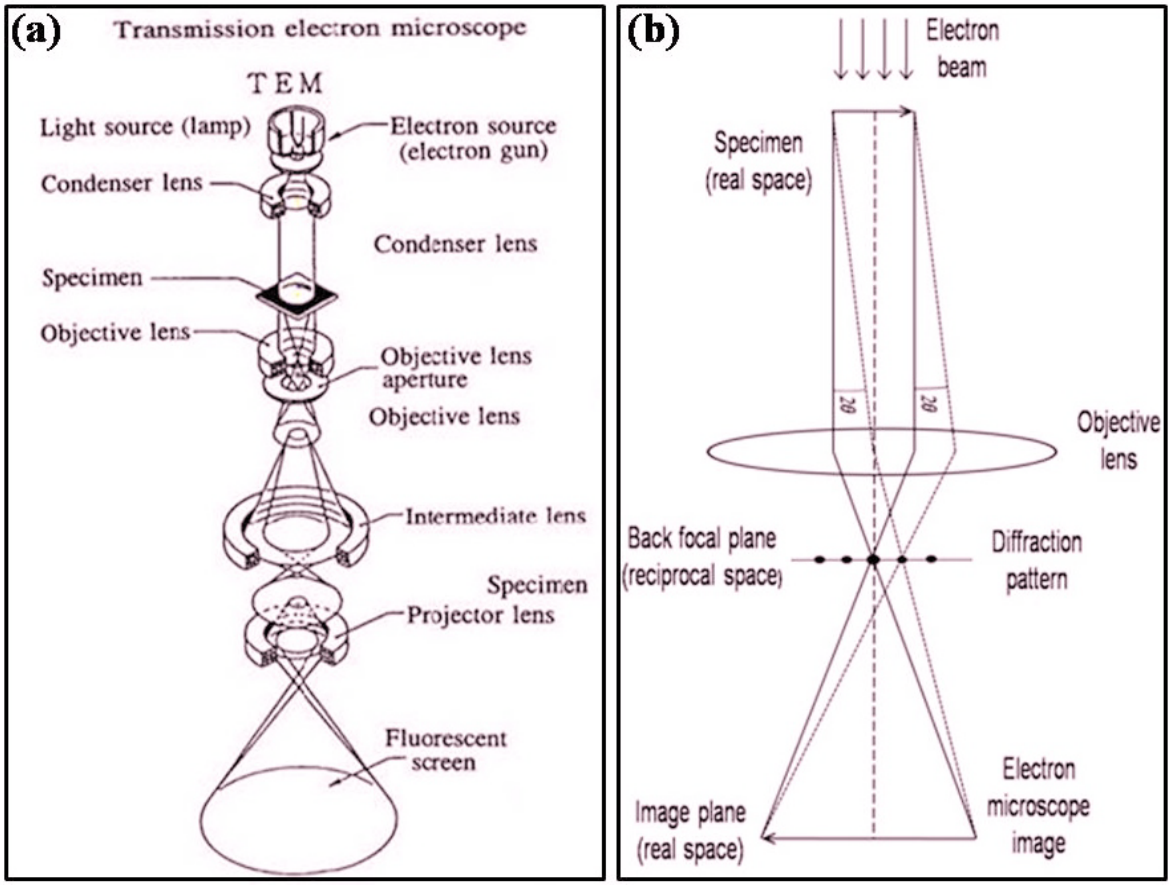

Figure 2.13: (a) A block diagram of TEM [adopted from http://www2.war wick.ac.uk /fac /sci/physics/current/postgraduate/regs/mpags/ex5/techniques/structural/tem/]. **(b)** A ray diagram for the diffraction mechanism in TEM [adopted from http://cnx.org/content/m 34 523/latest/?collecti--on=col10699/latest].

esent in the TEM column focuses the electrons which are scattered from one point of the sample into one point in the image plane. Just behind the image plane there is a back focal plane (also known as reciprocal plane) of the objective lens where electrons scattered by the atoms of the specimen in the same direction converge into a single point and thus formation of diffraction pattern takes place (Fig.2.12 (b)). The high resolution transmission electron microscopy (HRTEM) is an ultimate tool to investigate the properties of the materials on atomic scale. It is extensively used in the study of low-dimensional structures such as nanoparticles, nanowires, quantum wires, quantum dots and sp^2-bonded carbon (e.g. graphene, carbon nanotubes). In HRTEM, the phase of diffracted electron wave

remains conserved and it interferes with the phase of the transmitted wave either constructively or destructively. This technique of "phase-contrast imaging" is used to form images of columns of atoms. TEM (200 kV) used in the present work of thesis is **Philips CM 200 equipped with LaB_6 filament**.

TEM testing sample should be very thin (~100-150 nm thick) so that sufficient electrons can pass through it with minimum energy loss. Therefore, sample preparation for TEM analysis is a very important and specific to the material under investigation. Various techniques such as ultrasonic disk cutting, disc grinding, tripod polishes, dimpling and ion-milling have been developed so far for TEM sample preparation. In case of powder samples, material is first crushed into tiny pieces and then its small amount is dispersed ultrasonically either in H_2O or ethanol. For characterization 1-2 drops of the dispersion so obtained is placed on carbon-coated grid and let it dried for 10-15 minutes.

2.3.4 X-ray Photoelectron Spectroscopy (XPS)

X-ray photoelectron spectroscopy (XPS) is also known as Electron Spectroscopy for Chemical Analysis (ESCA). This technique is extensively utilized to study the chemical state, electronic state and atomic ratio of each element present in the test sample. In XPS analysis testing sample is irradiated by mono-energetic soft X-rays (photon energy 200-2000 eV) which causes the emission of photoelectrons from the surface of the sample. A block diagram of XPS is shown in Fig. 2.14. The kinetic energy of these photoelectrons is measured with the help of appropriate electron energy analyser and after utilizing the equation given below binding energy of the photoelectrons can be determined.

$$E_{\text{binding}} = E_{\text{photon}} - (E_{\text{kinetic}} + \phi) \tag{2.3}$$

where E_{binding} is the binding energy (BE) of the photoelectron, E_{photon} is the energy of incident X-ray photons, E_{kinetic} is the measured kinetic energy of the photoelectron and ϕ is the work function of the spectrometer.

The binding energy versus intensity of photoelectrons (counts/second) spectrum gives information about the presence of specific elements, their chemical states and their quantity in the test sample. In the present thesis work XPS analysis were performed using a monochromatic Al-Kα source (hν=1486.6 eV), a hemispherical analyzer and a multichannel detector. The typical vacuum in the analysis chamber during the measurements was in the range of 10^{-10} torr. Elemental compositions were determined

from the spectra acquired at pass energy of 117.4 eV. High-resolution spectra were obtained with analyzer pass energy of 29.35 eV at the step of 0.125 eV and 50 ms time per step. Ar^+ ion gun was used for surface cleaning and depth profiling.

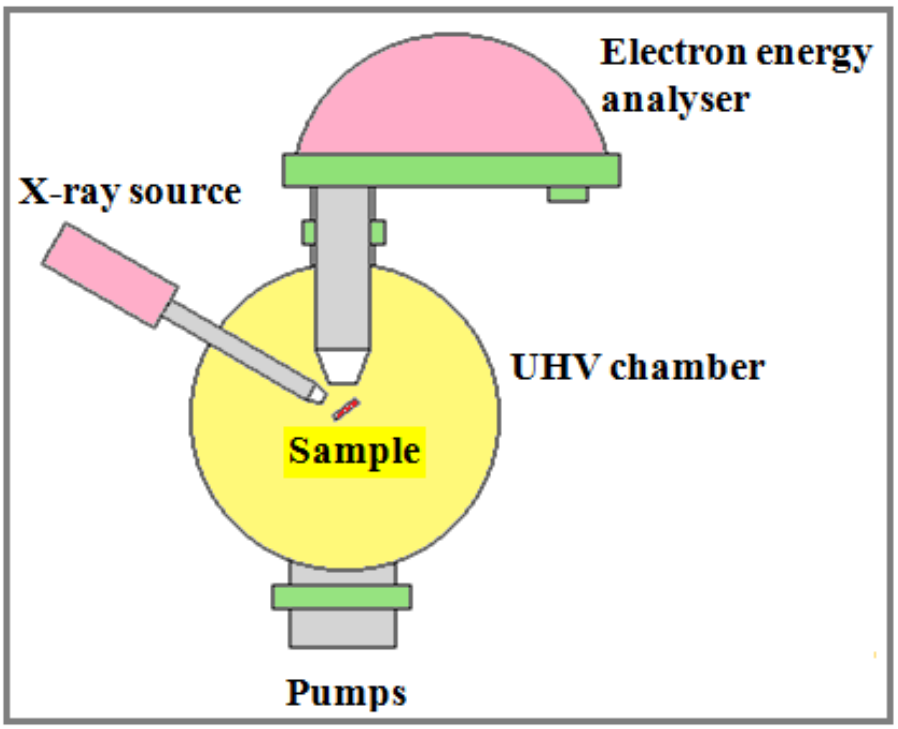

Figure 2.14: A block diagram of XPS.

2.3.5 Raman spectroscopy

Raman spectroscopy (named after Sir C. V. Raman) is a standard nondestructive specctroscopic technique extensively used to determine the vibrational, rotational and other low-frequency transitions in a molecular system. This technique is based on inelastic scattering in which frequency of incident monochromatic light photon changes after interaction with the sample under investigation. A block diagram of Raman spectroscopy is shown in Fig. 2.15. As the photons of laser light fall on the sample surface these are absorbed and re-emitted with frequency either higher or lower than the frequency of incident photon. This phenomenon, termed as Raman effect, is utilized in the investigation of vibrational, rotational and other low frequency modes of the test sample. Raman spectroscopy can be employed to investigate the properties of solid, liquid and gaseous samples. In the present thesis work Raman analysis of the samples was done using WITec

alpha 300SR instrument at 488 nm Ar-Ion Laser excitation and ANDOR 420 BR DD Pelti--er cooled (-72oC) CCD was used as detector.

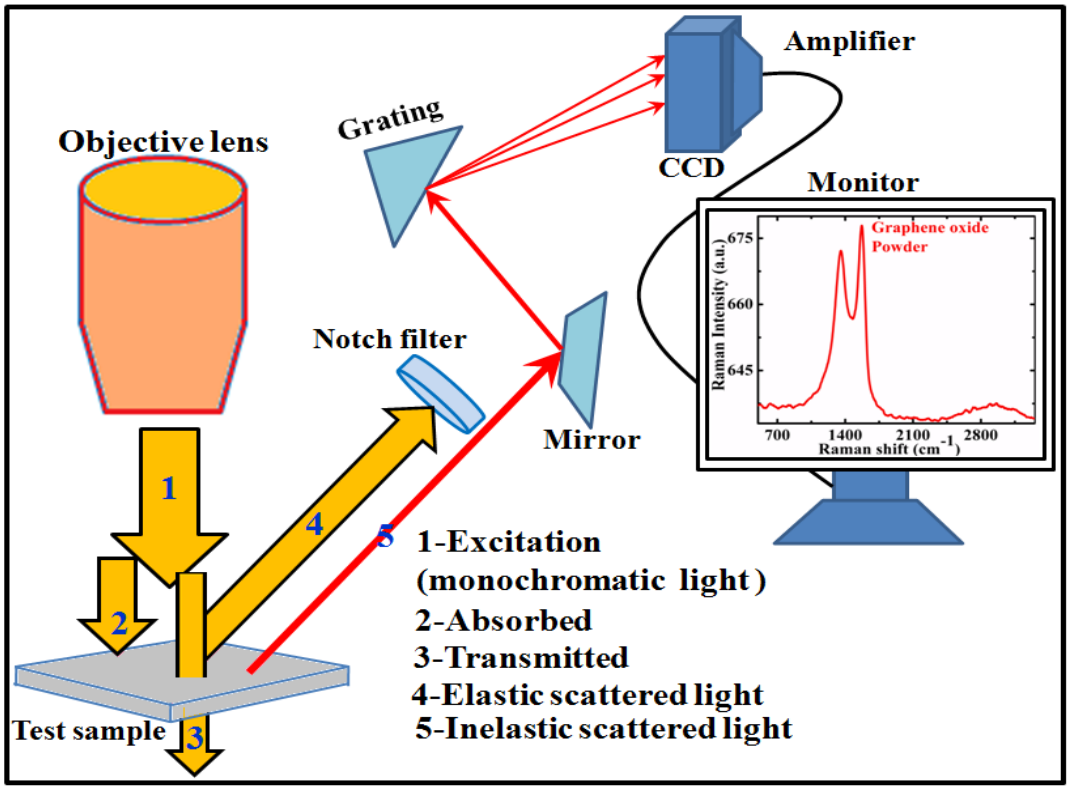

Figure 2.15: A block diagram representing Raman spectroscopy.

2.3.6 Photoluminescence (PL) Spectroscopy

Photoluminescence (PL) Spectroscopy is a nondestructive characterization technique used to probe the electronic structure of the material. This technique does not require any specific control over test environment as well as much sample manipulation. A block diagram of PL spectrometer used in the experiment is shown in Fig. 2.16. In photoluminescence when a test material absorbs incident photon (electromagnetic radiation), it goes to the higher energy state and then returns back immediately (~10 ns) in the lower energy state after re-emitting the photon. This process is termed as luminescence and it occurs for a fixed excitation energy of the incident photon. Although the period of absorption and re-emission of photon is very short but under few circumstances it can be increased up to minutes or hours. On this basis luminescence is mainly classified into two categories namely fluorescence and phosphorescence. Fluorescence is a fast process (lifetime ~ 10^{-9} - 10^{-7} s) in comparison to phosphorescence (lifetime from few seconds to

several minutes). Fluorescence from a test material vanishes as soon as the source of incident exciting light photon is switched off, in contrary phosphorescence can be seen for some times even after removal of exciting light source. In photoluminescence the energy of emitted light photon corresponds to the transition between excited state and the equilibrium state. However, the total intensity of emitted light is a relative contribution of the radiative process. Therefore, in the PL emission spectrum the intensity peaks are the finger prints of the energy of each excited level, which give information about the band gap, impurity levels, defects and the material quality. In the present thesis work the room temperature photoluminescence (PL) spectra were recorded using, FLSP-920 (Edinburgh) spectrometer with xenon flash lamp as the source of excitation.

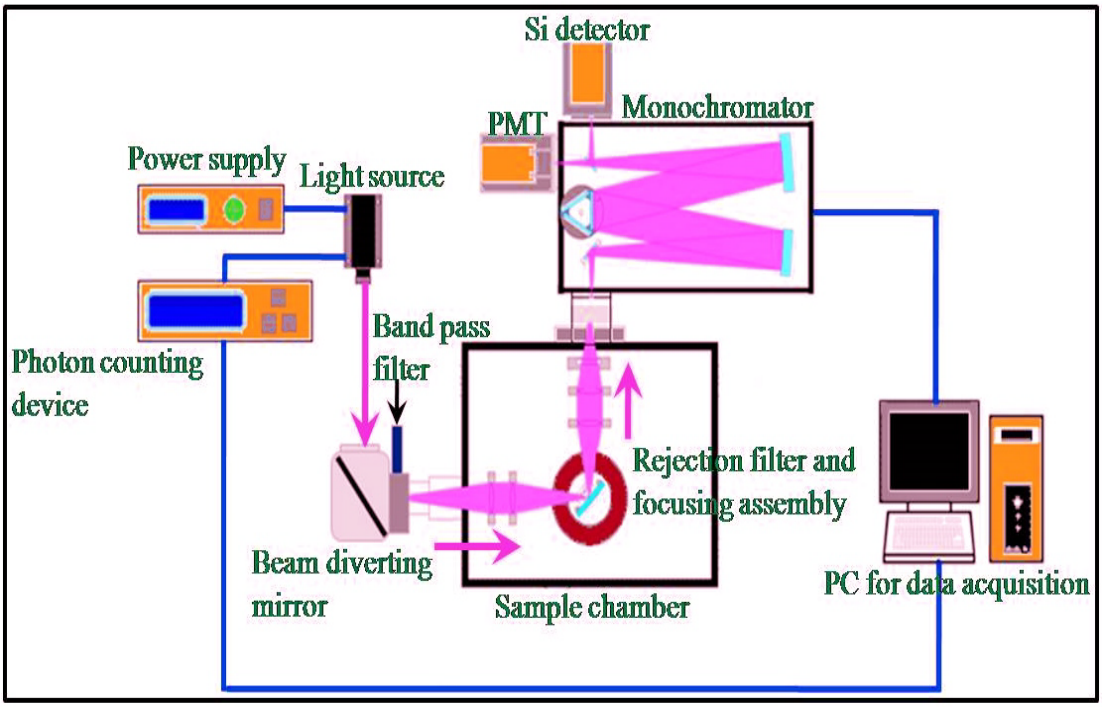

Figure 2.16: A block diagram of used photoluminescence spectrometer.

2.4 BRIEF SPECIFICATIONS OF THE INSTRUMENTS USED

(a) X-ray Diffractometer

Model	**:** Bruker AXS, D8 ADVANCE
Target	**:** Cu (Ni filtered Cu-Kα X-rays of wavelength 1.5406 Å)
Working Voltage	**:** 10 to 40 kV
Tube current	**:** 4.4 to 40 mA

(b) Field Emission Scanning Electron Microscope (FE-SEM)

Model **:** QUANTA 200F, FEI

Operating Voltage **:** 15 to 30 kV

Resolution **:** ≤ 2 nm

Vacuum in chamber **:** 10^{-8} Torr

(c) Energy Dispersive X-ray Analysis (EDAX)

Model **:** EDAX TSL, AMETEK

Operating Voltage **:** 15 to 30 kV

Element range **:** all above Be

(d) Transmission Electron Microscope (TEM)

Model **:** Philips CM 200

Filament **:** LaB6

Operating Voltage **:** 200 kV

Resolution **:** 0.1nm

(e) X-ray Photoelectron Spectroscope (XPS)

Model **:** PHI 5000 Versa Probe II (ULVAC – PHI, Inc., Japan)

Source **:** Monochromatic Al-Kα (hν=1486.6 eV)

Chamber vacuum **:** 10^{-10} torr

(f) Raman spectroscope

Model **:** WI Tec alpha 300SR

Source **:** Ar-Ion Laser

Detector **:** ANDOR 420BR DD Peltier cooled (-72°C) CCD

(g) Atomic Force Microscope (AFM)

Model **:** NT-MDT & NTEGRA

Operation mode **:** Tapping mode

Image analysis software **:** NOVA 1.0.26RC1

(h) Thermogravimetric Analysis (TGA)

Model **:** EXSTAR SII, TG/DTA 6300

Heating rate **:** 10°C/min

Environment **:** Nitrogen

(i) Fourier Transform Infrared Spectroscopy (FTIR)

Model **:** Thermo Nicolet Nexus FTIR spectrophotometer

(j) UV-Vis-NIR spectrophotometer

Model	**:** Varian Carry 5000 UV-Vis-NIR spectrophotometer
Light source	**:** Xenon lamp

(k) PL spectrometer

Model	**:** Edinburgh, FLSP-920
Light source	**:** Xenon flash lamp

(l) Programmable Electrometer

Model	**:** 617, Keithley Instruments, Inc, U.S.
Voltage range	**:** 0-250 V
Current range	**:** 1 pA-20 mA

REFERENCES

1. W. C. Cochran, F. Keller, “The finishing of Aluminum”, (ed. G.H. Kissin), New York Reinhold Publishing Corporation, 104–126 (1963).
2. F. A. Lowenheim, “Electroplating”, McGraw-Hill Book Company New York, 452–478 (1978).
3. S. Wernick, R. Pinner, P. G. Sheasby, “The Surface treatment and finishing of Aluminium and its alloys”, ASM International, Finishing Publication Ltd., 5th edition, 289–368 (1987).
4. U. Grüning, V. Lehmann, S. Ottow, K. Busch, “Macroporous silicon with a complete two-dimensional photonic band gap centered at 5 μm”, Appl. Phys. Lett., **68**, 747 (1996).
5. O. Jessensky, F. Müller, U. Gösele, “Microstructure and photoluminescence of electrochemically etched porous SiC”, Thin Solid Films, **297**, 224 (1997).
6. A. Motohashi, “Measurement of evolved hydrogen volume during anodization and its relationship to the anodization process”, Jpn. J. Appl. Phys., **39**, 363 (2000).
7. O. Bisi, S. Ossicini, L. Pavesi, “Porous silicon: A quantum sponge structure for silicon based optoelectronics”, Surf. Sci. Rep., **38**, 1 (2000).
8. M. Seo, T. Yamaya, “Selective formation of porous layer on n-type InP by anodic etching combined with scratching”, Electrochim. Acta, **51**, 787 (2005).
9. H. Hasegawa, T. Sato, “Electrochemical processes for formation, processing and gate control of III–V semiconductor nanostructures”, Electrochim. Acta, **50**, 3015 (2005).
10. H. Masuda, K. Fukuda, “Ordered metal nanohole arrays made by a two-step replication of honeycomb structures of anodic alumina”, Science, **268**, 1466 (1995).
11. K. Nielsch, J. Choi, K. Schwirn, R. B. Wehrspohn, U. Gosele, “Self-ordering regimes of porous alumina: The 10 porosity rule”, Nano Lett., **2**, 677 (2002).
12. O. Nishinaga, T. Kikuchi, S. Natsui, R. O. Suzuki, “Rapid fabrication of self-ordered porous alumina with 10-/sub-10-nm-scale nanostructures by selenic acid anodizing”, Sci. Rep., **3**, (2013).
13. J. Choi, R. B. Wehrspohn, J. Lee, U. Gösele, “Anodization of nanoimprinted titanium: a comparison with formation of porous alumina”, Electrochim. Acta, **49**, 2645 (2004).

14. P. Bourdet, F. Vacandio, L. Argème, S. Rossi, Y. Massiani, "Anodisation of sputtered titanium films: an electrochemical and electrochemical quartz crystal microbalance study", Thin Solid Films, **483**, 205 (2005).
15. H. Tsuchiya, J. M. Macak, A. Ghicov, L. Taveira, P. Schmuki, "Self-organized porous TiO2 and ZrO_2 produced by anodization", Corros. Sci. **47**, 3324 (2005).
16. H. Tsuchiya, P. Schmuki, "Thick self-organized porous zirconium oxide formed in H_2SO_4/NH_4F electrolytes", Electrochem. Commun. **6**, 1131 (2004).
17. H. Tsuchiya, P. Schmuki, "Self-organized high aspect ratio porous hafnium oxide prepared by electrochemical anodization", Electrochem. Commun., **7**, 49 (2005).
18. H.-C. Shin, J. Dong, M. Liu, "Porous tin oxides prepared using an anodic oxidation process", Adv. Mater., **16**, 237 (2004).
19. I. Sieber, H. Hildebrand, A. Friedrich, P. Schmuki, "Formation of self-organized niobium porous oxide on niobium", Electrochem. Commun., **7**, 97 (2005).
20. R. L. Karlinsey, "Preparation of self-organized niobium oxide microstructures via potentiostatic anodization", Electrochem. Commun., **7**, 1190 (2005).
21. N. Tasaltin, S. Öztürk, H. Yüzer, Z. Z. Öztürk, "Simple fabrication of hexagonally well-ordered AAO template on silicon substrate in two dimensions", Appl. Phys. A, **95**, 781 (2009).
22. A. P. Li, F. Muller, A. Birner, K. Nielseh, U. Gosele, "Hexagonal pore arrays with a 50–420 nm interpore distance formed by self-organization in anodic alumina", J. Appl. Phys., **84**, 6023 (1998).
23. H. Masuda, F. Hasegawa, S. Ono, "Self-ordering of cell arrangement of anodic porous alumina formed in sulfuric acid solution", J. Electrochem. Soc., **144**, L127 (1997).
24. D. C. Marcano, D. V. Kosynkin, J. M. Berlin, A. Sinitskii, Z. Sun, A. Slesarev, L. B. Alemany, W. Lu, J. M. Tour, "Improved synthesis of graphene oxide", ACS Nano, **4**, 4806 (2010**)**.
25. J. I. Paredes, S. V.-Rodil, A. M.-Alonso, J. M. D. Tascon, "Graphene oxide dispersions in organic solvents", Langmuir, **24**, 10560 (2008).
26. S. Stankovich, D. A. Dikin, R. D. Piner, K. A. Kohlhaas, A. Kleinhammes, Y. Jia, Y. Wu, S. T. Nguyen, R. S. Ruoff, "Synthesis of graphene-based nanosheets via chemical reduction of exfoliated graphite oxide", Carbon, **45**, 1558 (2007).

27. J. Chattopadhyay, A. Mukherjee, C. E. Hamilton, J. H. Kang, S. Chakraborty, W. Guo, K. F. Kelly, A. R. Barron, W. E. Billups, “Graphite epoxide”, J. Am. Chem. Soc., **130**, 5414 (2008**)**.
28. A. B. Bourlinos, D. Gournis, D. Petridis, T. Szabo, A. Szeri, I. Dekany, “Graphite oxide: Chemical reduction to graphite and surface modification with primary aliphatic amines and amino acids”, Langmuir, **19**, 6050 (2003).
29. Y. Chen, X. Zhang, P. Yu, Y. Ma, “Stable dispersions of graphene and highly conducting graphene films: a new approach to creating colloids of graphene monolayers”, Chem. Commun., **30**, 4527 (2009).
30. B. D. Cullity, S. R. Stock, “Elements of X-ray diffraction”, (Prentice Hall Publications, U.S.A.) (1999).
31. A. J. C Wilson, “Variance as a measure of line broadening”, Nature, **193**, 568 (1962).
32. G. R. Brooker, “Modern diffraction and imaging techniques in material science”, (eds. S. Amelincks, Geveres, G. Rement, J. Van Landuyt), (North-Holland publishing Co. Amsterdam), 533 (1970).
33. J. I. Goldstein, H. Yakowitz (ed.), “Practical scanning electron microscope”, (Plenum Press, New York) (1975).
34. J. W. Heal, J. T. Sparrow, P. M. Cross, “Use of the scanning electron microscope”, (Pergamon Press, Oxford) (1972).
35. P. J. Grundy, G. A. Jones, “The electron microscopy”, (Edward Arnold, London) (1976).
36. S. Amelinckx, “Handbook of microscopy: Applications in materials science”, Solid-State Physics and Chemistry, Volume **2**: Methods II”, (Wiley-VCH, Germany) (1996).
37. P. E. J. Flewitt, R. K. Wild, “Physical methods for materials characterization”, Chapter 6 (IOP Publishing Bristol, 1994)

SYNTHESIS OF ORDERED LUMINESCENT ZnO NANOWIRE ARRAY FROM AQUEOUS SOLUTION USING AAO TEMPLATE AND INVESTIGATING THEIR AMMONIA GAS SENSING PROPERTIES AT ROOM TEMPERATURE

3.1 INTRODUCTION

ZnO is one of the most interesting semiconducting materials with unique properties such as wide direct bandgap (3.37 eV), high excitation binding energy (60 meV) and high melting point (1975°C). Because of these properties it has versatile applications in piezoelectric, short wavelength optoelectronic devices such as light-emitting diodes (LEDs) and laser diodes (LDs), catalysis and photovoltaics [1-4]. Additionally, high mobility of conduction electrons, better chemical and thermal stability under ambient conditions and good activity in redox reactions make it a feasible gas sensor [5, 6]. ZnO nanostructures of different dimensions have been synthesized so far and among these one dimensional nanostructures with uniform diameter and length are most suited for device fabrication. Several techniques have been developed to synthesize ordered ZnO nanowires and among these, anodic alumina template (AAO) rout is the simplest and cheapest method to do so [7-11]. Recently, the AAO-template route has been the most impressive way because of its low growth temperature and good potential for large scale synthesis of ordered nanostructures [12-17].

In recent times, many research groups have demonstrated the excellent sensitivity, response and recovery characteristic of zinc oxide gas sensors fabricated with individual nano-structures (tubes, wires and rods) [18-20]. However, the large-scale fabrication process of these sensors still suffers from the intrinsic drawback of processing an individual nanostructure. To address this issue, we proposed an alternative route to minimize such drawbacks through a highly ordered template. The gas sensing properties of as synthesized ZnO nanowire array-based gas sensors have been investigated against NH_3, which is highly toxic but has wide-ranging commercial applications such as in chemical industries, fertilizer factories, food processing, air conditioning equipment and refrigerators as a coolant. It is also used in the manufacture of commercial explosives (e.g., trinitrotoluene (TNT), nitroglycerin, and nitrocellulose). The natural level of NH_3 in the

atmosphere is about 1–5 ppb and the odor threshold is about 5 ppm. The American Conference of Governmental Industrial Hygienists (ACGIH) has assigned for NH_3 a threshold limit value of 25 ppm for a normal 8 h work per day and 40 h work per week. Therefore, a system is required which can detect the presence of high as well as low concentrations of NH_3 in the environment. Various NH_3 sensors, including ZnO based sensors, have been reported so far but most of them are operated at high temperatures (up to 300 °C) to activate the adsorption and desorption processes of NH_3 which limits their use in low temperature applications [21-25]. Furthermore, low power consumption is the most important requirement for gas sensors, since they work day and night. Thus, to save energy and reduce the working temperature, researchers are currently looking for a smart portable NH_3 gas sensor with good response and recovery times that can be operated at room temperature.

In the present work, we explore the facile synthesis of highly ordered luminescent ZnO nanowire array using a low temperature anodic aluminum oxide (AAO) template method. Further, we have fabricated the ZnO nanowire array based gas sensor and investigated its NH_3 gas sensing properties including sensitivity, response and recovery times and gas sensing mechanism at room temperature.

3.2 EXPERIMENTAL WORK

In the present investigation first anodized aluminium oxide (AAO) templates, having ordered nanopores of 45–50 nm diameter and a thickness of 12 μm were fabricated by a two-step anodization process using Al foil with purity >99.9%, thickness 0.3 mm and width 30 mm (Merck, 1.01057.0250). The details of the whole AAO template fabrication process as well as its electrochemical detaching process from the Al substrate are given in section 2.2.1.1 of chapter 2. AAO templates fabricated in this way were subjected to pore widening treatment in 6 wt% phosphoric acid solution for 25 min at room temperature. In order to synthesize ZnO nanowires of uniform diameter and length, empty pores of the AAO templates were filled with saturated zinc nitrate solution using indigenously developed vacuum injection technique. A schematic diagram of vacuum-injection set-up is shown in Fig. 3.1 and a complete description of vacuum-injection process is given in section 2.2.1.2 of chapter 2. After filling process, the AAO-template was removed from the cylindrical base and annealed at 435°C for 40 h to obtain wurtzite ZnO nanowires. In order to collect the ordered ZnO nanowires, filled and annealed AAO template was thoroughly

dissolved in 0.1 M NaOH solution and the floating material was collected on a razor blade. This collected material was utilized in the fabrication of sensing device. The procedure of fabricating sensing device using so obtained ZnO nanowires has been described in section 2.2.1.3 of chapter 2.

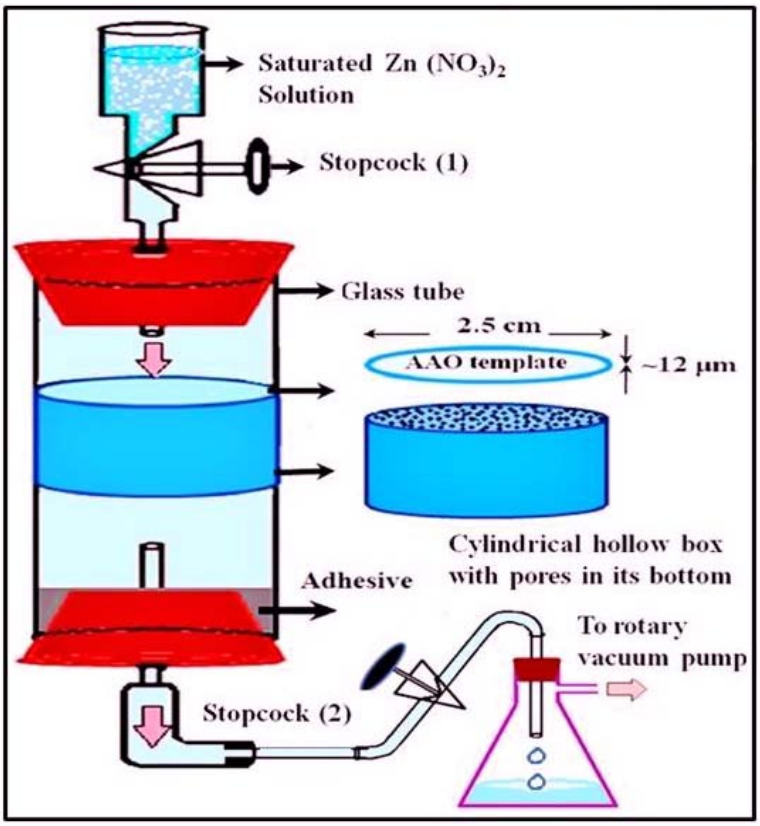

Figure 3.1: A schematic diagram of vacuum-injection set-up.

3.3 RESULTS AND DISCUSSION

3.3.1 Study of AAO template detaching process and microstructures of detached template

Previously several electrochemical [26-30] and non electrochemical methods [31, 32] have been reported to detach out AAO film from the Al substrate. But we found that the electrochemical method is a suitable method to get fully detached open-through alumina membrane because it is quite fast and environmental friendly. In electrochemical method only in one step we can get the detached template. For detaching process we took 70% perchloric acid aqueous solution in an electrochemical cell and applied 45 volts between Pt cathode and Cu anode just for 10 s at 1°C. In our case on applying voltage less

than 45 volts either the template remains attached with the Al substrate (35 volts) or detach incompletely from the Al substrate (40 volts). A typical current density-time transient recorded during the complete detaching process is shown in Fig. 3.2 (a). Fig. 3.2 (b) shows the completely detached AAO template supported on razor blade. It has been reported that the dissolution of Al_2O_3 film highly depends on the pH value of the solution and nature of the anions present in the solution. It has also reported that the solubility of Al_2O_3 film is more pronounced for pH < 5.0 and pH > 8.2 and for longer time of contact with the dissolving media [33]. Since the pH value of 70% $HClO_4$ is much lower than the pH value of 0.3 M oxalic acid (pH=1.52), therefore the threshold voltage of dissolution of Al_2O_3 at the barrier/electrolyte interface would decrease [34]. When electric pulse is applied the dis-

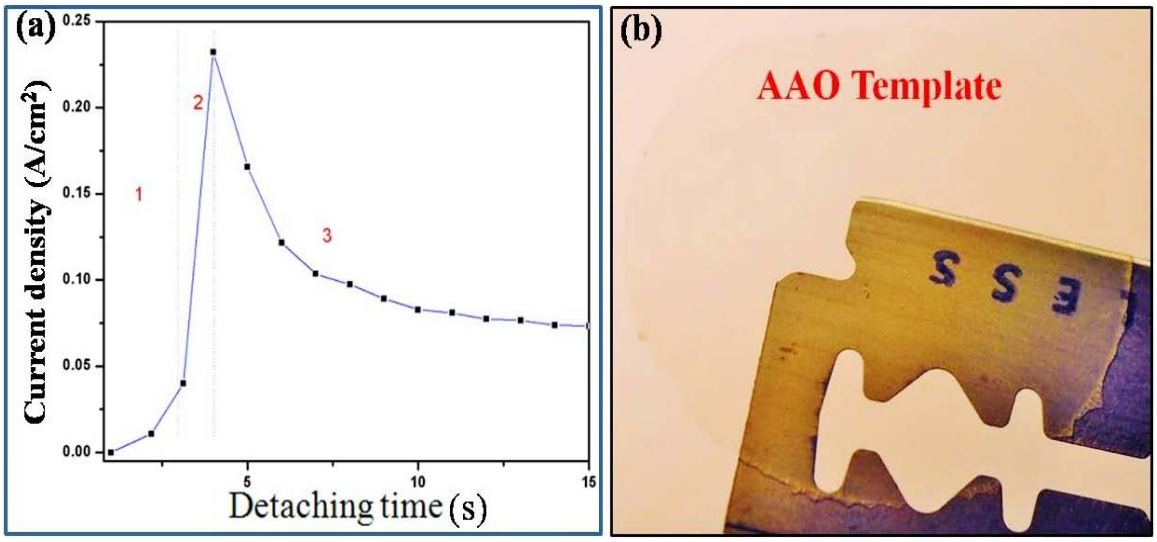

Figure 3.2: (a) Current density as a function of time during the detaching process of the AAO template from the Al substrate. **(b)** Detached AAO template supported on the razor blade.

solution of Al_2O_3 film first starts at the bottom of the nanopore instead of its side walls. This happens because the thinnest oxide layer is more likely to be at the bottom of each pore (curvature) where the resistance is lowest and the electric field strength is the highest [35]. The electric field strength within the barrier layer increases as it is thinned, and the increasing electric field strength further increases the thinning rate. Due to this thinning process bottom of the pores become open and perchloric acid directly comes in the contact of Al metal. Here perchloric acid reacts with Al metal at the metal/oxide interface (regime 2 of Fig. 3.2(a)). This leads the separation of AAO template from the Al base. Due to the reaction between Al and perchloric acid a new very thin Al_2O_3 layer gradually starts to

cover the Al substrate and current starts to decrease continuously (regime 3 of Fig. 3.2(a)). The detached Al_2O_3 is dipped into 6 wt% phosphoric acid solution for 25 min at room temperature to increase the diameter of the pores up to ~65 nm and to clean the surface of the template. This process also reduces the thickness of the template. Fig. 3.3 shows FE-SEM and AFM images of the AAO template synthesized in 0.3 M oxalic acid solution and detached away from Al base through electrochemical method. Fig. 3.3 confirms that a well-ordered nanoporous arrangement with a pore density about 0.94×10^{10} cm^{-2} has been achieved. Fig. 3.3 (a) and (b) respectively, are the FE-SEM images of the top and bottom

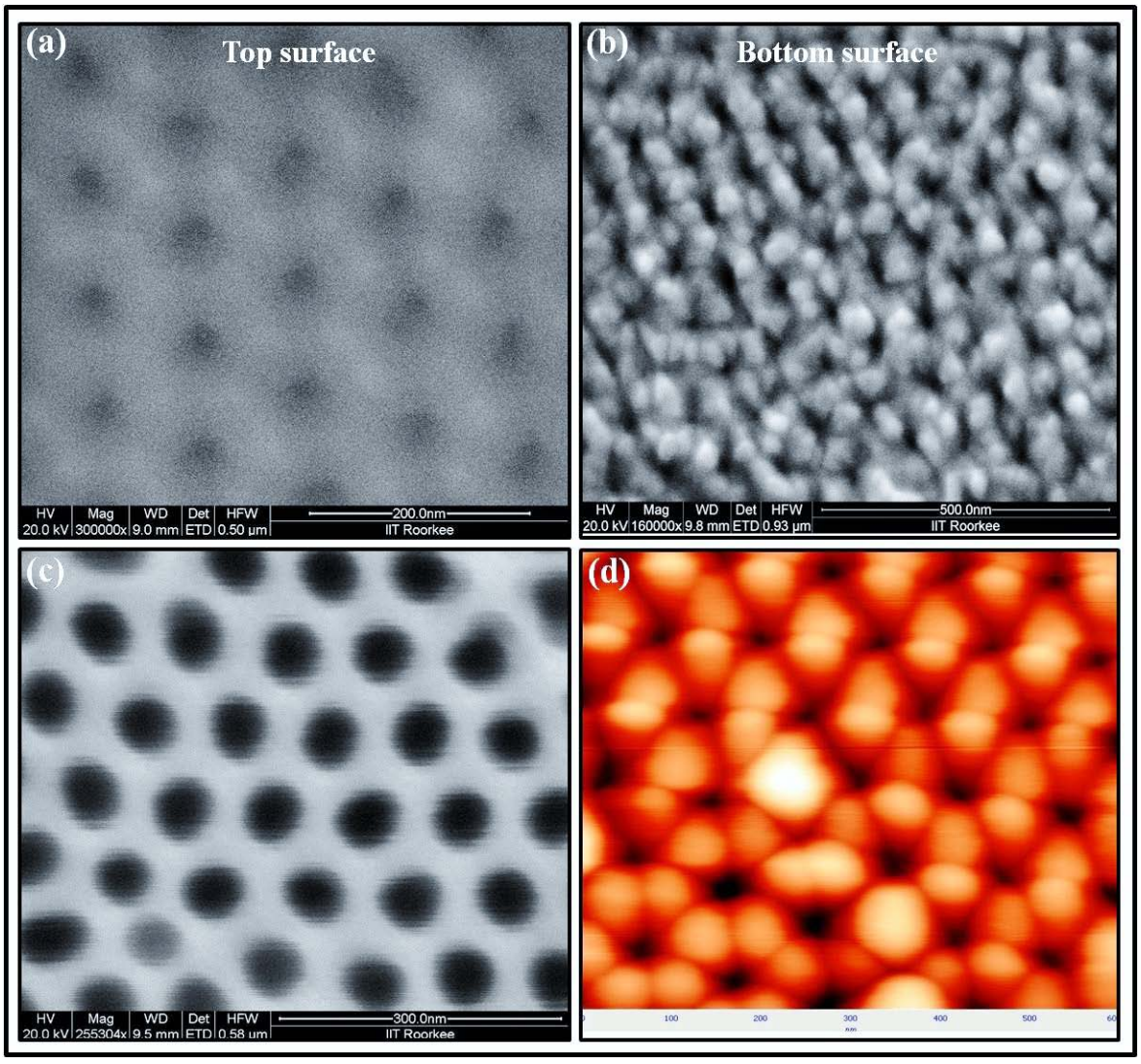

Figure 3.3: FE-SEM micrographs of the detached AAO template: **(a)** top view of the template, **(b)** bottom view of the template, **(c)** top view of the template after the pore widening treatment for 30 min in 6 wt% phosphoric acid solution at room temp and **(d)** Atomic force micrograph of the top surface of the template.

surface of the detached AAO templat**e,** while Fig. (c) is the FE-SEM image of the top surface of the template after pore widening treatment for 25 min in 6 wt% phosphoric acidsolution at room temperature. Fig. 3.3(d) is the AFM image of the top surface of the detached template. Fig. 3.3(a) shows that the diameter of the pores in the template is around 45–50 nm while Fig. 3.3(b) confirms that the pores are open through with diameter around 25–30 nm. Fig. 3.3(c) clearly shows that after pore widening process the pore diameter increases from 45–50 nm to ~ 65 nm.

3.3.2. FESEM and TEM studies of ZnO nanowires

Fig. 3.4(a) exhibits the FESEM image of the filled and annealed AAO-template and the inset shows a magnified view of the "A" region. Fig. 3.4(b) is the TEM micrograph of the filled AAO-template. Here we can see that most of the empty pores of the template are

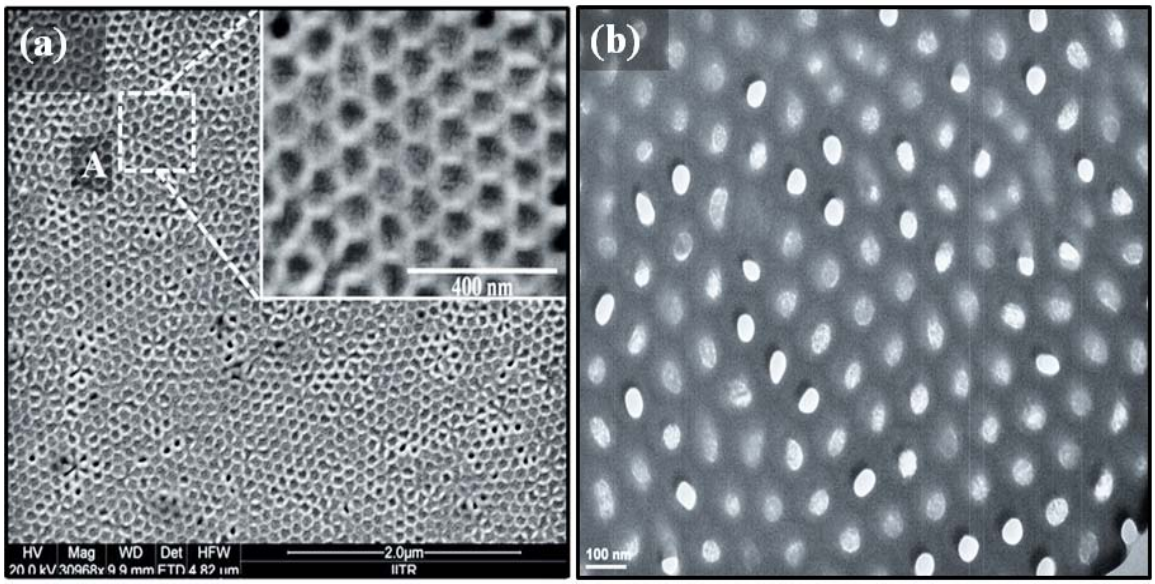

Figure 3.4: (a) FE-SEM micrographs of the filled AAO template. **(b)** TEM image of the filled AAO template.

completely filled with the material. To obtain free standing ZnO nanowires, the filled and annealed AAO template is dissolved from its bottom side in 0.1 M NaOH solution for 35 min at room temperature and then carefully rinsed away with deionized water. Fig. 3.5(a) presents the top view of the filled template after immersing it in 0.1 M NaOH solution for 20 min. Here tip of the ZnO nanowires embedded in the template can be seen clearly. Fig. 3.5(b) shows the FESEM image of the annealed template after partially dissolving it in 0.1 M NaOH solution for more than 20 min and the inset shows the EDX profile of the same.

In this image, standing ZnO nanowires partially embedded in the template are observed. Fig. 3.5(c) is the cross sectional FESEM image of a ZnO nanowire array after completely dissolving the alumina template in NaOH solution. It shows that the lengths of the nanowires are around 11 µm. Fig. 3.5(d) exhibits the FESEM image of free ZnO nano-

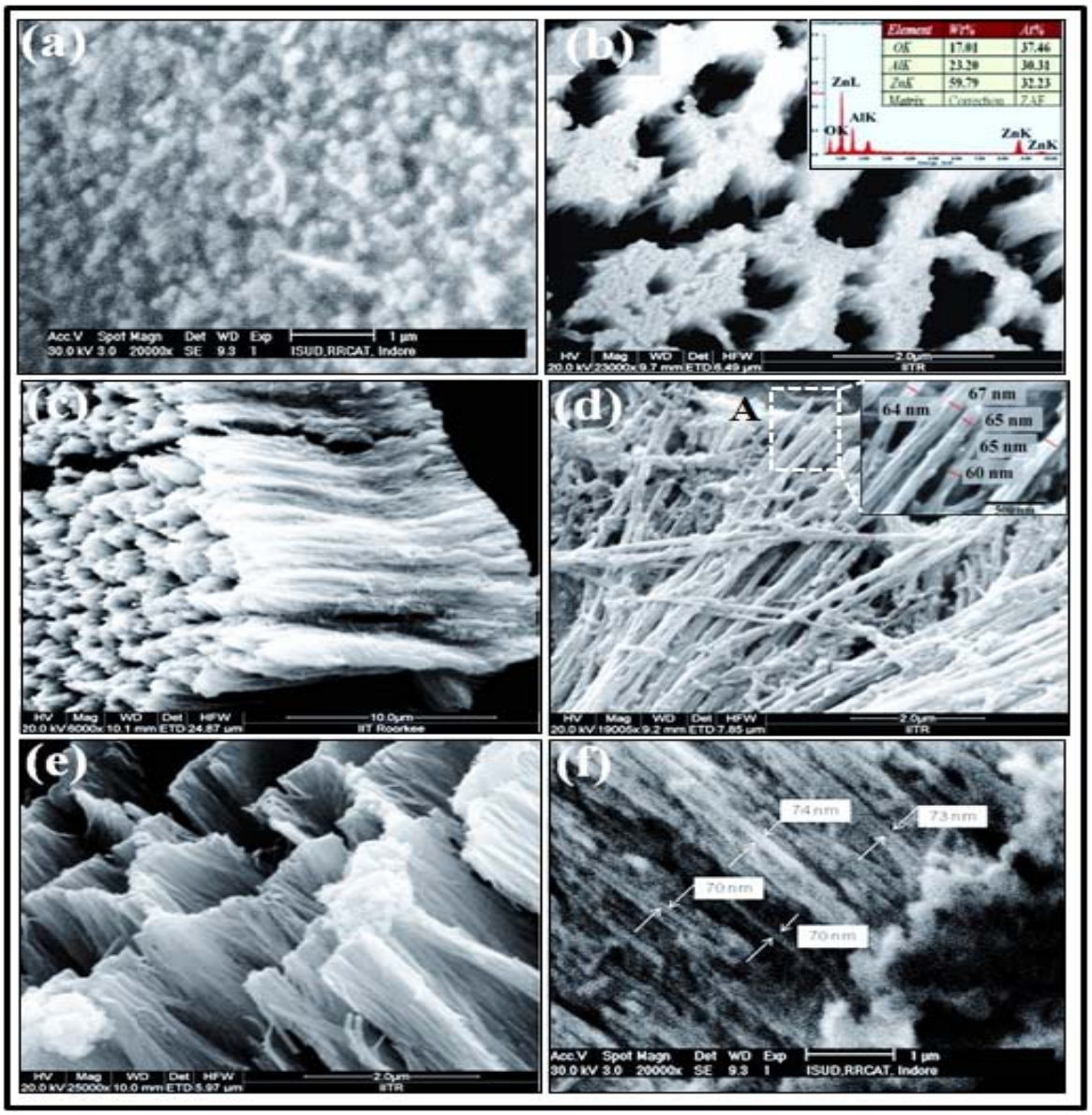

Figure 3.5: (a) SEM image of the annealed AAO template after dissolving in 0.1 M NaOH solution for 20 min. **(b)** FESEM image of nanowire array after partially dissolving the filled and annealed AAO template in 0.1 M NaOH solution and inset shows the EDX profile of the same. **(c)** Cross-sectional FESEM image of a ZnO nanowire array. **(d)** FESEM image of free nanowires and inset shows the magnified image of region "A". **(e)** Top view of ZnO nanowire array. **(f)** The cross-sectional view of the ZnO nanowire array.

wires which are almost parallel to each other with diameters between 60 and 70 nm. Fig. 3.5(e) shows the FESEM image of vertically aligned ZnO nanowires. The FESEM image of Fig. 3.5(f) shows the cross sectional view of the ZnO nanowires. This figure confirms that the nanowires are aligned and have uniform diameters throughout their lengths. The as synthesized nanowires have the high aspect ratio of ~138.9. Here we observe that the average diameter of the wires is slightly larger than the average pore size of the AAO template. This may due to two reasons: (1) the measured pore diameters are the value of the pore opening near the surface, (2) the diameters of the wires increase after they were released from the AAO template because of a coarsening transformation towards lower free energy by "balling up" (i.e., by increasing in diameter while decreasing in length to reduce the total surface area [36].

The TEM image, SAED pattern, HRTEM image and magnified HRTEM image of the as synthesized ZnO nanowires are shown in Fig. 3.6(a)–(d) respectively. In Fig. 3.6(a) the TEM micrograph shows that the nanowires have a smooth surface and an average dia-

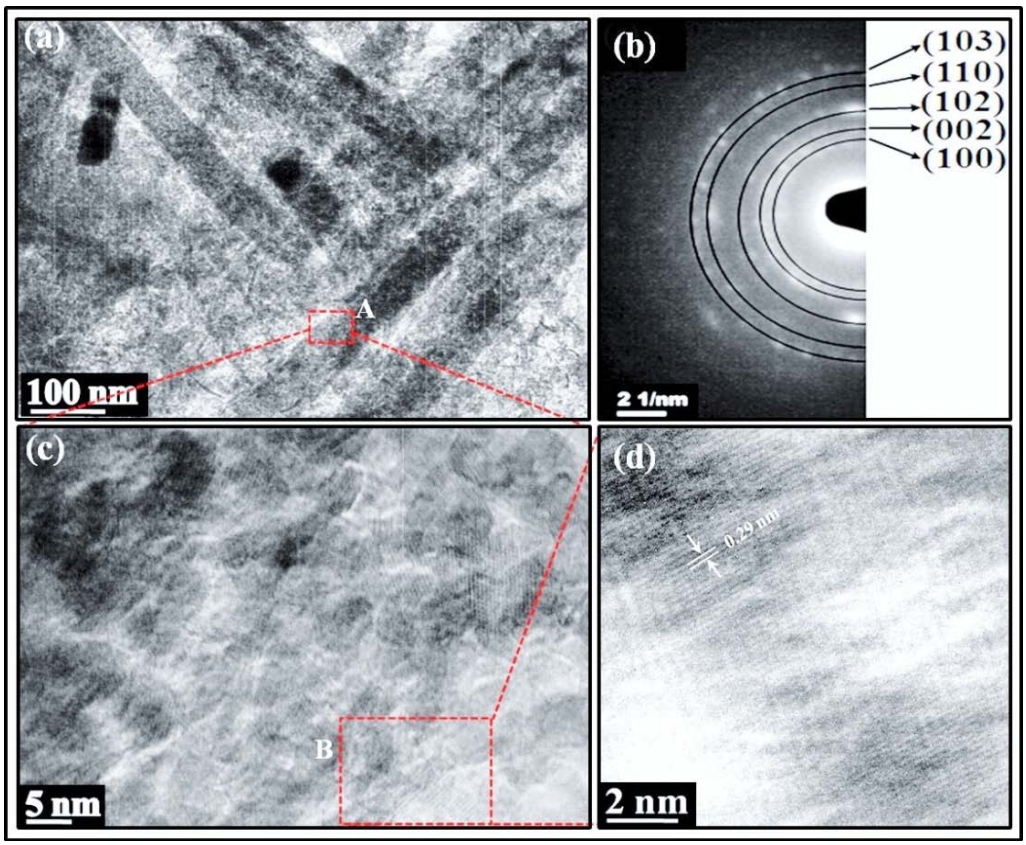

Figure 3.6: (a) TEM micrograph of ZnO nanowires. **(b)** Indexed SAED pattern of ZnO nanowires. **(c)** HRTEM image of a single ZnO wire showing inter-planar spacings and **(d)** magnified HRTEM image.

meter of ~67 nm. Fig. 3.6(b) is the selected area electron diffraction (SAED) pattern taken from a nanowire. Bright rings in the SAED pattern correspond to (100), (002), (102), (110) and (103) planes of polycrystalline ZnO phase. This confirms that the ZnO nano- wires have hexagonal wurtzite crystal structure. HRTEM image in Fig. 3.6(c) confirms the polycrystalline nature of ZnO nanowires and a magnified region "A" corresponds to a d-spacing value of ~0.29 nm corresponding to (100) planes of ZnO is shown in Fig. 3.6(d).

3.3.3. Optical studies

Photoluminescence (PL) is an important tool for direct optical investigation to explore electronic band structure and surface defect analysis. It can provide useful qualitative information about the interaction of free electrons on the surface of the AAO template with ZnO nanowires. Fig. 3.7(a) exhibits the excitation spectrum of the AAO/ZnO template at 490 nm emission which was evaluated by a pre-scan of the AAO/ZnO template assembly in the range of 200–900 nm. Fig. 3.7(b) consists of three broad strong green emission spectra peaks at 462, 502 and 490 nm upon 406 nm excitation wavelength corresponding to ZnO nanowires, the pristine AAO template and the AAO/ZnO assembly which are represented by curves 1, 2 and 3, respectively. Here, the emission spectrum of ZnO nanowires (curve 1) was obtained after subtracting curve 2 from curve 3 and the intensity of ZnO nanowire emission spectra (curve 1) was found to be 2.5

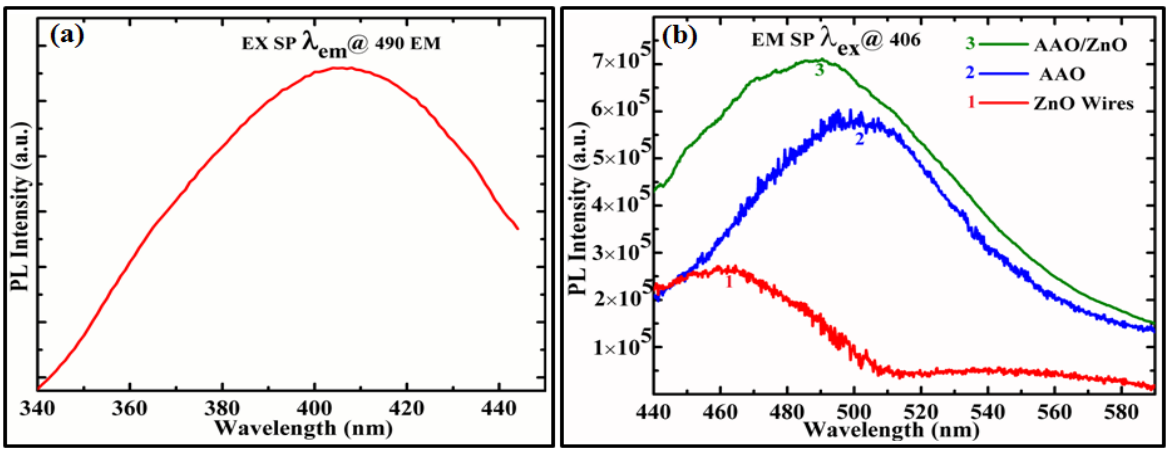

Figure 3.7: (a) The photoluminescence excitation spectra (PLE) of the AAO/ZnO assembly. **(b)** Three broad strong green emission spectra peaking at 462, 502 and 490 nm upon excitation at a wavelength of 406 nm corresponding to ZnO nanowires, the pristine AAO template, and the AAO/ZnO assembly which are represented by curves 1, 2 and 3 respectively.

times lower than that of the AAO/ZnO assembly (curve 3). The origin of the defect related electron–hole recombination process in ZnO nanowires has been extensively investigated, however, it remains debatable. Among the different mechanisms proposed to explain the visible luminance in ZnO nanowires to date, oxygen vacancies have been widely accepted as the most probable candidate [37]. In the present investigation, we have used the AAO template for synthesis of aligned ZnO nanowires which introduced intrinsic defects on the surface of ZnO nanowires in order to enhance the strong green emission compared to pristine AAO as well as ZnO as shown in Fig. 3.7(b) [38]. The broad emission peaks in the spectra are the consequence of different types of defects existing in the samples. We proposed that AAO plays a key role in enhancing the green emission in the AAO/ZnO hybrid structure. The strong interface formed during synthesis of ZnO nanowires on the AAO template, which creates higher defect densities in ZnO, gives rise to higher PL intensity in comparison to pristine ZnO and pristine AAO.

The other probable reason behind the strong luminescence in AAO/ZnO may be the higher interfacial area provided by ZnO nanowires to AAO. A higher surface to volume ratio leads to a higher concentration of defects induced by the AAO-template on the ZnO nanowire surface; as a result Vo+ (+1 charged O vacancy) from the ZnO surface and free electrons from AAO recombine strongly as compared to pristine ZnO to produce strong green emission.

3.3.4. Study of electrical and gas sensing properties of ZnO nanowire array

3.3.4.1. Study of electrical properties

When an ac electric field with magnitude 15 Vpp (peak to peak) at 0.5 MHz was applied between points“1” and “2” (Fig. 3.8(a)) (after placing a drop of suspension in the gap between the electrodes), electric field (E) induces charge separation and the resulting polarization develops a dipole moment which aligns the nanowires parallel to the field lines. In the case of non-uniform field distribution, the alignment force or the dielectrophoretic force ($\mathbf{F} \propto \nabla |\mathbf{E}|^2$ where ∇ is the gradient vector operator) moves the polarized structure towards the region of highest field density [39]. A ZnO nanowire array trapped between the two Cu electrodes due to this dielectrophoresis process is shown in Fig. 3.8(b).

The V–I characteristic of the ZnO nanowire array trapped between the electrodes (Fig. 3.8(b)) is shown in Fig. 3.9(a).

A Cu–ZnO nanowire array, which is basically a metal–semi-conductor–metal (MSM) structure, shows almost symmetric characteristics. Such MSM structures can be considered as being composed of two Schottky barriers connected back to back in series with a semiconducting material. If a barrier at both ends of the nanowire array possesses similar good quality contacts with approximately lower barrier heights, then symmetric characteristics are obtained [40]. The resistance of the nanowire array is of the order of 6 GΩ, which includes contact resistance as well. Such high resistivity is due to ZnO being a wide bandgap semiconductor (Eg = 3.3 eV) at room temperature [5].

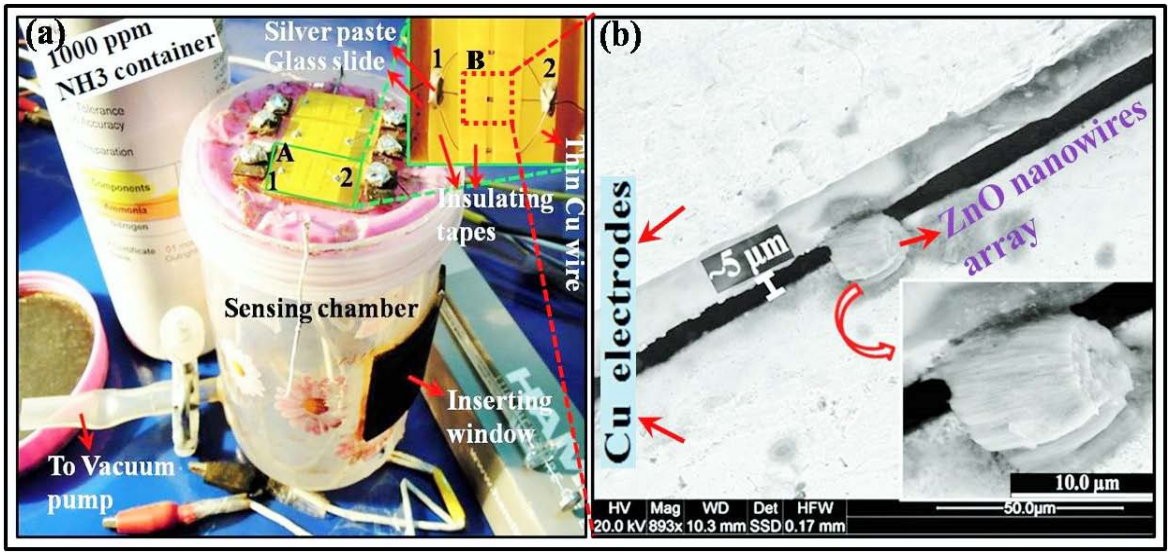

Figure 3.8: (a) Schematic diagram of the chamber used for gas sensing measurements, the inset shows the magnified "A" region of one of the glass plates which consists of 3 pairs of Cu electrodes and **(b)** magnified FESEM image of the "B" region which shows a nanowire array kept between the two electrodes.

3.3.4.2. Study of gas sensing properties

For investigating room temperature gas sensing properties of the trapped ZnO nanowire array, the sensor was kept in an air-tight box (volume 500 cm^3). 1000 ppm NH_3 (Chemtron Science Laboratories Pvt. Ltd, India) was used as the test gas, and by using an appropriate relation (capacity of syringe used × ppm level mentioned on canister = capacity of sensing container × required ppm level) different quantities of 1000 ppm NH_3 were inserted into the airtight sensing box through the inserting window using a micro-syringe so as to yield the desired ppm concentration of NH_3. A fixed bias of 0.1 V was applied across the electrodes (points "1" and "2" in Fig. 3.8(a)) and the change in the

resistance of the sensor was measured using a picoammeter. Before starting the measurement for every next NH_3 concentration, the test gas in the sensing chamber was pumped out using a vacuum pump so that the sensor recovered its initial resistance value (base line). Fig. 3.9(b) shows the response and recovery curves (in terms of resistance) of the ZnO nanowire array upon exposure to 10, 15, 25, 50, 75, 100 and 150 ppm NH_3 at room temperature. These curves show that the change in the resistance of the sensor sensibly depends on the NH_3 concentration and it increases with an increase in the value of NH_3 concentration. The % response (S) of this sensor for 50 ppm NH_3 is shown in Fig. 3.9(c). The % response (S) of a sensor is defined as $|(Ra-Rg)/Ra| \times 100$, where Ra and Rg are resistances of the sensor in air and gas, respectively. Fig. 3.9(c) shows that the response

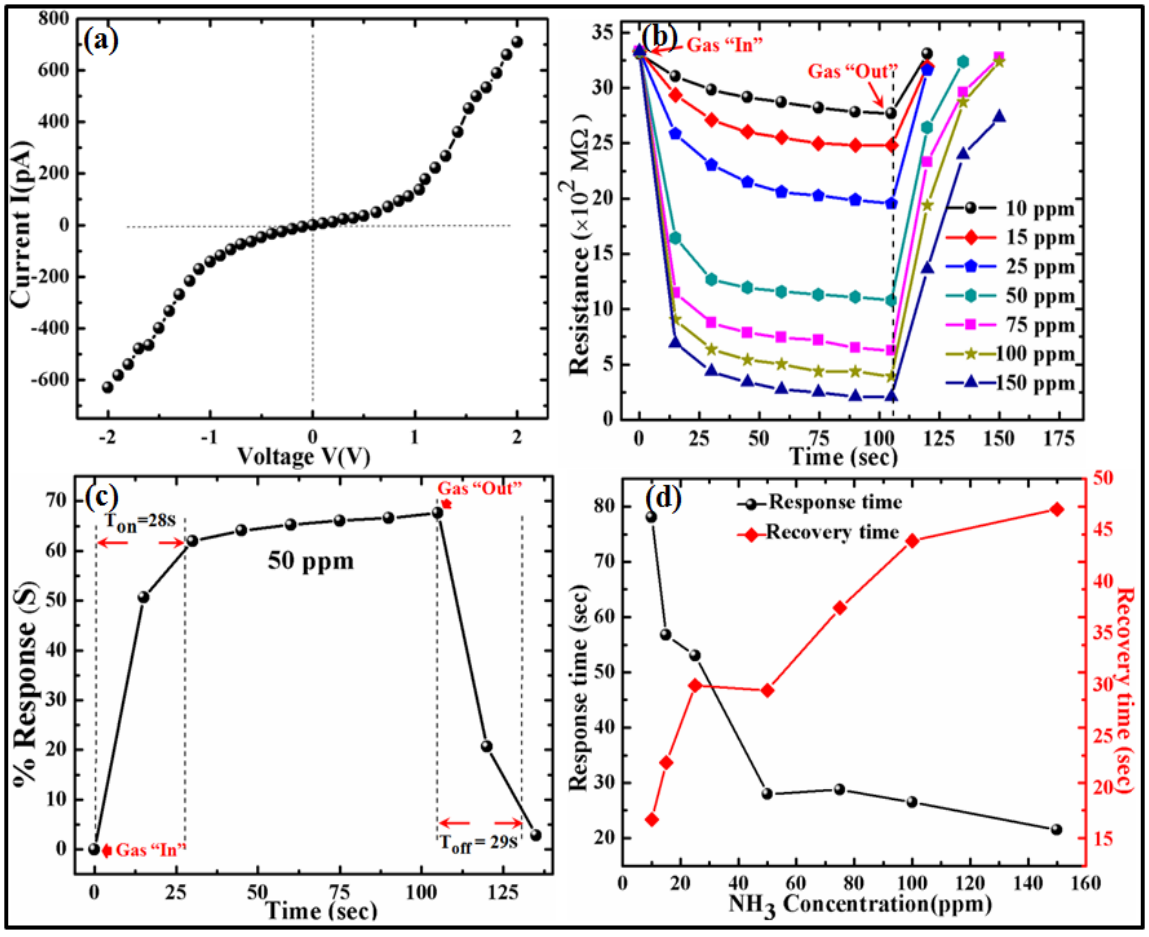

Figure 3.9: (a) V–I curve of a ZnO nanowire array kept between the two electrodes. **(b)** Variation in the resistance of ZnO nanowire array with time when exposed to different concentrations of NH_3 at room temperature. **(c)** Response curve of the sensor for 50 ppm NH_3 and the curve is utilized to calculate the response and recovery times. **(d)** Response and recovery times of the sensor with respect to the NH_3 concentration.

and recovery times (defined as the time required to reach 90% of the saturation value) of the sensor when exposed to 50 ppm NH_3 concentration are ~28 s and ~29 s, respectively. The response time of the sensor decreases with an increase in the gas concentration while the recovery time increases with an increase in the gas concentration. This behavior of the sensor is shown in Fig. 3.9(d). NH_3 concentration versus % response of the sensor is shown in Fig. 3.10. It can be seen that the % response increases almost linearly with increase in NH_3 concentration up to 75 ppm, and above 75 ppm the % response increases slowly with increase in NH_3 concentration.

The linear response of the sensor up to 75 ppm shows a power law dependence of the % response (S) on the gas concentration (C), i.e., $S = AC^{\alpha}$, where A is a constant [41, 42]. The reason behind the power law dependence is associated with the interaction or adsorption of NH_3 molecules on the sensing surface and with the change of surface potential. The power law fit to the linear portion of the response (S) and concentration (C) curve is shown in the inset of Fig. 3.10. The fitting data reveal that the value of α is about 0.75 which is in agreement with the predictions of the rational value (1 or 1/2) for the power law exponent.

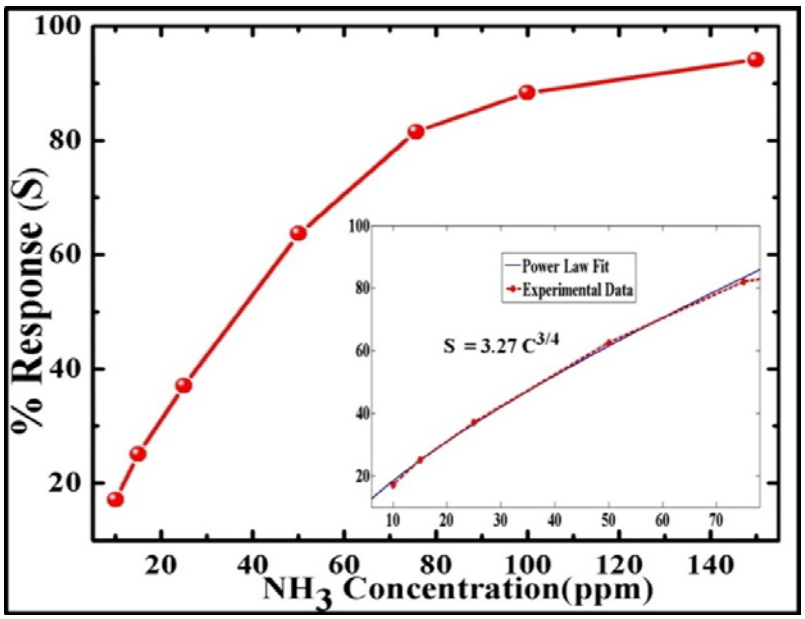

Figure 3.10: NH_3 concentration *vs.* response and the inset shows the power law fit to the linear portion of the curve.

3.3.4.3. Gas sensing mechanism

Most metal-oxide-semiconductor gas sensors work on the principle of a change in the

conductance of the sensing materials due to the interaction between the gas species and the adsorbed oxygen ions (O_2^-, $O^-$and O^{2-}). Initially, when a ZnO nanowire sensor is placed in an open atmosphere, the adsorbed oxygen ions (O_2^-, O^- and O^{2-}) extract electrons from the conduction band forming a depletion region which reduces the conducting width of ZnO wires and increases the potential barrier of the contacts between the nanowires and hence increases the resistance of the sensor. The nature and concentration of chemisorbed oxygen species strongly depend on temperature. O_2^- is commonly chemisorbed at lower temperatures (<100 °C). At higher temperatures O^- and O^{2-} are usually chemisorbed while O_2^- disappears rapidly [43]. On exposure to NH_3 at room temperature, O_2^- species at the sensor surface interact with NH_3 resulting in release of electrons. The reaction kinetics can be described as follows:

$$O_2(gas) \rightarrow O_2(ads) \tag{3.1}$$

$$O_2(ads) + e^- \rightarrow O_2^-(ads) \tag{3.2}$$

$$4NH_3 + 5O_2^- \rightarrow 6H_2O + 4NO + 5e^- \tag{3.3}$$

Thus, the trapped electrons are released back into the ZnO conduction band leading to an increase in the carrier concentration of the ZnO active layer. Thus the sensor resistance decreases upon exposure to NH_3 gas, as shown in Fig. 3.9(b).

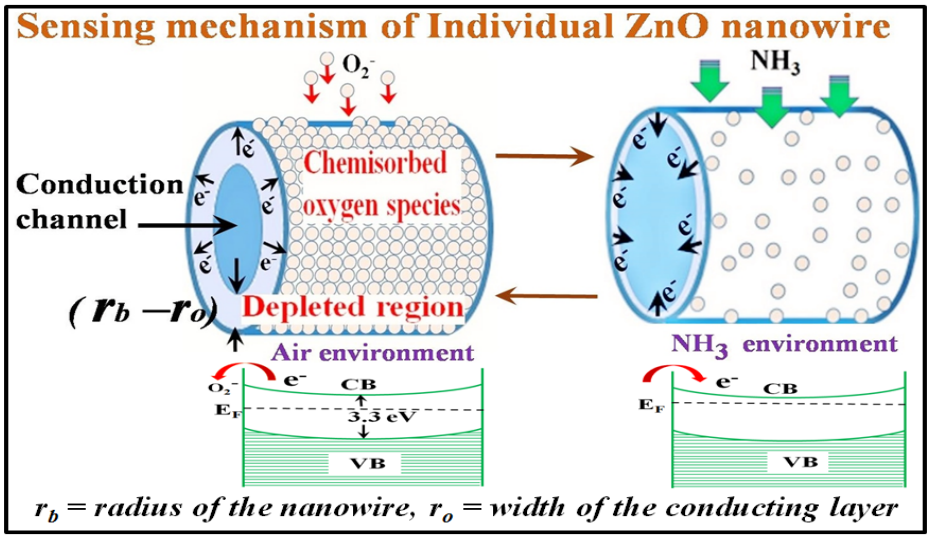

Figure 3.11: Sensing mechanism of an individual ZnO nanowire and energy level diagrams of the wire in air as well as in NH_3 environments.

The sensing properties of a sensor greatly depend upon the microstructural features of the sensing material, such as geometry, aspect-ratio and the connectivity among the nano-structures (wires, grains etc.). The sensing material in this sensor are ZnO nanowires which are vertically aligned and in contact with each other. These nanowires are in the form of a bundle and almost parallel to the gap between the electrodes. For ZnO wires in air the Debye length (the distance over which a local electric field affects the distribution of free charge carriers) is 30 nm which is comparable to the radius of our synthesized ZnO nanowires (~34 nm) [44, 45]. This implies that the nanowire is almost depleted and the surface depletion will greatly influence the density and mobility of the electrons in the nanowire. The sensing mechanism of an individual ZnO nanowire is shown in Fig. 3.11. Since here Debye length is comparable to the radius of the nanowire, in an air environment the adsorption of oxygen species (electron acceptor) on the surface of the nanowire shifts the Fermi level away from the conduction band whereas in an NH_3 environment due to the presence of oxygen vacancies the ZnO nanowire behaves as n-type semiconductor. In a nanowire array, the nanowires are in contact with each other; therefore the depletion layer will effectively modify the potential barrier at contact point between the wires. On considering the above facts and using a neck-grain boundary control model, total resistance (R) of the nanowire array can be written as [45, 46]

$$R = R_N + R_C \tag{3.4}$$

where R_N is the bulk resistance of the ZnO nanowires array and R_C is the contact resistance. On substituting the values of R_N and R_C in Eq. (3.4) total resistance,

$$R = \frac{L}{n\pi e[\mu_b n_b r_0^2 + n_d \mu_d (r_b^2 - r_0^2)]} + R_0 \exp\left\{-\frac{e\Delta V_b}{\kappa_B T}\right\} \tag{3.5}$$

Where L is the length of nanowires, n is the number of parallel ZnO nanowires in the array, e is the charge of the electron, μ_b is the electron mobility in the neutral layer, μ_d is the electron mobility in the depleted region, n_b is the free electron density in the nanowire, n_d is the free electron density in the depleted region, r_0 is the width of the conducting layer, r_b is the radius of the nanowire, R_0 is a constant term which depends on air resistance and other parameters, k_B is Boltzmann's constant, T is the absolute temperature and ΔV_b is the change in contact potential barrier, i.e. potential in air minus that in ammonia. The contact resistance of the ZnO nanowires is controlled by the interwire barriers at the contact and this potential barrier is the key factor in controlling the total resistance of the sensor (R)

and thus influences the transport of electrons between the wires. When the sensor is exposed to NH_3, due to the exchange of charge carriers between ammonia molecules and the adsorbed oxygen species the depletion width decreases. This will cause a decrease in barrier potential width and height at the contacts. Thus ΔV_b increases and the total resistance (R) of the nanowire sensor decreases. The % response of a sensor depends on the change in resistance (ΔR) upon exposure to the test gas. On increasing the gas concentration, ΔV_b increases and as a consequence sensor resistance decreases and hence the response of the sensor increases. On increasing NH_3 concentrations continuously, the change in contact potential barrier ΔV_b rapidly decreases and the slope of the response curve decreases with it (Fig. 3.10). The reason behind this is the decreased possibility of charge sharing between the ammonia and adsorbed oxygen due to reduction in the concentration of adsorbed oxygen species at the surface of the nanowire [47]. Thus the sensor saturates at higher concentrations as shown in Fig. 3.10. The bi-functional optical and gas sensing properties of this material create new avenues for optoelectronic and gas sensing applications.

3.4. CONCLUSIONS

In this chapter, we have fabricated AAO template using Al foil via anodization process and an electrochemical method is used to detach out AAO template from the Al base. Here we reported a simple cost effective technique to successfully synthesize luminescent ZnO nanowires, and the NH_3 gas sensing properties of the synthesized ZnO nanowires at room temperature. The main highlights of the work discussed here are given below:

1. Using anodization process well-ordered nanoporous AAO templates with a pore density
   of about 0.94×10^{10} cm^{-2} have been synthesized.
2. The detached AAO template so obtained is fully open through and less fragile relative to the templates obtained via other chemical methods.
3. Indigenously designed vacuum injection technique is a straightforward, quick and cost effective way to synthesize ZnO nanowires.
4. TEM analysis and FESEM micrographs reveal that as synthesized ZnO nanowires are dense, aligned, continuous with uniform diameter (between 60-70 nm) through-out the length (~11 μm) and polycrystalline in nature with hexagonal phase.

5. The photoluminescence spectrum reveals that the AAO/ZnO assembly has a strong green emission peaking at 490 nm upon 406 nm excitation wavelength. The AAO/ZnO has higher luminescence intensity compared to pristine ZnO due to its high surface to volume ratio.
6. In order to study the sensing characteristics of as synthesized nanowire array, a simple sensing system has been developed using a micromechanical technique.
7. The % response of the sensor for 50 ppm NH_3 concentration is ~ 68%.
8. The response and recovery times of this sensor, when exposed to 50 ppm NH_3 concentration, are ~ 28 s and ~ 29 s, respectively.

In summary, good quality ordered ZnO nanowires were synthesized using AAO template via vacuum injection technique and the sensor, fabricated using these wires, exhibits good response to an NH_3 atmosphere at room temperature. We believe that these simple and cost effective techniques can be extended to synthesize nanowire arrays of other metal/metal oxides and study their gas sensing properties towards various gases at room temperature. Furthermore, some optoelectronics devices may be developed using as grown nanowire array.

REFERENCES

1. K. Onenkamp, R.C. Word, C. Schlegel, "Vertical nanowire light-emitting diode", Appl. Phys. Lett., **85**, 6004 (2004).
2. H. Nanto, T. Minami, S. Takata, "Zinc-oxide thin-film ammonia gas sensors with high sensitivity and excellent selectivity", J. Appl. Phys., **60**, 482 (1986).
3. M. H. Sarvari, H. Sharghi, "Zinc oxide (ZnO) as a new, highly efficient, and reusable catalyst for acylation of alcohols, phenols and amines under solvent free conditions", Tetrahedron, **61**, 10903 (2005).
4. T. Yoshida, H. Minoura, "Electrochemical self-assembly of dye-modified zinc oxide thin films", Adv. Mater., **12**, 1219 (2000).
5. V. Srikant, D. R. Clarke, "On the optical band gap of zinc oxide", J. Appl. Phys., **83**, 5447 (1998).
6. F. M. Li, G. W. Hsieh, S. Dalal, M. C. Newton, J. E. Stott, P. Hiralal, A. Nathan, P. A. Warburton, H. E. Unalan, P. Beecher, A. J. Flewitt, I. Robinson, G. Amaratunga, W. I. Milne, "Zinc oxide nanostructures and high electron mobility nanocomposite thin film transistors", IEEE Trans. Electron Devices, **55**(11), 3001 (2008).
7. P. G. Su, C. T. Lee, C. Y. Chou, K. H. Cheng, Y. S. Chuang, "Fabrication of flexible NO_2 sensors by layer-by-layer self-assembly of multi-walled carbon nanotubes and their gas sensing properties", Sens. Actuators B, **139**, 488 (2009).
8. X. Wang, C. J. Summers, Z. L. Wang, "Large-scale hexagonal-patterned growth of aligned ZnO nanorods for nano-optoelectronics and nanosensor arrays", Nano Lett., **4**, 423 (2004).
9. L. E. Greene, M. Law, J. Goldberger, F. Kim, J. C. Johnson, Y. Zhang, R. J. Saykally, P. Yang, "Low-temperature wafer-scale production of ZnO nanowire arrays", Angew. Chem., Int. Ed., **42**, 3031 (2003).
10. W. Z. Liu, H. Y. Xu, L. Wang, X. H. Li, Y. C. Liu, "Size-controlled growth of ZnO nanowires by catalyst-free high-pressure pulsed laser deposition and their optical properties", AIP Adv., **1**, 022145 (2011).
11. L. Vayssieres, "Growth of arrayed nanorods and nanowires of ZnO from aqueous solutions", Adv. Mater., **15**, 464 (2003).
12. P. Wu, H. Zhang, Y. Qian, Y. Hu, H. Zhang, C. Cai, "Composition- and aspect-ratio-dependent electrocatalytic performances of one-dimensional aligned Pt–Ni nanostructures", J. Phys. Chem. C, **117**, 19091 (2013).

13. X. Zhao, Y. Wu, X. Hao, "Electrodeposition synthesis of Au-Cu heterojunction nanowires and their optical properties", Int. J. Electrochem. Sci., **8**, 1903 (2013).
14. X. T. Hoang, D. T. Nguyen, B. C. Dong, H. N. Nguyen, "Fabrication of carbon nanostructures from polymeric precursor by using anodic aluminum oxide (AAO) nanotemplates", Adv. Nat. Sci.: Nanosci. Nanotechnol., **4**, 035013 (2013).
15. M. A. Zeeshan, S. Pane, S. K. Youn, E. Pellicer, S. Schuerle, J. Sort, S. Fusco, A. M. Lindo, H. G. Park, B. J. Nelson, "Graphite coating of Iron nanowires for nanorobotic applications: synthesis, characterization and magnetic wireless manipulation", Adv. Funct. Mater., **23**, 823 (2013).
16. F. I. Dar, K. R. Moonooswamy, M. Es-Souni, "Morphology and property control of NiO nanostructures for supercapacitor applications", Nanoscale Res. Lett., **8**, 363 (2013).
17. X. Zhao, G. Meng, F. Han, X. Li, B. Chen, Q. Xu, X. Zhu, Z. Chu, M. Kong, Q. Huang, "Nanocontainers made of various materials with tunable shape and size", Sci. Rep., **3**, 2238 (2013).
18. Y. Dan, Y. Cao, T. E. Mallouk, S. Evoy, A. T. C. Johnson, "Gas sensing properties of single conducting polymer nanowires and the effect of temperature", Nanotechnology, **20**, 434014 (2009).
19. M. Yun, C. Lee, R. P. Vasquez, R. Penner, M. Bangar, A. Mulchandani, N. V. Myung, "Electrochemically grown single-nanowire sensors", Proc. SPIE-Int. Soc. Opt. Eng., **5593**, 200 (2004).
20. R. A. Michaels, "Emergency planning and the acute toxic potency of inhaled ammonia", Environ. Health Perspect., **107**, 617 (1999).
21. C. S. Rout, M. Hegde, A. Govindaraj, C. N. R. Rao, "Ammonia sensors based on metal oxide nanostructures", Nanotechnology, **18**, 205504 (2007).
22. D. R. Patil, L. A. Patil, "Ammonia sensing resistors based on Fe_2O_3-modified ZnO thick films", IEEE Sens. J., **7**(3), 434 (2007).
23. B. Timmer, W. Olthuis, A. van den Berg, "Ammonia sensors and their applications —a review", Sens. Actuators B, **107**, 666 (2005).
24. M. S. Wagh, G. H. Jain, D. R. Patil, S. A. Patil, L. A. Patil, "Modified zinc oxide thick film resistors as NH_3 gas sensor", Sens. and Actuators B, **115**, 128 (2006).
25. B. Karunagaran, P. Uthirakumar, S. J. Chung, S. Velumani, E.-K. Suh, "TiO_2 thin film gas sensor for monitoring ammonia", Mater. Charact., **58**, 680 (2007).

26. P. P. Mardilovich, A. N. Govyadinov, N. I. Mukhurov, A. M. Rzhevskii, R. Paterson, "New and modified anodic alumina membranes part I. thermotreatment of anodic alumina membranes", J. Membr. Sci., **98**, 131 (1995).
27. H. de L. Lira, R. Paterson, "New and modified anodic alumina membranes: Part III. Preparation and characterisation by gas diffusion of 5 nm pore size anodic alumina membranes", J. Membr. Sci., **206**, 375 (2002).
28. J. H. Yuan, F. Y. He, D. C. Sun, X. H. Xia, "A simple method for preparation of through hole porous anodic alumina membrane", Chem. Mater., **16**, 1841 (2004).
29. L. M. Gao, P. P. Wang, X. Q. Wu, X. P. Song, "Electro-chemical detachment process of through-hole porous anodic alumina membrane", J. Inorg. Mater., **20** (6), 1417 (2005).
30. Z. Shiyong, C. Karen, Y. Arthur, V. Teodor, "Preparation of open-through anodized aluminium oxide films with a clean method", Nanotechnology, **18**, 245304 (2007).
31. H. Masuda, A. Fukuda, "Ordered metal nanohole arrays made by a two-step replication of honeycomb structures of anodic alumina", Science, **268**, 1466 (1995).
32. T. T. Xu, R. D. Piner, R. S. Ruoff, "Atomic force microscopy study of clay nanoplatelets and their impurities", Langmuir, **19**, 1443 (2003).
33. P. P. Mardilovich, A. N. N. Govyadinov, N. I. Mukhurov, R. Paterson, "New and modified anodic alumina membranes part II. Comparison of solubility of amorphous (normal) and polycrystalline anodic alumina membranes", J. Membr. Sci., **98**, 143 (1995).
34. K. Nielsch, J. Choi, K. Schwirn, R. B. Wehrspohn, U. Gösele, "Self-ordering regimes of porous alumina: The 10 porosity rule", Nano Lett., **2**, 677 (2002).
35. F. Li, L. Zhang, R. M. Mitzger, "On the growth of highly ordered pores in anodized aluminum oxide", Chem. Mater., **10**, 2470 (1998).
36. T. Mingliang, X. Shengyong, W. Jinguo, K. Nitesh, W. Eric, L. Qi, C. M. Paul, C.W. H. Moses, M. E. Thomas, "Penetrating the oxide barrier in situ and separating freestanding porous anodic alumina films in one step", Nano Lett., **5**, 697 (2005).
37. B. K. Gupta, V. Grover, G. Gupta, V. Shanker, "Highly efficient luminescence from hybrid structures of ZnO/multi-walled carbon nanotubes for high performance display applications", Nanotechnology, **21**, 475701 (2010).
38. M. Wu, L. Yao, W. Cai, G. Jiang, X. Li, Z. Yao, "Preparation and photoluminescence of ordered ZnO nanowire arrays", J. Mater. Sci. Technol., **20**, 11 (2004).

39. H. A. Pohl, “The motion and precipitation of suspensoids in divergent electric fields”, J. Appl. Phys., **22**, 869 (1951).
40. D. Q. Wang, R. Zhu, Z. Y. Zhou, X. Y. Ye, “Electrical characteristics and optoelectronic properties of metal-semiconductor-metal structure with zinc oxide nanowires across Au electrodes”, Chin. Phys. B, **17**, 3875 (2008).
41. N. S. Ramgir, M. Ghosh, P. Veerender, N. Datta, M. Kaur, D. K. Aswal, S. K. Gupta, “Growth and gas sensing characteristics of p- and n-type ZnO nanostructures”, Sens. Actuators B, **156**, 875 (2011).
42. N. Yamazoe, K. Shimanoe, “Theory of power laws for semiconductor gas sensors”, Sens. Actuators B, **128**, 566 (2008).
43. J. C. Belmonte, J. Manzano, J. Arbiol, A. Cirera, J. Puigcorbe, A. Vila, N. Sabate, I. Gracia, C. Cane, J. R. Morante, “Micromachined twin gas sensor for CO and O_2 quantification based on catalytically modified nano-SnO_2”, Sens. Actuators B, **114**, 881 (2006).
44. O. Lupan, L. Chow, T. Pauporte, L. K. Onoa, B. Roldan Cuenya, G. Chai, “Highly sensitive and selective hydrogen single-nanowire nanosensor”, Sens. Actuators B, **173**, 772 (2012).
45. Z. Yang, L. M. Li, Q. Wan, Q. H. Liu and T. H. Wang, “High-performance ethanol sensing based on an aligned assembly of ZnO nanorods”, Sens. Actuators B, **135**, 57 (2008).
46. Y. Mas, W. L. Wang, K. J. Liao, C. Y. Kong, “Study on sensitivity of nano-grain ZnO gas sensors”, J. Wide Bandgap Mater., **10**, 113 (2002).
47. P. Feng, Q. Wan, T. H. Wang, “Contact-controlled sensing properties of flower like ZnO nanostructures”, Appl. Phys. Lett., **87**, 213111 (2005).

STUDY OF ELECTRICAL, OPTICAL, GAS SENSING AND ANTIBACTERIAL PROPERTIES OF TWO DIMENSIONAL REDUCED GRAPHENE OXIDE (rGO) THIN FILMS

4.1 INTRODUCTION

Graphene is a two dimensional (2D) atomic layer of carbon atoms arranged in honeycomb hexagonal lattice with sp^2 hybrization. In chapter-1 we have discussed about few basic properties of graphene. A lot of research has been performed to investigate the mechanical, electrical, chemical, biological, thermal and optical properties of this excellent material after its experimental discovery in 2004 [1, 2]. Graphene possesses very high charge carrier mobility ~ 200,000 cm^2 V^{-1} s^{-1}. Although in graphene valence and conduction bands touch each other at the Dirac point yet its band gap can be tuned easily from 0-2.5 eV [3, 4]. These unique properties of graphene have been utilized in fabricating graphene based electronic devices like super capacitors, lithium-ion batteries and solar cells [5-7]. Further, graphene with high surface to volume ratio offers a large exposed area for gas molecules and its high conductivity and metallic transport properties provide very little Johnson's noise. Additionally, in four probe measurements graphene forms ohmic contacts with the electrodes leading to linear dependence of current and voltage without distortion. Studies confirm that graphene could detect individual molecules of NO_2, NH_3, H_2O and CO at very low concentrations [8]. Among graphene, CNT and other wide-band-gap metal oxide gas sensing materials; the 2D configuration, superior mobility of charge carriers, optical opacity and tailored band gap make graphene a more promising material for single molecular gas sensor [9]. In addition to this, low power consumption is an important factor for the gas sensors. Thus, to save energy, it is desirable for sensors to work at room temperature and in this regard graphene based sensors seem better than other solid state gas sensors.

For fabrication of 2D reduced graphene based thin film gas sensors, graphene oxide (GO) is used as the raw material because GO is widely accepted as the parent material for the large scale synthesis of graphene at a relatively low cost [10]. Unlike graphene, GO can be dispersed in various solvents easily which makes it suitable for the synthesis of large area thin films and composites [11]. GO is electrically insulating and in order to make it

electrically active it must be deoxidized either thermally or chemically. However, the reduced graphene oxide (rGO) possesses lower electrical conductivity in comparison to the pristine graphene synthesized either by scotch tape or grown by CVD. Even though, rGO's conductivity is sufficiently high enough to be used in the fabrication of electronic devices [12]. Recently, many research groups are working on chemically derived rGO thin films, lattice modified rGO thin films, rGO hybrid films and rGO composite based gas sensors [13-18]. There are several techniques to utilize rGO in gas sensing applications and among most of these the gas sensing devices are fabricated using expensive nano-lithographic techniques which usually make rGO surface contaminated that greatly influences the transport properties as well as sensing performance of the devices [19, 20]. In addition to this, sensitivity and noise level of the rGO thin film based gas sensors are found to be inversely proportional to the thickness of the rGO film [21]. Therefore, rGO thin film based gas sensors which utilize standard four probe contacts seem more appropriate for gas sensing applications. However, rGO-based gas sensors require some improvements in their response, recovery times and selectivity at room temperature which may create new possibilities for innovation in rGO based gas sensing devices.

Here, in addition to gas sensing properties, we have also studied several other important (optical, electrical and antibacterial) properties of the same chemically derived rGO 2D thin film sample, fabricated by customized hydrazine hydrate vapor reduction method. Detailed morphogenesis studies have been probed through various microscopic techniques. GO thin film deposited onto the quartz substrate by spin coating was chemically reduced by hydrazine hydrate at 90°C and its properties like photo-luminescence (PL), electronic properties, gas sensing properties and antibacterial activity have been investigated. Cl_2 and NO_2 gas sensing properties of luminescent rGO thin film have been analyzed at room temperature in an indigenously built sensing chamber using four-probe standard measurement technique and the good response of the rGO thin films to Cl_2 and NO_2 gases for concentrations as low as 5 and 10 ppm, respectively, have been observed. Detection of chlorine is very important because it is widely used to disinfect water in industries, sewage plants and to bleach pulp in the paper mills [22]. It has large applications in pharmaceutical, agrochemical production, manufacturing of pesticides, refrigerants and synthetic materials. Chlorine is a toxic gas and exposure to its various concentrations have been reported to exhibit varying adverse effects on the human health and can be fatal after a few breaths at 1000 ppm [23]. The choice of another gas for sensing application is nitrogen dioxide (NO_2). NO_2 is very harmful to environment as well

as to living beings and it is mainly released in the environment by traffics vehicles, petrol and metal refining, other manufacturing industries and food processing. As a result, NO_2 may cause lung irritations, increase the susceptibility to infections, contribute to acid rains and play an important role in the formation of ozone in the lower atmosphere [24]. Therefore, it is highly desired to develop a smart portable inexpensive Cl_2 and NO_2 gas sensor with fast response and good recovery time. It has been reported in recent studies that graphene is biocompatible, less toxic to human and exhibits strong antibacterial activity [25-27]. So graphene may have potential biomedical application as a new effective antibiotic for the next generation. In order to explore the possible biomedical applications of the as grown GO and rGO thin films, we have investigated their antimicrobial activity against Gram-ve (E.coli) and Gram+ve (B. cereus) bacteria. However, to the best of our knowledge, the interaction and extraordinary antibacterial property of rGO/GO thin film with Gram +ve (B. cereus) bacteria has not yet been explored till date.

4.2 EXPERIMENTAL WORK

In the present investigations first GO was synthesized using "Improved Synthesis of Graphene Oxide" method reported by J. M. Tour et al. as described in section 2.2.2.1 of chapter-2 [28]. A dispersion of GO in ethanol (6 mg/ml) was used to fabricate GO thin film on the precleaned quartz substrate via programmable spin coater (Spin NXG P-1). Various strong chemical reductants have been used for the reduction of GO [29-32]. Here we used hydrazine vapor to reduce GO thin film into rGO. A brief description of synthesis process of GO thin film and its reduction to rGO is given in section 2.2.2.2 of chapter-2. Electrical and gas sensing properties of rGO thin film have been investigated using an assembly containing nichrome heater and temperature sensor inside an indigenously built stainless steel housing of volume 500 cm^3. A complete descripton of sensing set-up and the procedure of measurement is given in section 2.2.2.3 of chapter-2. Prior to measurements, the rGO thin film on the quartz substrate was heated at 110°C for 2 h to avoid the influence of moisture and other impurities present in the thin film. The standard four probe technique was used for electrical and gas sensing measurements to reduces the effect of contact resistance efficiently. Here gap among the four point contacts on the rGO thin film was kept less than 1 mm. After utilizing the relation (capacity of syringe used × ppm level mentioned on canister = capacity of sensing container × required ppm level) different quantities of 1000 ppm Cl_2 and NO_2 were inserted into the housing using plastic syringe so

as to yield a desired ppm concentration and the change in the resistance of the sensor was measured by a picoammeter. The structural analysis of the as-synthesized GO, rGO powders and thin film samples were performed by XRD. AFM and FESEM were used for the analysics of surface morphology. The microstructural characterizations were carried out by TEM and HRTEM. Sample quality and extend of graphitization of the rGO thin film were examined using XPS and Raman spectroscopy. The UV-vis spectra and PL spectroscopy were used to investigate the optical properties of GO and rGO samples.

4.3 RESULTS AND DISCUSSION

4.3.1 X-ray diffraction studies

X-ray diffractometer using Cu-Kα radiation of wavelength 1.54Å was utilized to characterize the pristine GO, rGO powders and thin film samples. As it is well known that in the thin film of rGO deposited on quartz substrate, the XRD peak of substrate dominates over the rGO thin film characteristic peak as shown in Fig. 4.1(a). For better understanding

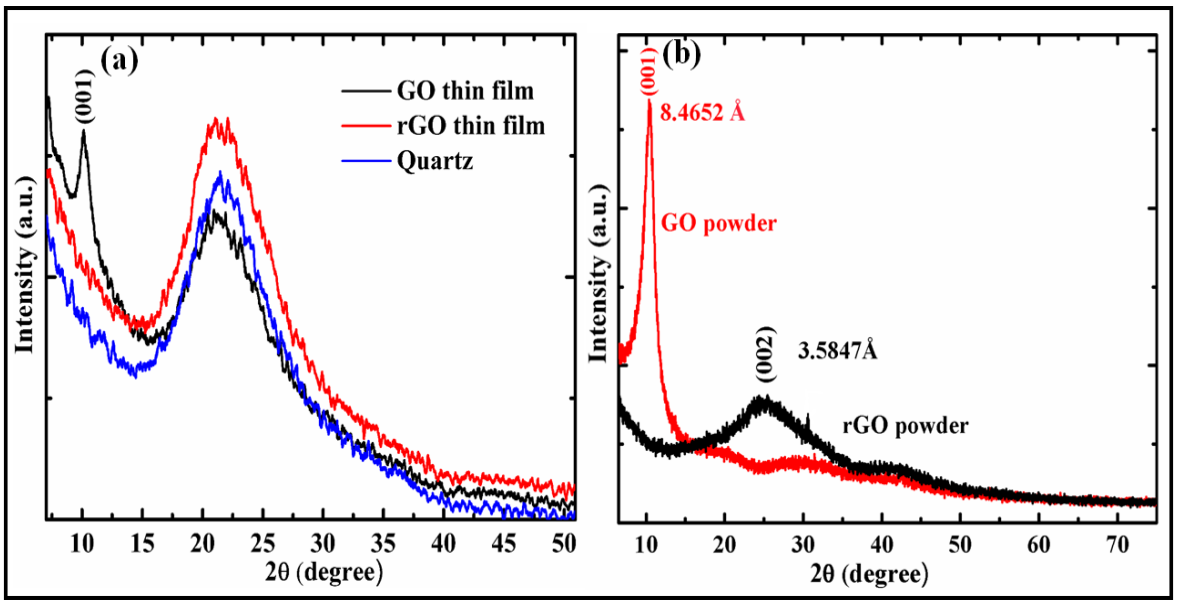

Figure 4.1: X-ray diffraction (XRD) spectra of GO and rGO thin films **(a)** and powders **(b)**.

, we have also done the XRD characterization of GO and rGO powders for the comparative studies as shown in Fig. 4.1 (b). The GO and rGO powders display characteristic d-values around 8.465 and 3.584 Å which could be attributed to (001) and (002) diffraction planes, respectively.

4.3.2 Microstructural studies

The surface morphology and microstructural characterization of the as prepared rGO thin film were explored by AFM, FESEM, TEM and HRTEM as shown in Fig. 4.2 (a)-(d), respectively. The obtained results reveal that the as-synthesized rGO thin film is about 15 nm thick and it consists of a few wrinkles, which are expected in graphene surfaces as shown by arrows in Fig. 4.2 (a) and (c). FESEM images also portrait that the film is almost

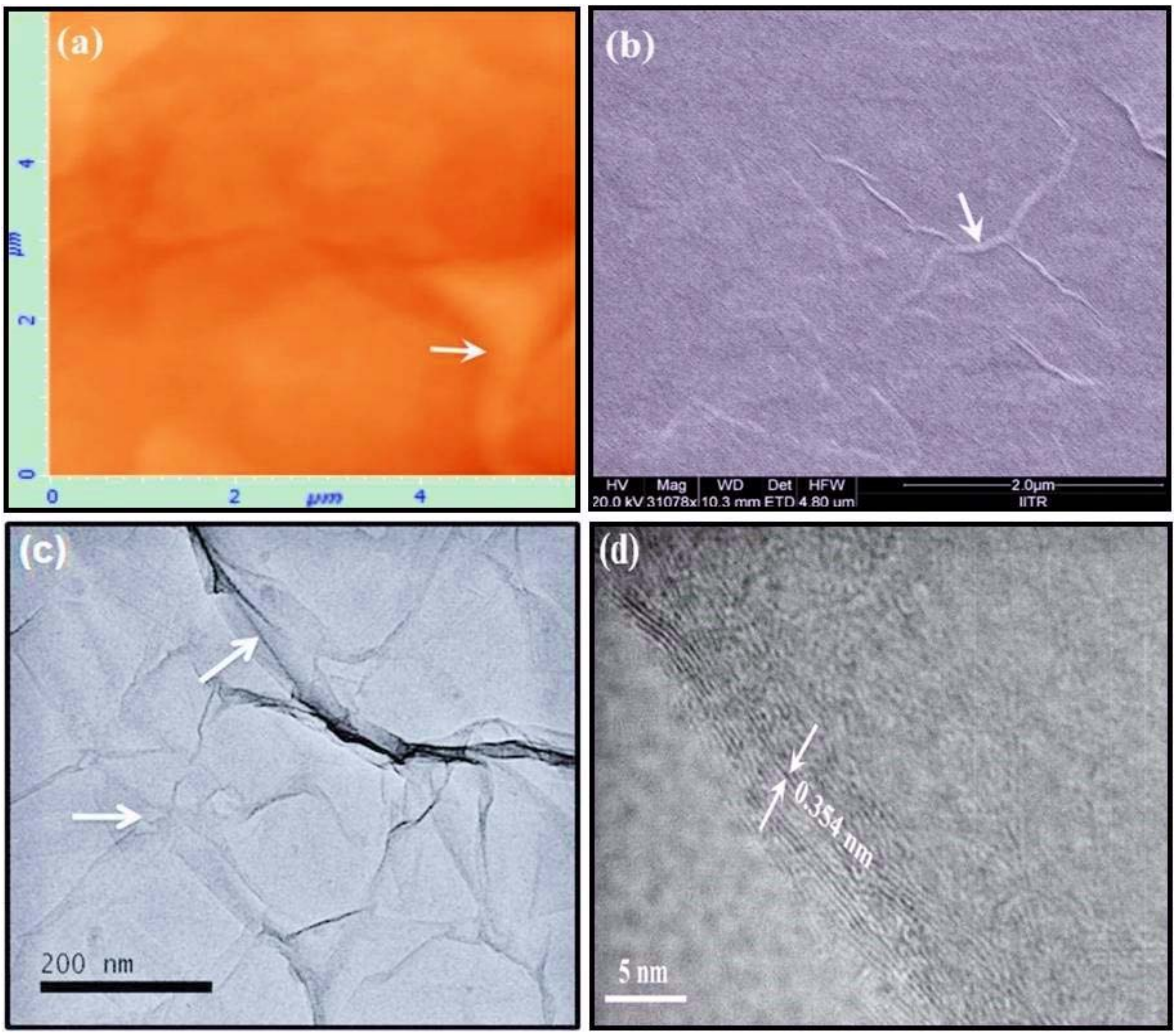

Figure 4.2: (a) AFM topographic image of rGO thin film on the quartz substrate. **(b)** FESEM image of the rGO thin film. **(c)** TEM image of the precursor solution showing wrinkled GO nanosheet. **(d)** HRTEM image of the rGO thin film.

continuous and homogeneous. The typical HRTEM image of rGO thin film is shown in Fig. 4.2(d). Precise observation of HRTEM indicates that the thin film exhibits the lattice fringes of spacing 0.354 nm, which corresponds to the (002) plane of graphite. This again confirms the reduction of GO to rGO.

4.3.3 Study of X-ray Photoelectron Spectroscopy (XPS)

XPS was utilized to study the chemical state and atomic ratio of each element present in the GO and rGO thin films. The survey spectra of GO and rGO thin films is shown in Fig. 4.3. It reveals that after hydrazine vapor reduction the intensity of O1s peak decreases while that of C1s peak increases. This confirms the de-oxygenation of GO thin film and formation of graphene after reduction. The survey spectra of GO contains only the peaks of C and O elements while the survey spectra of rGO contains an additional N1s peak .

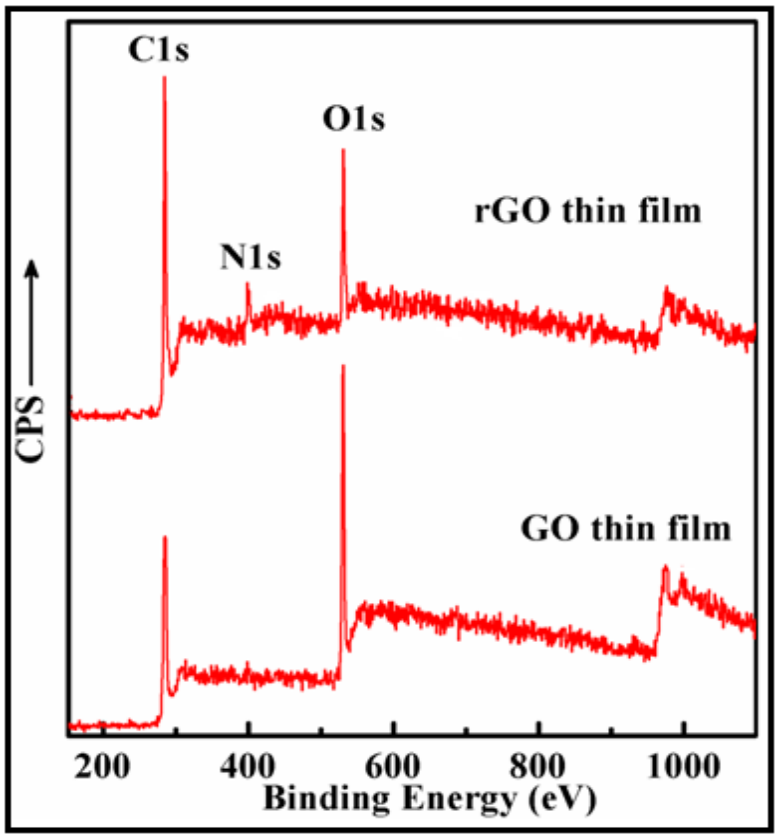

Figure 4.3: XPS survey spectra of GO and rGO thin films.

The high resolution core level XPS C1s spectra of GO was deconvoluted into four Gaussian components that correspond to non-oxygenated graphitic sp^2 carbon (C=C/C–C, 284.5 eV), epoxy and alkoxy (C–O, 286.6 eV), carbonyl (C=O, 287.8 eV) and carboxylate carbon (C–C=O, 289.1 eV) as shown in Fig. 4.4(a) [29]. The high resolution core level XPS C1s spectra of rGO was deconvoluted in the same way as XPS C1s spectra of GO and it possess similar four groups (graphitic carbon, epoxy, carbonyl and carboxylate) peaks mentioned above with an additional hydrazones C (C–N, 285.9 eV) peak which arises due to incorporation of nitrogen during hydrazine reduction as shown in Fig. 4.4 (b) [33]. C1s spectra of rGO indicates that after hydrazine reduction all the peak intensities related to the

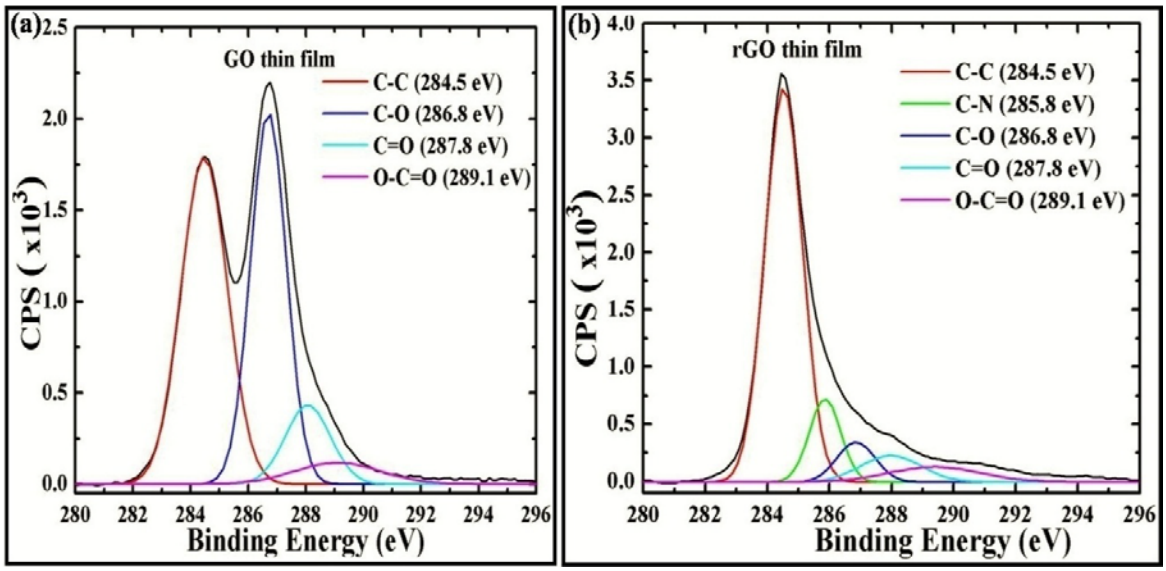

Figure 4.4: (a) and **(b)** are the high-resolution XPS C1s spectra of GO and rGO thin films, respectively.

bonding between carbon and oxygen atoms such as epoxy, carbonyl and carboxylate have decreased which suggest the removal of oxygenated functional groups. The calculated C/O ratio from the given XPS data increased from 1.4251 to 1.7931 symbolizing the reduction of GO. This confirms the formation of rGO [34].

4.3.4 Study of Raman spectra

The Raman spectroscopy is a fast powerful nondestructive characterization tool to examine the chemical structure, defects and disorder lines of a sample. The Raman spectra of chemically synthesized GO and rGO consist of D-band (1373 cm^{-1}), G-band (1602 cm^{-1}), 2D-band (2701 cm^{-1}), and D+G-band (2947 cm^{-1}) as shown in Fig. 4.5 [35]. The D-band arises due to the relaxation of k-point phonons of A1g symmetry while the G-band originates due to the first order Brillouin scattering of the E2g phonons of the planar sp^2 hybridized carbon atom [36]. The 2D band known as the second order overtone of the D band, arises due to two phonon double resonance raman process. 2D band is widely used to identify the number of graphene layers in the test sample because the broadening of the 2D band increases as the graphene thickness increases from single layer to multilayer [37]. The intensity of the D peak is directly related to the size of the sp^2 hybridized in plane carbon atoms. The raman spectra of GO and rGO support to verify the reduction process which occurs due to presence of hydrazine vapor in GO. After chemical reduction, the D

and G bands are still present but shifted to 1371 and 1598 nm, respectively and a relative change in the intensities of the D and G peaks can also be observed. Moreover, the I_D/I_G

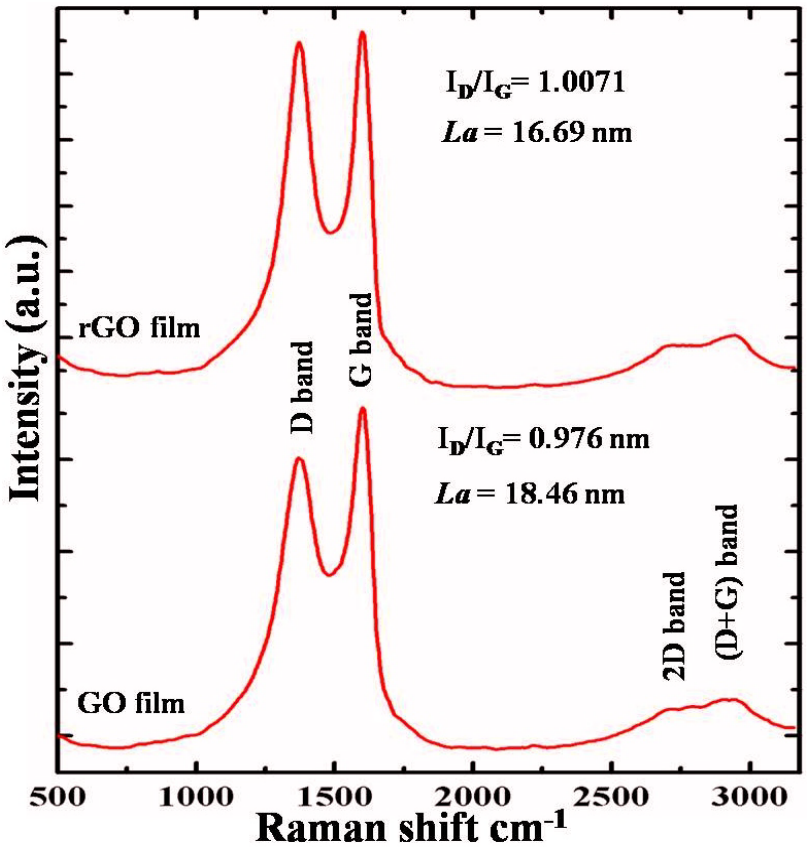

Figure 4.5: Raman spectra of GO and rGO thin films.

ratio has increased a little which reveals the decrease in size of sp^2 domains. The increase in intensity of the D peak itself points to the formation of more sp^2 domains. As the I_D/I_G ratio of rGO is more than that of GO, it can be concluded that more number of new domains of sp^2 hybridized carbon atoms are formed upon reduction with smaller size than those present in pristine GO [38]. Thus, the Raman spectrum analysis proves the reduction of GO by hydrazine hydrate. The I_D/I_G ratio can also be used to determine the in plane crystalline size (*La*) of the sample using the model given below [39]:

$$La\ (\text{nm}) = (2.4\times10^{-10})\ \lambda l^4\ (I_D/I_G)^{-1} \qquad (4.1)$$

Where λl (514.5 nm) is the wavelength of the excitation laser line used in the Raman experiment. Applying the stated formula, we get the *La* values of GO and rGO 17.23 and 16.69 nm, respectively, as listed in Table 4.1.

Table 4.1: I_D/I_G ratio and in plane crystalline size (*La*) of the GO and rGO thin films calculated using Raman spectra.

Sample Name	**(I_D/I_G) Peak intensity**	**(I_D/I_G) Fitted Area**	***La (nm)***
GO	0.8792	0.976	17.23
rGO	0.9110	1.0071	16.69

The lower value of *La* for rGO implies that after reduction of GO new sp^2 hybridized carbon clusters of smaller size are formed [40].

4.3.5 Study of UV-visible spectra

The UV-visible spectra of GO and rGO thin films on quartz substrates are shown in Fig. 4.6. These depict the sharp characteristic absorption peak of GO film at 227 nm,

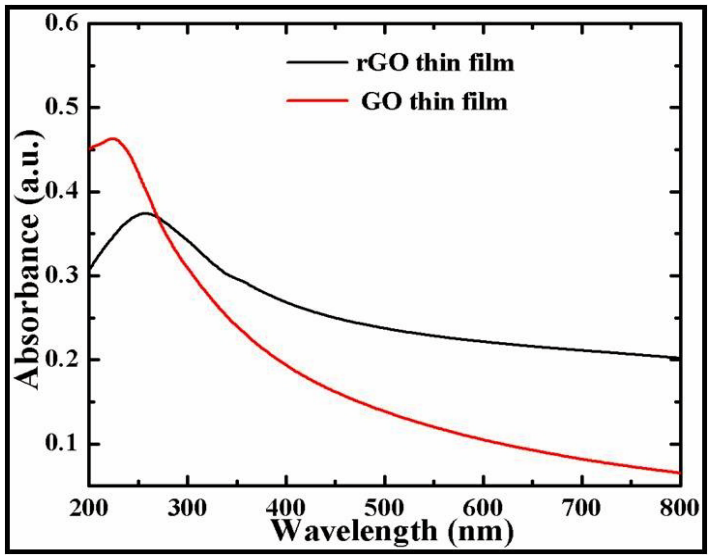

Figure 4.6: UV-visible spectra of GO and rGO thin films on quartz substrates.

attributed to the π→π* transitions of the C=C bonds in sp^2 hybridized regions, and the corresponding red shift to the 258 nm, for rGO, after hydrazine vapor reduction. The more the π-π* conjugation the less is the energy required for electronic transitions and hence

higher is the wavelength recorded [41]. No clear absorption edge is observed, suggesting absence of a well-defined band gap. The red shift in the absorption peak after reduction reflects increased π-conjugated electron concentration and structural ordering consistent with the restoration of sp^2 carbon atom which depicts the successful reduction of GO to rGO [42]. It is further evidenced by PL spectroscopy.

4.3.6 Study of photoluminescence (PL)

Recently, PL of chemically derived GO has been focal points of many research groups in worldwide and potentially demonstrated by several research groups [43-45]. The luminescence of GO was found to occur in the visible and near-infrared wavelengths range, a property functional for biosensing and fluorescence labeling and many bio-medical applications [43, 44]. Generally, the carbon materials containing a mixture of sp^2 and sp^3 bonding, the opto-electronic properties are determined by the states of the sp^2 sites [46]. The π and π*electronic levels of the sp^2 clusters lie within the band gap of σ and σ*states of the sp^3 matrix and are strongly localized [47-48]. The optical properties of disordered carbon thin films containing a mixture of sp^2 and sp^3 carbon have been widely investigated [49-53].

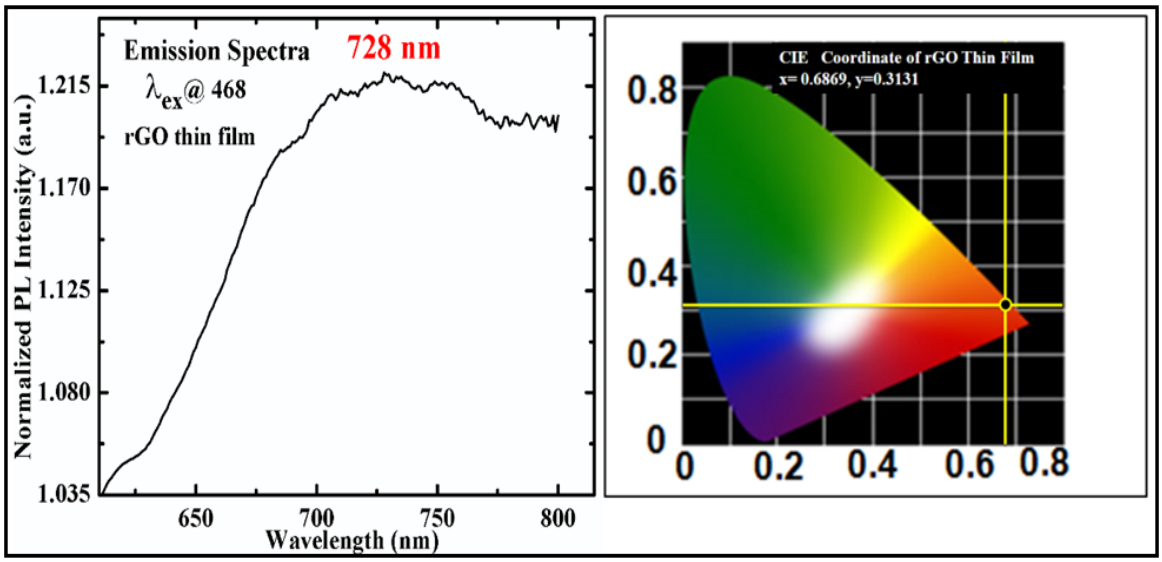

Figure 4.7: Room-temperature PL emission spectra of **(a)** rGO thin film and **(b)** CIE (International Commission on Illumination) color coordinate of PL emission.

The PL emission spectrum of rGO (Fig. 4.7 (a)) shows broader peak at around 728 nm upon 468 nm excitation which is attributed to the different size distribution of sp^2

clusters in the graphene lattice. Fig. 4.7 (b) exhibits the CIE (International Commission on Illumination) color coordinate of PL emission having x= 0.6869, y= 0.3131. The PL in rGO is a consequence of geminate recombination of localized e–h pairs in sp^2 clusters, which essentially behave as the luminescence centers or chromophores [54]. Since the band gap depends on the size, shape, and fraction of the sp^2 domains, the tunable PL emission can be achieved by controlling the nature of sp^2 sites. For example, PL energy linearly scales with the sp^2 fraction in disordered carbon systems [55]. For the comparative study, we excited the GO thin film with 468 nm excitation wavelength as shown in Fig. 4.8 (a). We observed that GO exhibits PL emission at 698 nm which is quite blue shifted in

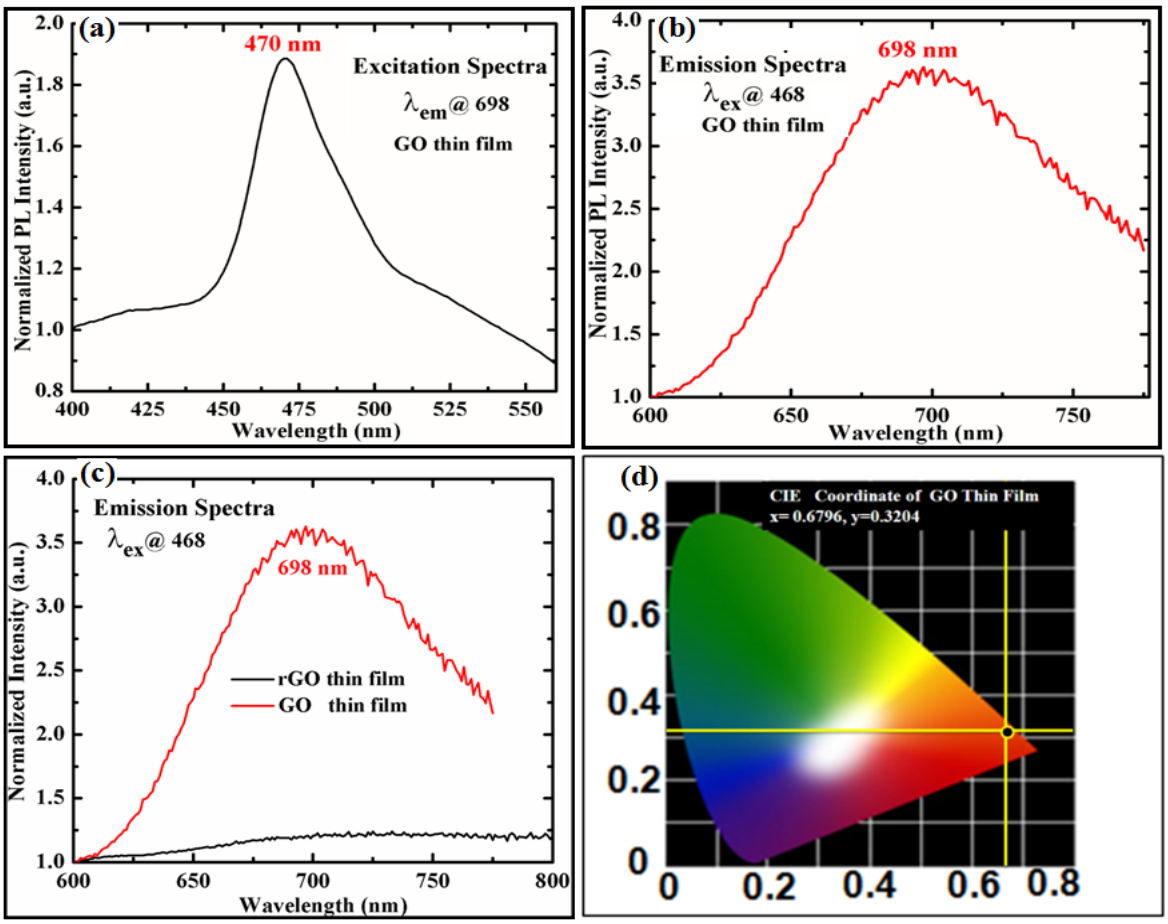

Figure 4.8: (a) Excitation spectrum of GO thin film upon 698 nm emission at room temperature**. (b)** Room-temperature PL emission spectra of rGO thin film and **(c)** comparative photoluminescence study of GO and rGO thin film upon 468 nm emission at room temperature. **(d)** CIE color coordinate of PL emission for GO thin film.

comparison to the rGO with higher PL intensity as shown in Fig. 4.8(b) and (c). It is interesting to note that CIE coordinate also shifted from x=0.6796, y= 0.3204 to x= 0.6869,

y= 0.3131 after reduction of GO thin film (Fig. 4.8(d)). The reduction having taken place for 180 mins, rGO demonstrates a decrease in PL intensity (quenching), along with a broadening of the signal. The energy gap between the π and π*states generally depends on the size of sp^2 clusters or conjugation length [46, 56]. From Raman, it has been suggested that GO consists of sp^2 clusters isolated within sp^3carbon matrix. As shown by Eda et al. [57] the quenching of the PL signal can be attributed to the percolation of the sp^2 clusters generated after reduction of the GO to rGO and removal of oxygen containing groups in the process. The electrical conductivity of rGO sheets can be directly related to the nature transport phenomenon by quantum tunneling and of sp^2 domains present in the material. A lesser number of sp^2 domain filled rGO will show transport phenomena by quantum tunneling and thus give significantly lower conductivity [57]. However, once the percolation of sp^2 sites occurs, hopping transport of electron takes over and the observed conductivity is significantly higher as observed in the present investigations. The availability of non radiative sites during the electron transport ensures that de-excitation does not release photons, and hence decrease in signal intensity [58]. The obtained PL results have good agreement with XPS and Raman data.

4.3.7 Study of electrical properties

Electrical characterization of the as-prepared rGO thin film has been carried out in

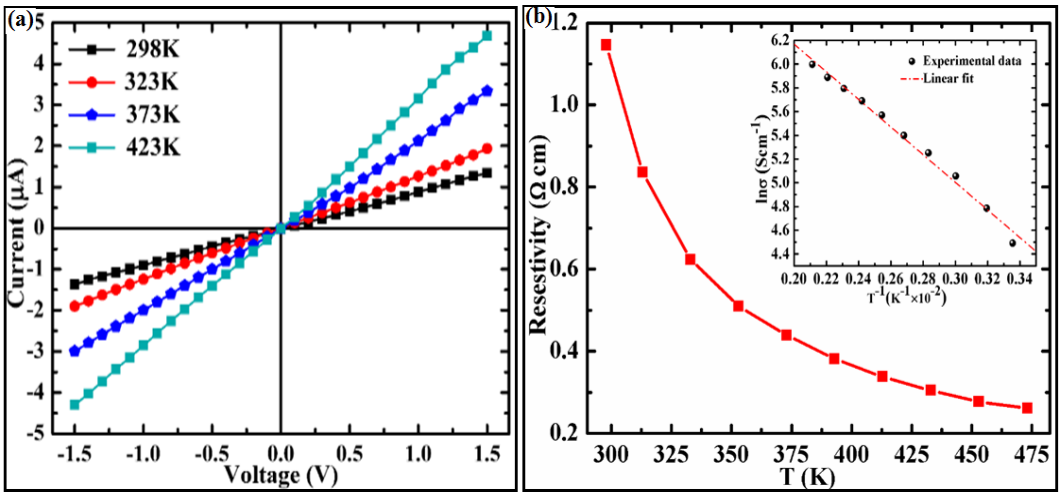

Figure 4.9: (a) High-temperature *I-V* curves of the rGO thin film exhibiting Ohmic characteristics. **(b)** Electrical resistivity of rGO thin film as a function of temperature and inset shows the Arrhenius fit to the natural logarithm of the measured conductivity (σ) of rGO thin film versus T^{-1}.

the temperature range of 293 K-473 K with the help of four-probe arrangement as shown in chapter -2 (Fig. 2.7(c)). Fig. 4.9(a) shows linear *I-V* curves of rGO thin film in the above mentioned temperature range, thus pointing to the ohmic nature of the sample. The linear behavior shows the metallic nature of the rGO thin film [59, 60]. Moreover, the rGO thin film resistance decreases exponentially with increase in temperature which is a characteristic of semiconductor as shown in Fig. 4.9(b). The occurence of metallic and semiconductiong behaviour suggest that graphene is a semi-metal [8]. Further, in a multilayered graphene, there is an opening of the band gap which results in the semiconducting behaviour of the prepared samples instead of the metallic nature as present in single layer graphene sheets. However in presence of the external in-plane, homogenous electric field applied along the edges, the band gap can be tuned to make graphene sample to behave like a metal, hence the ohmic nature of the *I-V* characteristic graph as shown in Fig. 4.9(a) [29, 61, 62]. The decrease in resistance with increase in temperature thus attributed to the fact that more electrons are excited into the conduction band from the valence band due to the excess thermal energy. Inset in Fig. 4.9(b) shows the natural logarithm of the measured conductivity (σ) of rGO thin film versus T^{-1}. The best fit to the experimental data follow the Arrhenius equation for extrinsic semiconductor in the mentioned temperature range and the estimated value of the activation energy obtained from Arrhenius curve fitting is ~ 0.2 eV which is close to the reported value [57].

4.3.8 Study of rGO thin film gas sensing properties

To examine the gas sensing properties of rGO thin film four probe electrical contacts were made on it using silver paste and different concentrations (ppm) of oxidizing gases Cl_2 and NO_2 were inserted into the sensing chamber at room temperature through the inlet valve using a plastic syringe. All the sensing data were recorded at room temperature and atmospheric pressure. Details of the sensing measurements are given in the experimental section. After chemical reduction of GO film some carboxylic and epoxide groups still remain attached to the basal plane as confirmed by XPS results. These residual groups are expected to have electron-withdrawing nature and thus increase the number of holes in the sample**.** This is the reason, rGO film acts as a p-type semiconducting material [63]. Cl_2 and NO_2 both are strong oxidizing gases with high electron withdrawing nature so when rGO film was exposed to different concentrations (ppm) of Cl_2 and NO_2 the adsorb molecules of these gases on the surface of rGO thin film extract electrons from the film surface and in this way increase the number of conduction holes in the sample which

results in a decrease in the resistance of the thin film sample. So NO_2 and Cl_2 gases behave as p-type dopants for the rGO film. Fig. 4.10 (a) and (b) show % change in the rGO film resistance upon exposure to different concentrations (ppm) of Cl_2 and NO_2, respectively. These curves show that % change in the resistance of the rGO film sensibly depends on the concentration of Cl_2 and NO_2 gases and it increases with increasing the concentrations of these gases. The % change in the rGO film resistance is defined as:

$$(R_g - R_a)/R_a \times 100 = \Delta R/R_a \qquad (4.2)$$

where, R_a and R_g are resistances of the rGO film in air and gas, respectively.

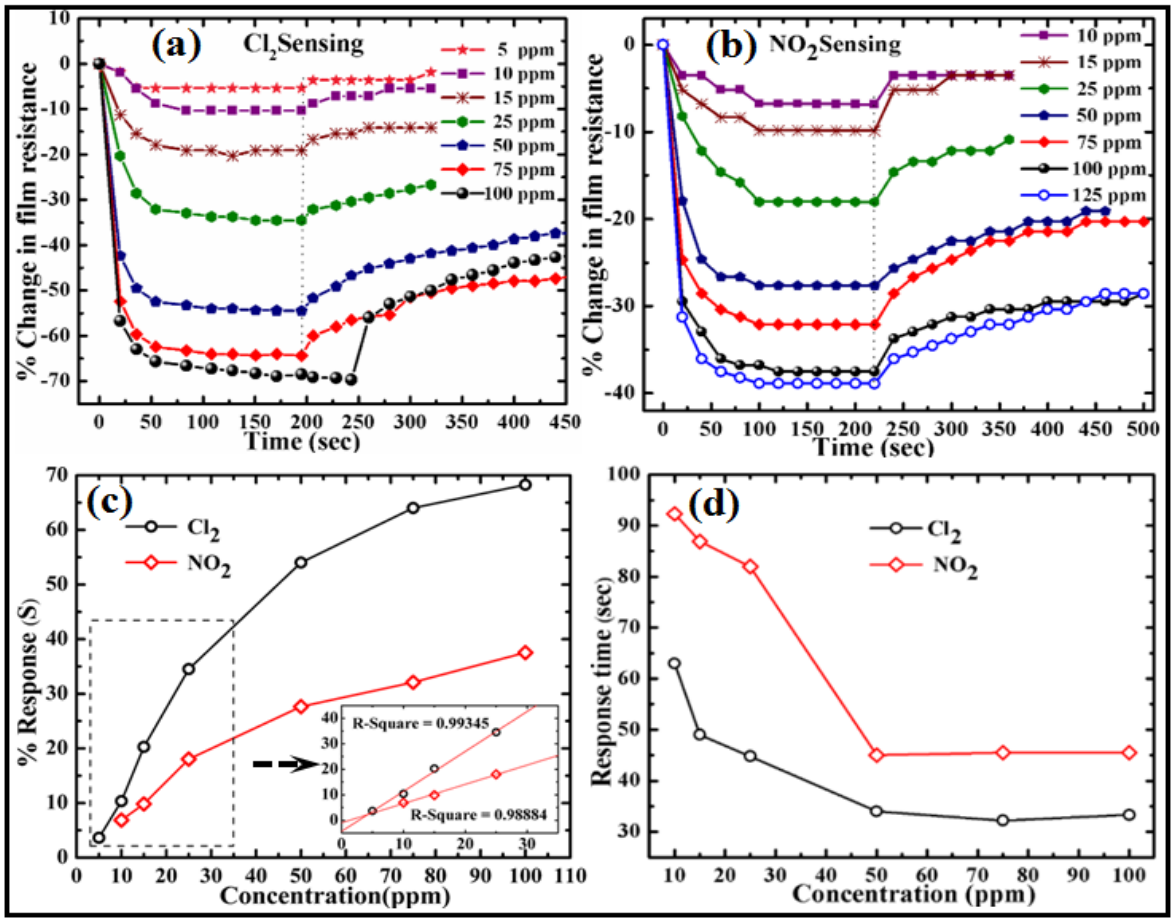

Figure 4.10: (a) and **(b)** are % change in the rGO thin film resistance versus time upon exposure to different concentrations of Cl_2 and NO_2 gases, respectively. **(c)** % Response of the rGO thin film versus Cl_2 and NO_2 concentrations. The inset shows the magnified image of the linear regions and red lines in the inset are linear fitting of the experimental data. **(d)** Response time of Cl_2 and NO_2 gases versus different concentrations.

We define the % response (S) of the rGO film sensor as the magnitude of the % change in the film resistance i.e.

$$\%\, response\ (S) = |(R_g - R_a)/R_a| \times 100 = |\Delta R / R_a| \qquad (4.3)$$

Fig. 4.10 (c) shows the % response (S) of the sensor versus Cl_2 and NO_2 concentrations. It can be seen that the value of % response (S) for Cl_2 is higher than that of NO_2, which implies that this sensor is more sensitive to Cl_2 than NO_2. It is also observed that % response (S) increases almost linearly with increasing the concentrations of both the test gases up to 30 ppm. Above 30 ppm, % response (S) increases slowly with the increase in the concentrations of the test gases, indicating that the sensor becomes more or less saturated. The probable reason behind this is the possibility of the reduced interaction between electrons and the chemisorbed Cl_2, NO_2 molecules on the rGO thin film surface at higher concentrations. Moreover, inset in Fig. 4.10 (c) shows a linear fit to the lower values of the concentrations of the test gases. The linear fit data for Cl_2 has a slope 1.569, while that for NO_2 is 0.989. This shows that the sensor shows better linearity for Cl_2 than NO_2 for future device integration. Fig. 4.10 (d) shows that the response times (defined as the time required to reach 90% of the saturation value) of the sensor when exposed to different concentrations of NO_2 and Cl_2. We observed that the response time of the sensor decreases with an increase in gas concentration for both the cases. It is so because at lower concentrations Cl_2 and NO_2 molecules take longer time to equilibrate on the rGO film

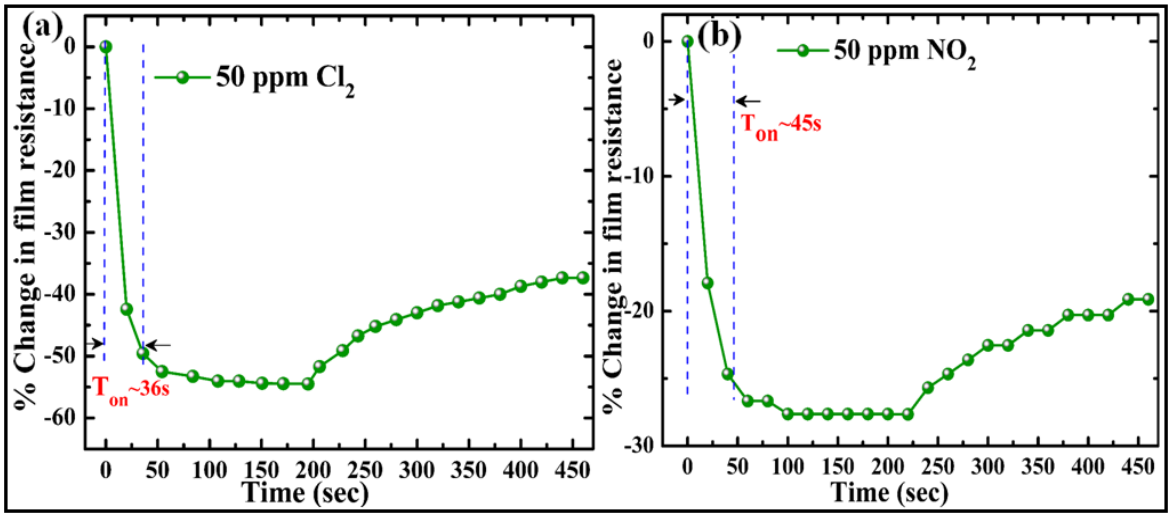

Figure 4.11: Response time curves of rGO thin films for fixed 50 ppm concentration of (a) Cl_2 gas (b) NO_2 gas.

surface. Sensor show lower response time for Cl_2 than NO_2 for the same ppm values of the concentration, for example for 50 ppm Cl_2 and NO_2, the response times are ~36s and ~45s, respectively (Fig. 4.11). It has to be taken into account that before starting the measurement for every next NO_2 and Cl_2 concentration the sensor should almost recover its initial resistance value (baseline) after degassing the sensing chamber. At room temperature, the recovery time (not shown here) of this sensor has been found much larger than the response time, which is attributed to the strong chemisorption of these test gases on the surface of rGO film and the strong chemisorptions may take place due to molecular interactions of these gases with higher-energy binding sites, such as structural defects, and residual oxygen functional groups [9]. Recovery time can be improved by some external means such as UV light exposure or thermal treatment as reported previously for graphene based sensors but these techniques have their own demerits [21, 64-66]. So, further work is going on to improve the recovery rate of these rGO based gas sensors in order to prevent the obstacle for their commertial application.

4.3.9 Study of antibacterial activity of GO and rGO thin films

We have investigated the bacterial toxicity of GO and rGO thin films for both Gram +ve (B. cereus) and Gram -ve (E. coli) models of bacteria. Both films and test cultures were incubated on LB agar plates at 37°C. Inhibition of bacterial growth has appeared as zone of clearance after 24 hours incubation. Along with GO and rGO films an uncoated quartz substrate was also kept as negative control. A brief description of experimental procedure is given in section 2.2.3 of chapter-2. Fig. 4.12 (a-b) show the antimicrobial activity of GO and rGO thin films on the quartz substrates. These figures clearly show that the rGO film inhibits the growth of both the bacteria, Bacillus cereus (B. cereus) and E. coli, effectively while GO film has comparatively mild antibacterial activity and no growth inhibition under bare quartz sheet. It can be concluded that rGO film possesses better antibacterial activity than GO film. The antibacterial activity of graphene based material is synergistic effect of oxidative and membrane stress [24], which depends on size, dispersibility and oxidation capacity of material in dispersion. However, for the material in while coating size and dispersibility are limited the antibacterial activity solely depends on oxidative effect. rGO shows much stronger oxidation effect than GO [67], which explains stronger antibacterial activity of rGO coating than GO. Furthermore, the stronger antibacterial activity is evidenced and clearly visualized by scanning electron microscopic analysis as shown in Fig. 4.12(c-f). Fig. 4.12(c) and (d) are the FESEM images of B.cereus

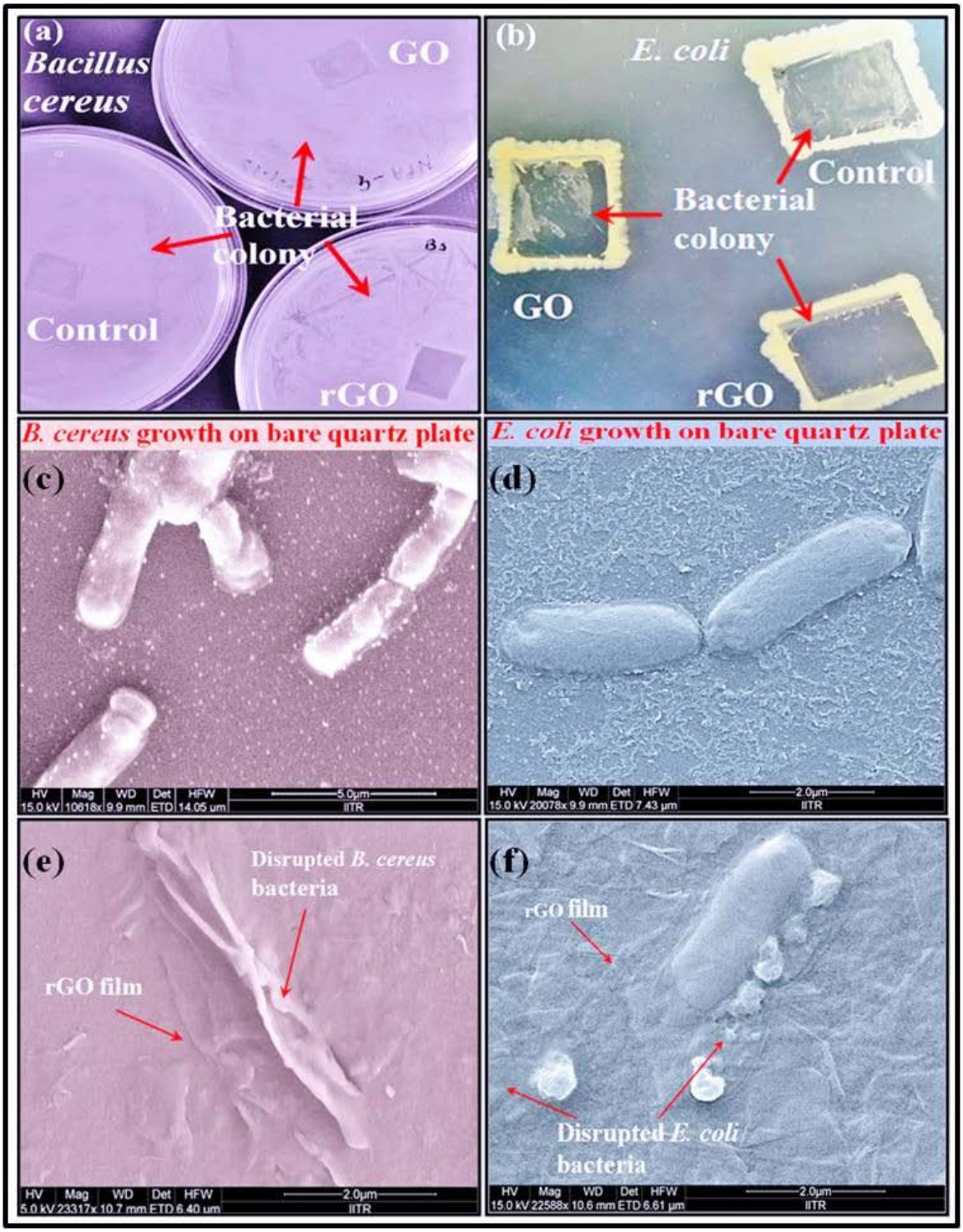

Figure 4.12: (a) and **(b)** are the digital photographs of bacterial colonies growth of Gram +ve bacteria (B. cereus) and Gram -ve bacteria (E. coli) on GO, rGO thin films and bare quartz substrate after incubation at 37°C for 24 hrs. Images **(c)** and **(d)** are the FESEM images of B. cereus and E. coli bacteria on bare quartz substrates, respectively, while FESEM Images **(e)** and **(f)**, respectively, show the disruption of B. cereus and E. coli bacteria via rGO film.

and E. coli bacteria on bare quartz substrates, respectively. Fig. 4.12(e-f) show the antibacterial activity of rGO film on B. cereus and E. coli bacteria respectively. These micrographs clearly demonstrate that the cells of both the bacteria have been disrupted effectively (as marked by arrows in Fig. 4.12(e) and (f)) by the rGO film which implies that rGO film possesses good antibacterial activity.

4.4 CONCLUSIONS

In this chapter, we synthesized GO thin films (~15 nm) on quartz substrates via spin coating and hydrazine vapor was used to reduce these films into rGO. Here we design a sensing set-up and nichrome heater to investigate the electrical and gas (NO_2, Cl_2) sensing properties of rGO thin films. We also investigated the optical and antibacterial properties of GO and rGO thin films. The main highlights of the work discussed here are given below:

1. XRD, TEM, XPS, Raman spectroscopy and PL studies confirm the formation of good quality luminescent GO and rGO thin films.
2. Such synthesized rGO thin films exhibit ohmic nature in four probe measurements and their resistance decreases with increasing temperature. Thus rGO thin film behaves like semi-metal with good electrical conductivity ~104 Sm^{-1} at room temperature.
3. rGO thin film exhibits good gas sensing properties for various concentrations of Cl_2 and NO_2 gases at room temperature and the percentage response for NO_2 and Cl_2 gases at fixed 50 ppm (parts per million) concentrations are found to be 27% and 54% respectively. This suggests that rGO sensor is more senestive to Cl_2 than NO_2.
4. Antibacterial activity of as-synthesized GO and rGO thin films were investigated against both Gram +ve (B. cereus) and Gram -ve (E. coli) models of bacteria and we observed that rGO thin film exhibits better bacterial toxicity than GO.

In summary, good quality GO and rGO thin films were synthesized via spin coating and hydrazine vapor reduction. We investigated the optical and antibacterial properties of GO and rGO thin films. We also analyzed the temperature dependent electrical and room temperature gas (NO_2, Cl_2) sensing properties of rGO thin film. The collective fast gas sensing response and good antibacterial property of rGO thin film suggest that this material could be an ultimate choice for next generation smart, portable two dimensional (2D) gas sensors as well as in various biomedical applications.

REFERENCES

1. A. K. Geim, “Graphene: Status and prospects”, Science, **324**, 1530 (2009).
2. A. K. Geim, K. S. Novselov, “The rise of graphene”, Nat. Mater., **6**, 183 (2007).
3. Y. Zhang, T.-T. Tang, C. Girit, Z. Hao, M. C. Martin, A. Zettl, M. F. Crommie, Y. R. Shen, F. Wang, “Direct observation of a widely tunable bandgap in bilayer graphene”, Nature, **459**, 820 (2009).
4. E. V. Castro, K. S. Novoselov, S. V. Morozov, N. M. R. Peres, J. M. B. Lopes dos Santos, Johan Nilsson, F. Guinea, A. K. Geim, A. H. Castro Neto, “Biased bilayer graphene: semiconductor with a gap tunable by the electric field effect”, Phys. Rev. Lett., **99**, 216802 (2007).
5. E. J. Yoo, J. Kim, E. Hosono, H. Zhou, T. Kudo, I. Honma, “Large reversible Li storage of graphene nanosheet families for use in rechargeable lithium ion batteries”, Nano Lett., **8**(8), 2277 (2008).
6. S. R. C. Vivekchand, C. S. Rout, K. S. Subrahmanyam, A. Govindaraj, C. N. R. Rao, “Graphene-based electrochemical supercapacitors”, J. Chem. Sci., **120**, 9 (2008).
7. X. Wang, L. Zhi, K. Mullen, “Transparent, conductive graphene electrodes for dye-sensitized solar cells”, Nano Lett., **8**, 323 (2008).
8. F. Schedin, A. K. Geim, S. V. Morozov, E. W. Hill, P. Blake, M. I. Katsnelson, K. S. Novoselov, “Detection of individual gas molecules adsorbed on graphene”, Nat. Mater., **6**, 652 (2007).
9. J. T. Robinson, F. K. Perkins, E. S. Snow, Z. Wei, P. E. Sheehan, “Reduced graphene oxide molecular sensors”, Nano Lett., **8**, 3137 (2008).
10. N. Hu, Y. Wang, J. Chai, R. Gao, Z. Yang, E. S.-W. Kong, Y. Zhang, “Gas sensor based on p-phenylenediamine reduced graphene oxide”, Sens. Actuators B, **163**, 107 (2012).
11. J. I. Paredes, S. Villar-Rodil, A. Martınez-Alonso, J. M. D. Tascon, “Graphene oxide dispersions in organic solvents”, Langmuir, **24**, 10560 (2008).
12. C. G-Navarro, R. T. Weitz, A. M. Bittner, M. Scolari, A. Mews, M. Burghard, K. Kern, “Electronic transport properties of individual chemically reduced graphene oxide sheets”, Nano Lett., **7**, 3499 (2007).

13. R. Ghosh, A. Midya, S. Santra, S. K Ray, P. K. Guha, "Chemically reduced graphene oxide for ammonia detection at room temperature", ACS Appl. Mater. Interfaces, **5**, 7599 (2013).
14. J. D. Fowler, M. J. Allen, V. C. Tung, Y. Yang, R. B. Kaner, B. H. Weiller, "Practical chemical sensors from chemically derived graphene", ACS Nano, **3**, 301 (2009).
15. W. Yuan, A. Liu, L. Huang, C. Li, G. Shi, "High-performance NO_2 sensors based on chemically modified graphene", Adv. Mater., **25**, 766 (2013).
16. L. Zhang, C. Li, A. Liu, G. Shi, "Electrosynthesis of graphene oxide/polypyrene composite films and their applications for sensing organic vapors", J. Mater. Chem., **22**, 8438 (2012).
17. R. Zou, G. He, K. Xu, Q. Liu, Z. Zhang, J. Hu, "ZnO nanorods on reduced graphene sheets with excellent field emission, gas sensor and photocatalytic properties", J. Mater. Chem., **A 1**, 8445 (2013).
18. Q. Lin, Y. Li, M. Yang, "Tin oxide/graphene composite fabricated via a hydrothermal method for gas sensors working at room temperature", Sens. and Actuators B, **173**, 139 (2012).
19. Y. Dan, Y. Lu, N. J. Kybert, Z. Luo, A. T. C. Johnson, "Intrinsic response of graphene vapor sensors", Nano Lett., **9**, 1472 (2009).
20. G. Lu, S. Park, K. Yu, R. S. Ruoff, L. E. Ocola, D. Rosenmann, J. Chen, "Toward practical gas sensing with highly reduced graphene oxide: A new signal processing method to circumvent run-to-run and device-to-device variations", ACS Nano, **5**, 1154 (2011).
21. W. Yuan, G. Shi, "Graphene-based gas sensors", J. Mater. Chem., **A 1**, 10078 (2013).
22. R. B. Evans, "Chlorine: State of the art", Lung, **183**, 151 (2005).
23. C. Winder, "The toxicology of Chlorine", Environmental Res. **85**, 105 (2001).
24. L. Talazac, J. Brunet, V. Battut, J. P. Blanc, A. Pauly, J. P. Germain, S. Pellier, C. Soulier, "Air quality evaluation by monolithic InP-based resistive sensors", Sen. Actuators B, **76**, 258 (2001) .
25. J. Yuan, H. Gao, C. B. Ching, "Comparative protein profile of human hepatoma HepG2 cells treated with graphene and single-walled carbon nanotubes: An iTRAQ-coupled 2D LC-MS/MS proteome analysis", Toxicology Letters, **207**, 213 (2011).

26. W. Hu, C. Peng, M. Lv, X. Li, Y. Zhang, N. Chen, C. Fan, Q. Huang, "Protein corona-mediated mitigation of cytotoxicity of graphene oxide", ACS Nano, **5**, 3693 (2011).
27. O. Akhavan, E. Ghaderi, "Toxicity of graphene and graphene oxide nanowalls against bacteria", ACS Nano, **4**, 5731 (2010).
28. D. C. Marcano, D. V. Kosynkin, J. M. Berlin, A. Sinitskii, Z. Sun, A. Slesarev, L. B. Alemany, W. Lu, J. M. Tour, "Improved synthesis of graphene oxide", ACS Nano, **4**, 4806 (2010).
29. S. Stankovich, D. A. Dikin, R. D. Piner, K. A. Kohlhaas, A. Kleinhammes, Y. Jia, Y. Wu, S. T. Nguyen, R. S. Ruoff, "Synthesis of graphene-based nanosheets via chemical reduction of exfoliated graphite oxide", Carbon, **45**, 1558 (2007).
30. J. Chattopadhyay, A. Mukherjee, C. E. Hamilton, J. H. Kang, S. Chakraborty, W. Guo, K. F. Kelly, A. R. Barron, W. E. Billups, "Graphite epoxide" J. Am. Chem. Soc., **130**, 5414 (2008).
31. A. B. Bourlinos, D. Gournis, D. Petridis, T. Szabo, A. Szeri, I. Dekany, "Graphite oxide: Chemical reduction to graphite and surface modification with primary aliphatic amines and amino acids", Langmuir, **19**, 6050 (2003).
32. Y. Chen, X. Zhang, P. Yu, Y. Ma, "Stable dispersions of graphene and highly conducting graphene films: A new approach to creating colloids of graphene monolayers", Chem. Commun., 4527 (2009).
33. R. J. Waltman, J. Pacansky, J. CW. Bates, "X-ray photoelectron spectroscopic studies on organic photoconductors-evaluation of atomic charges on chlorodiane blue and p-(diethylamino) benzaldehyde diphenylhydrazone", Chem. Mater., **5**, 1799 (1993).
34. Y. Zhou, Q. Bao, L. A. L.Tang, Y. Zhong, K. P. Loh, "Hydrothermal dehydration for the "green" reduction of exfoliated graphene oxide to graphene and demon stration of tunable optical limiting properties", Chem. Mater., **21**, 2950 (2009).
35. C. N. R. Rao, A. K. Sood, K. S. Subrahmanyam, A. Govindaraj, "Graphene: The new two-dimensional nanomaterials", Angew. Chem. Int. Ed., **48**, 7752 (2009).
36. M. A. Pimenta, G. Dresselhaus, M. S. Dresselhaus, L. G. Cancado, Z. A. Jorio, R. Saito, "Studying disorder in graphite-based systems by raman spectroscopy", Phys. Chem. Chem. Phys., **9**, 1276 (2007).

37. A. C. Ferrari, J. C. Meyer, V. Scardaci, C. Casiraghi, M. Lazzeri, F. Mauri, S. Piscanec, D. Jiang, K. S. Novoselov, S. Roth, A. K. Geim, "Raman spectrum of graphene and graphene layers", Phys. Rev. Lett., **97**,187401 (2006).
38. T. N. Narayanan, Z. Liu, P. R. Lakshmy, W. Gao, Y. Nagaoka, D. S. Kumar, J. Lou, R. Vajtai, P. M. Ajayan, "Synthesis of reduced graphene oxide-Fe_3O_4 multifunctio nal freestanding membranes and their temperature dependent electronic transport properties", Carbon, **50**, 1338 (2012).
39. B. Jayasena, S. Subbiah, "A novel mechanical cleavage method for synthesizing few-layer graphenes", Nanoscale Res. Lett., **6**:95, (2011).
40. L. G. Cançado, K. Takai, T. Enoki, M. Endo, Y. A. Kim, H. Mizusaki, A. Jorio, L. N. Coelho, R. M. Paniago, M. A. Pimenta, "General equation for the determination of the crystallite size L-a of nanographite by raman spectroscopy", Appl. Phys. Lett., **88**, 163106 (2006).
41. X. Gao, J. Jang, H. Nagase, "Hydrazine and thermal reduction of graphene oxide: Reaction mechanisms, product structures, and reaction design", J. Phys. Chem. C, **114**, 832 (2010).
42. G. Eda, M. Chhowalla, "Chemically derived graphene oxide: Towards large-area thin-film electronics and optoelectronics", Adv. Mater., **22**, 2392 (2010).
43. X. Sun, Z. Liu, K. Welsher, J. T. Robinson, A. Goodwin, S. Zaric, H. Dai, "Nano-graphene oxide for cellular imaging and drug delivery", Nano Res., **1**, 203 (2008).
44. Z. Liu, J. T. Robinson, X. Sun, H. Dai, "PEGylated nanographene oxide for deliv ery of water-insoluble cancer drugs", J. Am. Chem. Soc., **130**, 10876 (2008).
45. L. Zhengtang, M. V. Patrick, J. M. Eugene, A. T. C. Johnson, M. K. James, "Photoluminescence and band gap modulation in graphene oxide", Appl. Phys. Lett., **94**, 111909 (2009).
46. J. Robertson, E. P. O'Reilly, "Electronic and atomic structure of amorphous carbon", Phys. Rev. B, **35**, 2946 (1987).
47. C. Mathioudakis, G. Kopidakis, P. C. Kelires, P. Patsalas, M. Gioti, S. Logothetidis, "Electronic and optical properties of a-C from tight-binding molecular dynamics simulations", Thin Solid Films, **482**, 151 (2005).
48. C. W. Chen, J. Robertson, "Nature of disorder and localization in amorphous carb-on", J. Non-Cryst. Solids, **227**, 602 (1998).
49. J. Wagner, P. Lautenschlager, "Hard amorphous-carbon studied by ellipsometry and photoluminescence", J. Appl. Phys, **59**, 2044 (1986).

50. F. Demichelis, S. Schreiter, A. Tagliaferro, “Photoluimecence in a-C:H films”, Phys. Rev. B, **51**, 2143 (1995).
51. S. R. P. Silva, J. Robertson, Rusli, G. A. J. Amaratunga, J. Schwan, “Structure and luminescence properties of an amorphous hydrogenated carbon”, J. Philos. Mag. B, **74**, 369 (1996).
52. M. Koos, M. Fule, M. Veres, S. Toth, I. Pocsik, “Multi-band structure of amorphous carbon luminescence”, Diamond Relat. Mater., **11**, 1115 (2002).
53. R. J. Robertson, G. A. J. Amaratunga, “Photoluminescence behavior of hydrogenat--ed amorphous carbon”, J. Appl. Phys., **80**, 2998 (1996).
54. T. Heitz, C. Godet, J. G. Bouree, B. Drevillon, J. P. Conde, “Radiative and nonradiative recombination in polymerlike alpha-C : H films”, Phys. Rev. B, **60**, 6045 (1999).
55. J. Robertson, “Recombination and photoluminescence mechanism in hydrogenated amorphous”, Phys. Rev. B, **53**, 16302 (1996).
56. J. L. Bredas, R. Silbey, D. S. Boudreaux, R. R. Chance, “Chain-length dependence of electronic and electrochemical properties of conjugated system: polyphenelene, polythiophene, and polypyrole”, J. Am. Chem. Soc., **105**, 6555 (1983).
57. G. Eda, Y.–Y. Lin, C. Mattevi, H. Yamaguchi, H.-A. Chen, I.–S. Chen, C.-W. Chen, M. Chhowalla, “Blue photoluminescence from chemically derived graphene oxide”, Adv. Mater., **22**, 505 (2010).
58. G. Eda, C. Mattevi, H. Yamaguchi, H. Kim, M. Chhowalla, “Insulator to semimetal transition in graphene oxide”, J. Phys. Chem. C, **113**, 15768 (2009).
59. O. Akhavan, E. Ghaderi, “Escherichia coil bacteria reduce graphene oxide to bactericidal graphene in a self-limiting manner”, Carbon, **50**, 1853 (2012).
60. Q. Shao, G. Liu, D. Teweldebrhan, A. A. Balandin, “High-temperature quenching of electrical resistance in graphene interconnects”, Appl. Phys. Lett., **92**, 202108 (2008).
61. K.A. Ritter, J. W. Lyding, “Characterization of nanometer-sized, mechanically exfoliated graphene on the H-passivated Si(100) surface using scanning tunneling microscopy”, Nanotechnology, **19**, 015704 (2008).
62. C. N. R. Rao, K. S. Subrahmanyam, H. S. S. R. Matte, B. Abdulhakeem, A. Govindaraj, B. Das, P. Kumar, A. Ghosh, D. J. Late, “A study of the synthetic methods and properties of graphenes”, Sci. Technol. Adv. Mater., **11**, 054502 (2010).

63. S. Gilje, S. Han, M. Wang, K. L. Wang, R. B. Kaner, “A chemical route to graphene for device applications”, Nano Lett., **7**, 3394 (2007).
64. II-S. Kang, H.-M. So, G.-S. Bang, J.-H. Kwak, J.-O. Lee, C. W. Ahn, “Recovery improvement of graphene-based gas sensors functionalized with nanoscale heterojunctions”, Appl. Phys. Lett., **101**, 123504 (2012).
65. F. Yavari, Z. Chen, A. V. Thomas, W. Ren, H.-M. Cheng, N. Koratkar, “High sensitivity gas detection using a macroscopic three-dimensional graphene foam network”, Sci. Rep., **166**, (2011).
66. G. Lu, L. E. Ocola, J. Chen, “Gas detection using low-temperature reduced graphene oxide sheets”, Appl. Phys. Lett., **94**, 083111 (2009).
67. S. Liu, T. H. Zeng, M. Hofmann, E. Burcombe, J. Wei, R. Jiang, J. Kong, Y. Chen, “Antibacterial activity of graphite, graphite oxide, graphene oxide, and reduced graphene oxide: membrane and oxidative stress”, ACS Nano, **5**, 6971(2011).

SYNTHESIS OF rGO-ZnO NANOCOMPOSITE AND ITS GAS SENSING BEHAVIOR TOWARDS NO_2

5.1 INTRODUCTION

In chapter - 4 we discussed about the electrical and room temperature gas sensing properties reduced graphene oxide (rGO) thin films. In this chapter we have studied the electrical and gas sensing properties of rGO powder and rGO-ZnO nanocomposite. In the previous chapters we have pointed that graphene exhibits unique electronic properties like high charge-carrier mobility (200,000 $cm^2 V^{-1} s^{-1}$), tunable band gap (from 0-2.5 eV) [3], ballistic transport [4], quantum hall effect at room temperature [5] and a very high theoretical specific surface area (2630 m^2g^{-1}), i.e. highest surface area to volume ratio among known layered materials [6]. These properties collectively make graphene a potential material for gas sensing applications. Furthermore, with high surface area to volume ratio graphene offers a large exposed area for gas molecules and its high conductivity and metallic transport properties ($v_F = 10^6$ m/s) lead to very little Johnson's noise [7].

Graphene oxide (GO), synthesized by the chemical oxidation of graphite, is intrinsically hydrophilic and can be dispersed in various solvents just by sonication [8]. This dispersion of GO is widely accepted as the precursor material for large scale synthesis of reduced graphene oxide (rGO) films, rGO powder and various rGO based composite materials at relatively low cost [9]. To date various pristine rGO thin film based gas sensors have been fabricated using various techniques including expensive nano-lithography. But pristine rGO sensor exhibits poor sensing response and very long recovery time up to ~2 hrs. In order to improve recovery time, sensors are either heat treated or exposed to UV radiation [10]. Moreover, the nano-lithographic technique which is used to fabricate electrodes or patterns makes sample surface contaminated that greatly influences the charge transport and hence sensing performance of the devices [11, 12]. However, as sensing is a surface phenomena, decoration of graphene surface by metal nanoparticles (NP) or metal oxide nanostructures (NS) will affect the sensing performance

of the graphene based sensing devices. Several such graphene nanohybrids with improved sensing performance have been reported. These studies reveal that diameters, concentrations, distribution of NP/NS and temperature are the parameters which greatly influence the sensing performances of the gas sensors [13, 14].

Here, we synthesized rGO and reduced graphene oxide-zinc oxide nanocomposite (ZrGO) powder samples using hydrolysis method in which 85% hydrazine hydrate was utilized as the reducing agent. The detailed morphological studies have been probed through various microscopic techniques. Electrical and gas sensing properties of rGO and ZrGO powder samples have been investigated in an indigenously built sensing chamber using two terminal set-up with heating coil. We choose NO_2 as the test gas for our sensor because it is very toxic to environment as well as living beings and main air pollutant in the cities [15]. In the previous chapter we have discussed the importance of NO_2 detection and major sources of NO_2 in the environment. We have observed that ZrGO possesses better electrical and gas sensing properties than rGO sample. Sensing performance of ZrGO against different concentrations of NO_2 gas at room temperature as well as at higher temperatures has been investigated. We conclude that this material and sensing technique, which we have used here, can be utilized to develop a smart portable inexpensive NO_2 gas sensor with fast response and good recovery time.

5.2 EXPERIMENTAL WORK

The starting material, GO, was synthesized using “Improved Synthesis of Graphene Oxide” method reported by J. M. Tour et al. as described in section 2.2.2.1 of chapter-2 [16]. rGO and rGO-ZnO nanocomposite (ZrGO) were synthesized using hydrolysis method as described in section 2.2.4.1 of chapter-2. In order to find electrical and gas sensing properties of rGO and ZrGO powder samples a two terminal device was designed which consists of a nichrome coil heater, a thermocouple and two Pt wires of diameter 0.3 mm tightly wrapped about 1mm apart on a small quartz tube. A digital image of the designed sensing device, a schematic diagram of complete sensing set-up and the procedure of measurement are given in section 2.2.4.2 of chapter-2. Keithley-617 programmable electrometer was used to monitor the variations in electric current. For humidity measurements two probe arrangements was used to monitor the variation in electrical resistance with different RH% value at constant temperature and a hygrometer was used to monitor the changes of the humidity. The system possesses two channels. From one channel humid air is allowed to enter into other is used to take out the humid air.

The structural and morphological studies of the as-synthesized GO, rGO and ZrGO composite powder samples were performed using XRD, FESEM, TEM and HRTEM. The stability, quality and extend of graphitization of all the powder samples were examined via TGA, FTIR, XPS and Raman spectroscopy.

5.3 RESULTS AND DISCUSSION

5.3.1 X-ray diffraction studies

Fig. 5.1(a) shows the aqueous dispersions of GO, rGO and ZrGO samples. Fig. 5.1(b) represents the X-ray powder diffraction (XRD) patterns of GO, rGO and ZrGO powder samples. The XRD pattern of GO exhibits a characteristic intense peak (001) at 2θ = 10.442° with a layer-to-layer d spacing of 0.8465 nm. After reduction of GO to rGO with

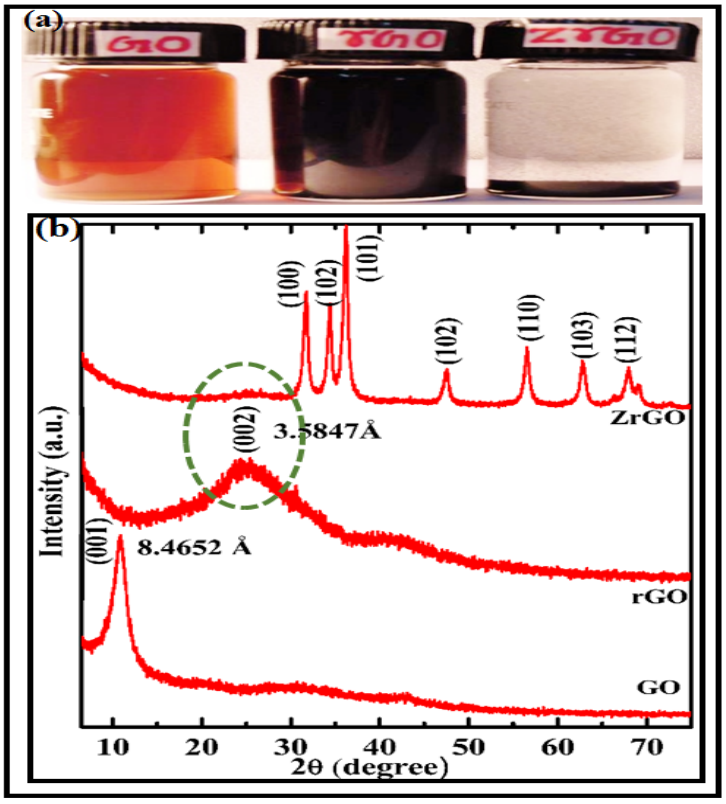

Figure 5.1: (a) Aqueous dispersions of GO, rGO and ZrGO samples. **(b)** X-ray diffraction (XRD) patterns of GO, rGO and ZrGO samples.

hydrazine hydrate, the 10.442° (2θ) peak disappears and a broad peak (002) with a d-spacing of 0.3585 nm appears, starting from 2θ value 13.5° to 35°. The higher d-spacing

value of GO sample suggests presence of single-molecule-thick layer of water molecules attached via intermolecular hydrogen bonding as they intercalate between the sheets, along with other oxygen containing chemical groups like epoxy , hydroxyl, carbonyl and carboxyl, bound covalently to sp^3 hybridized carbon atoms which get pushed out of plane as a result. This results in a more opened up structure. Upon reduction with hydrazine hydrate these intercalates are dispensed off to cause a reduction in the d-spacing [17-20]. Moreover, the broad peak in XRD pattern of rGO suggests that after reduction process the large scale long ranged ordering in the GO sheets have been disturbed to a great extent and there is a poor ordering of the graphene sheets along their stacking direction**.** The XRD pattern of ZrGO powder sample clearly demonstrates the formation of ZnO nanoparticles through the characteristic sharp peaks that are representatives of (100), (002), (101), (102), (110), (103) and (112) planes of wurtzite structure of ZnO. A small broad peak at $2\theta \sim 25°$ encircled by dotted lines in Fig. 5.1(b) verifies the presence of rGO in ZrGO nanocomposite.

5.3.2 Thermogravimetric analysis (TGA)

Fig. 5.2 demonstrates the thermogravimetric analysis (TGA) of the three samples. TGA measurements of the samples GO, rGO and ZrGO were performed to investigate their thermal stability. For TGA, the samples were heated under N_2 flow (200 ml/min) from room tempearture to 600°C with heating rate 10 °C/min. GO seems thermally unstable as it has started to lose weight with increase in temperature. GO sample looses its ~ 30% mass below 200°C due to evaporation of absorbed water. However maximum weight loss occurs at ~ 200°C which is attributed to the decomposition of the oxygen containing functional groups in the GO layers and the formation of CO, CO_2 and steam. Since in TGA, heating rate of the sample (10°C/ min) is quite high therefore, thermal decomposition of GO is accompanied by an energetically release of gas, resulting in a rapid thermal expansion of the material. This result has been verified by both a large volume expansion as well as greater weight (%) loss during a more rapid heating regime [19]. The rGO looses ~ 13 % mass at around 100°C which can be attributed to the water loss in the form of steam. The other downward trends above 200°C signify the removal of left over labile oxygen containning functional groups [21, 22]. The rGO is found much more stable than GO due to the removal of a larger number of oxygen containing functional groups by the reduction process. rGO retains its ~ 64% weight till 600°C and the % weight loss above 600°C is attributed to the degradation of the carbon skeleton. The

ZrGO nanocomposite is even more stable and shows much less weight loss than rGO. Thus it can be safely concluded that addition of ZnO nanoparticles increases the thermal stability of graphene Oxide (GO).

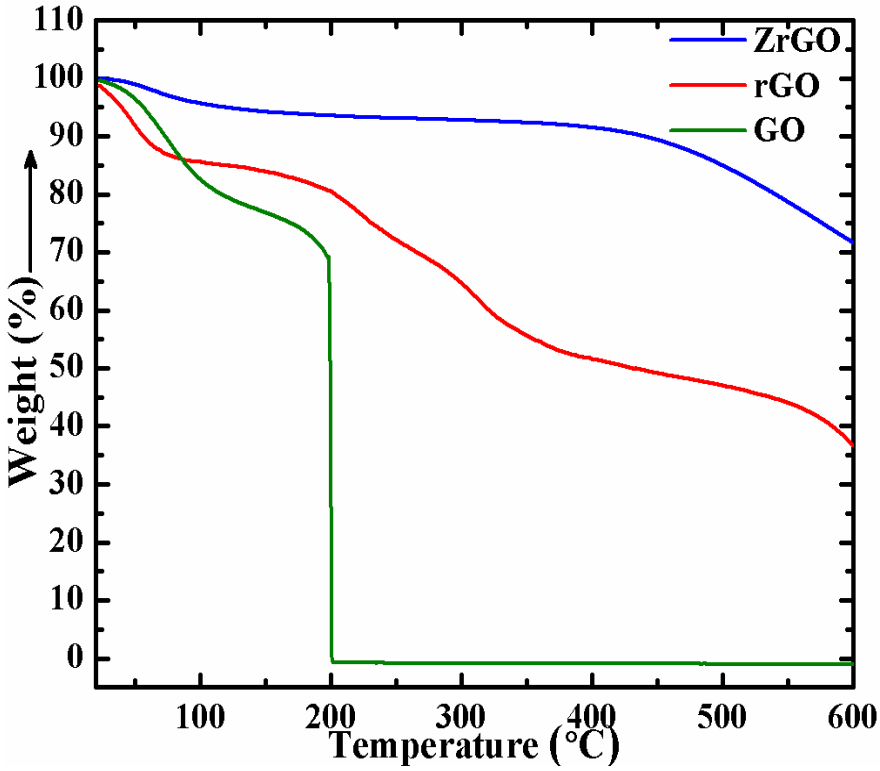

Figure 5.2: TGA profiles of GO, rGO and ZrGO samples.

5.3.3 Study of Fourier transform infrared (FTIR) spectroscopy

Fig. 5.3 demonstrates the FTIR transmittance spectra (KBr) of GO, rGO and the ZrGO powder samples. FTIR spectrum of GO sample illustrates a wide band at 3450 cm^{-1}, attributed to the O-H band stretching of the intercalated water that got trapped between the pristine graphite sheets upon oxidation, and troughs at 1055 cm^{-1}, 1740 cm^{-1}, 1625 cm^{-1} and 1232 cm^{-1} correspond to the epoxy or alkoxy (C-O), carboxylic or carbonyl (C=O), skeletal vibrations of unreacted pristine graphite C=C and C–OH stretching peaks, respectively [23]. In the FTIR spectrum of rGO, C=O and C–OH peaks have almost disappeared while intensity of the C-O peak has decreased. This provides an evidence for the substantial reduction of GO containing oxygen moieties under the action of hydrazine hydrate. Two new peaks in the rGO spectrum at 2924 and 2865 cm^{-1}, respectively, represent asymmetric and symmetric stretching CH_2 vibrations [23]. FTIR spectrum of

ZrGO is almost similar to that of rGO except an additional peak at 471 cm^{-1} which is attributed to the stretching mode of Zn-O [24].

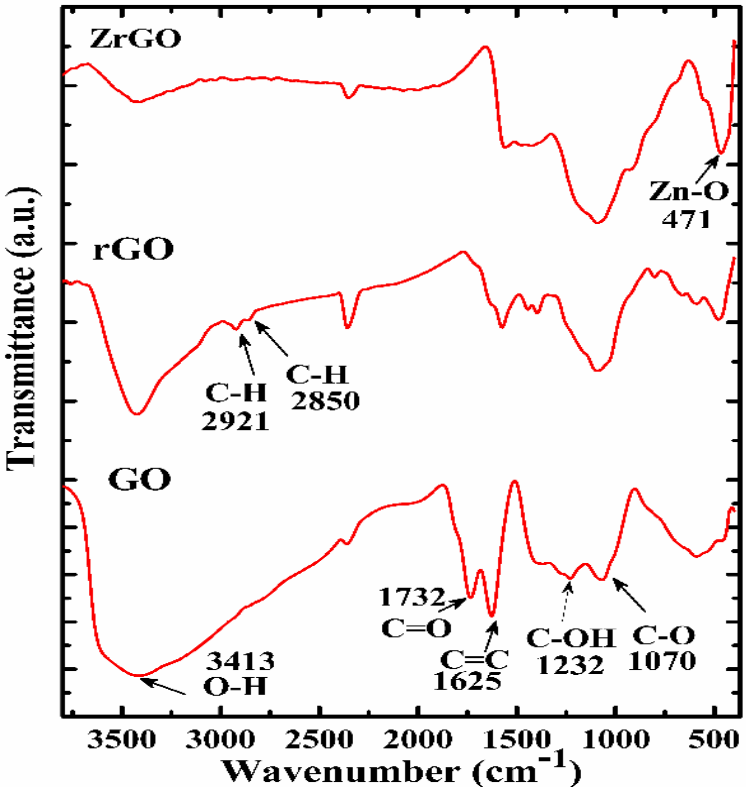

Figure 5.3: FTIR spectra of GO, rGO and ZrGO samples.

5.3.4 Study of Raman spectra

Raman spectroscopy is a standard nondestructive technique extensively used to investigate the order/disorder crystal structures of nanographitic materials such as carbon nanotubes, carbon fibers and glassy carbon etc. The Raman spectra of GO, rGO and ZrGO, as shown in Fig. 5.4, possess two most intense peaks, which correspond to the well known D and G bands. The existence of sharp D band (related to the order/disorder of the sample) reveals the defective nature of GO, rGO and ZrGO crystal structures while sharp G band is a representative of the stacking nature of the samples. The D-band originates due to the breathing mode of k-point phonons of A1g symmetry while the G-band arises due to the first order Brillouin scattering of the E2g phonons of the planar sp^2 hybridized carbon atoms [25]. The chemically synthesized GO shows a broad G band and an intense D band at 1597 cm^{-1} and 1368 cm^{-1}, respectively. In addition to the G and D bands, the Raman spectrum of ZrGO possesses a few extra peaks that are the signatures of the ZnO nanoparticles in the composite. The peak at 441 cm^{-1} is due to the non-polar Raman active

optical E2 (high) phonon mode, a characteristic branch of the wurtzite lattice structure of zinc oxide associated with the vibration of O atom [26]. The intensity of the peak is much reduced in comparison to that mentioned in literature for pure zinc oxide mainly due to ZrGO interaction. Further the peak of 585 cm^{-1} corresponds to the E1(LO) mode phonons arising from the defects such as oxygen vacancy or interstitial zinc in zinc oxides [27]. The strong intensity of the E1 (LO) mode in the Raman spectrum is attributed to the presence

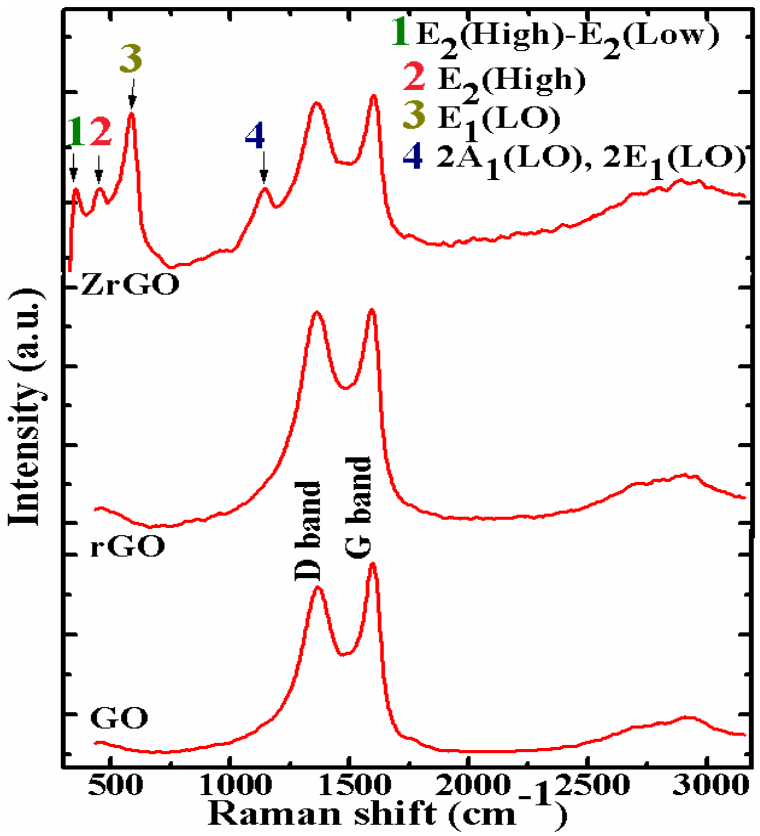

Figure 5.4: Raman spectra of GO, rGO and ZrGO samples.

of oxygen deficient ZnO nanoparticles in the composite. The peaks at 334 cm^{-1} and 1152 cm^{-1} arise due to multiple phonon scattering processes in ZrGO. Furthermore, the prominent feature at 334 cm^{-1} is assigned to the second order Raman scattering spectrum arising from zone-boundary phonons E2 (High)–E2 (Low) while the broad peak at 1152 cm^{-1} in the spectrum is contributed by 2A1 (LO) and 2E1 (LO) modes at the point of the Brillouin zone [28]. After reduction by hydrazine hydrate and decorating the graphene layer with ZnO nanoparticles a shifting in the positions as well as variation in the intensity ratio of G (I_G) and D (I_D) bands has been observed. It has been reported that the G band position in the Raman spectrum of graphene samples is highly sensitive to the impurity doping [29]. This is why the G band position in the Raman spectrum of ZrGO sample

shifts to higher frequency relative to the G band position in the Raman spectrum of pristine rGO sample. This blue shift in the G band is attributed to the electron accepting behavior of ZnO in the composite [30] and as a consequence of it ZrGO exhibits higher electric conductivity in comparison to the pristine rGO sample which will be discussed later. The intensity of D peak is directly related to the size of sp^2 hybridized in plane carbon atoms and after reduction, the increase in intensity of the D peak points to the formation of more sp^2 domains. However, change in relative intensities of the D and G peaks in the Raman spectra of GO, rGO and ZrGO helps to verify the reduction of GO [31] and a little increase in the I_D/I_G ratio reveals the decrease in size of sp^2 domains. The I_D/I_G ratio and the Raman excitation laser energy, El = 2.41 eV (λl = 514.5 nm), can be utilized to find out the in plane crystalline size (*La*) of the sample using the model given below [32]:

$$La\ (\text{nm}) = (2.4 \times 10^{-10})\ \lambda_l^4\ (I_D/I_G)^{-1} \qquad (5.1)$$

On applying the above formula, we get the *La* values of GO, rGO and ZrGO18.46 nm, 16.97 nm and 16.42, respectively as listed in Table 5.1.

Table 5.1: D band, G band positions, I_D/I_G ratio and in plane crystalline size (*La*) of the GO, rGO and ZrGO powder samples calculated using their respective Raman spectrum.

Sample	**D band position (cm^{-1})**	**G band position (cm^{-1})**	**(I_D/I_G) (Peak intensity)**	**(I_D/I_G) (Fitted Area)**	***La* (nm)**
GO	1370.01	1599.31	0.9569	0.9221	18.24
rGO	1363.98	1593.42	0.9978	0.9912	16.97
ZrGO	1363.98	1602.25	0.9989	1.0245	16.42

We observe that ZrGO sample exhibits smaller in-plane crystallite sizes (*La*) compared to the pure graphene rGO which is consistent to the previous results [29].

5.3.5 Study of X-ray Photoelectron Spectroscopy (XPS)

The chemical states of the elements present in the samples were investigated using X-ray photoelectron spectroscopy (XPS). The survey spectra of GO and rGO possess only peaks of C and O elements while that of ZrGO contains some extra addendum peaks of Zn

element as shown in Fig. 5.5(a). The survey spectrum of rGO sample shows that after reduction process the intensity of O1s peak decreases while that of C1s increases. The inte-

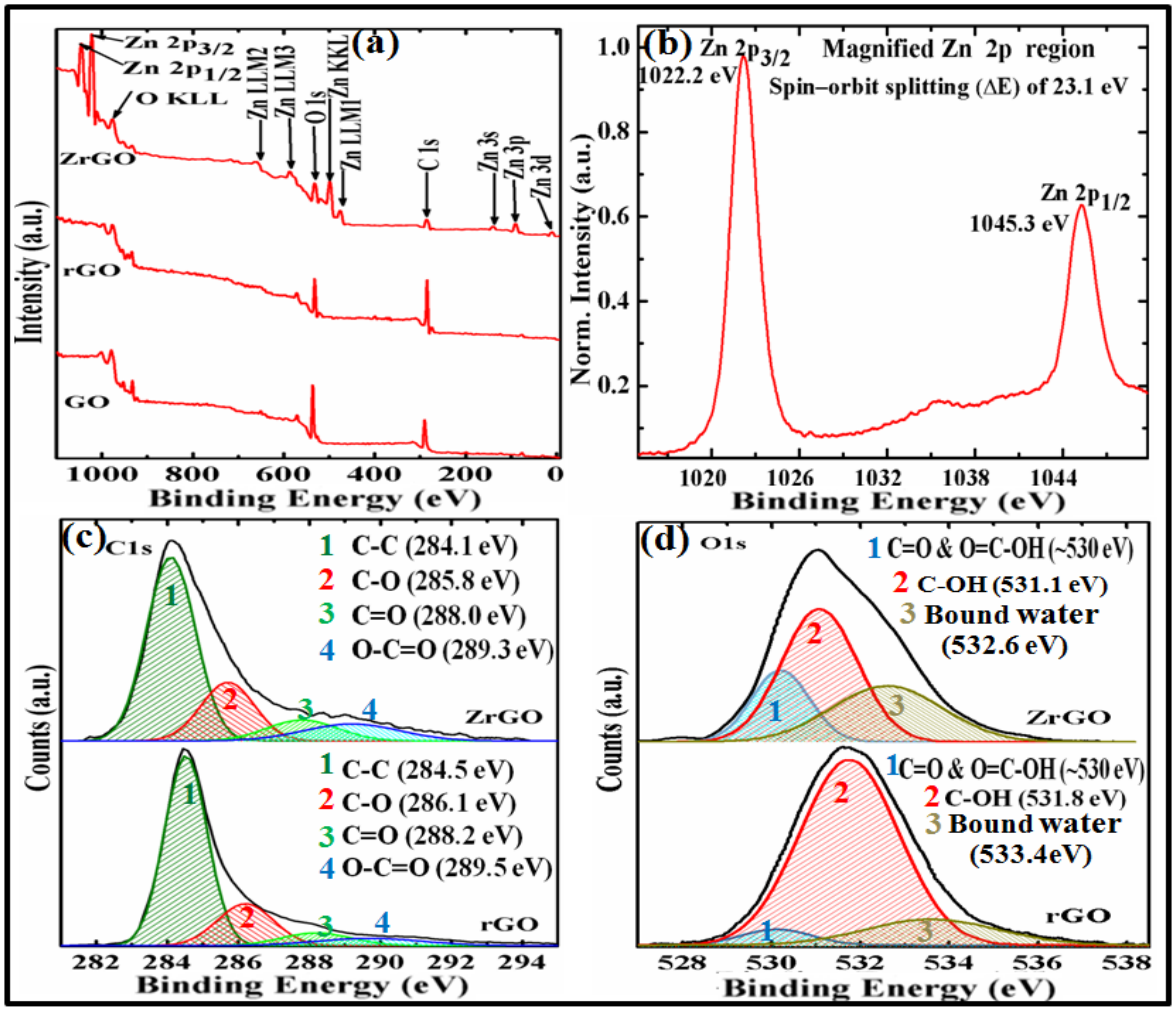

Figure 5.5: (a) XPS survey spectra of GO, rGO and ZrGO samples. **(b)** Magnified Zn2p core level XPS spectrum of ZrGO. **(c)** Deconvoluted high resolution XPS C1s core level spectra of rGO and ZrGO. **(d)** Deconvoluted high resolution XPS O1s core level spectra of rGO and ZrGO.

-nsities of O1s and C1s core-levels in the XPS spectrum of ZrGO are lower than that of rGO which imply the better reduction and the presence of lesser amount of carbon in the ZrGO in comparison to the pristine rGO sample. The possible reason for these is the partial decoration of graphene sheets by ZnO nanoparticles. In Fig. 5.5(b) the high-resolution scan of Zn 2p, shows doublet spectral lines at binding energies 1022.2 eV and 1045.3 eV which are attributed to Zn $2p_{3/2}$ and $2p_{1/2}$ electrons, respectively, with a spin-orbit splitting (ΔE) of 23.1 eV, which confirms that in ZrGO sample the chemical state of Zn^{++} remains

uninfluenced by the presence of rGO sheets. The distinct and sharp peak at binding energy 1022.2 eV is associated with the Zn species in the completely oxidized state [33]. The magnified core level XPS C1s spectrum of rGO and ZrGO samples were deconvoluted into four Gaussian peaks that correspond to following functional groups: non-oxygenated graphitic sp^2 carbon (C=C/C−C), epoxy, alkoxy (C−O), carbonyl (C=O) and carboxylates (O−C=O) as shown in Fig. 5.5(c) [19]. The C-C peak for ZrGO sample shifts a little bit towards lower binding energy in comparison to that of rGO which implies that in ZrGO sample ZnO behaves as a p-type dopant [34] and this result is consistent with Raman analysis. In Fig. 5.5(d) the O1s XPS spectrum of rGO is deconvoluted into three Gaussian peaks, which correspond to different oxygen species in the sample. The lower binding energy (~ 530 eV) peak is attributed to the doubly-bonded oxygen, i.e. C=O and O=C–OH groups, the most prominent central binding energy (531.8 eV) peak is linked up with singly-bonded oxygen containing functional group like alcohols, epoxies and ethers (C-OH) while the higher binding energy (533.4 eV) peak is attributed to the singly bonded oxygen in carboxyls, esters and the presence of bound water in the sample [35, 36]. The deconvoluted O1s XPS spectrum of ZrGO possesses similar peaks as of the O1s XPS spectrum of rGO, but these peaks shift to lower binding energy due to attachment of ZnO nanoparticles in ZrGO hybrids (Fig. 5.5(d)). Moreover, the intensities of lower and higher binding energy peaks increase whereas intensity of the central binding energy peak decreases as compared to rGO.

5.3.6 TEM and FESEM studies

TEM image 5.6 (a) shows that rGO sheet is continuous and consists of a few wrinkles, as shown by arrows in Fig. 5.6 (a), which are expected on the graphene surfaces. Fig. 5.6 (b) shows the rGO nanosheet decorated with quasi-spherical ZnO nanoparticles of size ~ 25 nm. The ZnO nanoparticles are agglomerated and randomly attached onto the surfaces of the graphene sheets. The arrows in Fig. 5.6 (b) show graphene sheet and ZnO nanoparticles anchored on it. The SAED pattern of ZrGO nanocomposite, in Fig. 5.6 (c), reveals that the ZnO nanoparticles are polycrystalline in nature with wurtzite structure, consistent with the XRD results. Fig. 5.6(d) exhibits HRTEM image of the ZrGO composite and magnified “A” region in Fig. 5.6(d) represents the HRTEM image of a rGO nanosheet which is 3 layers thick and possesses lattice fringes with estimated interplanar spacing of the order of 0.354 nm. The magnified “B” region in Fig. 5.6 (d) is the HRTEM image of an individual ZnO nanoparticle attached on the graphene surface. It reveals that

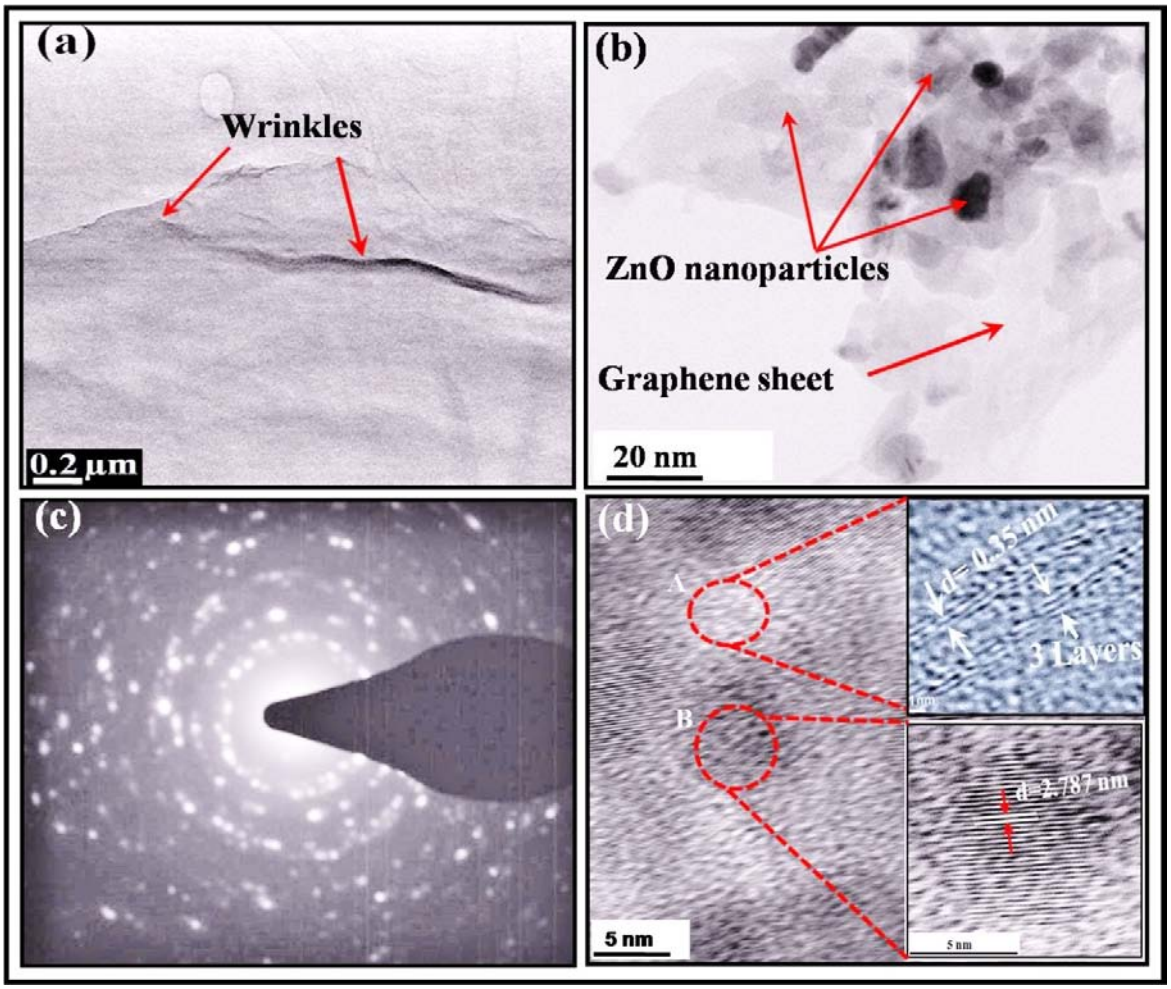

Figure 5.6: (a) TEM micrograph exhibits a continuous and wrinkled rGO nanosheet. **(b)** TEM image of rGO nanosheet decorated with quasi-spherical ZnO nanoparticles. **(c)** SAED pattern of ZrGO nanocomposite. **(d)** HRTEM image of ZrGO nanocomposite and magnified "A" represents HRTEM image of a rGO nanosheet while magnified "B" region represents HRTEM image of an individual ZnO nanoparticle attached on the graphene surface.

the lattice spacing between the two adjacent planes is of the order of 0.787 nm which corresponds to the (100) crystal plane of ZnO.

FESEM was used to study surface morphology and elemental analysis. Fig. 5.7 (a) and 5.7 (b) are the FESEM images of rGO and ZrGO powder samples, respectively. Fig. 5.7 (c) represents the EDX profile of a small physical area of ZrGO powder sample shown in Fig. 5.7 (b). The EDX profile (Fig. 5.7 (c)) exhibits strong carbon, oxygen and Zn peaks. The inset of Fig. 5.7 (c) shows the quantitative analysis of C, O and Zn in the sample. Fig.

5.7 (d) - (f) illustrate the uniform elemental distributions of C, O and Zn in the sample detected through the X-ray mapping process.

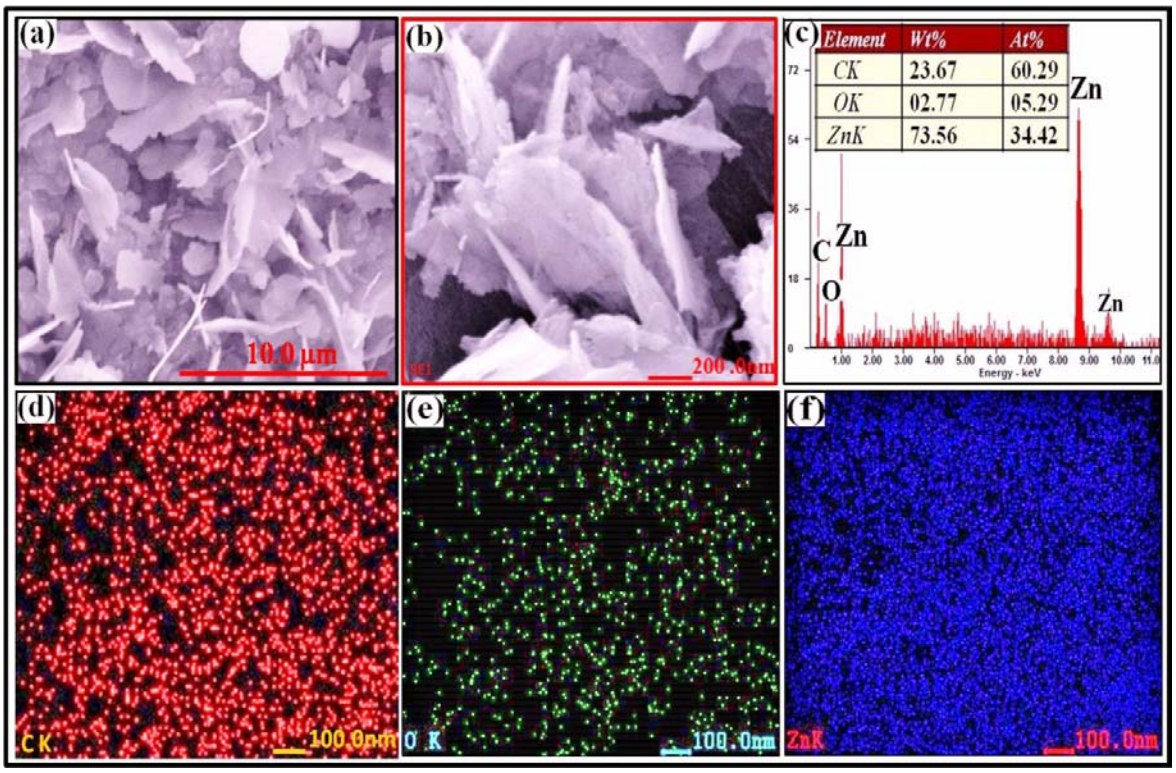

Figure 5.7: (a) and **(b)** FESEM images of rGO and ZrGO powder samples, respectively. **(c)** EDX profile of a small physical area shown in image **(b)**. **(d)** - **(f)** Uniform elemental distributions of C, O and Zn in the ZrGO sample detected after the x-ray mapping process.

5.3.7 Study of electrical properties

The electrical behavior of the as-prepared rGO and ZrGO powder samples was investigated in the temperature range 300 K-373 K with the help of two-terminal arrangement as shown in Fig. 2.9 (chapter-2) and the measured normalized resistance value of rGO is found consistent to the previously reported theoretical and experimental results [37, 38]. The resistivity of ZrGO sample is found several times lower than that of rGO. Since equal amount of GO and same synthesis technique was used for the synthesis of both rGO and ZrGO samples, therefore lower resistivity of ZrGO is the consequence of ZnO nanoparticles tightly bound to the surface of graphene sheet via electrostatic attraction between Zn^{++} and the negatively charged reduced graphene oxide sheets [39]. The *I-V* curves for rGO and ZrGO samples exhibit almost linear characteristics as shown in Fig. 5.8 (a) and (b), respectively, thus pointing to the ohmic nature of the samples in the above mentioned temperature range. This linear behavior of I-V curves exhibits the metallic natu-

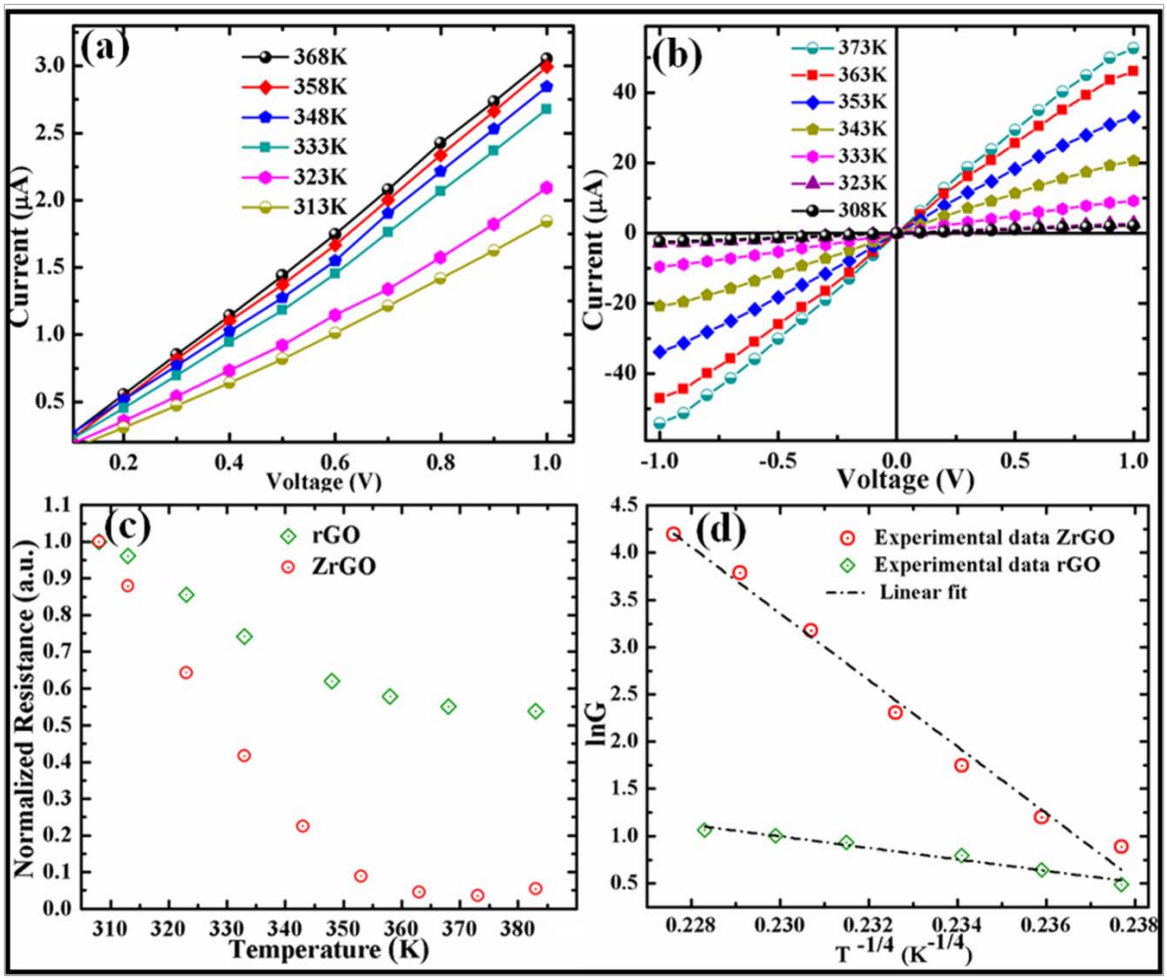

Figure 5.8: (a) *I-V* curves for rGO sample at different temperatures. **(b)** *I-V* curves for ZrGO sample at different temperatures. **(c)** Normalized resistance versus temperature curves for rGO and ZrGO samples. **(d)** lnG (conductance) versus $T^{-1/4}$ plot for rGO and ZrGO samples.

re of the rGO and ZrGO samples [40]. At a normal temperature ZrGO sample behaves as a p-type material so here we can assume that ZnO nanoparticles, decorated on the surface of rGO, shifts Fermi level downwards which increases the relative change in the resistivity as shown in Fig. 5.8 (c) [41]. However, this has to be investigated further. The conductivity of rGO is found lower than ZrGO and the possible reason for this is the presence of residual defects in rGO [42] which prevent the transport of charge carriers in it, while in case of ZrGO sample ZnO nanoparticles provide an alternating path for charge transport via hopping mechanism of charge transfer in the defected rGO. The conductivity of rGO and ZrGO samples depends on temperature and it decreases with increasing temperature as shown in Fig. 5.8 (c). However, this behavior highly depends on carrier-phonon scattering

with the temperature change [43]. Fig. 5.8 (d) represents lnG (conductance) versus $T^{-1/4}$ plot for rGO and ZrGO samples. Since rGO is a highly disordered system with low carrier density, therefore its temperature dependent transport mechanism could be analyzed with VRH model for 3D transport behavior using the general equation (5.2) [44] which fitted well to the experimental results as shown in Fig. 5.8 (d).

$$G(T) = G_1 \exp(- B/T^{1/4}) \quad (5.2)$$

where B is a constant given by $B = 2.1\ [1/(k_B\, \alpha^3\, D(\varepsilon_F))\ ]^{1/4}$, k_B is the Boltzmann constant, α is the charge carriers localization length and $D(\varepsilon_F)$ is the electronic density of states at Fermi level.

5.3.8 Study of gas sensing properties and mechanism

The chemical reduction of GO by hydrazine hydrate can not remove the oxygen containing functional groups (carboxylic and epoxide) compeletely and some of them still remain attached to the basel plane as confirmed by XPS results. These residual groups possibly increase the number of holes in the sample as these are considered to have electron-accepting behavior [45]. This is the reason, rGO normally acts as p-type semiconducting material. NO_2 gas is a strong oxidiging gas and known for its high electron withdrawing nature. When rGO and ZrGO coil sensors were exposed to different concentrations of NO_2 gas, the adsorbed electrophilic NO_2 molecules on the surfaces of rGO and ZrGO samples extract electrons from these sample surfaces. Therefore, exposure of both these sensing materials to NO_2 gas increases the number of conduction holes in the samples and hence reduces their resistance. Thus, we can conclude that NO_2 gas behaves as a p-type dopant for both rGO and ZrGO samples. Fig. 5.9 (a) shows % response (S) of the rGO and ZrGO sensors upon exposure to 50 ppm NO_2 concentration at room temperature. The % response (S) of the sensor is defined as:

$$\%\ \text{response (S)} = \left|\frac{R_g - R_a}{R_a}\right| \times 100 = \left|\frac{\Delta R}{R_a}\right| \quad (5.3)$$

where, R_a and R_g are resistances of the sensor in air and in test gas, respectively. Fig. 5.9 (a) reveals that for ZrGO sensor the values of % response (S) (14.3), response time (96 s) and recovery time (2030 s) (defined as the time required to reach 90% of the saturation value and 10% of base line value after degassing the sensing chamber, respectively) are

better than the values of % response (S) (10.8), response time (161 s) and recovery time (3340 s) for rGO sensor. This implies that ZrGO is better sensing material than rGO. Since

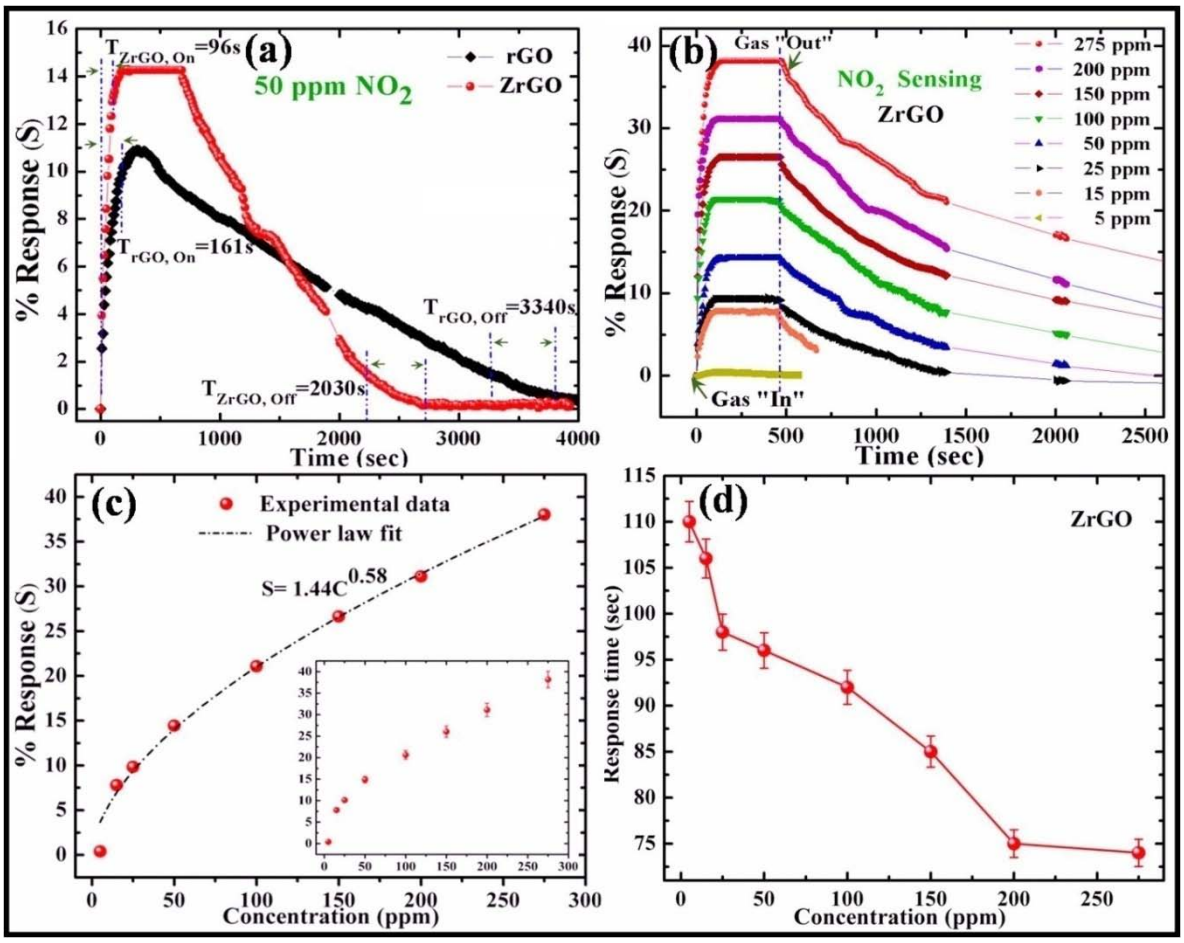

Figure 5.9: (a) % response (S) of the rGO and ZrGO sensors for 50 ppm NO_2 concentration. **(b)** % response of the ZrGO sensor for different concentrations (ppm) of NO_2 gas. **(c)** Power law fit to the % response (S) of the sensor versus NO_2 concentrations (C) and inset shows graph between the % response versus NO_2 concentrations with error bars. **(d)** Response times of the sensor as a function of different NO_2 concentrations.

all the identical parameters and equal amont of GO were used for the synthesics of rGO and ZrGO samples, therefore better sensing performance of ZrGO is attributed to the interaction of ZnO nanoparticles in this nanocomposite sample. Basically ZnO is an n-type semiconductor but in a composite its nature depends on the interaction of ZnO with graphene [46]. In ZrGO sample ZnO behaves as a p-type dopant which is confirmed by Raman spectroscopy, XPS results and better electrical properties of ZrGO than rGO sample. However, further investigation is required in order to understand the mechanism

involve in rGO - ZnO interaction for better NO_2 response of ZrGO than rGO. Fig. 5.9 (b) represents the % response (S) curves of ZrGO sensor upon exposure to different concentrations (ppm) of NO_2 gas at room temperature. Fig. 5.9 (b) reveals that the % response has sensible dependence on the concentration of NO_2 gas as it increases with increase in the concentration of the test gas. The % response for every next NO_2 concentration was measured when the sensor recovered its initial resistance value (baseline value) after degassing the sensing chamber. This sensor shows good % response above 5 ppm NO_2 concentration at room temperature. Moreover, the % response (S) of the sensor versus NO_2 concentrations (C) curve shows excellent power law ($S = AC^{\alpha}$, here A is a constant) dependence (Fig. 5.9 (c)) which arises due to the adsorption or interaction of NO_2 with the sensor surface and the change of surface potential. From this fit the calculated value of α is 0.58 which is in agreement with the predictions of rational value (1 or 1/2) for the power law exponent [47, 48]. The inset of Fig. 5.9 (c) shows the % response versus NO_2 concentrations graph with error bars. Fig. 5.9 (d) exhibits the response times curve of the sensor when exposed to different concentrations of NO_2. It revels that response time of the sensor decreases with an increase in gas concentration. This is so because at lower concentrations NO_2 molecules take longer time to equilibrate on the surface of sensing material. However, at room temperature the recovery times (not shown here) of this sensor for all concentrations have been found much larger than the response time, which is the consequence of strong chemisorption of NO_2 gas molecules on the surface of sensing material (ZrGO). The strong chemisorptions may take place due to the molecular interactions of NO_2 gas molecules with higher-energy binding sites, such as structural defects, and residual oxygen functional groups [49]. The recovery time of this sensor can be improved either by exposing it to UV light or providing some heat treatment through external source as reported previously for other graphene based sensors [50-53]. Fig. 5.10 (a) show % response (S) of the sensors for 50 ppm NO_2 concentration at different temperatures and to investigate the effect of temperature on performance of the sensor a graph is plotted between % response and temperature of the sensor (Fig. 5.10 (b)). It can be observed that the ZrGO sensor exhibits highest response (~ 32%) at 50°C which is about 2.2 times higher than the % response at room temperature and this increase in response might be due to higher rate of adsorption on the surface of ZrGO sample at 50°C. As the temperature increases bove 50°C the % response start decreasing but at the same time an improvement in the response and recovery times of the sensor has been observed. Fig. 5.10 (c) represents the variation of response and recovery times of the sensor with

respect to temperature for 50 ppm NO_2 concentration. The response and recovery times of ZrGO sensor are found to be in the range of 94-31 s and 2220-308 s, respectively. As the

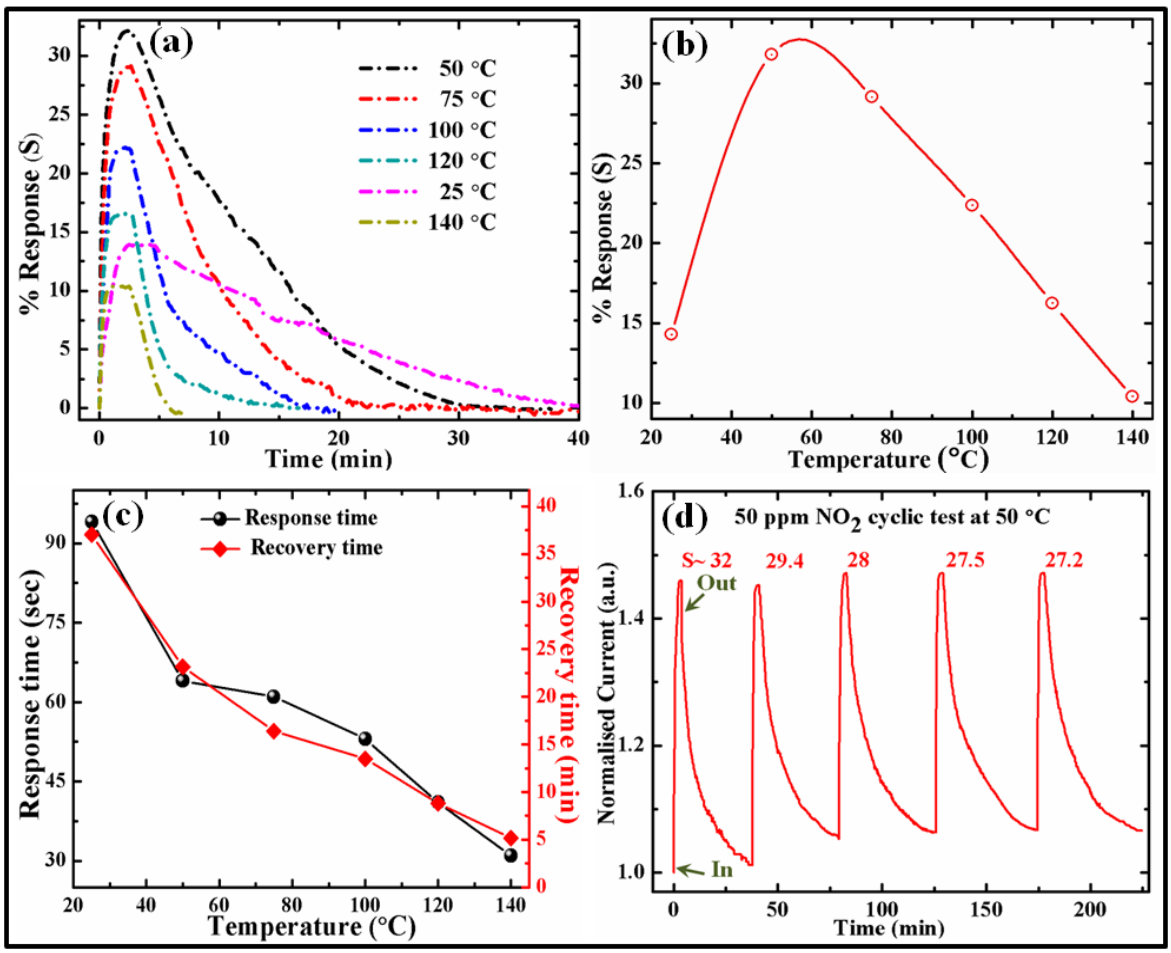

Figure 5.10: (a) % response of the sensor for 50 ppm NO_2 concentration at different temperatures. **(b)** % response versus temperature of the sensor for 50 ppm NO_2. **(c)** Variation of response and recovery times of the sensor with respect to temperature for 50 ppm NO_2 concentration and **(d)** % response of the sensors for 50 ppm NO_2 for five successive test cycles at 50 °C.

temperature increases above 50°C the sensor resistance gradually starts increasing (Fig. 5.8 (c)) and this increase in resistance may be due to surface oxidation of the reduced graphene oxide sheets in the ZrGO sample. At temperature larger than 50°C the sensor response starts decreasing upon exposure to 50 ppm concentration of oxidizing NO_2 gas which implies that above 50°C the sensing material start behaving some how like n-type material. Morover, at higher temperature the desorption of NO_2 gas molecules from the sensing surface will increase which leads to the improvement in the recovery times of the

sensor [54]. To demonstrate repeatability, ZrGO sensor was exposed to 50 ppm NO_2 for five successive cycles at 50°C and the result is shown in Fig. 5.10 (d). We observe that after repeating the sensing cycle, % response of the sensor decreases which may be attributed to the incomplete desorption of NO_2 gas molecules from the sensing surface. These remaining molecules on the sensing surface would, therefore, reduce the number of available adsorption sites for the next cycle of sensing and after a few cycles a state of saturation is reached at which the number of available adsorption sites becomes almost constant for every next cycle. The saturated value of % response of the ZrGO sensor after a few cycle is ~ 27%.

5.3.9 Effect of relative humidity (RH %) on resistance of the fabricated gas sensors

In order to explore the effect of relative humidity on resistance of the fabricated NO_2 gas sensors, we introduced different levels of relative humidity (RH%) into the test

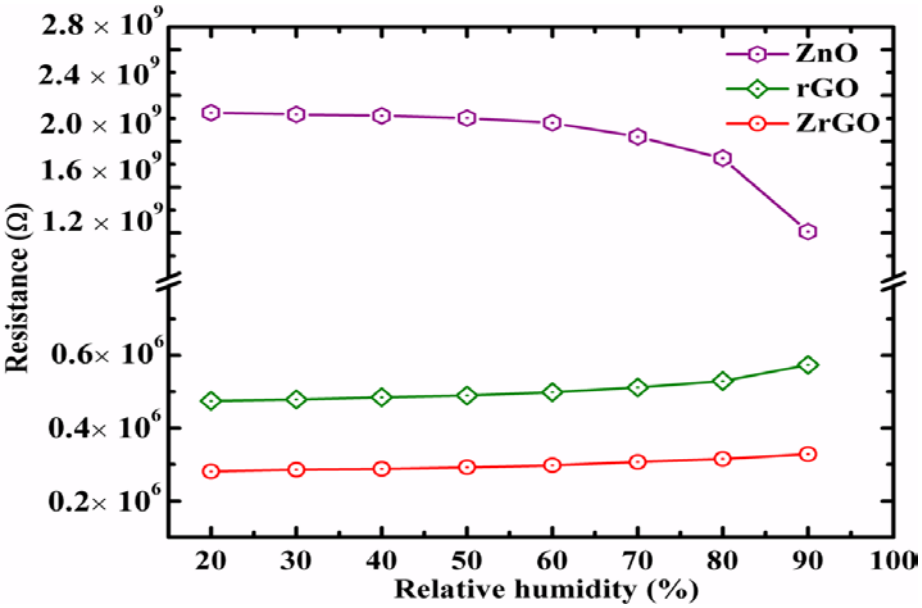

Figure 5.11: The resistance versus % relative humidity curves for ZnO, rGO and ZrGO nanocomposite.

chamber to measure the variation in resistance of the fabricated device. Fig. 5.11 represents the graphs between % relative humidity versus electrical resistance of the samples. The obtained results reveal that pristine ZnO sensor exhibits a noticeable variation in resistance after introducing 60% relative humidity. In case of rGO, the resistance varies after 70% relative humidity. The humidity effect on resistance of ZnO is due to its n-type behavior. Because, after introducing the higher humidity levels, amount of water molecules (H_2O) increases inside the test chamber which react with hexagonal ZnO structure via physical

absorption process. In this environment, water molecules release H^+ ions and OH^- is absorbed by Zn^{++}. As the H^+ ion moves freely together with the water, a decrease in the resistance of the ZnO sample is observed. Basically it happens due to occurrence of conduction process [55]. In case of the rGO, it is well established that the rGO behaves like p-type semiconductor. It means that electrical conduction in rGO persists due to dominance of holes. In this case after introducing the higher humidity, the available water molecules inside the chamber are adsorbed on the sensing surface of rGO. As, we know the available d localized π-electrons on the surface of rGO behaves like electron donor, therefore, an increase in humidity results in reduction of holes concentration in the p-type rGO which causes an increase in the resistance. It is interesting to explore the humidity effect on ZrGO nanocomposite because in this case, we observed that the stability of the nanocomposite system is higher in comparison to the pristine ZnO as well as rGO for an optimum concentration of ZnO in ZrGO nanocomposite. The observed result have good consistency with TGA data. Only slight variation in resistance was observed after introducing more than 75 % RH value which is highly desirable for gas sensing applications. The possible reason of stability as well as better sensing results may be due to optimum concentration of ZnO molecule in nanocomposite system which is controlled by introducing 20 ml of (10 mM) $ZnCl_2$ aqueous solution. We tried several concentration of $ZnCl_2$ solution ranging from 5-15 mM $ZnCl_2$ solution in 20 ml aqueous solution of GO. Beyond, 10 mM $ZnCl_2$ solution, the nanocomposite system behaves like pristine ZnO surface due to access deposition of ZnO molecules on rGO nanosheet surfaces. Similarly, lower concentration of $ZnCl_2$ (<10mM), the nanocomposite system behaves like rGO surfaces due to uncovered decorated ZnO molecules on rGO nanosheets. Particularly, at optimum concentration, all the available delocalized π-electrons conjugated with in-situ formation of ZnO molecules and cover all possible surface of rGO nanosheet, as a result, it exhibits excellent sensing property.

5.4 CONCLUSIONS

In this chapter, we synthesized rGO and ZrGO powder samples via hydrolysis method. Here we designed a two terminal device with heating coil and thermocouple to study the temperature dependent electrical and NO_2 gas sensing properties of rGO and ZrGO powder samples. The main highlights of the work discussed here are given below:

1. XRD, TGA, FTIR, RAMAN, XPS, TEM, FESEM and EDX measurements confirm the successful synthesis of GO, rGO and ZrGO composite samples. The elemental mapping evidences the homogeneous distribution of ZnO nanoparticles on the surface of rGO sheets in ZrGO sample.
2. TEM analysis reveals that rGO sheets are few layers thick and the size of ZnO nano particles attached with the sheets is smaller than 25 nm. .
3. TGA reveals that the thermal stability of ZrGO composite is much better than GO and rGO.
4. ZrGO composite possesses several times higher electrical conductivity than rGO and for 50 ppm NO_2 gas, ZrGO sensor exhibits higher % response and better response and recovery times than rGO sensor.
5. The ZrGO nanocomposite sensor shows highest response (~32%) for 50 ppm NO_2 at 50°C.
6. From the humidity results we observed that with increase in % relative humidity level the resistance of ZnO sensor decreases while that of rGO sensor increases and the resistance of ZrGO composite sensor exhibits a very little increment.

In summary, good quality rGO and ZrGO powder samples were synthesized and their electrical and NO_2 gas sensing properties were investigated. We also investigated the effect of % relative humidity levels on the resistance of the ZnO, rGO and ZrGO samples. We believe that present work can be extended to synthesize the various composite of graphene with other metal oxides and can be helpful to investigate their sensing properties for various gases at different temperatures.

REFERENCES

1. A. K. Geim, “Graphene: Status and prospects”, Science, **324**, 1530 (2009).
2. A. K. Geim, K. S Novselov, “The rise of graphene”, Nat. Mater., **6**, 191 (2007).
3. E. V. Castro, K. S. Novoselov, S. V. Morozov, N. M. R. Peres, J. M. B. L. dos Santos, J. Nilsson, F. Guinea, A. K. Geim, A. H. C. Neto, “Biased bilayer graphene: semiconductor with a gap tunable by the electric field effect”, Phys. Rev. Lett., **99**, 216802 (2007).
4. X. Du, I. Skachko, A. Barker, E. Y. Andre, “Approaching ballistic transport in suspended graphene”, Nat. Nanotechnol., **3**, 491(2008).
5. K. S. Novoselov, Z. Jiang, Y. Zhang, S. V. Morozov, H. L. Stormer, U. Zeitler, J. C. Maan, G. S. Boebinger, P. Kim , A. K. Geim, “Room-temperature quantum hall effect in graphene”, Science, **315**, 1379 (2007).
6. M. D. Stoller, S. Park, Y. Zhu, J. An, R. S. Ruoff, “Graphene-based ultracapacitors”, Nano Lett., **8**, 3498 (2008).
7. M. I. Katsnelson, K. S. Novoselov, A. K. Geim, “Chiral tunneling and the Klein paradox in graphene”, Nat. Phys., **2**, 620 (2006).
8. JI. Paredes, S. Villar-Rodil, A. Martinez-Alonso, J. M. D. Tascon, “Graphene oxide dispersions in organic solvents”, Langmuir, **24**, 10560 (2008).
9. N. T. Hu, Y. Y .Wang, J. Chai, R. G. Gao, Z. Yang, E. S. W. Kong, Y. F. Zhang, “Gas sensor based on p-phenylenediamine reduced graphene oxide”, Sens. Actuators B, **163**, 107 (2012).
10. W .Yuan, G. Shi, “Graphene-based gas sensors”, J. Mater. Chem., **A 1**, 10078 (2013).
11. Y. P. Dan, Y. Lu, N. J .Kybert, Z. T. Luo, A. T. C. Johnson, “Intrinsic response of graphene vapor sensors”, Nano Lett., **9**, 1472 (2009).
12. G. H. Lu, S. Park, K. H. Yu, R. S. Ruoff, L. E. Ocola, D. Rosenmann, J. H. Chen, “Toward practical gas sensing with highly reduced graphene oxide: a new signal processing method to circumvent run-to-run and device-to-device variations”, Acs Nano, **5**, 1154 (2011).
13. M. Gautam, A. H. Jayatissa, “Ammonia gas sensing behavior of graphene surface decorated with gold nanoparticles”, Solid-State Electron., **78**, 159 (2012).

14. G. Singh, A. Choudhary, D. Haranath, Amish G. Joshi Nahar Singh, S. Singh, R. Pasricha, "ZnO decorated luminescent graphene as a potential gas sensor at room temperature" Carbon, **50**, 385 (2012).
15. L. Talazac, J. Brunet, V. Battut, J. P. Blanc, A. Pauly, Germain Pellier S, C. Soulier, "Air quality evaluation by monolithic InP-based resistive sensors", Sens. Actuators B, **76**, 258 (2001).
16. D. C. Marcano, D. V. Kosynkin, J. M. Berlin, A. Sinitskii, Z. Sun, A. Slesarev, L. B. Alemany, W. Lu, J. M. Tour, "Improved synthesis of graphene oxide", ACS Nano, **4** (8), 4806 (2010).
17. C. Hontoria-Lucas, A. J. Lopez-Peinado, J. D. D. Lopez-Gonzalez, M. L. Rojas-Cervantes, R. M. Martin-Aranda, "Study of oxygen-containing groups in a series of graphite oxides: physical and chemical characterization", Carbon, **33**(11), 1585 (1995).
18. D. A. Dikin, S. Stankovich, E. J. Zimney, R. D. Piner, G. H. B. Dommett, G. Evmenenko, S. T. Nguyen, R. S. Ruoff, "Preparation and characterization of graphene oxide paper", Nature, **448**, 457 (2007).
19. S. Stankovich, D. A. Dikin, R. D. Piner, K. A. Kohlhaas, A. Kleinhammes, Y. Jia, Y. Wu, S. T. Nguyen, R. S. Ruoff, "Synthesis of graphene-based nanosheets via chemical reduction of exfoliated graphite oxide" Carbon, **45**, 1558 (2007).
20. Z. Fan , K. Wang, T. Wei, J. Yan, L. Song, B. Shao, "An environmentally friendly and efficient route for the reduction of graphene oxide by aluminum powder", Carbon, **48**, 1686 (2010).
21. N. Hu, R. Gao, Y. Wang, Y. Wang, J. Chai, Z. Yang, E. S.-W. Kong, Y. Zhang, "The preparation and characterization of non-covalently functionalized graphene", J. Nanosci. Nanotechnol., **12**, 99 (2012).
22. G. Wang, Z. Yang, X. Li, C. Li, "Synthesis of poly (aniline-co-o-anisidine)-intercalated graphite oxide composite by delamination/reassembling method", Carbon, **43**(12), 2564 (2005).
23. S. Wang, P.-J. Chia, L.-L. Chua, L.–H. Zhao, R.-Q. Png, S. Sivaramakrishnan, M. Zhou, R. G.-S. Goh, R. H. Friend, A. T.–S. Wee. Peter K.-H. Ho, "Band-like transport in surface-functionalized highly solution-processable graphene nano sheets", Adv. Mater., **20**, 3440 (2008).

24. R.Y. Hong, J. H. Li, L. L. Chen, D. Q. Liu, H. Z. Li, Y. Zheng, J. Ding, "Synthesis, surface modification and photocatalytic property of ZnO nanoparticles", Powder Technol., **189**, 426 2009).
25. M. A. Pimenta, G. Dresselhaus, M. S. Dresselhaus, L. G. Cancado, Z. A. Jorio, R. Saito, "Studying disorder in graphite-based systems by Raman spectroscopy", Phys. Chem. Chem. Phys., **9**, 1276 (2007).
26. V. Pachauri, C. Subramaniam, T. Pradeep, "Novel ZnO nanostructures over gold and silver nanoparticle assemblies", Chem. Phys. Lett., **423**, 240 (2006).
27. X.-Yun Ye, Y.-M. Zhou, Y.-Q. Sun, J. Chen, Z.-Q. Wang, "Preparation and characterization of Ag/ZnO composites via a simple hydrothermal route", J. Nanopart Res., **11**, 1159 (2009).
28. R. Cusco, E. A.-Llado, J. Ibanez and L. Artus, "Temperature dependence of Raman scattering in ZnO", Phys. Rev. B, **75**, 165202 (2007).
29. L. S. Panchakarla, K. S. Subrahmanyam, S. K. Saha, A. Govindaraj, H. R. Krishnamurthy, U. V. Waghmare, C. N. R. Rao, "Synthesis, structure and properties of Boron and Nitrogen-doped graphene", Adv. Mater., **21**, 4726 (2009).
30. Y. Y. Hui, G. Tai, Z. Sun, Z. Xu, N. Wang, F. Yan, S. P. Lau, "n- and p-Type modulation of ZnO nanomesh coated graphene field effect transistors", Nanoscale, **4,** 3118 (2012).
31. T. N. Narayanan, Z. Liu, P. R. Lakshmy, W. Gao, Y. Nagaoka, D. S. Kumar, Jun Lou, R. Vajtai, P. M. Ajayan, "Synthesis of reduced graphene oxide–Fe_3O_4 multifunctional freestanding membranes and their temperature dependent electronic transport properties", Carbon, **50**, 1338 (2012).
32. B. Jayasena, S. Subbiah, "A novel mechanical cleavage method for synthesizing few-layer graphenes", Nanoscale Res. Lett., **6**(95), 1 (2011).
33. A. Prakash, S. K. Misra, D. Bahadur, "The role of reduced graphene oxide capping on defect induced ferromagnetism of ZnO nanorods", Nanotechnology, **24**, 095705 (2013).
34. Q. Su, S. Pang, V. Alijani, C. Li, X. Feng, K. Mullen, "Composites of graphene with large aromatic molecules", Adv. Mater., **21**(31), 3191 (2009).
35. L. Al-Mashat, K. Shin, K. K.-zadeh, J. D. Plessis, S. H. Han, R. W. Kojima, R. B. Kaner, D.Li, X. Gou, S. J. Ippolito, W. Wlodarski, "Graphene/polyaniline nanocomposite for Hydrogen sensing", J. Phys. Chem. C, **114**, 16168 (2010).

36. R. Rozada, J. I. Paredes, S. V.-Rodil, A. M.-Alonso, J. M. D. Tascon, "Towards full repair of defects in reduced graphene oxide films by two-step graphitization", Nano Res., **6**(3), 216 (2013).
37. F. Vasko, V. Ryzhii, "Voltage and temperature dependencies of conductivity in gated graphene", Phys. Rev. B, **76**, 233404 (2007).
38. Q. Shao, G. Liu, D. Teweldebrhan, A. A. Balandin, "High-temperature quenching of electrical resistance in graphene interconnects", Appl. Phys. Lett., **92**, 202108 (2008).
39. S. Stankovich, R. D. Piner, X. Q. Chen, N. Q. Wu, S. T. Nguyen, R. S. Ruoff, "Stable aqueous dispersions of graphitic nanoplatelets via the reduction of exfoliated graphite oxide in the presence of poly(sodium 4-styrenesulfonate)", J. Mater. Chem., **16** 155 (2006).
40. O. Akhavan, E. Ghaderi, "Escherichia coli bacteria reduce graphene oxide to bactericidal graphene in a self-limiting manner", Carbon, **50** 1853 (2012).
41. G. Giovannetti, P. A. Khomyakov, G. Brocks, V. M. Karpan, J. van den Brink, P. J. Kelly, "Doping graphene with metal contacts", Phys. Rev. Lett., **101** 026803 (2008).
42. V. Lopez, R. S. Sundaram, C. G.-Navarro, D. Olea, M. Burghard, J. G.-Herrero, F. Zamora, K. Kern, "Chemical vapor deposition repair of graphene oxide: a route to highly conductive graphene monolayers", Adv. Mater., **21**, 4683 (2009).
43. A. Seeger, K. Clausecker, "A new method for solving the boltzmann equation for electrons in crystals", phys. status solidi B, **46** (1), 137 (2006).
44. J. R. Hauptmann, T. Li, S. Petersen, J. Nygard, P. Hedegard, T. Bjornholm, B. W. Laursen, K. Norgaard, "Electrical annealing and temperature dependent transversal conduction in multilayer reduced graphene oxide films for solid-state molecular devices", Phys. Chem. Chem. Phys., **14**, 14277 (2012).
45. S. Gilje, S. Han, M. Wang, K. L. Wang, R. B. Kaner, "A chemical route to graphene for device applications", Nano Lett., **7**, 3394 (2007).
46. W. Geng, X. Zhao, H. Liu, X. Yao, "Influence of interface structure on the properties of ZnO/graphene composites: a theoretical study by density functional theory calculations", J. Phys. Chem. C, **117**, 10536 (2013).
47. N. S. Ramgir, M. Ghosh, P. Veerender, N. Datta, M. Kaur, D. K. Aswal, S. K. Gupta, "Growth and gas sensing characteristics of p- and n-type ZnO nanostructures", Sens. Actuators B, **156**, 875 (2011).

48. N. Yamazoe, K. Shimanoe, “Theory of power laws for semiconductor gas sensors”, Sens. Actuators B, **128**, 566 (2008).
49. J. T. Robinson, F. K. Perkins, E. S. Snow, Z. Q Wei, P. E. Sheehan, “Reduced graphene oxide molecular sensors”, Nano Lett., **8**, 3137 (2008).
50. D. R. Patil and L. A. Patil, “Ammonia sensing resistors based on Fe_2O_3-modified ZnO thick films”, Sensors IEEE, **7**, 434 (2007).
51. I. S. Kang, H. M. So, G. S. Bang, J. H. Kwak, J. O. Lee, C. W. Ahn, “Recovery improvement of graphene-based gas sensors functionalized with nanoscale heterojunctions”, Appl. Phys. Lett., **101,** 123504 (2012).
52. F. Yavari, Z. Chen, A. V. Thomas, W. Ren, H. M. Cheng, N. Koratkar, “High sensitivity gas detection using a macroscopic three-dimensional graphene foam network”, Scientific Rep., **1**, 166 (2011).
53. G. Lu, L. E. Ocola, J. Chen, “Gas detection using low-temperature reduced graphene oxide sheets”, Appl. Phys. Lett., **94**, 083111 (2009).
54. P. Qi , O. Vermesh , M. Grecu , A. Javey , Q. Wang, H. Dai, S. Peng, K. J. Cho, “Toward large arrays of multiplex functionalized carbon nanotube sensors for highly sensitive and selective molecular detection”, Nano Lett., **3** (3), 347 (2003).
55. J. Shah, R. K. Kotnala, “Humidity sensing exclusively by physisorption of water vapors on magnesium ferrite”, Sens. Actuators B, **171**, 832–837 (2012).

CONCLUSIONS AND RECOMMENDATIONS

CONCLUSIONS

In this chapter, we briefly summarize the work as presented in the chapters 3-5 of this thesis. In this chapter we have also added the overall comments and conclusive remarks. This thesis contains the synthesis and study of nanostructures in powder forms like ZnO nanowires, GO (graphene oxide), rGO (reduced graphene oxide) and rGO-ZnO nanocomposite (ZrGO) as well as thin films such as GO, rGO. The main aim of this thesis work was to synthesize ordered ZnO nanowires, GO, rGO thin films, rGO and ZrGO nanocomposite and study their electrical and gas sensing properties. In order to investigate the electrical and gas sensing properties of such synthesized powder nanostructures and thin films we designed proper gas sensing set-ups. The summary of the work presented in chapters 3-5 is described below.

1. In the third chapter we described the synthesis of porous anodic alumina (AAO) template and its detaching process from the Al substrate. FESEM analysis shows that in detached AAO template nanopores are open through with diameter ~ 45–50 nm. We have observed that such synthesized AAO templates possesses pore density of the order of 0.94×10^{10} cm^{-2}. When detached AAO template is dipped into 6 wt% phosphoric acid solution for 25 min at room temperature, the diameter of its pores increase up to ~65 nm. After this pore widening process empty pores of AAO template were filled with saturated Zn $(NO_3)_2$ solution via indigenously developed vacuum injection technique. Filled AAO template was first dried in an electric oven at ~ 70°C for 6 h and after that annealed at 435°C for 40 h in order to obtain wurtzite ZnO nanowires. To get ZnO nanowires, filled and annealed AAO template was dissolved in 0.1 M NaOH solution and the floating material was collected on the surface of a razor blade. FESEM micrographs show that such synthesized ZnO nanowires are 11 μm long and have diameters between 60-70 nm. TEM analysis reveals that ZnO nanowires are polycrystalline in nature and possess hexagonal wurtzite crystal structure. Micrographs show that ZnO nanowires are continuous

and uniform throughout the length. The photoluminescence spectra reveal that the AAO/ZnO assembly, pristine AAO template and ZnO nanowires have strong green emission peaks at 490, 502 and 462 nm upon excitation at a wavelength of 406 nm. We observed that the intensity of AAO/ZnO assembly emission spectra is ~ 2.5 times higher than the intensity of ZnO nanowire emission spectra. We proposed that AAO plays a key role in enhancing the green emission in the AAO/ZnO hybrid structure. The strong interface formed during synthesis of ZnO nanowires on the AAO template, which creates higher defect densities in ZnO, gives rise to higher PL intensity in comparison to pristine ZnO and pristine AAO. In order to investigate the electrical and gas sensing properties of as synthesized ZnO nanowire array we designed a simple sensing system using micromechanical technique. Here, we used dielectrophoresis process to trap a ZnO nanowires in the gap between two Cu electrodes. Such fabricated sensing device is basically a metal–semiconductor–metal (MSM) structure which exhibits symmetric *I-V* characteristics. The resistance of this sensor is of the order of 6 GΩ and this is due to ZnO being a wide bandgap semiconductor (Eg = 3.3 eV) at room temperature. Here we investigated the response of this sensor for different concentrations (10, 15, 25, 50, 75, 100 and 150 ppm) of NH_3 gas at room temperature. ZnO nanowires are generally n-type and in an open atmosphere, the adsorbed oxygen ions (O^{2-}, O^- and O^{2-}) extract electrons from the conduction band and thus increases the resistance of the sensor. In NH_3 atmosphere, NH_3 interacts with O^{2-} species, adsorbed at the sensor surface and the trapped electrons are released back into the ZnO conduction band leading to a decrease in sensor resistance. We observe that the resistance of this sensor decreases significantly with increase in the value of NH_3 concentration. For 50 ppm NH_3 concentration the values of % response, response time and recovery time of this sensor are ~ 68%, ~28 s and ~29 s, respectively. It was noticed that % response of this sensor increases almost linearly with increase in NH_3 concentration up to 75 ppm and for concentration values higher than this, % response increases slowly. So we conclude that at room temperature this sensor suits well for lower concentrations of NH_3 and saturates at higher values.

2. In the fourth chapter we studied the electrical, optical, gas sensing and anti bacterial properties of graphene oxide (GO) and reduced graphene oxide (rGO) thin films. Starting material GO powder was synthesized via "Improved synthesis of graphene oxide" method. A dispersion of GO powder in ethanol (6 mg/ml) was used to fabricate GO thin film (~15 nm) on the precleaned quartz substrate via spin coater and hydrazine vapor was used to reduce GO thin film into rGO. Microscopic techniques such as FESEM, TEM, HRTEM and AFM reveal that rGO thin film is ~15 nm thick, continuous, uniform and possesses a few wrinkles on its surface. XRD peak of substrate dominates the thin film characteristic peak of rGO and to verify this fact we have shown the XRD pattern of GO and rGO powder samples. HRTEM image of rGO thin film shows the lattice fringe with spacing of 0.354 nm, which correspond to the (002) plane of graphite. Raman spectra, XPS and UV-visible spectra confirm the reduction of GO into rGO. The PL emission spectra of rGO thin film exhibits broader peak at around 728 nm upon excitation at a wavelength of 468 nm which is attributed to the different size distribution of sp^2 clusters in the rGO lattice. We have observed that after reduction of GO thin film to rGO CIE (International Commission on Illumination) coordinates shift from x=0.6796, y= 0.3204 to x= 0.6869, y= 0.3131 and a quenching of PL signal in rGO thin film is attributed to the percolation of the sp^2 clusters generated after reduction of GO to rGO and removal of oxygen containing groups in the process. For the investigation of electrical and gas sensing properties of rGO thin film we designed a sensor base with four probe and nichrome heater. Electrical behavior of rGO thin film was investigated in the temperature of 293 K-473 K. *I-V* curves reveal that rGO thin film with four probe contacts shows ohmic behavior. We also observed that resistance of rGO thin film decreases exponentially with increase in temperature which is a characteric of semiconductor. These two properties collectively suggest that rGO thin film behaves as semi-metal. Gas sensing properties of rGO thin film were investigated in a self designed sensing set-up. Here different concentrations of Cl_2 and NO_2 gases were inserted into the sensing chamber through the inlet valve with the help of a calibrated plastic syringe and variation in system resistance was recorded at room temperature and atmospheric pressure. Being strong oxidizing gases Cl_2 and NO_2 behave as p-type dopants for

the rGO thin film. Therefore, on exposing the sensor to Cl_2 and NO_2 gases the number of conduction holes in the sample increase and hence a decrease in the resistance of the thin film sensor is observed. The % resonse of this sensor increases almost linearly with increasing the concentrations of both the test gases (Cl_2 and NO_2) up to 30 ppm. However, this sensor exhibits higher value of % response (S) for Cl_2 gas than that of NO_2 and for 50 ppm Cl_2 and NO_2 gases the response times of this sensor are ~36s and ~45 s, respectively. In this chapter we have also investigated the antibacterial properties of GO and rGO thin films against both Gram +ve (B. cereus) and Gram -ve (E. coli) models of bacteria. Here we observed that in comparasion to GO thin film, rGO film exhibits better bacterial toxicity for both the bacteria.

3. In the fifth chapter we investigated the electrical and gas sensing properties of rGO powder and rGO-ZnO nanocomposite (ZrGO). In this chapter we synthesized rGO and ZrGO powder samples via hydrolysis method followed by annealing in nitrogen atmosphere at 500 °C for 5 h. The XRD pattern of ZrGO sample confirms the presence of wurtzite ZnO particles in the composite and a small broad peak at $2\theta \sim 25°$ corresponding to (002) plane of graphite verifies the existence of rGO in ZrGO nanocomposite. TGA results show that rGO sample is thermally more stable than GO because a large number of oxygen containing functional groups have been removed during synthesis as a result of reduction process. We observed that the stability of ZrGO nanocomposite is even much better than rGO which implies that addition of ZnO nanoparticles increase the thermal stability of graphene Oxide (GO). FTIR, Raman spectra and XPS studies give information about sample quality and extent of graphitization. In the Raman spectra of graphitic materials like graphene, G band position is highly sensitive to the impurity doping in the sample. In the Raman spectra of ZrGO sample G band position shifts to higher frequency in comparison to the G band position of pristine rGO sample. This blue shift in the position of G band is attributed to the electron accepting behavior of ZnO nanoparticles in ZrGO composite sample. In the similar way C-C peak in the XPS high resolution spectrum of ZrGO shifts a little bit towards lower binding energy which implies that in ZrGO composite sample ZnO behaves as a p-type dopant. Through Raman study we observed that ZrGO sample possesses smaller in-plane

crystallite size (*La*) compared to the GO and pristine rGO. TEM analysis shows that rGO sheets are continuous with a few wrinkles and quasi-spherical ZnO nanoparticles of size 20-25 nm are agglomerated and randomly attached onto these. SAED pattern of ZrGO nanocomposite reveals that ZnO nanoparticles are polycrystalline in nature with wurtzite structure. HRTEM image shows that rGO nanosheet is about 3 layers thick with estimated inter-planar spacing of the order of 0.354 nm. FESEM micrographs and X-ray elemental mapping show that ZnO nanoparticles are uniformly distributed in ZrGO composite. To investigate the electrical and gas sensing properties of rGO and ZrGO powder samples we design a two Pt electrode coil sensor with nichrome heater and a K-type thermocouple. Results show that resistivity of ZrGO sample is several time lower than the resistivity of rGO. The *I-V* curves for rGO and ZrGO samples, in the temperature range 300 K-373 K, exhibit almost linear characteristics which represent the ohmic nature of the samples. We observed that conductivity of both rGO and ZrGO samples decreases with increasing temperature. Being highly disordered systems the temperature dependent transport mechanism in rGO and ZrGO samples were analyzed through VRH model for 3D transport behavior which, fitted well to the experimental results. At room temperature for 50 ppm concentration of NO_2 gas, ZrGO based sensor exhibits better % response (14.3), response time (96 s) and recovery time (2030 s) in comparasion to % response (S) (10.8), response time (161 s) and recovery time (3340 s) for rGO sensor. Thus we conclude that for NO_2 gas sensing ZrGO is a better material than rGO and such performance of ZrGO is attributed to the interaction of ZnO nanoparticles with rGO in this nanocomposite sample. Here we observed that at room temperature this sensor exhibits good % response above 5 ppm NO_2 concentration and % response increases with increase in the concentration of this test gas. We have also investigated the effect of temperature on % response of the ZrGO sensor for 50 ppm NO_2 concentration. We observed that ZrGO sensor exhibits highest response (~ 32%) at 50°C and as the temperature increases bove 50°C the % response start decreasing but at the same time an improvement in the response and recovery times of the sensor has been observed. We have also checked the behaviour of ZrGO sensor for five successive cycles of 50 ppm NO_2 at 50°C. It is noticed that initially after each cycle %

response decreases but latter it become constant. The decreases in % response after sensing cycle is possibly attributed to the incomplete desorption of NO_2 gas molecules from the sensing surface. We have also investigated the effect of relative humidity (RH%) on the resistance of ZnO, rGO and ZrGO samples. Here as the level of RH% in the test chamber increases the resistance of ZnO sensor decreases while that of rGO sensor increase and the resistance of ZrGO composite sensor exhibit a very little increment.

Thus based on the present thesis work finally we concluded that ordered ZnO nanowire array based gas sensor exhibits excellent NH_3 gas sensing properties at room temperature and multifunctional rGO thin films show good electrical conductivity, optical properties, Cl_2 and NO_2 gas sensing properties and bacterial toxicity. rGO-ZnO nanocomposite (ZrGO) sample exhibits better electrical and NO_2 gas sensing properties than that of rGO sample.

FUTURE RECOMMENDATIONS

1. Effect of other interferences gases such as CO, NO and O_3 etc. on the sensing properties of ZnO nanowire array based gas sensor and ZrGO composite sensor requires investigation. This will help in improving the quality of these sensors.
2. Since gas sensing properties depend on porosity of the sensing material therefore, in future by controlling the thickness of different material films on the porous AAO substrate we can examine the gas sensing properties of different materials.
3. Vacuum injection technique, which we have developed to synthesis ordered ZnO nanowires can be extended to nanowire array of other metal/metal oxides.
4. We have synthesize rGO-ZnO nanocomposite and observed that it possesses better gas sensing properties in comparison to pristine rGO. In the same way we can synthesize nanocomposite of rGO with different metal oxides can investigate their electrical as well as gas sensing properties.